7-20-2015

Development of Perovskite/Fluorite based Materials for Oxygen Transport Membrane System

Sapna Gupta
University of Connecticut - Storrs, sapnitt@gmail.com

Development of Perovskite/Fluorite based Materials for Oxygen Transport Membrane System

Sapna Gupta, Ph.D.

University of Connecticut, 2015

Judicious selection of mixed ionic–electronic conducting (MIEC) perovskite oxide as oxygen transport membrane (OTM) offers the potential to enhance overall process economics and systems performance for a wide variety of industrial applications ranging from clean and efficient energy conversion (oxy-combustion) to selective gas separation (high purity oxygen production) and value added chemicals (syngas and liquid fuel) production with near-zero greenhouse gas emissions.

Lanthanum chromite (perovskite) and aliovalent doped zirconia (fluorite) based composites have been considered as promising material of choice for use as electrochemically active components in oxygen transport membrane. Inter–cationic diffusion and formation of secondary compounds due to the interaction between the perovskite and fluorite, however, modifies the thermo-physical and electrochemical properties of such systems leading to the performance and structural degradation. The properties of the lanthanum chromite, required for optimum oxygen transport can be tuned and stabilized through selection of dopant's type and level.

In this study, phase transformation, stability and thermal-electrical properties of un-doped lanthanum chromite ($LaCrO_3$) have been evaluated. Furthermore, the role of various A (Sr) and B-site (Mn, Fe, Ni and Ti) dopants on the crystal structure, densification, electrical conductivity, thermal expansion, electrochemical performance and thermochemical stability of lanthanum

chromite is investigated to enlighten ‘composition-structure-property-stability’ correlations and achieve OTM materials requirement. The effect of oxygen partial pressure and Cr: M (B-site dopants; e.g. Fe) ratio on the processing (sintering behavior), thermal-electrical properties and stability (surface, bulk and interfacial) of $La_{1-x}Sr_xCr_{1-y}M_yO_{3-\delta}$ (with and without fluorite phase) are studied in detail. Perovskite – fluorite interactions in the composite results in the secondary compound formation (e.g. $SrZrO_3$) during exposure to reducing atmospheres. Mechanisms for the formation of the secondary compounds are established.

This study demonstrates the stability of lanthanum chromite based materials increases with increase in Cr:M ratio. In contrast, densification and performance decreases with the increase in the ratio. Optimization of the required properties is accomplished by introducing variation in the doping type and level of A-site (alkaline earth metals; Sr) and B-site (transition metals; Mn, Fe, Ni and Ti) dopants. In summary, this thesis presents the research work performed on the fundamental understanding and development of the perovskite/fluorite based materials for oxygen transport membrane system. The materials stability and performance are also demonstrated utilizing real-world OTM fabrication and operating conditions.

Development of Perovskite/Fluorite based Materials for Oxygen Transport Membrane System

Sapna Gupta

B.Tech., National Institute of Technology (NIT), Tiruchirappalli, 2010

A Dissertation

Submitted in Partial Fulfillment of the

Requirements for the Degree of

Doctor of Philosophy

at the

University of Connecticut

2015

APPROVAL PAGE

Doctor of Philosophy Dissertation

Development of Perovskite/Fluorite based Materials for Oxygen Transport Membrane System

Presented by

Sapna Gupta, B.Tech.

Major Advisor_____
Prabhakar Singh

Associate Advisor_____
Steven Suib

Associate Advisor_____
Jonathan Lane

Associate Advisor_____
Ramamurthy Ramprasad

Associate Advisor_____
Ugur Pasaogullari

University of Connecticut

2015

Acknowledgements

I would like to thank my major advisor Professor Prabhakar Singh for his support and guidance through my Ph.D. years at the Center for Clean Energy Engineering (C2E2), and for encouraging my participation in the leadership/outreach activities that helped in my professional growth. I am grateful to thank the Emeritus Prof. K.T. Jacob from the Indian Institute of Science for his immense support and encouragement to pursue my doctoral studies. I would like to thank my advisory committee of Dr. Jonathan Lane, Prof. Steven Suib, Prof. Ramamurthy Ramprasad and Prof. Ugur Pasaogullari for their help and suggestions throughout my Ph.D. I would also like to acknowledge Prof. Pamir Alpay for his support as Materials Science and Engineering (MSE) Head of Department.

I am thankful to my past and present research group members: Michael Keane, Manoj Mahapatra, Na Li, Gavin Ge, Keling Zhang, Boxun Hu, Kailash Patil, Mahesh Venkataraman, Su Heo, Chiying Liang, Byung Jun and Gyuho Song for their helpful discussions and making the lab an enjoyable experience. I would also like acknowledge my other C2E2 (Rishabh, Venkat and Guangliang) and MSE (Austin, Alan, Chen, Nasser, Cheng, Louis, Adam and Jim) colleagues for their support, encouragement and making my graduate school life a pleasant experience.

I am happy to acknowledge the Center staff including Mark and Garry for helping me in setting up my experiments, and also Terry, Sheila, Raelene and Amy for their administrative assistance. Thanks to Mark and Joe in the machine shop for designing and fabricating parts for my experimental setups. C2E2 and IMS are acknowledged for providing analytical support and characterization test facility. I would also like to thank Roger for his help in conducting FIB/TEM based characterization.

Praxair Inc. (Praxair Technology Center) is specially acknowledged for providing materials and technical support for my research studies. Thanks to my intern manager Dr. Jonathan Lane and supervisor Dr. Pawel Plonczak and other team members including Dr. Jamie Wilson, Dr. Max Christie, Dr. Zigui Lu, Mr. Tim Schwartz, Mr. Arthur Grant and Mr. Javier Gonzalez for their direction and insight during my internship at Praxair Inc.

Financial support from US Department of Energy (DE-FC26-07NT43088), Praxair Inc., and the Center for Clean Energy Engineering are much appreciated.

I would also like to thank "Connecticut Technology Council" for honoring with the "2015 Woman of Innovation" award in the category of "Collegian Innovation and Leadership".

A special thanks to my parents, family and friends for their ongoing love, unconditional support and motivation for years.

Table of Contents

LIST OF FIGURES

CHAPTER 1: INTRODUCTION

LIST OF TABLES

CHAPTER 1: INTRODUCTION

CHAPTER 2: PHASE TRANSFORMATION, ELECTRICAL CONDUCTIVITY AND THERMAL EXPANSION OF LANTHANUM CHROMITE

CHAPTER 3: ELECTROCHEMICAL DETERMINATION OF GIBBS ENERGY OF FORMATION OF LANTHANUM CHROMITE USING A COMPOSITION-GRADED BIELECTROLYTE

CHAPTER 4: THERMODYNAMIC PROPERTIES OF $LaCrO_4$, La_2CrO_6, and $La_2Cr_3O_{12}$, AND SUBSOLIDUS PHASE RELATIONS IN THE SYSTEM LANTHANUM-CHROMIUM-OXYGEN

CHAPTER 12: PERFORMANCE AND POST-TEST CHARACTERIZATION OF OTM SYSTEM IN EXPERIMENTAL COAL GASIFIER

CHAPTER 1: INTRODUCTION

1.1. Motivation

Oxygen transport membrane offers potential for applications in a wide variety of industrial processes ranging from high purity oxygen separation from air to oxy-combustion of carbonaceous and hydrocarbon fuels as well as production of syngas for subsequent conversion to liquid fuels and hydrogen. Efficient and clean oxy-combustion of fossil fuels enables reduction of greenhouse gas emissions responsible for global climate change [1, 2]. In the oxy-fuel combustion process, oxygen is separated from air and exclusively used for the fuel combustion unlike conventional combustion process where air is used as an oxidant. Use of oxygen results in significant increase in the process efficiency resulting in decrease in fuel consumption, heat loss, reduction in the size of the flue gas and NO_x emissions treatment. The replacement of air to oxygen in the natural-gas fired furnaces, for example, reduced the fuel consumption and NO_x emissions from 15% to 50% and from 50% to 90% respectively [1]. The flue gas after oxy-combustion predominantly consists of CO_2 and steam. After condensation of steam through cooling, the available CO_2 gas is easily captured, stored, and/or used for chemical production by well-established industrial technologies. Higher flame stability, better heat transfer characteristics, reduced gas volume and lower particulate emissions are other advantages of the oxy-fuel combustion process [2].

For oxy-combustion, it is to be noted that high purity oxygen makes a difference not only by reducing the harmful gas emissions (e.g. NO_x and SO_x) but also, it is important

for CO_2 capture from the flue gas [3,4]. This is because, the CO_2 purity level in the flue gas decreases with decrease in O_2 purity level. Lower purity oxygen containing impurities (e.g. nitrogen) are amenable to forming NO_x as a combustion product, and be present with others (SO_x, Ar, N_2 etc.) in the flue gas. Lower purity oxygen used in oxy-combustion process is also considered detrimental to compression and liquefaction processes commonly used for the transportation of CO_2. Large scale conventional transportation process for transporting CO_2 includes the use of gas pipelines, ships and vessels. For such processes, it is required to compress CO_2 to supercritical state (~ 80-150 bars) for pipeline transport. On the other hand, CO_2 needs to be liquefied (~ 6.5 bars and -51°C) for ship transport [4]. It is often found difficult to compress as well as liquefy the CO_2 gas stream if the impurities level is high (approximately greater than 4%) [4]. The impurities present in the post combustion CO_2 gas stream as well as compressed gas stream can also cause corrosion when introduced into the pipeline [3,4]. The presence of inert constituents (e.g. N_2, Ar, He etc.) in the gas stream is also required to be removed and controlled as it can also increase the critical pressure of CO_2 in the pipeline [3]. Gas conditioning (a sub-system to remove impurities from CO_2 gas stream) step is conventionally incorporated to purify CO_2 along with CO_2 compression and drying. The specific energy requirement for gas conditioning is 100-200 kWh/ton (t) captured CO_2 (~ 360-720 kJ/kgCO_2). However, for approximately pure CO_2 stream, the energy requirement for compression is significantly reduced to 90 kWh/t captured CO_2 (~ 324 kJ/kgCO_2) [4].

An oxygen transport membrane (OTM) is required to separate high-purity oxygen from air for oxy-combustion of fuel [5-13]. The high-purity oxygen also finds application in metallurgical (iron and steel plants), chemical, petrochemical, medical and paper industries, welding and cutting [14]. Fig. 1.1 shows a simplified process flow diagram depicting the use of an oxygen transport membrane (air separation unit) in an integrated gasification combined cycle (IGCC) [15].

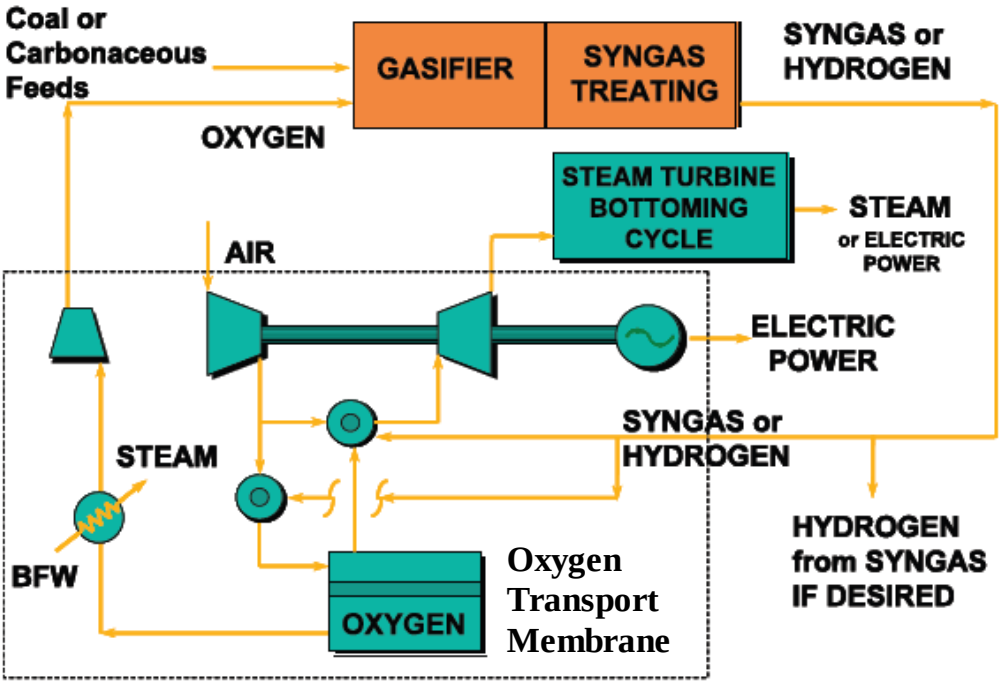

Fig. 1.1. Simplified process flow diagram of an oxygen transport membrane integrated in IGCC (BFW: Boiler Feed Water) [15].

In the IGCC process, oxygen separated from air (air separation unit) reacts with coal particles or slurry to produce syngas at high temperature and pressure (~1000°C and ~394.8 atm) [16]. The syngas undergoes a water-gas shift reaction ($CO + H_2O \leftrightarrow CO_2 + H_2$) and further converts to hydrogen and carbon dioxide. In this process, after removal of

the carbon dioxide, the hydrogen is used in a gas turbine to generate electricity. The hot exhaust gases are used to heat the water in the heat recovery steam generator (HRSG) for use in the steam turbine. Thus the IGCC process provides dual benefits: syngas production and power generation along with the carbon dioxide sequestration. In addition, the overall efficiency of the process is 45-50 %, which is significantly higher than the conventional gasification process (32-38%) [16].

Table 1.1 summarizes the advantages and disadvantages of the conventional and advanced oxygen separation techniques currently being developed [1, 14-21]. The two commercial methods currently used to separate oxygen from air are: 1) cryogenic and 2) pressure swing adsorption. In the cryogenic method, high purity oxygen (≥99%) is produced on a large industrial scale by fractional distillation of air at low temperature and pressure [17]. First, air is compressed between 4-10 atm and cooled to ambient temperature (30°C). It is then passed over the fixed bed of adsorbents (activated alumina/molecular sieve) to remove trace contaminants, i.e., water, carbon dioxide and hydrocarbons. The purified air is again cooled to its liquefaction temperature (approximately -185°C), after which distillation occurs and the products (nitrogen, oxygen, and argon) are obtained at low pressure column. Oxygen which has the highest boiling point (-182.8°C) among the components is obtained from the bottom of the low pressure column. A simplified schematic of the cryogenic method is shown in Fig. 1.2 [18]. This method is energy intensive, less efficient, and more expensive than the pressure swing adsorption method.

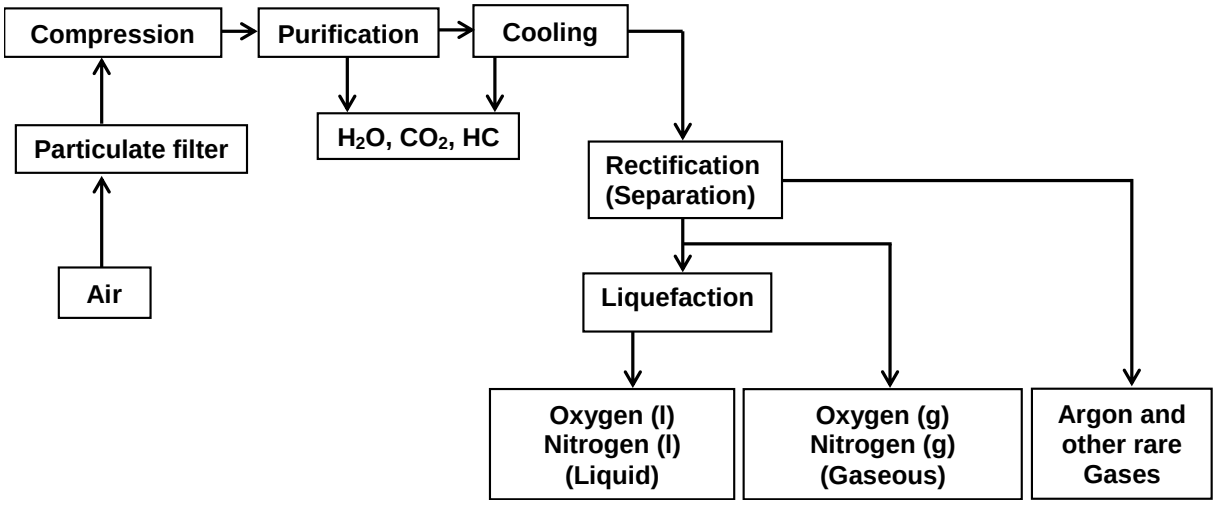

Fig. 1.2. Flow diagram of cryogenic distillation process [18].

The pressure swing technique separates oxygen from air by selectively adsorbing nitrogen from compressed air at high pressure on active carbon or a zeolite [19]. The pressure is reduced after the separation to desorb the nitrogen. In Fig. 1.3, a schematic shows the pressure adsorption technique for air separation [19]. The process is discontinuous and suitable only for small-scale production when the oxygen purity (90-95%) is not an end-use concern.

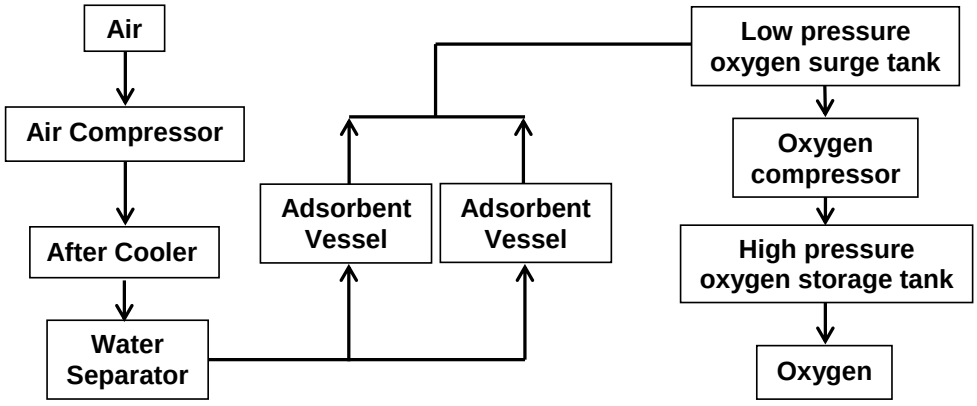

Fig. 1.3. Flow diagram of pressure adsorption technique for air separation [19].

Table 1.1. Advantages and disadvantages of various oxygen separation techniques [1, 14-21].

Types/methods	Principle/driving force	Advantages	Disadvantages	Applications
Pressure swing adsorption	Adsorption/desorption	• Less expensive • More efficient	• Low purity oxygen (90–95%) • Batch process (does not provide continuous oxygen gas flow) • Not suitable for large scale applications (integration with power or IGCC) • Multiple stage air separation technique • Large volume space required for the plant/equipment set up	• Waste water treatment – wet oxidation • Chemical leaching for minerals extraction
Cryogenic distillation	Fractional distillation	• High purity oxygen (≥99%)	• Expensive (responsible for 15% of the total plant capital cost when integrated with IGCC) • Installed capital cost ($US2008/kWe) and energy consumption (kWh/t_{o_2}) in oxy-fuel or IGCC plant are 310–500 and 245–670 respectively (higher than ceramic membrane) • Compared to ceramic membrane; lower power production (409 MW), thermal efficiency (45.2%HHV – High heating value), and higher cost of electricity (55.5 mills/kWh) are obtained (when integrated with IGCC) • With integration of cryogenic air separation unit into a power plant, the overall efficiency drop of a power plant is estimated to be 8–10% • Multiple stage separation process • Large volume space required • Energy intensive • Less efficient • No heat recovery (oxygen gas stream needs to be heated up and pressurized when integrated with gasification or power cycle)	• Welding, medical, and petrochemical industries • Syngas production and oxy-combustion
Ceramic oxygen transport membrane	Electric potential/partial pressure gradient	• High purity oxygen (≥99%) • Installed capital cost ($US2008/kWe) and energy consumption (kWh/t_{o_2}) in oxy-fuel or IGCC plant are 260–295 and 100–655 respectively (lower than cryogenic air separation) • Compact (do not require large space) • Single stage air separation process • Heat recovery (high temperature process and more suitable to be combined with power generation cycle) • Cost savings (35–40% over a cryogenic process with IGCC) • Less power consumption (comparatively 37% less with IGCC) • With OTM integration into a power plant, the effective energy demand is estimated to be reduced to 147 kWh/t_{o_2} when compared to 235–250 kWh/t_{o_2} for cryogenic air separation • Compared to cryogenic, higher power production (420 MW), thermal efficiency (46.5% HHV – High heating value), and lower cost of electricity (51.9 mills/kWh) are obtained (when integrated with IGCC)	• Long term sustainability • High oxygen flux	• Syngas production and oxy-combustion • Welding, medical, and petrochemical industries

High-purity oxygen (≥ 99%) separation from air using a dense ceramic material, an oxygen transport membrane, is a relatively new and developing technology. In this method, oxygen from air transports through the ion conducting ceramic material as oxygen ions by either an electrical or chemical driving force. In comparison to the cryogenic and pressure swing methods, oxygen production by dense ceramic membranes has distinct advantages (Table 1.1): (i) ~ 40% lower cost of oxygen generation than existing technologies, (ii) the process is more efficient, (iii) there is lower power usage, and (iv) the method enables heat recovery when integrated with the power generation, and combustion units [14]. In addition, when integrated into power or gasification combined cycle, the oxygen gas stream need not to be heated to high temperature and pressurized, as is needed for the cryogenic technique.

As mentioned above and Table 1.1, the ceramic membranes are more advantageous than other existing technologies for oxygen separation especially when integrated with combustion and/or gasification cycle for oxy-combustion and/or syngas production. Pressure swing adsorption technique choice is eliminated for oxy-combustion and/or syngas production not only because it provides low purity oxygen, but also, the technique is only suitable for small to medium scale plant (20-100 tons/day) [22]. In addition, it is a batch (discontinuous) process. The process is not appropriate for integration into the combustion and/or gasification cycle. On the other hand, even though cryogenic technique provides high purity oxygen at large scale (beyond 100-300 tons/day), the process power consumption is high and the efficiency is low [22]. For oxy-combustion and syngas production, the cryogenic cycle integration into power plant

requires large volume space, high installment capital cost ($310-500/kWe), large energy consumption (245-670 kWh/tO_2), and drops down the total efficiency of the plant by 8-10% [20]. When compared to cryogenic technique, ceramic membranes requires less installment cost ($260-295/kWe), power consumption (100-655 kWh/tO_2), and volume space on integration with power plants [20]. In addition, the process is single stage, and enables heat recovery. In other words, unlike cryogenic technique, it is a high temperature process and the permeated oxygen gas stream need not to be heated up and pressurized when integrated with gasification or power cycle. Overall, the ceramic membranes are beneficial (especially for oxy-combustion and syngas production) in terms of power consumption, volume space, heat recovery, installment cost, power production of the plant, and efficiency (Table 1.1).

Ceramic oxygen transport membranes can be divided into two groups based on the driving force used for the oxygen separation process: 1) electrically driven membrane also known as passive membrane and 2) chemical potential/oxygen partial pressure-driven membrane also known as active membrane. In passive membrane, the dense ceramic is predominantly an ionic conductor that transports oxygen ions under applied electrical potential. This process is economic and reliable for high purity oxygen production with precise control on produced oxygen volume [23]. An external electrical circuit and power source are required to transport electrons across the membrane to maintain charge neutrality and the membrane, therefore, is called electrically driven. The flux of electrons is required to maintain electro-neutrality according to Kröger-Vink notation:

$$O_O^{\times} \leftrightarrow \frac{1}{2}O_2(g) + V_O^{\cdot\cdot} + 2e^- \quad (1)$$

where e^- and $V_O^{\cdot\cdot}$ refers to electron and oxygen vacancy respectively. The symbol $\times$ and represents neutral and positive charge respectively.

In the oxygen partial pressure-driven active membrane, the dense ceramic, employed for the separation of oxygen, is a mixed ionic-electronic conductor (MIEC). An oxygen partial pressure differential between an oxidizing (air at 0.21 atm) and reducing gas (fuel at 10^{-22} atm) exists across the membrane as a driving force for the oxygen separation. It allows oxygen ions transport from the high oxygen partial pressure side to the low oxygen partial pressure side; meanwhile, electrons move in the opposite direction within the membrane and complete the internal electric circuit. Therefore, no external circuit or electrical power is required for the electron conduction [23]. For the pressure-driven MIEC based membrane, the driving force (electrochemical potential) for the transport of ion and electron species relates to the mass flux as shown in the general MIEC transport equation below [24]:

$$J_i^{mass}(x,t) = -\frac{\sigma_i(x,t)}{(z_i e)^2}\frac{\partial \tilde{\mu}_i(x,t)}{\partial x} \quad (2)$$

where x is position, t is time, i is the species of charge carrier, z_i is the number of charges carried by species i, e is the electron charge, $J_i^{mass}(x,t)$ is the carrier mass flux, $\sigma_i(x,t)$ is the electrical conductivity. The electrochemical potential, $\tilde{\mu}_i(x,t)$ is given by

$$\tilde{\mu}_i(x,t) = \mu_i(x,t) + z_i e\varphi(x,t) \quad (3)$$

where $\mu_i(x,t)$ and $\varphi(x,t)$ are chemical and electrical potential respectively.

The electrochemical potential is dependent on oxygen chemical potential (Eq. (4)) across the membrane and electrical potential (Eq. (5)), leading to the migration of oxygen ions from the air side (higher P'_{O_2}) to the fuel side (lower P_{O_2}), and electrons to the opposite side [24]. At time, $t = 0$ under steady state condition:

$$\mu_{O_2} = \mu^{\circ}_{O_2} + K_B T \ln \frac{P_{O_2}}{P'_{O_2}} \quad (4)$$

$$\frac{d\varphi(x)}{dx} = -E = -\frac{k_B T}{eL} \ln \frac{\sigma_{ion} + \sigma_{el}(L)}{\sigma_{ion} + \sigma_{el}(0)} \quad (5)$$

where μ_{O_2} is the chemical potential of the oxygen, $\mu^{\circ}_{O_2}$ is the chemical potential of pure oxygen, K_B is the Boltzmann constant, T is temperature, E is the electrical field, P_{O_2} and P'_{O_2} are oxygen partial pressure at the fuel side and air side, respectively, σ_{ion} represents ionic conductivity, and σ_{el} is electronic conductivity. The length of the membrane is x = 0 at the permeate side and x = L at the feed side.

Fig. 1.4a and 4b show schematics of operation for the pressure and electrically driven oxygen transport membrane. The differences between the pressure-driven (active) and electrically driven (passive) membranes are tabulated in Table 1.2 [25-33]. Mixed ionic-electronic conductivity required for pressure-driven membrane can be found in either single phase mixed conducting perovskite oxide (cobaltite, ferrite) or dual phase composites consisting of ionic and electronic phase materials. In the case of dual phase membranes, the ionic phase transports oxygen while the electronic phase transports electron. However, oxygen ions cannot transport through the bulk membrane via purely electron conducting phase, resulting in decreased oxygen permeability and flux. For this reason, mixed ionic-electronic perovskite phase is preferred for oxygen ion migration

through the bulk membrane [34]. It is challenging to obtain high electronic as well as ionic conductivity in a single perovskite phase. The ionic conductivity of MIEC perovskite is generally found to be less than fluorite phase. For example, the ionic conductivity of $LaCoO_{3-\delta}$ and $La_{0.7}Sr_{0.3}Co_{0.7}Cr_{0.3}O_{3-\delta}$ perovskites are ~2×10^{-4} and ~10^{-3} S cm^{-1} at 1000°C in air, respectively, which is less than ~0.1 S cm^{-1} for most commonly used fluorite phase ($Zr_{0.8}Y_{0.2}O_{2-\delta}$) [35-36]. Therefore, it is preferable that mixed conducting perovskite is combined with fluorite phase to form a composite with relatively high ionic conductivity. Subsequently, the combination of perovskite and fluorite phase provides higher performance/oxygen flux in OTM when compared to single phase. For instance, the oxygen flux (J_{O_2}) of $Ce_{0.8}Gd_{0.2}O_{2-\delta}$ fluorite phase is ~9.9×10^{-10} mol cm^{-2} sec^{-1} under oxygen partial gradient maintained by air at the feed side and Ar at the permeate side (air/Ar). However, when combined with MIEC $La_{0.8}Sr_{0.2}Fe_{0.8}Co_{0.2}O_{3-\delta}$ perovskite in the ratio of 48:52 (wt. %), the J_{O_2} increases to ~6.3×10^{-8} mol cm^{-2} sec^{-1} (air/He) at 950°C [37]. Similarly, the J_{O_2} for single phase $La_{0.8}Sr_{0.2}Cr_{0.5}Fe_{0.5}O_{3-\delta}$ perovskite is ~2.5×10^{-7} mol cm^{-2} sec^{-1} and increases to ~2.6×10^{-6} mol cm^{-2} sec^{-1} (air/CO) for $La_{0.8}Sr_{0.2}Cr_{0.5}Fe_{0.5}O_{3-\delta}/Zr_{0.84}Y_{0.16}O_{1.92}$ composite at 950°C [31, 38]. The oxygen flux performance of different single phase perovskite as well as dual phase with fluorite is summarized later in the oxygen flux section. For dual phase membranes, it is to be noted that there is a challenge of compatibility, structural and chemical stability (e.g. thermal expansion match, interfacial reaction) as discussed in subsequent sections.

Table 1.2. Differences between active and passive oxygen transport membrane [25-33].

	Active	Passive
Advantages	• No external voltage/power source and electrodes required • Need mixed ionic-electronic conductor materials	• Control on amount of oxygen produced via supply of external voltage • External voltage/power source and electrodes required
Materials example	$(La_{0.75}Sr_{0.25})_{0.95}Cr_{0.6}Fe_{0.4}O_{3-\delta}$, $(La_{0.75}Sr_{0.25})_{0.95}Cr_{0.5}Mn_{0.5}O_{3-\delta}$, $La_{0.4}Ca_{0.6}Co_{0.2}Fe_{0.8}O_{3-\delta}$, $LaFe_{0.8}Ni_{0.2}O_{3-\delta}$, $Zr_{0.84}Y_{0.16}O_{1.92}$ + $La_{0.8}Sr_{0.2}Cr_{0.5}Fe_{0.5}O_{3-\delta}$, and $Gd_{0.2}Sr_{0.8}FeO_{3-\delta}$ + $Ce_{0.8}Gd_{0.2}O_{1.9}$	$(ZrO_2)_{0.8}(Y_2O_3)_{0.20}$, $Bi_{1.5}Y_{0.3}Sm_{0.2}O_3$ and $Gd_{0.2}Ce_{0.6}$ $Pr_{0.2}O_{2-\delta}$
Phase	Mixed ionic-electronic phase	Ionic phase
Driving force	Oxygen partial pressure gradient	Electric potential

The exchange of oxygen between the membrane surface and gas phase takes place in several steps for the reduction and transport of oxygen: adsorption and dissociation of oxygen molecules, oxygen transport via oxygen vacancies across the membrane, and desorption and association of oxygen ions [39-41]. This is explained in detail later in the oxygen flux section. MIEC's eliminate the necessity for an electrode. To enhance the oxygen surface exchange and improve the overall oxygen flux, however, a porous surface exchange (air side) and intermediate layer (fuel side) is integrated in the active membrane [39-40,42].

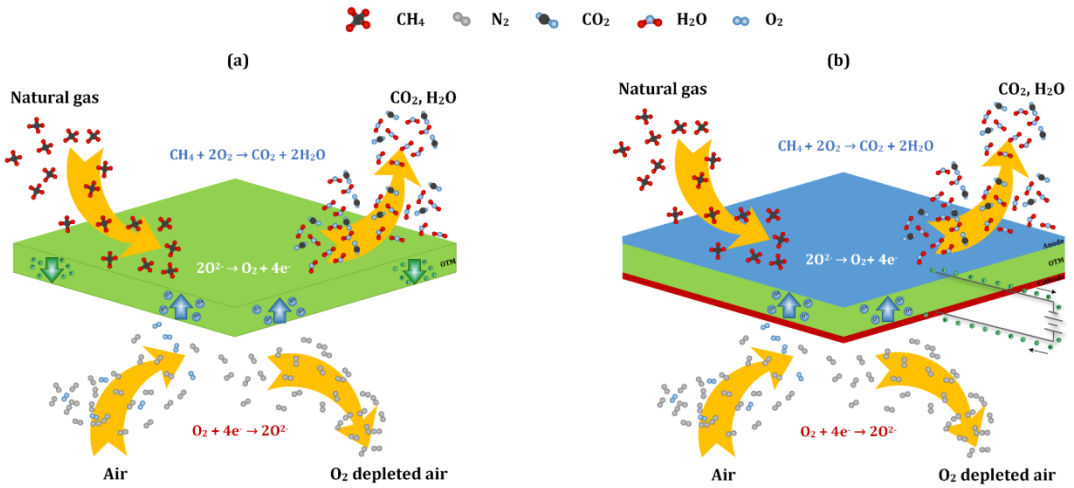

Fig. 1.4. Schematic of the working principle of oxygen transport membrane (OTM): (a) Partial pressure driven/Active (Mixed ionic electronic conductor), (b) Electrically driven/Passive (Ionic conductor).

1.2. Materials for oxygen transport membrane

MIEC's are considered for use as oxygen transport membranes (OTM) as well as the intermediate and surface exchange layer for separating oxygen from air [43-45]. A MIEC based OTM (Fig. 1.4a) device operates at ~1000°C and oxygen partial pressure of ~0.21-10^{-22} atm for oxy-combustion of fuel [46]. MIECs are also used as electrodes in other solid state devices (e.g. solid oxide fuel/electrolyzer cells) under exposure at 650-1000°C and ~0.21-10^{-22} atm P_{O_2} [47].

To obtain high purity oxygen through oxygen permeation, the OTM should be dense (≥94%) to avoid contaminants and the mixing of air and fuel. OTM should be resilient to the aggressive operating environment (~1000°C and ~0.21-10^{-22} atm) for more

than 40,000 h and also cost effective [48]. The key requirements for oxygen transport membrane are summarized in Table 1.3 [43-48].

Generally, electronic and/or MIEC perovskite oxides are used as electronic and fluorite oxides as ionic phase constituents for OTM. Dual phase composites consisting of MIEC perovskites and fluorite phases are recognized to promote higher oxygen flux. Y/Sc doped ZrO_2, and Gd/Sm doped CeO_2 or ZrO_2-CeO_2 system doped with Y, Sc, Gd, and/ or Sm are commonly used as ionic phase [34, 49]. ABO_3, Ruddlesden-Popper ($K_2NiF_4/A_{n+1}B_nO_{3n+1}$ structure), and ordered double perovskites ($AA´Co_2O_{5+x}$, A = RE, Y and A´= Ba, Sr) have been investigated as MIEC phases [39-40]. The structural and thermo-chemical stability of the $A^{3+}B^{3+}O_3$ are superior to the other types of perovskites and have been studied for OTM application [43,52-54].

Table 1.3. Materials' key requirement for active OTM [43-48].

- Dense (≥94%) membrane
- High mixed ionic-electronic conductivity
- High stability in a wide range of P_{O_2} ~ 0.21-10^{-22} atm at the OTM operating temperature (~1000°C)
- High electro-catalytic activity (low polarization resistance)
- High oxygen flux (≥ 10^{-6} mol s^{-1} cm^{-2})
- Thermal expansion coefficient of 9.5-12.0 × 10^{-6} $°C^{-1}$ similar to those of the adjacent materials
- High mechanical strength including interfacial strength to withstand the differential partial pressure, handling, vibration during transportation and operation
- Excellent thermal cycling resistance
- Excellent chemical resistance to withstand both oxidizing and reducing atmosphere at ~1000°C
- Resistance to aging of materials (long-term (≥40,000 h) materials stability in aggressive operating condition)

Structure: no change in crystal symmetry and minimal chemical expansion to minimize change in lattice volume

Microstructure: no change in microstructure (grain growth, secondary phase formation, surface segregation; pore growth and densification for adjacent intermediate and surface exchange layers and electrodes)

Chemical: no solid-solid and solid-gas interaction to change the chemical formula by formation of new compounds, precipitation of oxides, reduction of oxides into metallic form, evaporation of materials

Mechanical: Acceptable creep rate: ~10^{-10} s^{-1} yielding a tolerable strain of ~1% per year)

ABO_3 Perovskite

An ideal ABO_3 perovskite is cubic, where A and B are two cations bonded with oxygen anions. The ionic radii of B cation (r_B) is smaller than A cation (r_A). B cation has 6-fold coordination, whereas A cation has 12-fold coordination with oxygen ions as shown in Fig. 1.5. The stability of a perovskite structure is defined by the Goldschmidt tolerance factor, which is used to measure the degree of distortion of a perovskite from ideal cubic lattice, t as [55]:

$$t = \frac{r_A + r_O}{\sqrt{2}(r_B + r_O)} \quad (6)$$

where r_A, r_B and r_O are ionic radii of the respective ions. The perovskite structure is stable for $0.77 \leq t \leq 1.00$ [56].

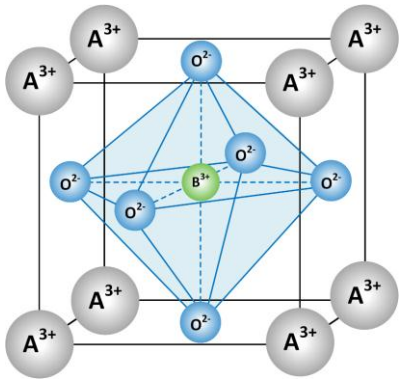

Fig. 1.5. Ideal perovskite structure of ABO_3.

The thermo-physical properties such as thermal expansion and electrical conductivity of ABO_3 perovskites depend on the structure and the ionicity difference (Δf_i) between A-O and B-O bonds. Lattice distortion from the cubic symmetry (t=1) is associated with a high degree of anisotropy in oxygen sites, and an increase in lattice distortion decreases the ionic conductivity. In other words, ionic conductivity improves with higher structural symmetry as observed for $LaCoO_3$. The migration energy of oxygen ions depends on the critical radius of the saddle point for oxygen migration, electrostatic bonding energy, and Jahn-Teller effect, which represents a geometric distortion of a non-linear molecular system (e.g., octahedral complexes) to reduce its symmetry and energy. Higher the value of the saddle point radius, lower is the oxygen migration energy [57-59]. The ionic conductivity and thermal expansion coefficient increases with a lower ionicity difference (Δf_i) between A-O and B-O bonds [60-63]. For instance, thermal expansion and the oxygen ionic conductivity of $La_{1-x}Sr_xFe_{1-y}Co_yO_{3-\delta}$ perovskite increases with decrease in Δf_i [61]. Because, the oxygen ion become unstable when the difference in the ionicity is small and results into the increase in the oxygen ion

mobility. The ionic conductivity dependence on the Jahn-Teller effect has yet to be understood. The ionic and electronic conductivity of ABO_3 can also be tuned by introduction of dopants at A and B-site. For example, when divalent acceptor ion is partially substituted at trivalent A-site, the charge compensation for electro-neutrality is occurred either by an increase in the valence state of the B-site ion (electronic compensation) and/or oxygen vacancies formation (ionic compensation) [56]. If doped with transition metals, the increase in the valence state of B-site cation results into an increase in B^{4+}/B^{3+} redox couples which act as hopping sites for electronic conduction and increases the conductivity. On the other hand, the ionic conductivity increases if the charge balance is compensated by creation of oxygen vacancies.

Lanthanide series element (La) as A-site cation and transition metals (Cr, Fe, Mn, Ni and Co) as B-site cation in ABO_3 perovskite have been investigated [64-67]. These perovskite can be categorized as chromite, ferrite, manganite, nickelate, and cobaltite. The stability of the undoped perovskite at 1000°C is in the increasing order of $LaCrO_{3-\delta}$ (10^{-22} atm) > $LaFeO_{3-\delta}$ (10^{-17} atm) > $LaMnO_{3-\delta}$ (10^{-15} atm) > $LaCoO_{3-\delta}$ (10^{-7} atm) > $LaNiO_{3-\delta}$ ($10^{-0.6}$ atm) [66], where δ represents oxygen deficiency.

Major advantages and disadvantages of the perovskites are outlined in Table 1.4 [69-76]. It is clear from the table that lanthanum ferrite, manganite and nickelate are not stable in a wide range of P_{O_2} (0.21-10^{-22} atm) at ~1000°C, which is one of the key requirements for OTM. As mentioned in the Table 1.4, even though ferrites provide high mixed ionic (~0.05 S cm^{-1} at 900°C) - electronic (~100 S cm^{-1} at 1000°C) conductivity as well as higher activity for oxygen reduction, high thermal expansion coefficient

($23.8\times10^{-6}\,K^{-1}$ for T > 600°C) and its decomposition into La_2O_3 and Fe metal in reducing atmosphere ($\leq 10^{-17}$ atm) at 1000ºC, eliminates this choice for OTM. Similarly, cobaltites are not suitable for OTM due to high thermal expansion coefficient ($20\times10^{-6}\,K^{-1}$) and its decomposition into La_2CoO_4 and CoO at lower P_{O_2} (< 10^{-7} atm) and OTM operating temperature (~1000°C). Likewise, manganites provide high electrical conductivity (83 S cm^{-1} at 800°C) but also, decompose into La_2O_3 and MnO in reducing atmosphere ($\leq 10^{-15}$ atm) at 1000°C. Furthermore, nickelates are not stable and decomposes into La_2NiO_4 and NiO below $10^{-0.6}$ atm at 1000°C. Poor stability of various perovskites (ferrites, cobaltites, manganites) prohibits their application in the emerging power generation system and related device (OTM). On the other hand, chromites are stable under OTM operating conditions (~1000°C and ~0.21-10^{-22} atm.), while the required thermo-physical properties can be achieved by using suitable dopants. Lanthanum chromite-based materials are also considered for solid oxide fuel cell interconnects because of superior stability and good electrical conductivity [77-83]. This suggests that chromite is the best choice of material for OTM from stability point of view, the subject of this review paper. In this review article, we have a) critically analyzed and examined the pertinent information on lanthanum chromite based perovskites in terms of chemistry, structure, and properties required for OTM systems, b) correlated the 'chemistry-structure-property-stability' relationships, and c) suggested approaches for tuning the desired properties and reliability. Further, challenges and future research directions are discussed.

Table 1.4. Advantages and disadvantages of various perovskite oxides [56-63].

Perovskites	Ionic/electronic/mixed	Advantages	Disadvantages
Chromites	Predominantly electronic	• Higher stability ($0.21–10^{-22}$ atm at ~1000 °C) • Good electrical conductivity (0.6–1.0 $S cm^{-1}$ at 1000 °C)	• Low density (<60%) and ionic conductivity
Ferrites	Mixed ionic–electronic	• Exhibits high ionic (0.05 $S cm^{-1}$ at 900 °C) and electronic conductivity (~100 $S cm^{-1}$ at 1000 °C) • Higher activity for oxygen reduction with oxygen flux (1.8×10^{-6} $mol cm^{-2} s^{-1}$)	• High thermal expansion coefficient ($23.8 \times 10^{-6} K^{-1}$ for $T > 600$ °C) • Decomposes into La_2O_3 and Fe in reducing atmosphere ($\leq 10^{-17}$ atm) at 1000 °C • Ferrites are more prone to lattice structure distortion due to the possibility of Fe disproportionation occurring from change in valence state ($Fe^{3+}/Fe^{2+}/Fe^{4+}$)
Manganites	Predominantly electronic	• High electrical conductivity (83 $S cm^{-1}$ at 800 °C)	• Decomposes into La_2O_3 and MnO in reducing atmosphere ($\leq 10^{-15}$ atm) at 1000 °C • Low ionic conductivity (1.10×10^{-7} $S cm^{-1}$ at 900 °C)
Nickelates	Predominantly electronic	• Good electrical conductivity (~10 $S cm^{-1}$ at 800 °C) • Higher activity for oxygen reduction with oxygen flux ($\sim 1.6 \times 10^{-8}$ $mol cm^{-2} s^{-1}$)	• Not stable and decomposes into La_2NiO_4 and NiO in reducing atmosphere ($< 10^{-0.6}$ atm) at 1000 °C • Exolution of Ni metal when heavily doped (~50%)
Cobaltites	Mixed ionic–electronic	• Higher activity for oxygen reduction with oxygen flux ($0.3–3 \times 10^{-7}$ $mol cm^{-2} s^{-1}$) • High electronic conductivity (103 $S cm^{-1}$ at 1000 °C) and ionic conductivity (10^{-3} $S cm^{-1}$ at 900 °C) and density (≥90%)	• High thermal expansion coefficient ($20 \times 10^{-6} K^{-1}$) • Decomposes into La_2CoO_4 and CoO in reducing atmosphere ($< 10^{-7}$ atm) in reducing atmosphere at 1000 °C • Similar to ferrites, cobaltites are also more prone to lattice structure distortion due to the possibility of Co disproportionation occurring from change in valence state ($Co^{3+}/Co^{2+}/Co^{4+}$)

1.3. Fabrication

The fabrication techniques for the OTM, still an infant technology, are not widely published and remain mostly trade secret or industry specific information. As with other solid state electrochemical devices (solid oxide fuel cells and electrolyzers), there are planar and tubular configurations for OTM as shown in Fig. 1.6 [15, 84-87]. Different fabrication technologies are discussed in brief based on the literature for SOFCs.

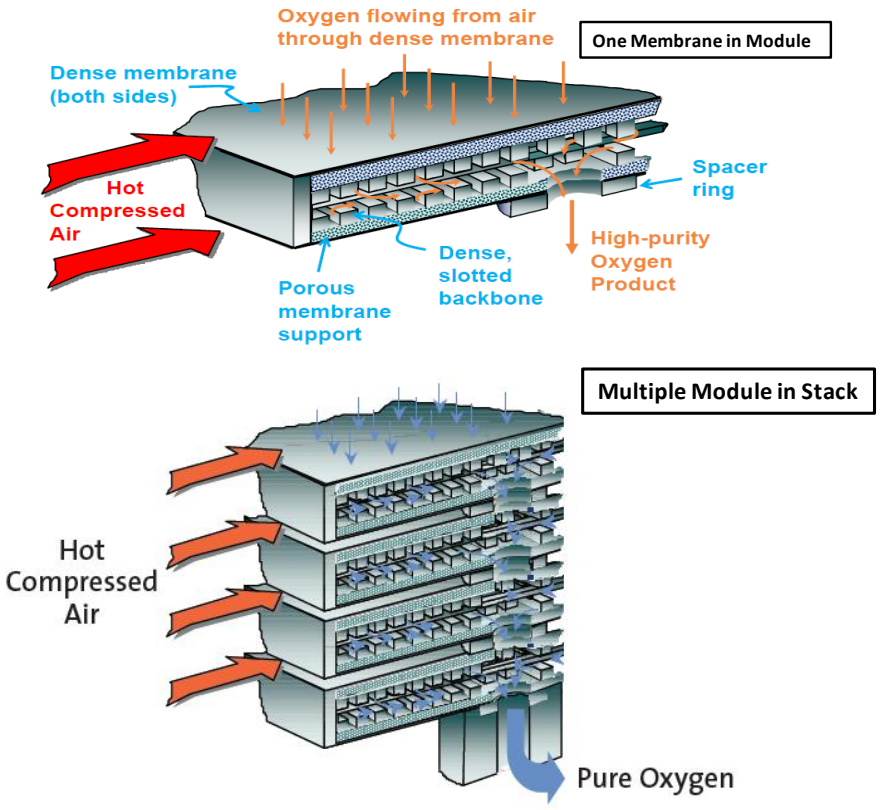

(a)

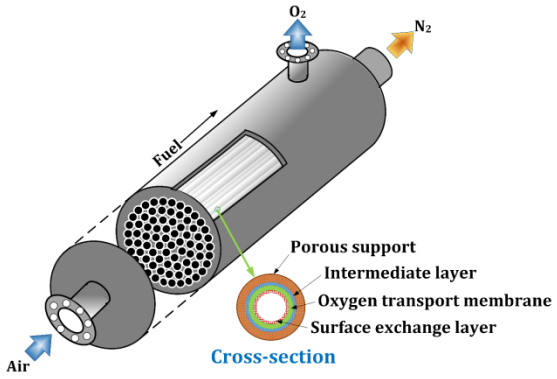

(b)

Fig. 1.6. Oxygen transport membrane configuration: (a) Planar (single and multiple module) [84], (b) Tubular (with cross-section).

1.3.1. *Fabrication Techniques*

For both planar and tubular configurations, the porous electrodes used in passive OTM, porous surface exchange and intermediate layers used in active OTM, and dense oxygen separation layers are coated on a 0.5-4.0 mm thick porous substrate. Porous substrates, which also provide mechanical strength and the gas flow path, are generally prepared by conventional ceramic routes such as pressing (planar type), slip casting (planar and tubular type), and extrusion (tubular type) followed by respective drying and sintering/co-firing [85]. Subsequent layers (5-50 μm thick) are coated on the porous substrate by various techniques: screen printing; tape casting; wet chemical methods such as slip casting, spraying, and sol-gel coating; plasma spraying; and gas phase deposition such as physical vapor deposition (PVD) and chemical vapor deposition (CVD) [85-95]. All of these techniques have inherent advantages and disadvantages. Screen printing and tape casting offer low cost, ease in controlling the coating thickness, and suitability for porous and dense microstructures through suitable thermal treatment (drying, binder removal, and sintering steps) [87, 97]. These techniques are limited to simple planar configuration and cannot be applied for complex shaped substrates such as tubular configurations. Other techniques are applicable for both planar and tubular configurations. Wet chemical methods are economical but require critical thermal treatments to develop crack free microstructures, which are difficult to control. Plasma spraying, PVD, and CVD techniques are not economical, but the desired microstructures can theoretically be achieved through control of the choice of solid targets (for PVD), solid or liquid precursors for plasma spray, and liquid precursor for CVD; plasma/gas phase deposition

rate by instrumentation, chamber atmosphere, and substrate temperature without any sintering step. The distinct advantages of the plasma spraying, PVD, and CVD are threefold. Plasma spraying and PVD are in-sight controlled. For all three methods, in contrast with wet processing methods, multiple layers can be deposited in a few hours. The grain size and orientation can be tuned by optimization of instrumental parameters. It is known that smaller the grain size, higher is the catalytic activity for oxygen reduction and flux in OTM. Small grain size (nm), the size and distribution of open pores, and the material's stability can be maintained during processing and fabrication due to the absence of the high temperature sintering step [81, 88-91, 93-94]. However, the grains grow and the microstructure changes due to active grain growth kinetics during long-term exposure at high temperature and reduced atmosphere. In reality, the deposited layers are co-fired at higher temperature (1200-1500°C) to achieve strong interfacial bonding and to maintain material stability at the relatively low operating temperature (~1000°C).

A brief introduction on the deposition techniques that could be used for planar and tubular OTM and their principles are summarized below followed by the advantages and disadvantages outlined in Table 1.5 [87-92, 98]. However, detailed information about the individual techniques and the corresponding figures are mentioned elsewhere in the cited references.

1.3.1.1. *Wet chemical methods*

Slip casting: A slurry consisting of submicron sized powders, a liquid medium (ethanol, isopropanol etc.), organic binders, and additives are prepared to meet the prescribed flow-ability, suspension stability, and sedimentation requirements. When poured on a porous

substrate, the slurry migrates through the porous support and a smooth and homogenous powder layer is formed on the surface. The layer is then dried, and subsequently sintered. A schematic of a vacuum slip casting method is shown in Fig. 1.7 [87].

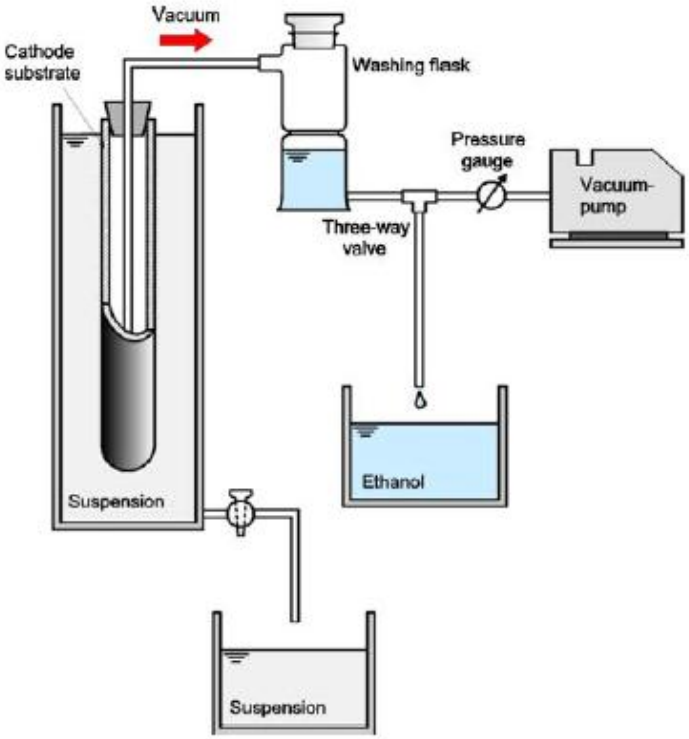

Fig. 1.7. Schematic of vacuum slip casting for tubular configuration [Reprinted from reference 87 with permission].

Slurry spraying: A liquid suspension of powders is sprayed on a substrate using a spray gun. The coated layer is then dried and sintered. This technique can be used for complex shapes, but the thickness at the edges of a component is difficult to control. A schematic of the spraying method is illustrated in Fig. 1.8 [87].

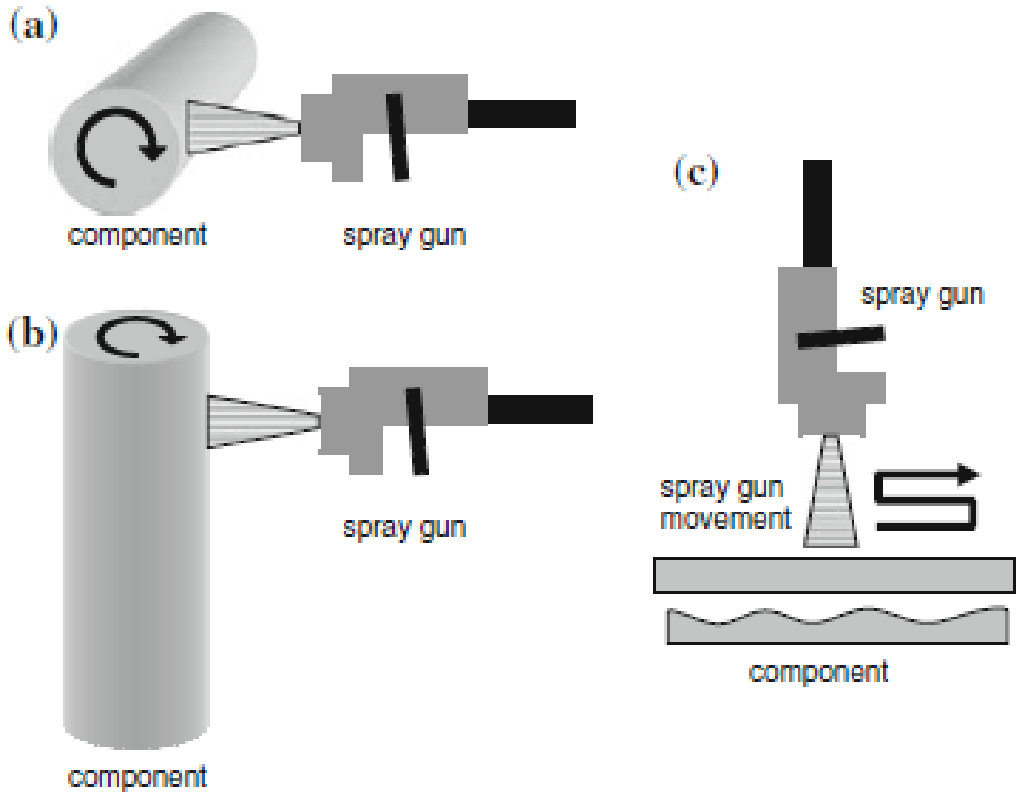

Fig. 1.8. Positions of spray gun and components to be coated: a) horizontal/horizontal, b) horizontal/vertical, both with tubular design and c) vertical/horizontal with planar design [Reprinted from reference 87 with permission].

Sol-gel deposition: In this method, a substrate is dipped into a stable suspension (sol) and then dried. The required coating thickness is generally obtained through multiple dipping and drying sequences. After obtaining the required thickness, the coating is sintered to develop the desired microstructure. This method is suitable for porous microstructures. A schematic is shown in Fig. 1.9 [87].

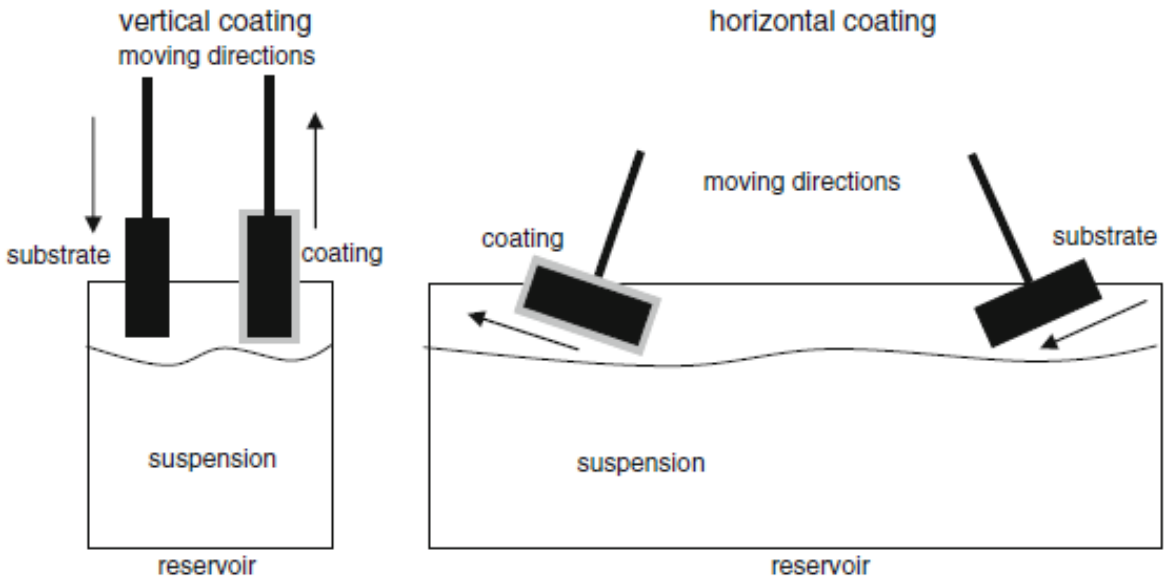

Fig. 1.9. Sol-gel dip coating technique [Reprinted from reference 87 with permission].

1.3.1.2. *Plasma spraying technique*

In plasma spray technique, plasma created by high voltage (DC power, RF induction) electrodes melt particles which travel (100-1200 m/s velocity) through the plasma jet and deposits on the substrate via rapid solidification [87-89, 99]. Plasma jet temperatures vary between 6727-19727°C. A schematic of a plasma spray apparatus is shown in Fig. 1.10 [88]. The powders can be deposited on the substrate at atmospheric pressure in the case of the atmospheric plasma spray (APS) method; under vacuum (10^{-2} - 10^{-3} atm) condition in the case of the vacuum plasma spray (VPS) method, and at low pressure ($<10^{-3}$ atm) in the case of the low pressure plasma spray method.

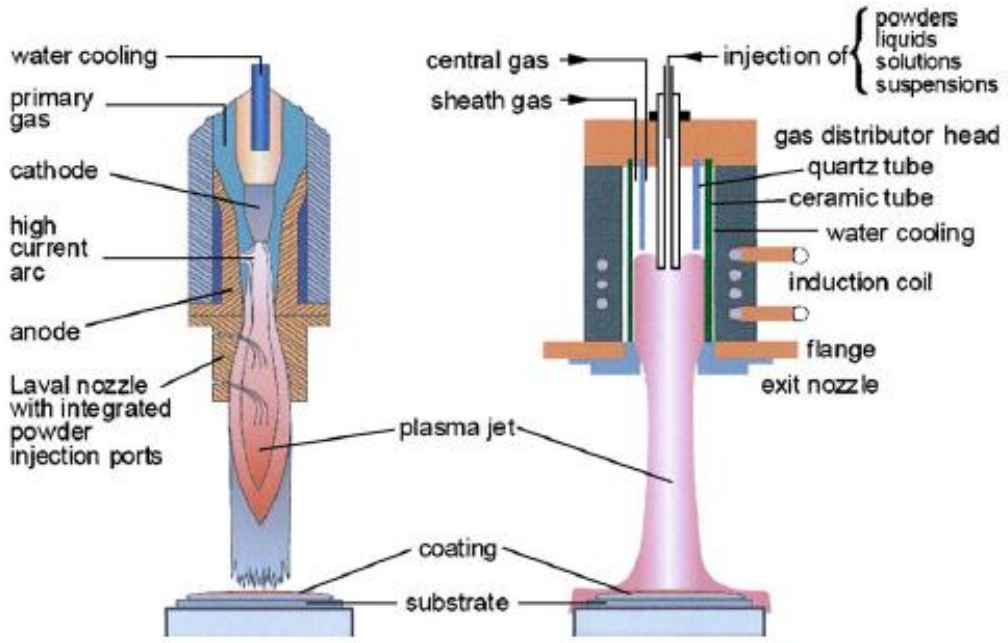

Fig. 1.10. Schematics of DC and RF plasma spraying apparatus [Reprinted from reference 88 with permission].

1.3.1.3. *Physical vapor deposition (PVD)*

In the physical vapor deposition (PVD) technique, atoms from a solid target are transported via gas phase and deposited on a substrate [87-88, 91]. Three common methods are used for the evaporation of solid targets: electron beam evaporation (EB-PVD), where electric energy is converted into heat at the sample surface; sputtering process, where material is removed from a target (cathode) using positively charged ions of a noble gas (argon); and pulsed laser ablation, in which high laser intensity is used to evaporate the material from the target surface. The schematics of the different PVD techniques are shown in Fig. 1.11 [91].

Table 1.5. Advantages and disadvantages of various fabrication techniques [87-92, 98].

Fabrication Techniques	Deposition rate/thickness	Advantages	Disadvantages	Examples of related materials
Wet chemical				
Slip casting	1–20 μm	• Economical/low cost • Dense/porous microstructure	• Required drying and sintering steps • Defect (cracks) in microstructure due to uncontrolled drying and sintering • High temperature sintering can lead to interaction between different materials in composites resulting in materials instability	YSZ, LSM
Spraying	5–100 μm	• Economical/low cost • Dense/porous microstructure	• Difficult to coat the edges of a complex shaped article (hill and valley type surface) • Required drying and sintering steps • Defect (cracks) in microstructure due to uncontrolled heating and sintering • High temperature sintering can lead to interaction between different materials in composites-materials instability	YSZ
Sol–gel	10 nm–10 μm	• Economical/low cost • Dense/porous microstructure	• Required drying and sintering steps • Defect (cracks and pores) in microstructure due to uncontrolled drying and sintering • High temperature sintering can lead to interaction between different materials in composites resulting in materials instability • Not an established methods like other techniques	YSZ, LSM
Plasma spraying			*In-sight technique*	
Atmospheric	50–300 μm	• In-principle, no sintering step is required • Faster than wet chemical technique • Controlled stoichiometry and high purity • Dense microstructure	• High cost • Micro-cracks and pores in microstructure • Thermal stress • Difficult to deposit 2–10 μm thick layer	YSZ
Vacuum	30–150 μm	• In-principle, no sintering step is required • High deposition rate – less fabrication time • Faster than wet chemical technique • Thinner layers	• High cost • High temperature process • Decomposition of perovskites due to use of inert/reducing gas (argon, hydrogen) • Non-uniform thickness and lower densification	YSZ, LSM
Low pressure	20–100 μm	• In-principle, no sintering step is required • Faster than wet chemical technique • Less thermal gradient • Thinner layers • Faster deposition	• High cost • Decomposition of perovskites due to use of inert/reducing gas (argon, hydrogen)	YSZ
Physical vapor deposition			*In-sight technique*	
Electron beam evaporation	1.5–2 μm	• High power density (evaporation rate control over a wide range) and deposition rate • Minimized film contamination • Control on the film growth rate and crystallite size depending on e-beam gun power	• High cost • Tensile stress in the deposited film	YSZ, Sm-doped ceria $(Ce_{0.9}Gd_{0.1})O_{1.95}$
Sputtering	~1 μm	• Control on varying grain size with columnar structure • Easy attainment of nano-sized grain	• Expensive • Low deposition rate	YSZ, LSM, $La_{0.50}Sr_{0.50}CoO_3$
Laser ablation	Å-a few μm	• Flexible and capable of forming multi-component thin films from a single source target	• Complex physical method • Scaling up issue	$LaCrO_3$-based materials, YSZ, CGO, bilayer consisting of Sm-doped ceria (SDC) and lanthanum strontium, gallate manganite (LSGM)

Table 1.5. *(Continued)*

Fabrication Techniques	Deposition rate/thickness	Advantages	Disadvantages	Examples of related materials
Chemical vapor deposition				
MO CVD	4–15 μm	• Low temperature required • Easy control of film composition and irregular surface	• Low deposition rate	LSM, YSZ, $YBa_2Cu_2CoO_{7-\delta}$
Electrochemical vapor deposition	30–40 μm	• Higher deposition rate • Long-term stability of deposited thin film	• High cost • High deposition temperature is required	YSZ

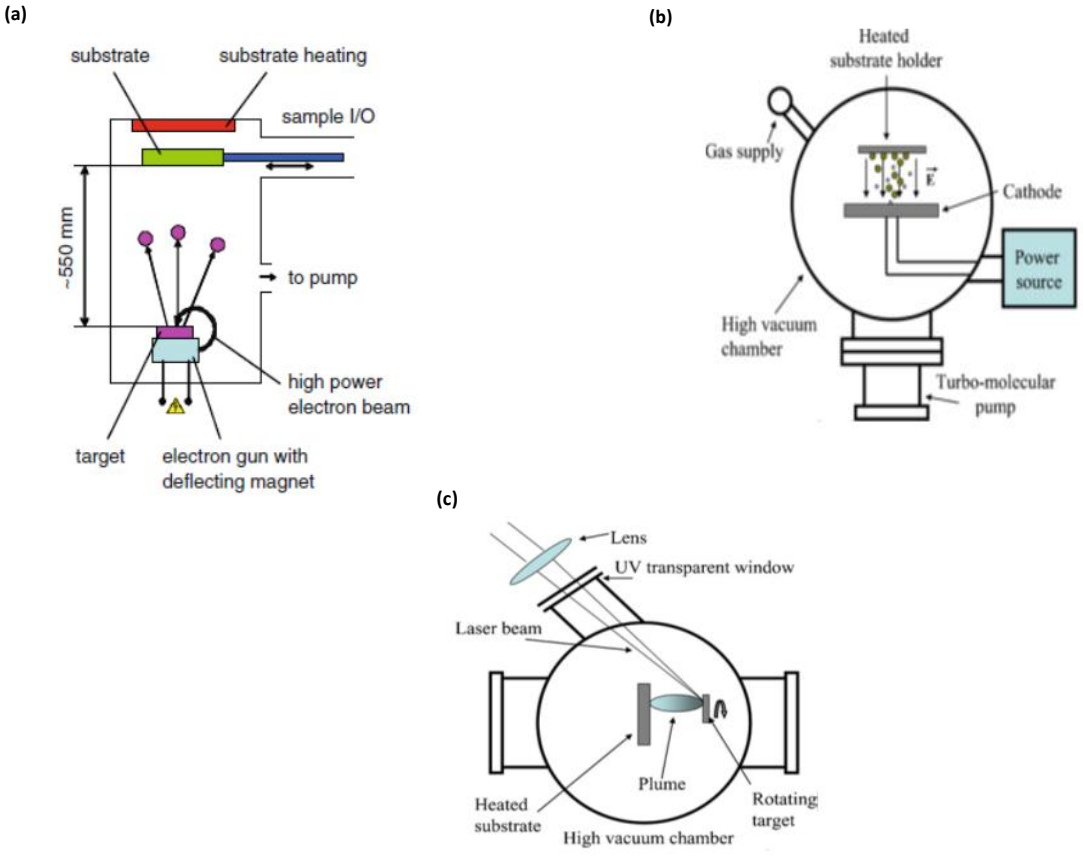

Fig. 1.11. Schematics of physical vapor deposition techniques: (a) Electron beam (EB) PVD, (b) Sputtering, and (c) Laser ablation [Reprinted from reference 91 with permission].

1.3.1.4. *Chemical vapor deposition (CVD)*

In chemical vapor deposition, a precursor (generally metal halides and metal-organic compounds with low vaporization temperature and high vapor pressure) is heated /decomposed to form active gas phase/species. The gaseous species transports into the reaction chamber and reacts to form the compounds on a substrate. Unlike PVD, chemical reactions and diffusion occur in CVD [98]. MOCVD refers to the CVD technique when metal- organic precursors are used for the deposition. Electrochemical vapor deposition (EVD) is another mode of CVD used to deposit dense ion or electron-conducting oxide films on a porous substrate. EVD uses oxygen ion transport through an oxygen ion permeable membrane to enable the chemical reactions and subsequent deposition and growth of the oxides. The schematics of CVD and EVD techniques are shown in Fig. 1.12 [98].

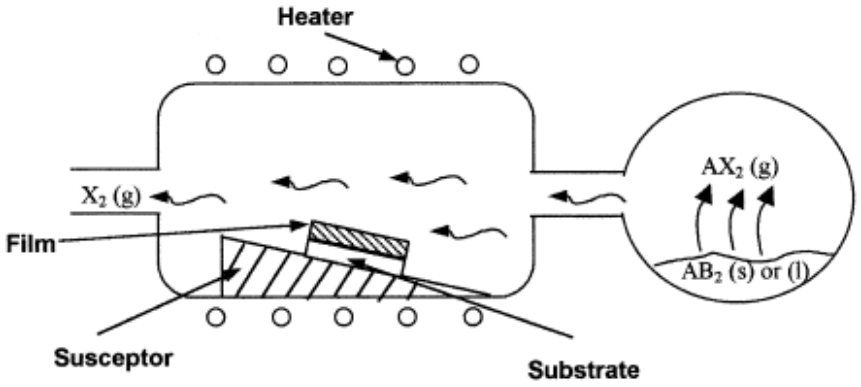

(a)

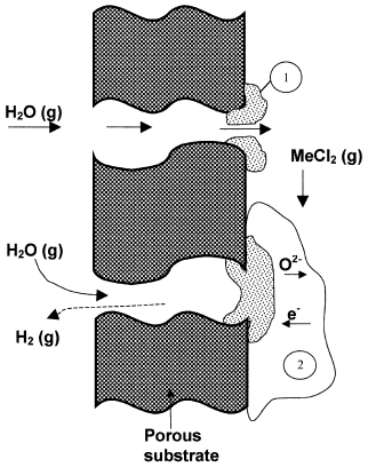

Stage 1: Pore closure via CVD

$$MeCl_2\,(g) + H_2(g) = MeO(s) + 2HCl(g)$$

Stage 2: Scale growth via EVD

$$H_2O(g) + 2e \rightarrow H_2(g) + O^{2-}$$

$$MeCl_2(g) + O^{2-} \rightarrow MeO(s) + Cl_2(g) + 2e$$

(b)

Fig. 1.12. Schematics of (a) CVD, and (b) EVD techniques [Reprinted from reference 98 with permission].

1.4. Lanthanum chromite ($LaCrO_3$) based perovskites for OTM

Despite having good electrical conductivity (0.6-1.0 S/cm at 1000°C) and superior chemical stability in a wide P_{O_2} range (0.21-10^{-22} atm) at high temperature (~1000°C), undoped $LaCrO_3$ is not suitable for OTM due to lack of ionic conduction and densification. To densify and obtain the desired thermal and electrical properties, dopants are introduced at A-site as well as B-site of lanthanum chromite. Sr and Ca are used as A-site dopants while transition metals (Mn, Co, Fe, Ni, Ti, Cu, and Al) are considered for

B-site dopants. A-site dopants are generally acceptor type and enhance densification as well as electrical conductivity. B-site dopants are introduced to maintain thermal and crystal structure stability, and to further increase the electrical conductivity (induce oxygen vacancy for ionic conduction). Below are some general defect reactions (Kröger-Vink notation) that can occur when $LaCrO_3$ is doped at A-site with alkaline earth metals (A = Sr, Ca) and/or transition metals (M = Mn, Co, Fe, Ni, Ti, Cu, and Al) at B-site. These reactions modify the thermal-electrical-mechanical properties and stability of $LaCrO_3$ based materials as explained later in the individual sections.

1) When alkaline earth metal (A=Sr, Ca) is partially doped at A-site and/or B-site, and the material is exposed to oxidizing atmosphere:

$$\mathrm{La}_{\mathrm{La}}^{\times} + \mathrm{Cr}_{\mathrm{Cr}}^{\times} \xrightarrow{\mathrm{A}} \mathrm{A}'_{\mathrm{La}} + \mathrm{Cr}_{\mathrm{Cr}}^{\cdot} \quad (7)$$

where $\mathrm{La}_{\mathrm{La}}^{\times}$ refers to La^{3+} on La^{3+} sites, $\mathrm{Cr}_{\mathrm{Cr}}^{\times}$ refers to Cr^{3+} on Cr^{3+} sites, $\mathrm{A}'_{\mathrm{La}}$ is single negatively ($'$) charged; A^{2+} is substituted on the La^{3+} site and $\mathrm{Cr}_{\mathrm{Cr}}^{\cdot}$ represent Cr^{4+} on Cr^{3+} site. The symbols $\times$ and $\cdot$ represents neutral and positive charges, respectively. When A^{2+} partially substitutes La^{3+} at A-site, a single negative charge is induced and compensated by the $\mathrm{Cr}^{3+} \rightarrow \mathrm{Cr}^{4+}$ transition.

2) When alkaline earth metal (A=Sr, Ca) is partially doped at A-site and/or B-site, and the material is exposed to reducing atmosphere:

$$2\mathrm{La}_{\mathrm{La}}^{\times} + \mathrm{O}_{\mathrm{O}}^{\times} \xrightarrow{\mathrm{A}} 2\mathrm{A}'_{\mathrm{La}} + \mathrm{V}_{\mathrm{O}}^{\cdot\cdot} + \frac{1}{2}\mathrm{O}_2 \quad (8)$$

$$2\mathrm{Cr}_{\mathrm{Cr}}^{\cdot} + \mathrm{O}_{\mathrm{O}}^{\times} \rightarrow 2\mathrm{Cr}_{\mathrm{Cr}}^{\times} + \mathrm{V}_{\mathrm{O}}^{\cdot\cdot} + \frac{1}{2}\mathrm{O}_2 \quad (9)$$

where A'_{La} is single negatively ($'$) charged; A^{2+} is substituted on the La^{3+} site, $La^{\times}_{La}$ refers to La^{3+} on La^{3+} sites, $Cr^{\times}_{Cr}$ refers to Cr^{3+} on Cr^{3+} sites, $Cr^{\cdot}_{Cr}$ represent Cr^{4+} on Cr^{3+} site and $V^{\cdot\cdot}_{O}$ represent oxygen vacancy. The symbols $\times$ and $\cdot$ represents neutral and positive charges, respectively. When A^{2+} is partially substituted at A-site and an induced negative charge on A is then compensated by the formation of oxygen vacancies. On the other side, Cr^{4+} reduces to $Cr^{3+}$and oxygen vacancies formation occur for charge compensation.

3) When transition metal (M= Mn, Co, Fe, Ni, Ti, Cu, and Al) is partially doped at B-site and/or at A-site, and the material is exposed to oxidizing atmosphere:

$$\frac{1}{2}O_2 + V^{\cdot\cdot}_{O} + 2M^{\times}_{M} = O^{\times}_{O} + 2M^{\cdot}_{M} \quad (10)$$

where $M^{\times}_{M}$ refers to M^{3+} on M^{3+} sites, $M^{\cdot}_{M}$ refers to M^{4+} on M^{3+} sites, and $V^{\cdot\cdot}_{O}$ refers to oxygen vacancy with two positive charges. Transition metals (e.g. Mn and Co) can exist in M^{3+} and M^{4+} valence state in oxidizing atmosphere, and the charge compensation occurs by oxygen vacancy. In addition, when A^{2+} partially substitutes La^{3+} at A-site, a single negative charge is induced and compensated by the $M^{3+} \rightarrow M^{4+}$ transition. The cation site vacancy formation can also occur for charge compensation of M^{4+} on M^{3+} site with an extra positive charge as shown below:

$$3M^{\times}_{M} \rightarrow 3M^{\cdot}_{M} + V'''_{M} \quad (11)$$

where $M^{\times}_{M}$, $M^{\cdot}_{M}$ and V'''_{M} denotes M^{3+} on M^{3+} site leading to neutral ($\times$) charge, M^{4+} on M^{3+} site with an extra positive ($\cdot$) charge, and Mn^{3+} cation vacancy with three negative ($'$) charges respectively.

4) When transition metal (M= Mn, Co, Fe, Ni, Ti, Cu, and Al) is partially doped at B-site and/or alkaline earth metal (A) at A-site, and the material is exposed to oxidizing atmosphere:

$$\frac{1}{2}O_2 + V_O^{\cdot\cdot} + 2M_M^{\times} = O_O^{\times} + 2M_M^{\cdot} \quad (12)$$

$$\frac{1}{2}O_2 + V_O^{\cdot\cdot} + 2M_M' = O_O^{\times} + 2M_M^{\times} \quad (13)$$

where $M_M^{\times}$ refers to M^{3+} on M^{3+} sites, $M_M^{\cdot}$ refers to M^{4+} on M^{3+} sites, M_M' refers to M^{2+} on M^{3+} sites, and $V_O^{\cdot\cdot}$ refers to oxygen vacancy with two positive charges. In reducing atmosphere, the oxygen vacancies formation occur for charge compensation when $M^{4+} \rightarrow M^{3+}$ and $M^{3+} \rightarrow M^{2+}$.

While introduction of dopants successfully tailor the desired thermal expansion and electrical conductivity behavior, the mechanical integrity and thermochemical stability are compromised due to oxygen non-stoichiometry and resultant defect chemistry. The lattice volume of lanthanum chromite based perovskite increases during heating and decreases during cooling due to generation of oxygen vacancies by dopants (Eq. (8), (10) and (13)) and reduced oxygen partial pressure (P_{O_2}), resulting in, respectively, compressive and tensile stress during thermal cycling. The OTM is also exposed to a stress gradient due to variation in lattice volume originating from the (P_{O_2}) gradient. The type and level of dopants and oxygen non-stoichiometry on the mechanical properties of lanthanum chromite have been correlated in this review article.

The thermochemical stability of lanthanum chromite based perovskite is discussed from three aspects: bulk chemical stability, interface stability, and surface

segregation. The bulk stability mainly depends on the decomposition and/or formation of secondary phases in the doped lanthanum chromite. Interface stability depends on the interaction between lanthanum chromite and adjacent materials such as zirconia and ceria. Surface segregation is predominant for A-site dopants and dominated by defect chemistry. It is to note that oxygen flux determines the performance of OTM materials. The oxygen flux in a single phase, dense lanthanum chromite perovskite depends on the tolerance factor, ionic conductivity, oxygen non-stoichiometry, and defect chemistry introduced by dopants.

The effect of type and level of different A-site and B-site dopants on lanthanum chromite densification and properties has been critically analyzed in this review article in the individual sections below. The discussed properties include thermal expansion, electrical conductivity, mechanical property, thermochemical stability (bulk, interface, and surface) and oxygen flux. Apart from chemistry and structure, the effect of dopant induced oxygen non-stoichiometry and defect chemistry on each properties have also been evaluated.

1.4.1. Crystal structure and phase transition

$LaCrO_3$ is orthorhombic at room temperature and has three temperature dependent polymorphs: magnetic phase transition from an anti-ferromagnetic to a paramagnetic state at ~15 °C [99-101], orthorhombic to rhombohedral transformation at ~ 260°C [100-102], and rhombohedral to cubic structure at ≥1200°C [103-104]. The orthorhombic to rhombohedral phase transition (~ 260°C) leads to compression of the lattice with a volume contraction of ~0.138% arising from the deformation and shrinkage of the

$[CrO_6]^{6-}$ octahedral [101]. The change in lattice volume can generate internal stress, contributing to mechanical failure during thermal cycling (start up and shut down).

Dopants in $LaCrO_3$ shift the phase transition temperature. Sr and Ca- dopants decrease the magnetic transition temperature due to a reduction in magnetic ordering arising from the change in lattice structure corresponding to the Cr^{3+} (d^3) to Cr^{4+} (d^2) transition for charge compensation (Eq. (14)) [102-106]. For example, magnetic transition temperature decreases by ~10°C for both $La_{0.9}Sr_{0.1}CrO_3$ and $La_{0.9}Ca_{0.1}CrO_3$ on doping [102-106]. When Sr^{2+} (or Ca^{2+}) partially substitutes La^{3+} at A-site, a single negative charge is induced and compensated by the $Cr^{3+} \rightarrow Cr^{4+}$ transition as shown below:

$$La_{La}^{\times} + Cr_{Cr}^{\times} \xrightarrow{Sr} Sr'_{La} + Cr_{Cr}^{\cdot} \quad (14)$$

where Sr'_{La} is single negatively ($'$) charged; Sr^{2+} is substituted on the La^{3+} site and $Cr_{Cr}^{\cdot}$ represent Cr^{4+} on chromium site. The symbols $\times$ and $\cdot$ represent neutral and positive charges, respectively.

The charge neutrality in Sr or Ca-doped $LaCrO_3$ can also be maintained by the creation of oxygen vacancies (Eq. (15)) which are pronounced in reducing atmosphere. Oxygen vacancies are also considered to produce larger deformations in the lattice and lower the magnetic ordering of Cr^{3+} to a greater extent. The magnetic transition temperature of $La_{1-x}(Sr/Ca)_xCrO_{3-\delta}$ with oxygen deficiencies further decreases by ~10°C for x=0.1 [105-106].

$$2La_{La}^{\times} + O_O^{\times} \xrightarrow{Sr} 2Sr'_{La} + V_O^{\cdot\cdot} + \frac{1}{2}O_2 \quad (15)$$

where Sr'_{La} is single negatively ($'$) charged; Sr^{2+} is substituted on the La^{3+} site and $V_O^{\cdot\cdot}$ represent oxygen vacancy. The symbols × and · represents neutral and positive charges, respectively. Similar to Eq. (14), Sr^{2+} is partially substituted at A-site and an induced negative charge on Sr is compensated by the formation of oxygen vacancies in reducing gas atmosphere.

The orthorhombic to rhombohedral phase transition temperature (~ 260°C) of alkaline earth metal- doped $LaCrO_3$ is found to be dependent on the average ionic radius (r_A) of the A-site. The average ionic radius for $La_{1-x}(Sr/Ca)_xCrO_3$ can be calculated by using Shannon's effective ionic radii in below equation [107]:

$$r_A = (1-x)r_{La^{3+}} + x r_{AE^{2+}} \quad (16)$$

where $r_{AE^{2+}}$ is the ionic radius of alkaline earth metal ions (Sr/Ca).

The average ionic radius of $La_{0.9}Sr_{0.1}CrO_3$ is 0.1368 nm and the rhombohedral phase transition temperature is ~42°C. For $La_{0.9}Ca_{0.1}CrO_3$, the average ionic radii is 0.1342 nm and the transition temperature is ~307°C due to the smaller ionic radii of Ca^{2+} (0.134nm) compared to Sr^{2+} (0.144 nm). The transition temperature shifts below room temperature (-173°C) for $La_{1-x}Sr_xCrO_3$ ($x \geq 0.2$) [105]. Smaller the average ionic radius, higher is the transition temperature of alkaline earth doped $LaCrO_3$ as shown in Fig. 1.13. Substitution of La^{3+} with Ca^{2+}/Sr^{2+} alkaline earth ions changes oxidation state of chromium ion ($Cr^{3+} \rightarrow Cr^{4+}$) to maintain charge neutrality, leading to rearrangement of constituent ions in the crystal structure of $La_{1-x}(Ca/Sr)_xCrO_3$ with decreasing $(Cr^{4+}/Cr^{3+}) - O^{2-}$ and $O^{2-} - O^{2-}$ ionic distances [105-106]. The ionic distances decrease and $[CrO_6]^{-6}$

octahedral units shrink with increase in the Ca/Sr-content; leading towards the orthorhombic to rhombohedral phase transformation [105].

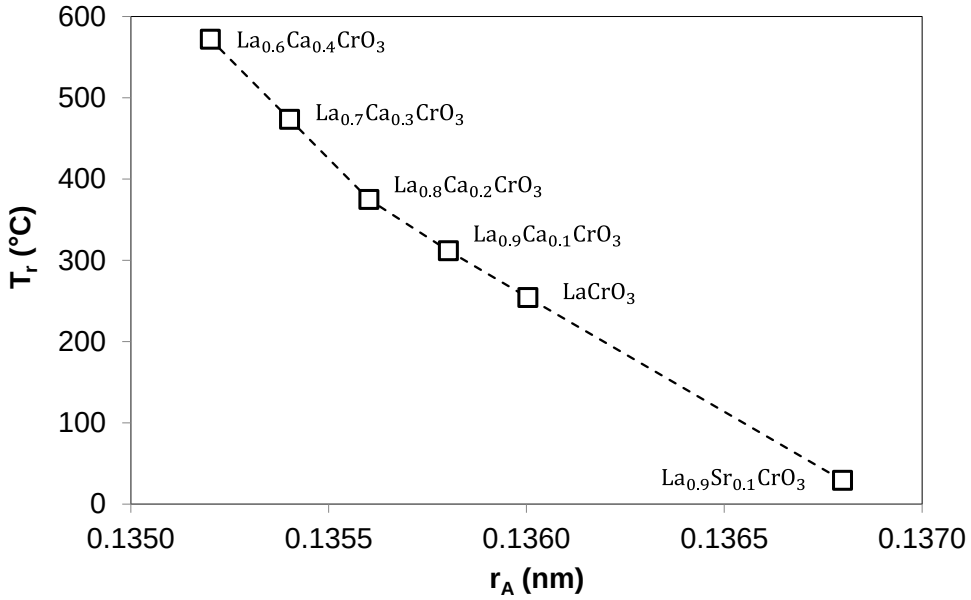

Fig. 1.13. Orthorhombic to rhombohedral phase transition temperature versus A-site average ionic radii (r_A) for $La_{1-x}(Sr/Ca)_xCrO_3$ (Reproduced from reference 105 with permission).

In addition to A-site dopants, the B-site dopants can also effect the phase transformation of $LaCrO_3$. However, the knowledge of B-site dopants effects on the phase transformation and transition temperatures is limited in the literature as mentioned here. For $La(Cr,Ni)O_3$ or $LaCrO_3$-$LaNiO_3$ system, it is noticed that the $LaCrO_3$ orthorhombic structure is maintained up to 60% Cr is replaced by Ni. However, the structure changes to rhombohedral with further increase in Ni content [108]. This is probably due to the formation of oxygen vacancies into the lattice of $LaCrO_3$ for the compensation of Ni^{2+}. With increase in nickel content, oxygen vacancies increases and

reaches a saturation point where the perovskite structure does not allow any more oxygen defects formation. This stage is reached at a 40 mole percent (m/o) of $LaNiO_3$ content. On further doping, Ni^{3+} formation occurs for charge compensation with linear decrease in the lattice parameter and rhombohedral phase formation [108].

In case of A and B-site simultaneously doped $La_{0.75}Sr_{0.25}Cr_{0.5}Mn_{0.5}O_3$, the existence of cubic phase is observed like undoped $LaCrO_3$ at high temperature (≥1000ºC). Using high-temperature neutron diffraction, it is identified that $La_{0.75}Sr_{0.25}Cr_{0.5}Mn_{0.5}O_3$ exists in rhombohedral ($R\bar{3}c$) phase up to 400°C [109]. However, the main peak splitting corresponding to rhombohedral phase decreases at ≥ 500°C and become insignificant when the temperature approaches 1000°C. The peak splitting disappearance with increase in temperature corresponds to less distortion of the lattice and a higher symmetry phase i.e. cubic ($Pm\bar{3}m$) formation. This indicates co-existence of cubic phase with rhombohedral. The fraction of cubic phase is calculated as 85.5% at 1000°C using Rietveld analysis and the transition of $R\bar{3}c \rightarrow Pm\bar{3}m$ is tend to complete at 1100°C [109]. The reason for the phase transformation is not known. However, it could be due to the possible existence of different valence state of Mn (+2, +3 and +4). This leads to form oxygen vacancies for the charge compensation (Eq. (12) and (13)), and may result into less distortion of the lattice at higher temperature.

Distortion of the perovskite lattice and change in crystal structure from lower to higher symmetry or vice-versa can also be explained using tolerance factor. The tolerance factor of perovskite determines their symmetry and approaches one for ideal cubic symmetry. The tolerance factor of $LaCrO_3$ is <1 (t = 0.968, according to Eq. (6)). The use

of alkaline earth metals as the A-site dopant tend to increase the tolerance factor and symmetry of $LaCrO_3$ [57-58, 82]. The B-site dopants (transition metal) also tune the tolerance factor but are used mainly to tailor redox properties [110-111]. This corresponds to the change in average ionic radii of the A-site and B-site on doping. Initially, the average A-site ionic radius (r_A) for undoped $LaCrO_3$ is 0.136 nm. On substitution, it increases to 0.1368 nm for $La_{0.9}Sr_{0.1}CrO_3$ based on Shannon's ionic radii formula. As the r_A increases, the tolerance factor will also increase according to the Eq. (6). For instance, tolerance factor of $La_{0.9}Sr_{0.1}CrO_3$ increased to 0.981 from 0.968 on doping $LaCrO_3$. Subsequently, the lower symmetry orthorhombic phase transforms to higher symmetry rhombohedral structure at lower temperature i.e. ~42ºC rather than ~260ºC [105]. On the other hand, the phase transformation increases to ~307°C from ~260ºC for $La_{0.9}Ca_{0.1}CrO_3$ [105]. This is because, the tolerance factor of $LaCrO_3$ decreases to 0.962 from 0.968 when partially substituted with Ca. The tolerance factor of $LaCrO_3$ can be further improved by doping with transition metals (M = Mn, Ni, Al etc.) at the B-site of $La_{0.9}Sr_{0.1}Cr_{0.9}M_{0.1}O_3$ as shown in Fig. 1.14 [112]. However, the symmetry is reduced when doping with Mg, Ti and Fe. The reason is not well understood. This might be due to a large distortion of the $[CrO_6]^{6-}$ octahedral in perovskite structure resulting in a lower tolerance factor, depending on their ionic radii and valence state of dopants.

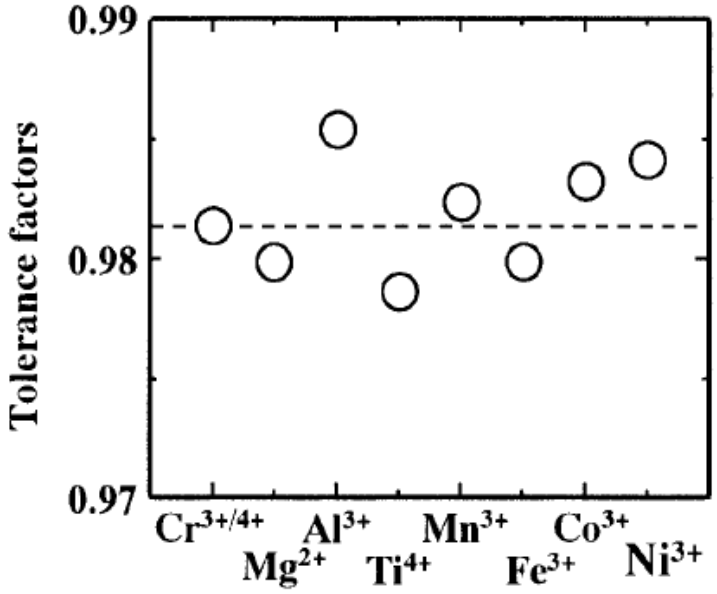

Fig. 1.14. Tolerance factor (t) of $La_{0.9}Sr_{0.1}Cr_{0.9}M_{0.1}O_3$ (M = Mg, Al, Ti, Mn, Fe, Co, Ni)]. The broken line corresponds to $La_{0.9}Sr_{0.1}CrO_3$ tolerance factor [Reprinted from reference [112 with permission].

1.4.2. Sintering

A dense, pore and crack free OTM is required for oxygen ion and electron transport through the bulk, prevention of air/fuel gas mixing, and leakage. Sintering is a process by which densification occurs at high temperature by atomic level mass transport. An OTM fabricated by any abovementioned techniques requires sintering step.

The relative density of $LaCrO_3$ sintered at 1450°C-1600°C in air is ~50% with a porous microstructure (Fig. 1.15a) [113-115]. The poor sinterability of $LaCrO_3$ is due to volatilization of chromium species (CrO_3, CrO_2, CrO) among which CrO_3 is the predominant vapor species above 1000^{o}C [116-118]. The chromium species evaporated

from the bulk condenses at irregular contact points (grain boundaries) of higher surface energy and deposit as Cr_2O_3 at the inter-particle necks as shown in the SEM micrograph in Fig. 1.15b. As a result, further atomic diffusion (driving force for densification) impedes and the inter-particle neck grows leading to porous microstructure [113]. The mechanism of $CrO_3\uparrow$ formation and Cr_2O_3 deposition is given in the following reaction [118]:

$$Cr_2O_3 + 3/2\ O_2 \leftrightarrow 2CrO_3\uparrow \quad (17)$$

Few approaches have been considered to improve the densification of $LaCrO_3$: reduced sintering atmosphere, liquid phase sintering, and addition of various A-site and B-site dopants. In reducing atmosphere, the vapor pressure of CrO_3 decreases significantly. For example, it decreases from ~10^{-6} to 10^{-17} atm when P_{O_2} decreases from ~1 to 10^{-15} atm (calculated using HSC Chemistry 6.0). Subsequently, Cr_2O_3 deposition at the inter-particle necks is inhibited resulting in higher densification [119].

In case of liquid phase sintering, a secondary phase of lower melting point assists in further densification of $LaCrO_3$ [118]. The liquid phase wets the solid particles/grains, disintegrates and dissolves the particles due to capillary force, and enhances the mass transfer through the liquid phase; resulting in higher densification [121].

1.4.2.1. *Role of dopants*

Addition of A-site and B-site dopants are used to enhance densification. Most commonly used A-site dopants are calcium and strontium. Many researchers have investigated the densification mechanism of $LaCrO_3$ by alkaline earth metals (Ca, Sr) substitution at A-site [114-115, 122-125]. It is observed that A-site dopants enhances

$LaCrO_3$ sintering by the formation of liquid phase ($CaCrO_4$/$SrCrO_4$) which dissolves back into the lattice with increase in temperature. Further enhancement on densification of $LaCrO_3$ can be achieved by B-site doping with transition metals (Mn, Ni, Co and Fe) [124-125]. Transition metals assist densification by cation vacancies formation which facilitates mass transport (Eq. (11)) or lowering the melting temperature of liquid phases facilitating liquid phase sintering. Detailed information is provided on the effect of A and B-site dopants on densification of $LaCrO_3$ in individual sub-sections below.

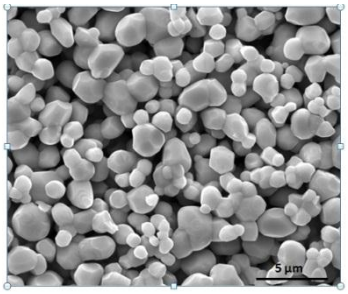

(a)

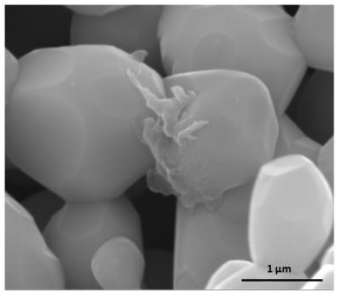

(b)

Fig. 1.15. Microstructures of $LaCrO_3$ sintered at 1450°C in air for 10 h: (a) lower magnification to show the porosity, (b) higher magnification with Cr_2O_3 deposition at inter-particle neck [113].

1.4.2.1.1. *A-site dopants*

Mori et al. [114] have shown the effect of alkaline earth metals (Ca, Sr) substitution on $LaCrO_3$ densification. It has been observed that the liquid phase $CaCrO_4$ starts to form at ~1000°C for Ca-doping in $La_{1-x}Ca_xCrO_3$ ($0 \leq x \leq 0.3$). The liquid phase wets the solid particles and enhances the densification. At high temperature (1230-1330°C), the $CaCrO_4$ phase re-dissolves into the chromite matrix according to the below reaction:

$$0.9\ LaCrO_3 + 0.1\ AECrO_4\ (\text{liquid}) \rightarrow\ La_{0.9}AE_{0.1}CrO_3 +\ 0.05\ O_2(\text{gas}) \qquad (18)$$

where AE stands for alkaline earth metals i.e. Sr or Ca.

The density increases with increase in dopant concentration ($0 \leq x \leq 0.3$) at 1600°C in air. The highest density of ~68% is achieved for $x = 0.3$ in $La_{1-x}Ca_xCrO_3$ sintered at 1600°C in air for 20 h [114]. To further improve the density, both A-site excess and A-site deficient $La_{0.7}Ca_xCrO_3$ ($0.25 \leq x \leq 0.35$) are studied [124]. The A-site deficient ($x = 0.28, 0.29$) Ca-doped lanthanum chromite provides <60% density even at 1550°C. Formation of transient liquid phase ($CaCrO_4$) leads to the partial densification (<60%) of the material between 850 and 1100°C for A-site deficient $La_{0.7}Ca_xCrO_3$ ($0.25 \leq x \leq 0.30$). The A-site excess ($x = 0.31, 0.32$) Ca-doped $LaCrO_3$ shows >90% at 1400°C. For A-site excess $La_{0.7}Ca_xCrO_3$ ($0.30 < x < 0.35$), another phase namely $Ca_3(CrO_4)_2$ forms at 1090°C in addition to $CaCrO_4$. Melting of $Ca_3(CrO_4)_2$ at ≤1253°C helps in further densification (>90%) of the material by liquid phase sintering. Both the secondary phases re-dissolve into the chromite after densification as temperature increases. Fig. 1.16 shows the SEM micrograph for $(La_{0.6}Ca_{0.4})_{1.02}CrO_3$ (>95% dense) heated to 1350°C (2h)

and air quenched to room temperature (RT) [128]. A comparative plot of A-site deficient, stoichiometric and A-site excess Ca-doped $LaCrO_3$ in Fig. 1.17 shows variation in density with calcium content (x) at ~1600°C [114-115, 123]. The variation in results is mostly due to the varying composition with different Ca-content. The density increases with increase in x due to the formation of lower melting phases: $CaCrO_4$ for A-site deficient and both $CaCrO_4$ and $Ca_3(CrO_4)_2$ for A-site excess $La_{0.7}Ca_xCrO_3$ ($0.25 \leq x \leq 0.35$). Consequently, A-site excess doped $LaCrO_3$ has higher density.

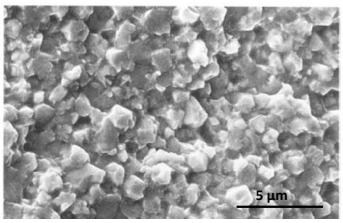

Fig. 1.16. SE- micrograph for $(La_{0.6}Ca_{0.4})_{1.02}CrO_3$ heated to 1350°C (2h) and air quenched to RT [Reprinted from reference 128 with permission].

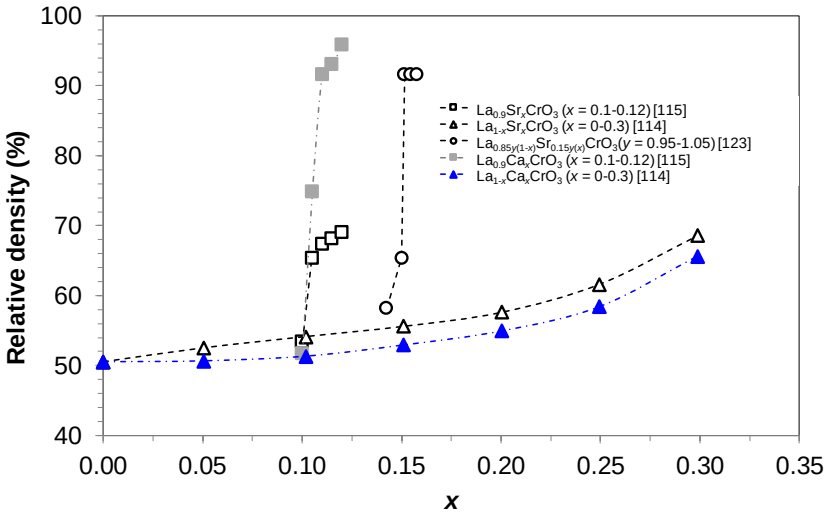

Fig. 1.17. Relative density of A-site (Sr,Ca) doped $LaCrO_3$ vs x in $La_{1-x}(Sr/Ca)_xCrO_3$ at 1600°C [114-115, 123].

Similarly, the partial substitution of La by Sr in the material ($La_{1-x}Sr_xCrO_3$) enhances densification due to the formation of $SrCrO_4$ phase (melting point ~1256°C) [114, 122]. For x = 0.3 in $La_{1-x}Sr_xCrO_3$, the density is ~ 65% at 1600°C [114]. Simner et al. [122] have provided the sintering mechanism for $(La_{0.7}Sr_{0.3})_xCrO_3$ ($0.95 \leq x \leq 1.05$) in air between 1100-1700°C. A-site deficient (x<1) $(La_{0.7}Sr_{0.3})_xCrO_3$ shows formation of only one lower melting phase i.e. $SrCrO_4$ at 1250°C while both phase $SrCrO_4$ and $Sr_{2.67}(CrO_4)_2$ phases form for A-site excess (x>1) $(La_{0.7}Sr_{0.3})_xCrO_3$. The highest density (>80%) was observed by $(La_{0.7}Sr_{0.3})_xCrO_3$ (x = 1.01) at 1400°C. Fig. 1.17 shows the density increase in $LaCrO_3$ with doped Sr-content at 1600°C. Ding et al. [128] have also shown similar results for $La_{0.85}(AE)_{0.15}CrO_3$ (AE = Ca, Sr) densification.

The effect of simultaneous Sr and Ca doping on the $LaCrO_3$ sintering further increases the density [130]. For example, the density of $La_{0.75}Ca_{0.25}CrO_3$, $La_{0.75}Sr_{0.25}CrO_3$, and $La_{0.75}Ca_{0.10}Sr_{0.15}CrO_3$ sintered at 1400°C for 24 h in air are 70%, 73%, and 84%, respectively. The possible reason is the formation of different liquid phases ($SrCrO_4$, $Sr_{2.67}(CrO_4)_2$, $CaCrO_4$, $Ca_3(CrO_4)_2$) at different temperatures enhancing the mass transport and subsequent densification.

1.4.2.1.2. *A and B-site dopants*

Another possibility of improving densification is the transition metals substitution at B-site of Sr-doped $LaCrO_3$ [124,127, 129]. It has been suggested that the secondary phases with variable melting temperature form due to reaction of transition metals with $SrCrO_4$ [126]. These liquids have higher wettability and lower viscosity which facilitate liquid phase sintering. The B-site doping can also lead to the formation of cation

vacancies (Eq. (11)) which can increase atomic diffusion and subsequent densification. In addition, the transition metal (B-site) dopants can increase the densification due to the higher diffusion coefficient of the transition metals.

Recently, it is notified that calcination temperature of Sr (A-site) and Fe (B-site) doped lanthanum chromite plays an important role on the densification of $La_{0.8}Sr_{0.2}Cr_{1-x}Fe_xO_{3-\delta}$ (x = 0.1-0.5) [120]. The amount of $SrCrO_4$ increases with decrease in calcination temperature. Higher amount of $SrCrO_4$ was detected when the calcination temperature decreased from 1200ºC to 900ºC. This is due to low solubility of $SrCrO_4$ at lower temperatures. Therefore, higher densities (84-97%) of sintered (1400°C) $La_{0.8}Sr_{0.2}Cr_{1-x}Fe_xO_{3-\delta}$ (x = 0.1-0.5) were obtained when calcined below 1200ºC due to the presence of higher amount of liquid phase. The density of $La_{0.8}Sr_{0.2}Cr_{1-x}Fe_xO_{3-\delta}$ increases with increase in Fe-dopant level. For instance, the density increases from ~84% (x = 0.1) to ~97 (x = 0.5). On the other hand, the amount of $SrCrO_4$ decreased with increase in Fe-doping level from 5.8 mol % (x = 0.1) to 2.7 mol % (x = 0.5) in the calcined samples at 1000ºC [120]. The reason for the variation in the amount of $SrCrO_4$ with increase in Fe-doping level is not provided. However, it could be due to the higher amount of Fe doping stabilizes the perovskite phase at lower temperature and therefore, suppresses the ex-solution of $SrCrO_4$.

Simner [126] and Ding et al. [129] have provided detailed experimental analysis on sinterability of transition metal doped $La_{0.85}Sr_{0.15}Cr_{1-x}M_xO_3$ (M = transition metal). The density comparison of various transition metal doped $La_{0.85}Sr_{0.15}Cr_{1-x}M_xO_3$ (M=Ni, Co and Cu) is shown in Fig. 1.18 [126, 129]. The density increases with increase in

temperature (1300-1650°C). Nickel, cobalt, and copper have significant effect on the densification [126, 129, 131]. The trend shows nickel substitution provides the highest density. It is postulated that the transition metal decreases the formation melting temperature of liquid phases in $La_{0.85}Sr_{0.15}Cr_{1-x}M_xO_3$ and enhance densification although no evidence is available [132].

Koc et al. [133] have shown the increased densification of $La_{0.9}Sr_{0.1}Cr_{1-x}Mn_xO_3$ when Cr is partially substituted with Mn as shown in the micrograph (Fig. 1.19). The increase in density from ~78% for x = 0.5 to ~95% for x = 0.7 at 1475°C is suggested due to the presence of higher Mn^{4+} ions resulting in more cation site vacancies facilitating mass transport [133]. The defect reaction for the formation of cation site vacancies on Mn^{3+} to Mn^{4+} transition can be written as:

$$3Mn_{Mn}^{\times} \rightarrow 3Mn_{Mn}^{\cdot} + V_{Mn}^{'''} \qquad (19)$$

where $Mn_{Mn}^{\times}$, $Mn_{Mn}^{\cdot}$ and $V_{Mn}^{'''}$ denotes Mn^{3+} on Mn^{3+} site leading to neutral (×) charge, Mn^{4+} on Mn^{3+} site with an extra positive (·) charge, and Mn^{3+} cation vacancy with three negative (´) charges respectively.

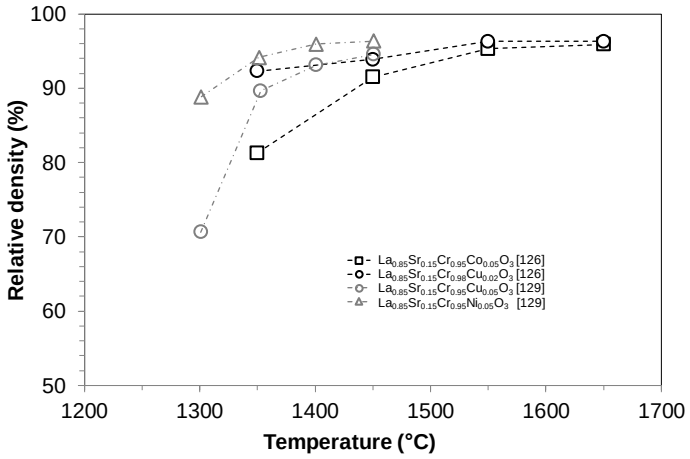

Fig. 1.18. Relative density of A-site (Sr) and B-site (Ni, Co and Ni) doped $LaCrO_3$ vs temperature and *x* in $La_{0.85}Sr_{0.15}Cr_{1-x}M_xO_3$ (M=Co, Cu, Ni) [126, 129].

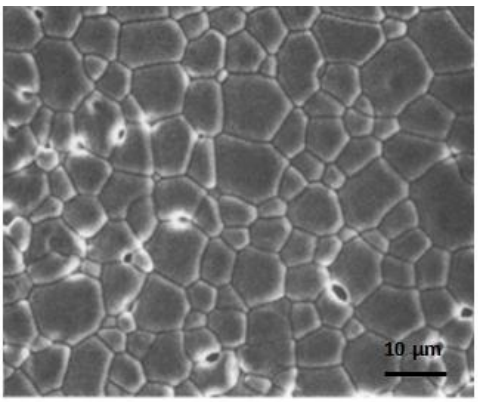

Fig. 1.19. SE-micrograph of $La_{0.9}Sr_{0.1}Cr_{0.3}Mn_{0.7}O_3$ sintered at 1475°C for 48h [Reprinted from reference 133 with permission].

1.4.3. Oxygen non-stoichiometry

Undoped lanthanum chromite is a stoichiometric oxide at least upto 1000°C and 0.21-10^{-20} atm P_{O_2} range [134-135]. On tailoring $LaCrO_3$ composition by dopants, deviation of oxygen content is often observed to maintain the charge neutrality in the crystal structure and thermodynamic equilibrium [47, 136-137]. The deviation of oxygen content, δ, is known as oxygen non-stoichiometry. For example, 20 mol% Ca doping creates 1.2 mol% oxygen vacancies (Eq. (8)) [99]. Increment in oxygen deficiency with reducing P_{O_2} is due to generation of higher oxygen vacancies. However, only reducing atmosphere is not responsible to induce detectable oxygen vacancies in doped $LaCrO_3$

[111,134]. This may be attributed to the bonding and packing structure of doped $LaCrO_3$ [137].

The stability of the material tends to decrease with increase in δ due to the lattice expansion and stress generation in presence of the oxygen vacancies. This may lead to failure of the membrane when the vacancies are present in excess. Dissociation of the chromite based materials is also possible due to large variance in δ [138].

1.4.3.1. *A-site dopants*

Fig. 1.20a shows the effect of type and amount of dopants, and P_{O_2} on oxygen non-stoichiometry while Fig. 1.20b shows the temperature effect [138-142]. A general trend is followed. The amount of oxygen non-stoichiometry increases with dopant concentration, temperature and P_{O_2}. On partial substitution of lanthanum (La^{3+}) with alkaline earth metals (Sr^{2+}/Ca^{2+}) to form $La_{1-x}Sr_xCrO_{3-\delta}$, a loss of positive charge is compensated by $Cr^{3+} \rightarrow Cr^{4+}$ (Eq. (14)) in oxidizing atmosphere. However, the Cr^{4+} reduces to Cr^{3+} in reducing atmosphere and the charge compensation is occurred by the formation of oxygen vacancy (Eq. (9)).

With increase in dopant (Sr and Ca) concentration, oxygen vacancies concentration also increases to maintain the charge electro-neutrality in reducing atmosphere. The oxygen non-stoichiometry (δ) deviation increases further with increase in temperature and decrease in P_{O_2} as shown in Fig. 1.20b [140]. Oxygen vacancies (oxygen non-stoichiometry) promote oxygen ion conduction. Therefore, the increase in oxygen vacancies corresponds to increase in oxygen ion conductivity of Ca/Sr doped

$LaCrO_3$ with decrease in P_{O_2}. For instance, the ionic conductivity of $La_{0.9}Ca_{0.1}Cr_{1.03}O_{3-\delta}$ increases from 1.59×10^{-6} to 3.53×10^{-5} S cm^{-1} when P_{O_2} decrease from 0.21 to 10^{-15} atm at 1015°C, respectively. Similarly, Sr-doped $La_{0.87}Sr_{0.13}Cr_{1.03}O_{3-\delta}$ oxygen ion conductivity increases from 4.01×10^{-6} S cm^{-1} at P_{O_2}~ 0.21 atm to 1.95×10^{-5} S cm^{-1} at P_{O_2}~ 10^{-15} atm and 1015°C.

It is to note that the type of commonly used A-site dopants i.e. Sr and Ca has no distinct effect on oxygen non-stoichiometry (Fig. 1.20a) and a saturation value in oxygen stoichiometry is observed at half of the substituents, i.e., *x*/2. Also, there is no significant difference in the oxygen ionic conductivity of Sr/Ca doped $LaCrO_3$ at different P_{O_2}. This means the defect reaction kinetics is same for both the dopants [140].

1.4.3.2. *B-site dopants*

For B site dopants, no specific relation between oxygen non-stoichiometry with type and concentration can be drawn because of limited information [138]. Unlike A-site dopants, the oxygen non-stoichiometry varies differently depending on the type of B-dopants. At 800°C and $P_{O_2}<10^{-10}$ atm, the amount of oxygen nonstoichiometry increases in the order of Ni>Co>Mg>Fe>Ti for 10 mol% B-site doping [138]. No significant variation in oxygen non-stoichiometry is observed for $LaCr_{0.9}Ti_{0.1}O_{3-\delta}$ perovskite at 800°C in the wide range of P_{O_2}(~10^{-5}-10^{-20} atm) [138]. This is associated with no change in the valence state of titanium in the perovskite. Fig. 1.20c shows the deviation in δ for B-site doped $LaCr_{0.9}M_{0.1}O_{3-\delta}$ (M = Fe, Ni and Co) at 1000°C in the P_{O_2} range of ~10^{-5}-10^{-20} atm. Comparatively, less deviation in δ is observed for Fe than Ni and Co-doping.

However, the oxygen stoichiometry for Ni and Co dopants is comparable as shown in Fig. 1.20c. The possible reason is the existence of different oxidation state of B-site dopants. For instance, cobalt exists in mixed valence state i.e. Co^{2+}/Co^{3+} [138]. On the other hand, the reduction of $Co^{3+} \rightarrow Co^{2+}$ also leads to the formation of oxygen vacancies for the charge balance in reducing gas atmosphere.

Point defects including oxygen vacancies in oxides may interact with lattice ions and other defects by columbic attraction with negative ions/cation vacancy resulting in the formation of localized defect cluster, repulsion between similarly charged ions/defects, and localized change in energy bandwidth [136, 137, 143, 144]. Interaction of oxygen vacancy with lattice is proven for doped $LaCrO_3$ but the type and extent of interaction has not been understood [139]. The interaction of defects among themselves and lattice depends on dopant type and level. The interaction is stronger for B-site dopants than A-site dopants [138-139, 141]. This suggests that the defect reaction kinetics for B-site doping is more complex than A-site doping.

1.4.3.3. *A-site and B-site dopants*

No specific trend is observed for type and concentration for simultaneous A and B-site doped $LaCrO_3$ [141, 145, 146-148]. For example, oxygen non-stoichiometry increases with increase in Al doping for 10 mol% Ca-doped $LaCrO_3$ but decreases with increasing Ti doping in 30 mol% Sr doped $LaCrO_3$ [141, 145]. Al exists only in Al^{3+} state. Subsequently, Al will create oxygen vacancies by substituting Cr^{4+} ions in doped $LaCrO_3$, resulting in increasing oxygen non-stoichiometry with Al content for $La_{0.9}Ca_{0.1}Cr_{1-y}Al_yO_{3-\delta}$ [145]. On the other hand, Ti may exist in Ti^{3+} and Ti^{4+} valance states [148].

Depending on Cr^{4+} amount in $LaCrO_3$, there will be a redox reaction involving Ti and Cr valance change compensating the charge balance associated with partial molar free energy, sufficient to reduce significant oxygen vacancies [137, 148]. Fig. 1.20d shows the change in oxygen non-stoichiometry for simultaneously doped $La_{0.7}Sr_{0.3}Cr_{1-x}Ti_xO_{3-\delta}$ (x = 0.1-0.3) and compared with only A-site doped $La_{0.7}Sr_{0.3}CrO_{3-\delta}$ at 1000°C in the P_{O_2} range of 0.21 – 10^{-20} atm. It is observed that the simultaneously Sr (A-site) and Ti (B-site) doped $La_{0.7}Sr_{0.3}Cr_{1-x}Ti_xO_{3-\delta}$ (x = 0.1-0.3) shows less deviation from oxygen stoichiometry when compared to Sr-doped $La_{0.7}Sr_{0.3}CrO_{3-\delta}$. This is associated with the existence of Ti^{4+} acting as donor dopant which can compensates for the loss of the positive charge for Sr^{2+} rather than oxygen vacancy formation in reducing gas atmosphere [143]. With increase in Ti doping, the deviation goes further down (Fig. 1.20d) due to increase in Ti^{4+} and donor dopant.

Fig. 1.20e shows the comparison of oxygen non-stoichiometry of $La_{0.75}Sr_{0.3}Cr_{0.7}Ti_{0.3}O_{3-\delta}$, $La_{0.75}Sr_{0.25}Cr_{0.5}Mn_{0.5}O_{3-\delta}$, and $La_{0.75}Sr_{0.25}Cr_{0.5}Fe_{0.5}O_{3-\delta}$ as a function of P_{O_2} (~1-10^{-25} atm) at 1000ºC [141]. It is observed that Sr and Ti simultaneously doped $La_{0.75}Sr_{0.3}Cr_{0.7}Ti_{0.3}O_{3-\delta}$ does not show any significant deviation from oxygen stoichiometry when compared to $La_{0.75}Sr_{0.25}Cr_{0.5}Mn_{0.5}O_{3-\delta}$ and $La_{0.75}Sr_{0.25}Cr_{0.5}Fe_{0.5}O_{3-\delta}$. This is because Mn and Fe can exist in different valence state of 4+, 3+ and 2+. Due to the change in valence state of Mn/Fe, the charge compensation occurs by oxygen vacancies formation in the LSCM/LSCF perovskite lattice, resulting in larger deviation from oxygen stoichiometry. For instance, this is shown in Eq. (20) and (21) for LSCF perovskite [141].

$$\frac{1}{2}O_2 + V_O^{\cdot\cdot} + 2Fe_{Fe}^{\times} = O_O^{\times} + 2Fe_{Fe}^{\cdot} \quad (20)$$

$$\frac{1}{2}O_2 + V_O^{\cdot\cdot} + 2Fe_{Fe}' = O_O^{\times} + 2Fe_{Fe}^{\times} \quad (21)$$

where $Fe_{Fe}^{\times}$ refers to Fe^{3+} on Fe^{3+} sites, $Fe_{Fe}^{\cdot}$ refers to Fe^{4+} on Fe^{3+} sites, Fe_{Fe}' refers to Fe^{2+} on Fe^{3+} sites, and $V_O^{\cdot\cdot}$ refers to oxygen vacancy with two positive charges.

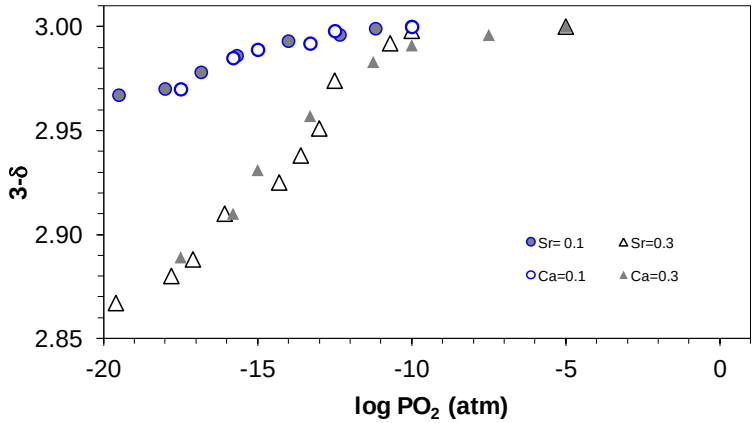

(a)

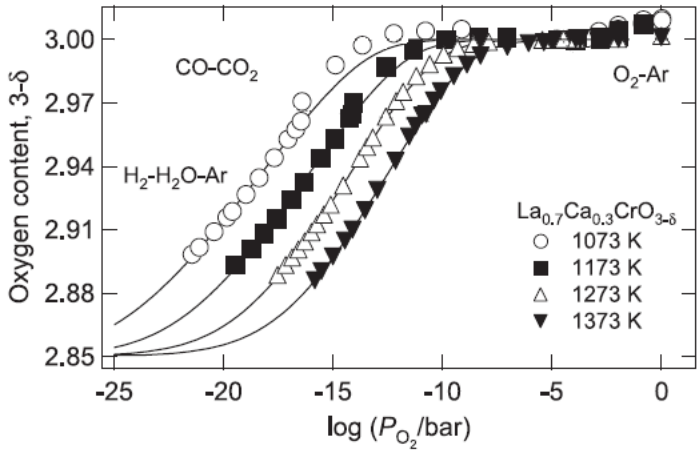

(b)

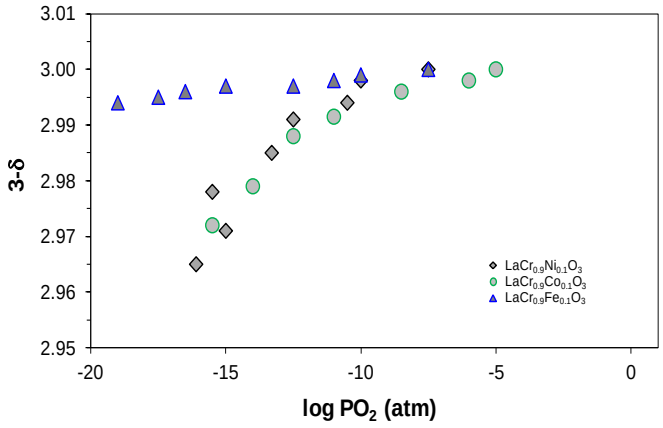
3.01
3.00
2.99
2.98
2.97
2.96
2.95
3-δ
-20
-15
-10
-5
0
log PO2 (atm)
LaCr0.9Ni0.1O3
LaCr0.9Co0.1O3
LaCr0.9Fe0.1O3

(c)

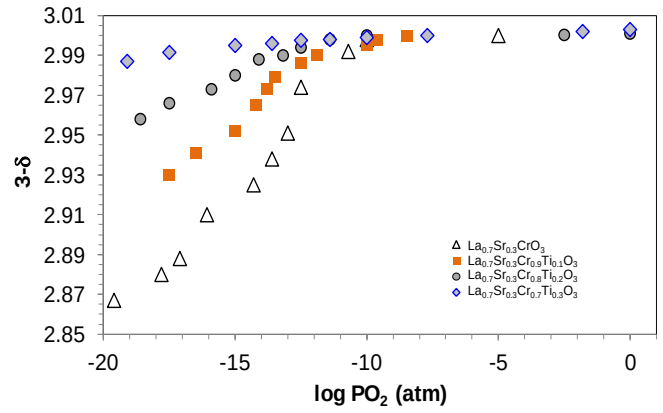
3.01
2.99
2.97
2.95
2.93
2.91
2.89
2.87
2.85
3-δ
-20
-15
-10
-5
0
log PO2 (atm)
La0.7Sr0.3CrO3
La0.7Sr0.3Cr0.9Ti0.1O3
La0.7Sr0.3Cr0.8Ti0.2O3
La0.7Sr0.3Cr0.7Ti0.3O3

(d)

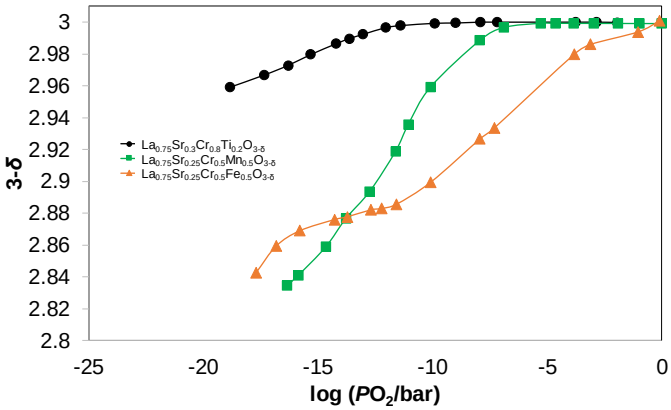
3
2.98
2.96
2.94
2.92
2.9
2.88
2.86
2.84
2.82
2.8
3-δ
-25
-20
-15
-10
-5
0
log (PO2/bar)
La0.75Sr0.3Cr0.8Ti0.2O3-δ
La0.75Sr0.25Cr0.5Mn0.5O3-δ
La0.75Sr0.25Cr0.5Fe0.5O3-δ

(e)

Fig. 1.20. Oxygen non-stoichiometry of $La_{1-x}A_xCr_{1-y}B_yO_{3-\delta}$: a) A-site (Sr/Ca) doping; b) variation with temperature, c) B-site doping (Fe/Ni/Co), and d) Simultaneous A (Sr) and B-site (Ti) doping e) Simultaneous A (Sr) and B-site (Ti/Mn/Fe) at 1000°C [138-142].

According to the above oxygen non-stoichiometry discussion, it would be beneficial to dope lanthanum chromite based material with Sr and Ti dopants at A-site and B-site respectively for higher redox stability of OTM. On the other hand, it is known that oxygen ion conductivity increases with increase in oxygen vacancies or decrease in P_{O_2} . For example, $(La_{0.75}Sr_{0.25})_{0.95}Cr_{0.5}Mn_{0.5}O_{3-\delta}$ ionic conductivity increases from 3.1×10^{-5} to 2.2×10^{-4} when P_{O_2} decrease from 0.21 to 10^{-15} atm at 950°C, respectively. [149] The corresponding transference number (the fraction of the total current carried by a given ion (O^{2-}) in OTM, $t_{ion} = \frac{\sigma_{ion}}{\sigma_{ion}+\sigma_{el}}$) also increases from 8.9×10^{-7} to 5.6×10^{-5} S cm^{-1} with increase in oxygen ion conductivity, respectively. The oxygen vacancies also increase with increase in dopant level. For instance, the ionic conductivity of $(La_{0.75}Sr_{0.25})_{0.95}Cr_{1-x}Fe_xO_{3-\delta}$ is 0.056 S cm^{-1} (x = 0.3, δ = 0.16) and 0.079 S cm^{-1} (x = 0.4, δ = 0.19) at 950ºC and P_{O_2}~10^{-17} atm [33]. Similarly, the transference number increases from 0.04 to 0.15, respectively. With increase in Fe-doping level, the ionic conductivity increases due to increase in oxygen vacancy concentration. It is noted that higher ionic conductivity and transference number is obtained for Fe-doping. This could be due to the variation in the disproportion of valence state of Mn/Fe and oxygen vacancies formation.

This suggests that Fe doping at B-site would be more beneficial over Mn-doping to induce mixed ionic-electronic conductivity in lanthanum chromite based materials.

However, Ti-doping would be suitable from redox stability point of view. From author's perspective, it is suggested to use co-doping of transition metal (e.g. Fe) at B-site with Ti to obtain mixed conductivity and redox stability at the same time. However, an in-depth study is required to understand the co-doping effect and optimize doping level.

Microscopic level change in crystal lattice due to oxygen non-stoichiometry significantly affects $LaCrO_3$ properties such as thermal expansion, electronic and ionic conductivity, catalytic property for oxygen reduction, and thermo-mechanical and thermochemical stability [33, 111, 134, 136-137, 142, 146-152]. The effect of oxygen non-stoichiometry on $LaCrO_3$ properties will be discussed in subsequent sections.

1.4.4. Thermal expansion

$LaCrO_3$-based perovskites are in contact with fluorite phases such as YSZ (yttria-stabilized zirconia), ScSZ (scandia stabilized zirconia) or GDC (gadolinium doped cerium oxide) in dual phase composite OTM and adjacent component layers (intermediate and surface exchange layers) consisting of perovskite-fluorite composites [153-154]. Thermal expansion mismatch between $LaCrO_3$-based perovskites and the adjacent materials can lead to thermal stress (σ) according to the equation [155] below:

$$\sigma = \frac{\mathrm{E}}{1-\vartheta}\Delta\alpha(T - \mathrm{T_0}) \qquad (22)$$

where, E is the Young modulus and ϑ is the Poisson ratio of the $LaCrO_3$ based perovskites, $\Delta\alpha$ is the difference in thermal expansion coefficient (TEC) between $LaCrO_3$ based perovskite and the adjacent material, T is the operating temperature and $\mathrm{T_0}$ is the stress free temperature. The fabrication temperature is generally considered as $\mathrm{T_0}$ which

can be the operating temperature if the stress is relaxed due to material deformation. If $T < T_{0,}$ compressive and tensile stress will be developed, respectively, for positive and negative value of $\Delta\alpha$. Cracks and warpage may develop at the interfaces of adjacent materials and components due to thermal stress, leading to gas leakage and mechanical failure during operation and thermal cycling during start up and shut down. The tolerable TEC difference is ~1.0 $\times 10^{-6}$ °C^{-1} [156-157]. The fluorite phase considered for OTM is either YSZ or GDC or ScSZ. The thermal expansion coefficient (TEC) of 8YSZ (8 mol % yttria doped zirconia) is ~10.3$\times 10^{-6}$ °C^{-1} up to 1000°C under both oxidizing and reducing atmosphere [112, 158]. The TEC of GDC20 (20 mol % gadolinium doped ceria) and 8ScSZ (8 mol % scandia doped zirconia) are ~12.9$\times 10^{-6}$ °C^{-1} and 11.9$\times 10^{-6}$ °C^{-1} in the temperature range of 50-900°C and 370-1000°C, respectively [159-160]. However, in GDC, Ce^{4+} reduces to Ce^{3+}, and the charge compensation occurs by the formation of oxygen vacancies as shown in the below redox reaction:

$$2Ce_{Ce}^{\times} + O_{O}^{\times} \rightarrow \frac{1}{2}O_2(g) + V_{O}^{\cdot\cdot} + 2Ce_{Ce}' \qquad (23)$$

where $Ce_{Ce}^{\times}$ refers to Ce^{4+} on Ce^{4+} site, Ce_{Ce}' refers to Ce^{3+} on Ce^{4+} site, and $V_{O}^{\cdot\cdot}$ refers to oxygen vacancy with two positive charges.

It indicates that GDC is not very stable in reducing atmosphere due to the oxygen vacancies formation leading to significant increase in lattice expansion. This generates micro-cracks as well as pin holes on the surface and at the fracture of GDC electrolyte. [161] Yttria-stabilized zirconia (YSZ) is one of the most common oxygen ion conductive and stable material which can be used as a fluorite phase in oxygen separation membrane and the other layers [42, 162-163].

For the above reason, the lanthanum chromite based membranes are expected to have similar thermal expansion coefficient (TEC) as fluorite phase (YSZ). However, the average TEC of $LaCrO_3$ was measured in the range of 8.1-8.6×10^{-6} °C^{-1} in both air and H_2 atmosphere in the temperature range of 50-1000°C [99, 112, 134, 162]. The thermal expansion coefficient of $LaCrO_3$ is 4.6 ×10^{-6} °C^{-1} and 9.4 ×10^{-6} °C^{-1} in the temperature range of ~40-275°C and ~290-1050°C respectively [165]. Recently, the change in TEC due to high temperature cubic phase formation at ~1300°C is reported as 9.8×10^{-6} °C^{-1} in the temperature range of 1100-1395°C [113].

Under OTM operating conditions, the TEC of lanthanum chromite based material can be influenced by three factors: change in valence state and ionic radius of dopant, oxygen nonstoichiometry or oxygen loss, and decrease in elastic modulus or interatomic bond strength [112]. The variation in valence state of cation-dopant changes the ionic radii of the cation and increases/decreases the lattice dimension [166]. Oxygen nonstoichiometry or oxygen loss introduces oxygen vacancies into the lattice, resulting in the lattice expansion [166]. Dopants in $LaCrO_3$ can result into deformation of chromium-oxygen polyhedral and weakens the Cr-O covalent bond linkages. The decrease in inter-atomic bond strength or elastic modulus could increase the probability of the lattice to expand more on increasing the temperature and lead to higher thermal expansion. The TEC of doped-$LaCrO_3$ depends on the type and level of dopants. Therefore, dopant type and their concentration are needed to control the TEC and stability of the membrane material under the OTM operation conditions.

1.4.4.1. *A-site dopants*

Alkaline earth metals, Ca (0.134 nm) and Sr (0.144 nm) have comparable ionic radii to La^{3+} ion (0.136 nm) [167]. When $LaCrO_3$ is doped at A-site by divalent alkaline earth metals (Ca, Sr), the La^{3+} ions are substituted by Ca^{2+}/Sr^{2+}. To maintain the electroneutrality, the decrease in positive charge is compensated by a change in valence state of chromium from Cr^{3+} to Cr^{4+} (Eq. (14)), resulting in the lattice contraction due to change in ionic radii ($r_{Cr^{4+}} < r_{Cr^{3+}}$). In reducing atmosphere, the charge is compensated by the formation of oxygen vacancies (Eq. (15)) resulting into an increase in thermal expansion. This can also be due to increase in cation-cation repulsion as in-between bridging oxygen ion is removed (oxygen vacancy formation) [168]. Fig. 1.21 shows the TEC of $La_{1-x}(Sr/Ca)_xCrO_3$ with various dopant concentrations (x = 0.1-0.3) and YSZ in air and H_2 atmosphere in the temperature range of 50-1000°C [112, 129, 134, 169]. The TEC of both Sr and Ca doped $LaCrO_3$ increases with increase in dopant concentration. This is explained by the increase of the thermal expansion coefficient of O^{2-}–O^{2-} and Cr^{3-}–O^{2-} distances using molecular dynamics calculation [103]. However, the TEC variation for $La_{1-x}Ca_xCrO_3$ is significantly larger than $La_{1-x}Sr_xCrO_3$. According to Fig. 1.21, $La_{1-x}Sr_xCrO_3$ (x ~ 0.1) appears to be a promising candidate with comparable TEC as YSZ (~10.3×10^{-6} °C^{-1}) in both air and H_2 atmosphere. It is noted that there is a variation in the thermal expansion coefficient of same composition reported by different authors. The reason for the variation is not known. Sr-doped $LaCrO_3$ is more preferred than Ca due to comparable TEC with YSZ [132].

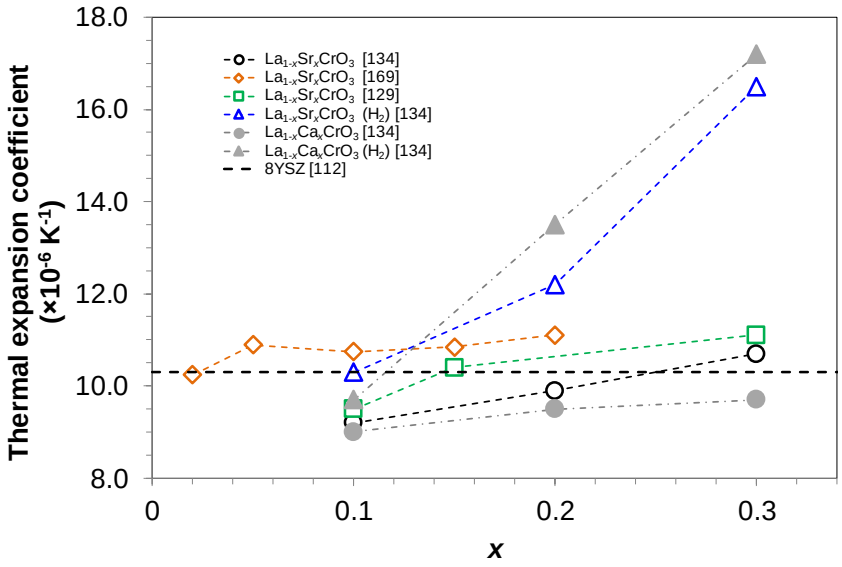

Fig. 1.21. Thermal expansion coefficient of $La_{1-x}(Sr/Ca)_xCrO_3$ in air and H_2 with 8YSZ [112,129,134,169]

1.4.4.2. *A and B-site dopants*

Transition metals (Mn, Ni, Fe, Co, Al and Ti) as B-site dopant also tune the TEC of $LaCrO_3$ based perovskites [112, 169-171]. The mechanism for change in the thermal expansion of $La_{1-x}Sr_xCrO_3$ doped with transition metal can be explained by varying average ionic radius of B-site dopants [112, 132]. Mori et al. [112] have illustrated the same by plotting the subtracted TEC of $La_{0.9}Sr_{0.1}Cr_{1-x}M_xO_3$ (x = 0.05 ; M = Mg, Al, Ti, Mn, Fe, Co, Ni) from $La_{0.9}Sr_{0.1}CrO_3$ in the temperature range of 50-1000°C versus ionic radii of B-site dopant in air and H_2 atmosphere as shown in Fig. 1.22a and b, respectively. The increment in TEC is the most for cobalt dopant. At low temperature, cobalt ions exist in 3+ valence state with low spin and ionic radius of 0.068 nm. With increasing temperature (up to -73°C), it transforms from low to high spin state with ionic radii of

0.075 nm. Further increase in temperature transforms the pair of low and high spin cobalt with 3+ valance state to low spin cobalt with 2+ (r = 0.079 nm) and 4+ (r = 0.067 nm) valence state [112, 172-173]. This shows that the increase in the TEC is related to the change in valence state of B-site dopant, ionic radii and/or spin [172]. Similarly, the higher TEC of Mn-doped $La_{0.9}Sr_{0.1}Cr_{1-x}Mn_xO_3$ is due to the change in valence state between Mn^{4+} (0.067 nm), Mn^{3+} (high-spin, 0.078 nm), and Mn^{2+} ions (low-spin, 0.081 nm) leading to the increase in average ionic radii of B-site cation at high temperature [112]. Lower thermal expansion of $La_{0.85}Sr_{0.15}Cr_{0.95}Ni_{0.05}O_3$ is observed when Cr is substituted by Ni due to increase in inter-atomic bond strength [132, 172]. Fig. 1.23 shows the deviation in thermal expansion coefficient of $La_{1-y}Sr_yCr_{1-x}M_xO_3$ (y = 0.05 or 0.1 and x = 0.05; M = Mg, Al, Ti, Mn, Fe, Co, Ni) with 8YSZ in air and H_2 gas [112, 129, 171].

It has been observed that the A-site deficiency can significantly reduce the volume expansion [149]. Tao et al. [149] have measured the average thermal expansion coefficient (TEC) of $(La_{0.75}Sr_{0.25})_{0.95}Cr_{0.5}Mn_{0.5}O_{3-\delta}$ (LSCM) to be $9.3 \times 10^{-6}\ °C^{-1}$ in air, close to YSZ ($10.3 \times 10^{-6}\ °C^{-1}$) in the temperature range of 60-950°C. Another study on $(La_{0.75}Sr_{0.25})_{0.95}Cr_{0.5}Mn_{0.5}O_{3-\delta}$ composition has shown linear TEC of ~$12.7 \times 10^{-6}\ °C^{-1}$ and ~$11.7 \times 10^{-6}\ °C^{-1}$ in oxidizing ($P_{O_2} = 0.21$ atm) and reducing atmosphere (P_{O_2}= 5×10^{-21} - 3×10^{-14}atm) respectively in the temperature range of 650-950°C [32]. The average thermal expansion coefficient of $La_{0.75}Sr_{0.25}Cr_{0.5}Mn_{0.5}O_3$ is reported to be $11.4 \times 10^{-6}\ °C^{-1}$ in air between 30 and 900°C [174], which is higher than the TEC ($9.3 \times 10^{-6}\ °C^{-1}$) reported by Tao et al. [149]. The TEC of

$La_{0.75}Sr_{0.25}Cr_{0.5}Mn_{0.5}O_3$ is reduced to 10.3×10^{-6} °C^{-1} with the addition of YSZ phase forming LSCM (50%)/YSZ (50%) composite. This results into TEC match of the composite with YSZ [174]. However, an addition of Sm-doped ceria ($Ce_{0.8}Sm_{0.2}O_{1.9}$-SDC) fluorite phase to LSCM does not significantly change the TEC when compared to LSCM. The TEC's of LSCM – *x*SDC (*x* = 10-50 wt. %) range from 11.7×10^{-6} °C^{-1} - 11.5×10^{-6} °C^{-1} and similar to LSCM (11.6×10^{-6} °C^{-1}) in the temperature range of RT-800ºC [175].

$(La_{0.75}Sr_{0.25})_{0.95}Cr_{1-x}Fe_xO_{3-\delta}$ (*x* = 0.3-0.4) has been considered to be one of the promising material for fuel side electrode [33, 120], and can be used as OTM. This is because; it provides the combination of high electrochemical activity and good chemical compatibility with electrolyte. It is reported that the average TEC's of $(La_{0.75}Sr_{0.25})_{0.95}Cr_{1-x}Fe_xO_{3-\delta}$ (0.3-0.4) are almost independent of *x*, and lies in between 11.1-11.3×10^{-6} °C^{-1} in air and 10.3-10.5×10^{-6} °C^{-1} in $CO\text{-}CO_2$ (P_{O_2}~10^{-12} atm at 1097ºC) gas atmosphere in the temperature range of 27ºC-1097ºC. The TEC is slightly lower in the reducing gas atmosphere. However, it is still thermally compatible with the most commonly used solid electrolyte i.e. YSZ [33]. Under similar conditions, it is observed that the chemical strain (due to oxygen partial pressure gradient) of $(La_{0.75}Sr_{0.25})_{0.95}Cr_{0.5}Mn_{0.5}O_{3-\delta}$ is 3-5 times lower than $(La_{0.75}Sr_{0.25})_{0.95}Cr_{1-x}Fe_xO_{3-\delta}$ [33, 174]. This corresponds to higher thermo-mechanical stability of LSCM as needed for oxygen transport membrane and its intermediate layer (fuel oxidation layer).

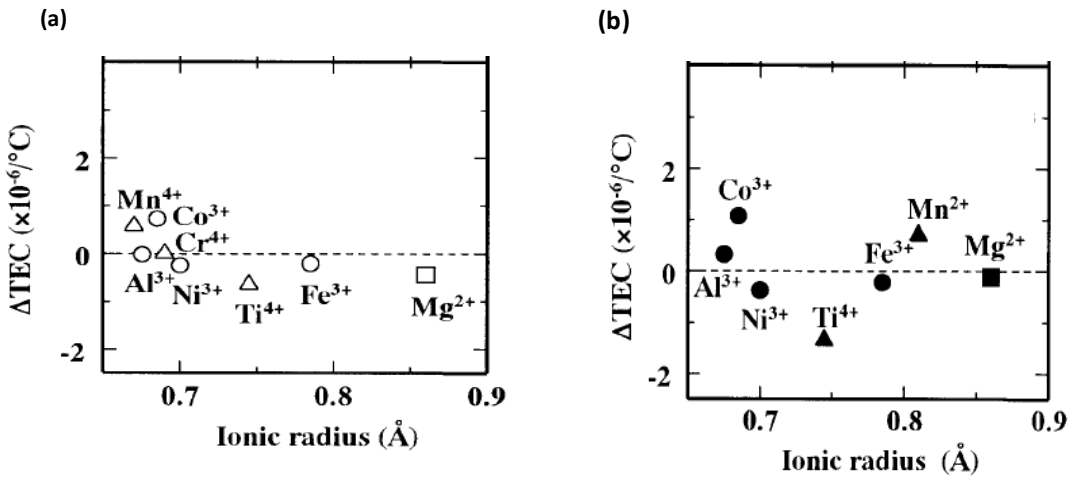

Fig. 1.22. a) Subtracted TEC of $La_{0.9}Sr_{0.1}Cr_{1-x}M_xO_3$ (x = 0.05; M = Mg, Al, Ti, Mn, Fe, Co, Ni) with $La_{0.9}Sr_{0.1}CrO_3$ versus ionic radii of B-site dopant in air and b) H_2 atmosphere. The subtracted zero TEC values correspond to the broken line [Reprinted from reference 112 with permission].

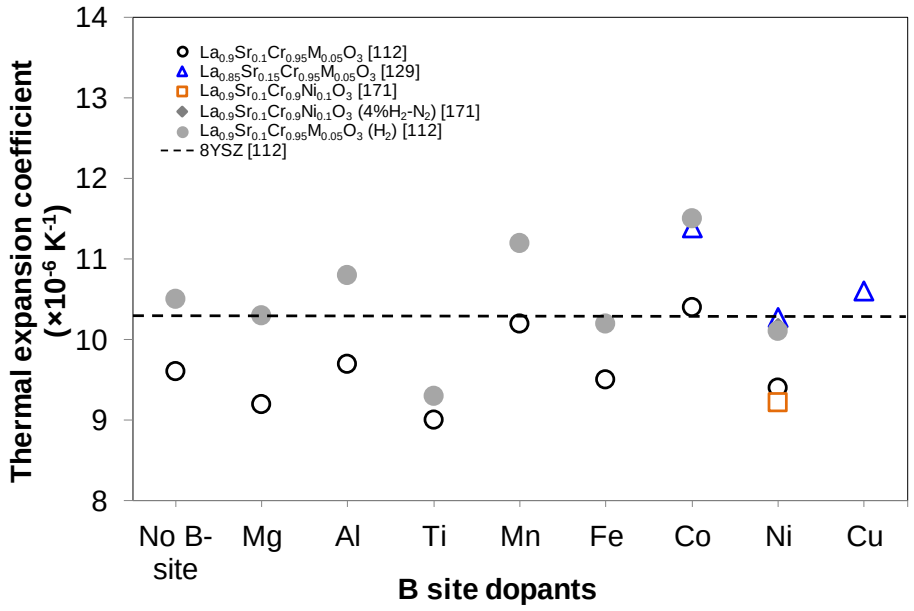

Fig. 1.23. Comparison of thermal expansion coefficient of A-site (Sr) and B-site (M = Mg, Al, Ti, Mn, Fe, Co, Ni, Cu) doped $LaCrO_3$ with (----) 8YSZ in air and H_2 (~50-1000°C) [112, 129, 171].

1.4.5. Electrical conductivity

Oxygen transport membrane (OTM) simultaneously requires electronic and ionic conductive species in the material in case of active OTM where voltage or flow of electron is not externally supplied. $LaCrO_3$ is a p-type electronic conductor and conducts holes by small polaron hopping mechanism [176-177] and has a conductivity of 0.6-1.0 Scm^{-1} at 1000°C in air [134, 176-177]. The absence of long range order due to the distorted structure of a material leads to localization of charge carrier (hole). The strong interaction between the carrier and phonon results into small polaron formation which move further by activated hopping [134, 178]. Introduction of dopants increases electronic conductivity and induces ionic conductivity in the $LaCrO_3$ by tailoring the defect chemistry as well as crystal structure and chemical bonding [135, 179-180]. In addition to the dopants, oxygen partial pressure (P_{O_2}) also varies the electrical conductivity of $LaCrO_3$ based materials. At lower P_{O_2}, the electrical conductivity decreases due to the reduction in the charge carriers responsible for p-type conduction as the charge compensation on doping occurs by the formation of oxygen vacancies. However, the formation of oxygen vacancies will enhance the oxygen transport and ionic conductivity.

1.4.5.1. *A-site dopants*

When La^{3+} (0.136 nm) ions in $LaCrO_3$ is substituted by Sr^{2+} (0.144 nm) and Ca^{2+} (0.134 nm) at A-site, the single negative charge on Sr (Sr'_{La}) is compensated by a $Cr^{3+} \rightarrow Cr^{4+}$ transition (Eq. (14)) giving rise to the formation of small polaron. As a

result, the conductivity of $LaCrO_3$ increases ($\leq$ 35% Sr) due to the polaron hopping between Cr^{3+} and Cr^{4+} ions [177, 181-182]. The expression for electrical conductivity of alkaline earth metal doped $LaCrO_3$ can be written as [134, 183]:

$$\sigma = \frac{1}{T}\frac{e^2a^2}{6K_B\tau_o}\,[Cr^{3+}][Cr^{4+}]\exp\left(-\frac{E}{k_BT}\right) \quad (24)$$

where σ, T, e, k_B, a, τ_o, $[Cr^{3+}]$, $[Cr^{4+}]$ and E are the electrical conductivity, absolute temperature, elementary electric charge, Boltzmann constant, distance traversed in a hop, average free time, Cr^{3+} mole fraction, Cr^{4+} mole fraction and activation energy/hopping energy of small polaron respectively.

There is another postulation for the increase in conductivity of $LaCrO_3$ when doped with Ca/Sr at A-site. According to the electronic band structure of $La_{1-x}M_xCrO_{3-x/2}$ (M=Ba, Sr and Ca) based on *ab initio* calculations, the charge carriers adjacent to the top of valence band increases with decrease in band gap for Ba, Sr and Ca doping [167]. The A-site dopants (Ba, Sr and Ca) shift the conduction band of $LaCrO_3$ down by 0.08, 0.13, and 0.14 eV, respectively. Accordingly, the energy band gap between top of the valence band and bottom of the conduction band of $LaCrO_3$ decreases from 0.95 to 0.87, 0.82, and 0.81 eV respectively (Fig. 1.24) [167]. The difference in the electronic band structure and electrical conductivity of A-site doped $LaCrO_3$ is due to the difference in the ionic radii of La^{3+} and $Ca^{2+}/Sr^{2+}/Ba^{2+}$. A larger ionic radius of A-site dopant distorts the perovskite lattice, and results into scattering of the charge carriers [167]. This is why Ba ($r_{Ba^{2+}}$ = 0.161nm) is not an appropriate dopant for $LaCrO_3$ because it has larger radii (18.4%) than La ($r_{La^{3+}}$ = 0.136nm). In addition, $BaCr_2O_4$ secondary phase formation in case of $(La_{0.70}Ba_{0.30})CrO_3$ eliminates Ba as the choice of dopant [181].

The electrical conductivity variation with temperature and concentration of alkaline earth metal dopants (Sr, Ca) are shown in Fig. 1.25a (air) and b (H_2 atmosphere) [134, 167, 182-184]. The conductivity increases with increase in temperature and dopant concentration. Predominantly, $LaCrO_3$ shows lower conductivity on Sr-doping than Ca in air. This might be due to the smaller lattice parameter of $LaCrO_3$ on Ca-doping than Sr [177]. However, $La_{1-x}Sr_xCrO_3$ results into higher conductivity in reducing atmosphere (H_2 gas) depending on the dopant concentration. It has been observed that the conductivity of $La_{1-x}Sr_xCrO_3$ increases up to $x \leq 0.35$ and then starts to decrease in air. This may be due to the formation of oxygen vacancies for charge compensation of Sr^{2+} rather than $Cr^{3+} \rightarrow Cr^{4+}$ transition when $x \geq 0.35$ [182]. The conductivity of $La_{1-x}Ca_xCrO_3$ ($x = 0.2, 0.5$) also decreases with higher dopant concentration [183].

In addition to dopants, oxygen vacancies also form in reducing atmosphere (low P_{O_2}) to maintain charge neutrality due to change in Cr^{4+} to Cr^{3+} valance state (Eq. (9)). The ionic conductivity increases due to the formation of oxygen vacancies. Apart from dopant level, the oxygen defect concentration depends on oxygen partial pressure (P_{O_2}) and temperature (Fig. 1.20), resulting into change in conductivity [184].

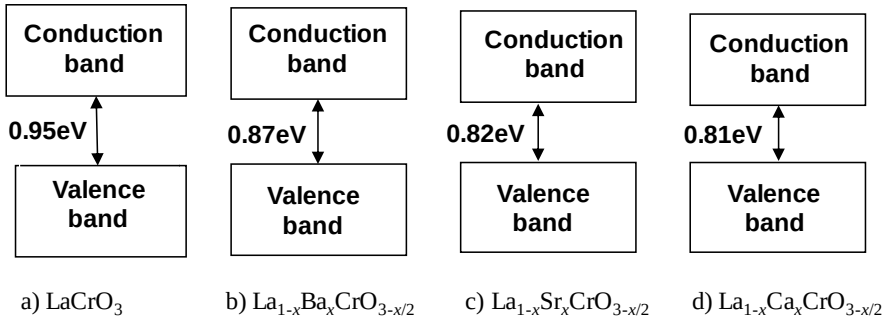

Fig. 1.24. Electronic band structure of $LaCrO_3$ and $La_{1-x}M_xCrO_{3-x/2}$ (M=Ba, Ca and Sr).

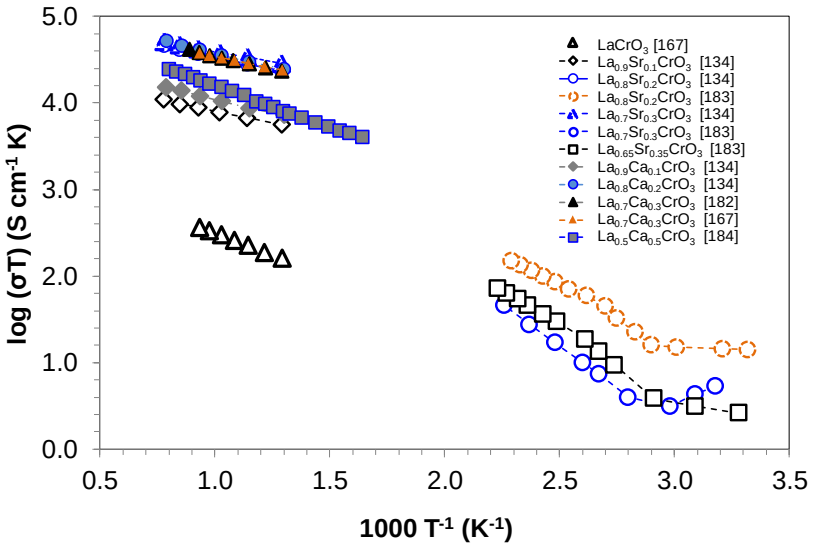

(a)

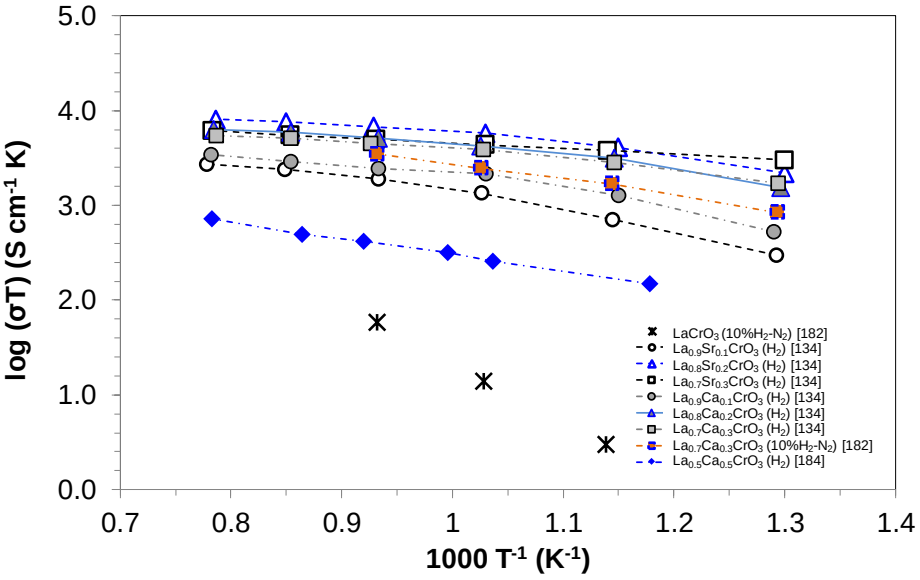

(b)

Fig. 1.25. Electrical conductivity of A-site (Sr, Ca) doped $LaCrO_3$ as a function of temperature with various dopant levels: (a) air, (b) H_2 atmosphere [134, 167, 182-184].

1.4.5.2. *A and B-site dopants*

$La_{1-x}Sr_xCrO_3$ is doped with transition metals (e.g., Ni, Co, Cu, Mn, Ti) to enhance the conductivity along with other properties. Nickel is most stable in its +2 valence state and increases the number of Cr^{4+} ions when doped in $La_{1-x}Sr_xCrO_3$ to maintain electroneutrality, contributing to p-type conduction [129, 172]. Similarly, cobalt doped $La_{1-x}Sr_xCrO_3$ shows higher conductivity due to the increase in Co^{2+} ions with temperature and conversion of Cr^{3+} to Cr^{4+} for the charge compensation. Copper can exist simultaneously in +2 and +3 valence state. However, Cu^{2+} contributes towards the increase in charge carriers and electrical conductivity [172].

$La_{1-x}Ca_xCrO_3$ doped with transition metals (Ni, Fe, and Mn) has also been investigated [185]. Iron exists in +3 valence state in $La_{1-x}Ca_xCr_{1-x}Fe_xO_3$ (x = 1/4, 1/3) [186]. Therefore, the increase in the valence state of chromium ions and the generation of holes for the conduction is mostly due to Ca substitution on La-site. Similarly, the electrical conductivity varies with Cr^{4+} ions on manganese doping [172, 185, 187-188]. However, the charge compensation for Ca-doping in $La_{0.9}Ca_{0.1}Cr_{0.5}Mn_{0.5}O_3$ is done by $Cr^{3+} \rightarrow Cr^{4+}$ and partly by $Mn^{3+} \rightarrow Mn^{4+}$ [185]. This is due to slightly less ionization energy of the 3d electron of the Cr^{3+}(48.6 eV for $3d^3$) than Mn^{3+} (50.6 eV for $3d^4$) unlike Fe^{3+} (53.7 eV for $3d^5$) [185]. In case of Fe and Mn doped $La_{1-x}Ca_xCrO_3$, it is considered that the further change in conductivity is due to the dopants effect on band structure [172].The higher valence Cr^{4+} ions and the electrical conductivity of the compound $La_{0.9}Ca_{0.1}Cr_{0.5}M_{0.5}O_3$ (M = Ni, Fe and Mn) increases in the order of $La_{0.9}Ca_{0.1}Cr_{0.5}Ni_{0.5}O_3$ (23.3 S cm^{-1}) > $La_{0.9}Ca_{0.1}Cr_{0.5}Fe_{0.5}O_3$ (3.0 S cm^{-1}) > $La_{0.9}Ca_{0.1}Cr_{0.5}Mn_{0.5}O_3$ (2.2 S cm^{-1}) at

727ºC [185]. Fig. 1.26 also shows the change in electrical conductivity of different compositions with varying dopant level and increase in temperature in air (and $La_{0.75}Ca_{0.25}Cr_{0.5}Mn_{0.5}O_3$ in 5%H_2-Ar atmosphere) [33, 129, 131, 134, 189]. In case of nickel dopant, the conductivity increases with concentration from x = 0.1 to x = 0.5. The highest conductivity (72.8 S cm^{-1}) is observed for $La_{0.9}Sr_{0.1}Cr_{0.5}Ni_{0.5}O_3$ at 800°C. Above x = 0.5, the conductivity starts to decrease from 72.8 (x = 0.5) to 69.2 (x = 0.6) S cm^{-1} due to the formation of secondary phases (Sr_2CrO_4, $(La_{01.4}Sr_{0.6})NiO_4$, $(La_{01.6}Sr_{0.4})NiO_4$) [131].

Composition with ~50% Co, Ni and Cu doping are not stable under fuel atmosphere since the dopants tend to reduce into metal [188]. It is known that the FeO and MnO are stable in fuel atmosphere. However, FeO reduces to metal at 1000°C and $P_{O_2} \sim 10^{-15}$ atm (calculated using HSC Chemistry 6.0). MnO is more stable when compared to FeO [188]. In addition, the possibility of the presence of lower coordination Mn^{3+} (five-fold) unlike Cr^{3+} (six-fold) may improve the oxygen–ion migration by inducing oxygen vacancies for oxygen transport. Thus, manganese doping can provide the mixed ionic-electronic conductivity in $La_{0.9}Sr_{0.1}Cr_{1-x}Mn_xO_3$ depending on its concentration [188]. The conductivity of $La_{0.9}Sr_{0.1}Cr_{1-x}Mn_xO_3$ increases with increase in temperature and Mn content up to $x \leq 0.5$ as shown in Fig. 1.26.

(La, Sr)(Cr, Mn)$O_{3-\delta}$ and (La, Sr)(Cr, Fe)$O_{3-\delta}$ perovskite based materials are promising candidates for OTM [32, 33, 120, 149-150, 175, 188-192]. Because, these materials can provide the mixed ionic-electronic conductivity, high electrochemical activity, in both reducing and oxidizing conditions. In addition, these materials are compatible with other components of the electrochemical system. Tao et al. [149] have

measured the total conductivity of $La_{0.75}Sr_{0.25}Cr_{0.5}Mn_{0.5}O_{3-\delta}$ as 38.6 and 1.49 S cm^{-1} at 900°C in air and 5%H_2-Ar respectively. Recently, Kharton et al. [32] have reported a similar perovskite oxide, $(La_{0.75}Sr_{0.25})_{0.95}Cr_{0.5}Mn_{0.5}O_{3-\delta}$ a promising material for SOFC anode which can also be used for OTM. The material exhibits the p-type electronic conductivity of 20–35 S cm^{-1} in oxidizing and moderately reducing atmosphere (> 10^{-12} atm) in the temperature range of 750-1000°C. The ionic conductivity of $(La_{0.75}Sr_{0.25})_{0.95}Cr_{0.5}Mn_{0.5}O_{3-\delta}$ is ~ 3×10^{-5} S cm^{-1} at 950ºC and ~0.01 atm. There is no significant change in the electronic and ionic conductivity of $(La_{0.75}Sr_{0.25})_{0.95}Cr_{0.5}Mn_{0.5}O_{3-\delta}$ in the P_{O_2} ranging from 0.01-10^{-12} atm. However, the ionic conductivity increases (~3.5×10^{-4} S cm^{-1} at ~10^{-14} atm) significantly with further decrease in P_{O_2} (< 10^{-12} atm) [32]. On the other hand, the electronic conductivity decreases down to 1.3 S cm^{-1}. This is due to significant oxygen release and increase in the oxygen vacancy concentration below oxygen partial pressure of ~10^{-12} atm [32].

Electrical conductivity of $La_{0.8}Sr_{0.2}Cr_{0.5}Fe_{0.5}O_{3-\delta}$ is 21.9 S cm^{-1} in oxidizing (air) and 6.4 S cm^{-1} in reducing (5%H_2-Ar) gas atmosphere at 800ºC [120]. The conductivity decreases in reducing gas atmosphere due to reduction in the valence state of Cr^{4+} to Cr^{3+} (Eq. (9)) and Fe^{4+}/Fe^{3+} to Fe^{2+} (Eq. (12) and Eq. (13)), resulting in charge carrier reduction by oxygen vacancies formation for charge compensation. For instance, the conductivity of $(La_{0.75}Sr_{0.25})_{0.95}Cr_{0.7}Fe_{0.3}O_{3-\delta}$ decreases from ~31.6 S cm^{-1} to ~2 Scm^{-1} when P_{O_2} decreases from 0.21 to ~10^{-18} atm at 900ºC [33]. Under similar conditions (850ºC and 10^{-18} atm), the conductivity of $(La_{0.75}Sr_{0.25})_{0.95}Cr_{0.7}Fe_{0.3}O_{3-\delta}$ (1.8 S cm^{-1}) and $(La_{0.75}Sr_{0.25})_{0.95}Cr_{0.6}Fe_{0.4}O_{3-\delta}$ (0.7 S cm^{-1}) are lower than $(La_{0.75}Sr_{0.25})_{0.95}Cr_{0.5}Mn_{0.5}O_{3-\delta}$

(2.3 S cm^{-1}) [33]. This is probably due to the variation in the disproportion of valence state of Mn/Fe and oxygen vacancies formation. Higher conductivity of doped lanthanum chromite material is preferred in both oxidizing and reducing gas atmosphere for OTM. Therefore, $(La_{0.75}Sr_{0.25})_{0.95}Cr_{0.5}Mn_{0.5}O_{3-\delta}$ would be preferred for use in OTM. It is also noticed that Ni-doping (23.3 S cm^{-1}) at B-site of Ca-doped lanthanum chromite provides highest conductivity when compared to Mn (2.2 S cm^{-1}) and Fe (3.0 S cm^{-1}) doped $La_{0.9}Ca_{0.1}Cr_{0.5}M_{0.5}O_3$ (M = Ni, Fe and Mn) at 727ºC in oxidizing atmosphere [185]. However, the conductivity of Ni doped lanthanum chromite is not provided in the literature and needs further investigation in reducing atmosphere to be considered for OTM application.

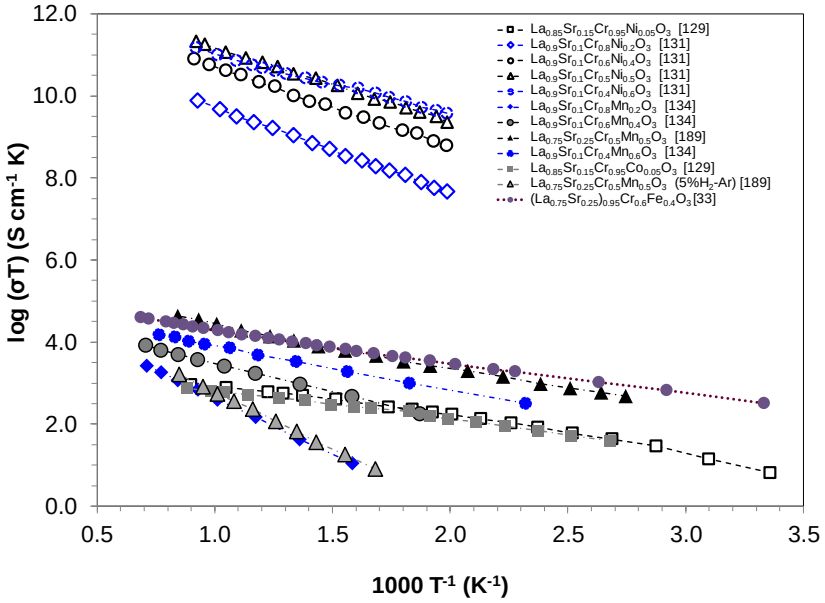

Fig. 1.26. Electrical conductivity of A-site (Sr) and B-site (Ni, Mn, Co, Fe) doped $LaCrO_3$ as a function of temperature with various dopant levels [33, 129, 131, 134, 189].

1.4.6. Mechanical behavior

Mechanical integrity of the OTM is required at high temperature under simultaneous exposure to both oxidizing and reducing atmospheres to prevent cracking, warpage and mechanical failure. Materials used in oxygen transport membrane may be subjected to mechanical and thermal stresses during fabrication or system in operation. Strength of the materials is dependent on materials composition, dopant level, temperature, and P_{O_2} gradient.

The mechanical properties (elastic modulus, fracture toughness, fracture strength, and Weibull modulus) of doped lanthanum chromite tend to vary with different dopant type and level at OTM operating conditions (1000°C and 0.21-10^{-22} atm) as shown in Table 1.6 [110, 155, 193-197]. It is observed that the flexure strength of the material increases with increase in the level of A-site dopants (Sr and Ca) due to enhanced densification [110, 193]. For example, $La_{0.85}Ca_{0.15}CrO_3$ (~ 87% dense) and $La_{0.8}Ca_{0.2}CrO_3$ (~95%) have flexural strength of 61 ± 11.5 and 96 ± 14.4 MPa respectively at 25°C and 0.21atm [193]. Also, the flexure strength of $La_{0.9}Sr_{0.1}CrO_3$ (~80 MPa) is lower than $La_{0.8}Sr_{0.2}CrO_3$ (~105MPa) at 600°C in air (0.21atm) [110].

Sr/Ca doped $LaCrO_3$ are further doped with transition metals (Al, Cu, Co and Fe) at B-site to improve the flexure strength, mean fracture strength, and fracture toughness by minimizing the internal stresses due to the existing oxygen deficiency [194]. For $La_{0.8}Ca_{0.2}Cr_{0.9}M_{0.1}O_{3-\delta}$ (M = Al, Cu, Co, Fe) system, the mechanical properties are found to be affected with the type of B-site dopants. The flexure and mean fracture strength of $La_{0.8}Ca_{0.2}Cr_{0.9}M_{0.1}O_{3-\delta}$ increases in the order of $La_{0.8}Ca_{0.2}Cr_{0.9}Cu_{0.1}O_{3-}$

$_{\delta}$> $La_{0.8}Ca_{0.2}Cr_{0.9}Co_{0.1}O_{3-\delta}$> $La_{0.8}Ca_{0.2}Cr_{0.9}Fe_{0.1}O_{3-\delta}$> $La_{0.8}Ca_{0.2}Cr_{0.9}Al_{0.1}O_{3-\delta}$. The reliability of a material is determined by Weibull modulus. Fu et al. [194] have found that the Weibull modulus and reliability of $La_{0.8}Ca_{0.2}Cr_{0.9}M_{0.1}O_{3-\delta}$ (M = Al, Cu, Co, Fe) increases in the order of Cu>Fe>Al>Co. Most of the mechanical properties mentioned in the Table 1.6 cannot be compared either due to the varying dopant level or different set of conditions applied while measuring the properties. It suggests the need of consistent data on mechanical properties of lanthanum chromite based materials under identical conditions. Although the reasons for the change in mechanical properties with different dopants and their level are not clear, the possible reasons could be the difference in structure and microstructure (grain, pore size and their distribution, inter-atomic bond strength, lattice distortion, and oxygen non-stoichiometry) of the investigated doped $LaCrO_3$. The partial substitution of A-site dopant changes the valence state of Cr^{3+} to Cr^{4+} (Eq. (14)) which has smaller ionic radii. In addition, the transition metals (M = Fe, Co and Mn) can exist in more than one valence state (M^{2+}, M^{3+} and M^{4+}) depending on temperature and oxygen partial pressure. This may lead to change in lattice structure which might induce stress/strain in the membrane due to change in the inter-atomic bond length. It has been studied that the strength and hardness of these materials varies with the amount of porosity [102, 108, 198]. The relation between porosity (p), elastic modulus (E), shear modulus (G) and Poisson's ratio (ϑ) is given below [195]:

$$E = E_o \frac{(1-p^2)}{(1+b_E p)}, G = G_o \frac{(1-p^2)}{(1+b_G p)} \text{ and } \vartheta = 0.25 \frac{4\vartheta_o + 3p - 7\vartheta_o p}{1+2p-3\vartheta_o p} \quad (25)$$

where $b_E = 2 - 3\vartheta_o$ and $b_G = \frac{11-19\vartheta_o}{4+4\vartheta_o}$. E_o, ϑ_o and G_o are elastic modulus, Poisson's ratio and shear modulus at zero porosity respectively.

According to the above relation, the elastic and shear modulus decreases with increase in porosity. This corresponds to the decrease in strength of the material. For example, a dense $La_{0.8}Ca_{0.2}CoO_3$ (99% dense) has a bending strength of 150 MPa whereas $LaCoO_3$ (83% dense) and $La_{0.8}Sr_{0.2}CoO_3$ (90% dense) have lower strength of 53 MPa and 76 MPa, respectively [198].

Table 1.6. Mechanical properties of various doped lanthanum chromite materials [110, 155, 193-197].

Mechanical properties of various doped lanthanum chromite materials [109,154,192–196].

Composition	Temperature (°C)	Oxygen partial pressure (atm)	Elastic modulus (GPa)	Poisson's ratio	Fracture toughness (K_{IC}-MPa $m^{1/2}$)	Flexure strength (MPa)	Mean fracture strength (MPa)	Micro hardness (GPa)	Weibull modulus
8 YSZ	RT	0.21	190	0.308	1.61	416	214	–	5.7
	800	0.21	157	0.313	–	–	146	–	8.6
	900	0.21	–	–	1.02	–	–	–	
10 CGO	RT	0.21	200	0.328	–	–	120	–	3.8
	800	0.21	200	–	–	–	169	–	5.7
$La_{0.9}Sr_{0.1}CrO_3$	600	0.21	–	–	–	~80	–	–	–
$La_{0.8}Sr_{0.2}CrO_3$	600	0.21	–	–	–	~105	–	–	–
$La_{0.7}Sr_{0.3}CrO_{3-\delta}$	1400	0.21	–	–	–	~98	–	–	10
$La_{0.85}Ca_{0.15}CrO_3$	RT	0.21	–	–	–	61 ± 11.5	–	–	–
$La_{0.8}Ca_{0.2}CrO_3$	RT	0.21	–	–	–	96 ± 14.4	–	–	–
$La_{0.8}Ca_{0.2}CrO_{3-\delta}$	RT	0.21	73.5 ± 7.9	–	3.52 ± 0.11	131.3	91.2 ± 11	4.33 ± 0.24	8.7
$La_{0.75}Ca_{0.25}CrO_3$	RT	0.21	~180	–	~2.1	122.7 ± 26	–	–	–
	RT	10^{-10}	~180	–	~2	145	–	–	–
	RT	10^{-16}	~175	–	~1.4	~15	–	–	–
$La_{0.7}Ca_{0.3}CrO_3$	RT	0.21	~181	–	–	107.4 ± 5.9	–	–	–
	RT	10^{-10}	~178	–	–	107.4 ± 5.9	–	–	–
	RT	10^{-16}	~175	–	–	~15	–	–	–
$La_{0.7}Ca_{0.3}CrO_{3-\delta}$	1400	0.21	–	–	–	~220	–	–	11.3
$La_{0.8}Sr_{0.2}Cr_{0.92}Co_{0.08}O_3$	RT	0.21	–	–	–	62	–	5.98	–
$La_{0.7}Sr_{0.3}Cr_{0.9}Co_{0.1}O_3$	1000	0.21	–	–	–	103	–	–	9.7
$La_{0.2}Sr_{0.8}Fe_{0.8}Cr_{0.2}O_{3-\delta}$	RT	0.21	–	–	0.5–0.8	–	167	5.2	5.2
	1000	0.21	–	–	–	–	108	–	–
$La_{0.8}Ca_{0.2}Cr_{0.9}Al_{0.1}O_{3-\delta}$	RT	0.21	91.5 ± 10.3	–	4.02 ± 0.12	98.9	80.8 ± 8.7	7.35 ± 0.42	9.4
$La_{0.8}Ca_{0.2}Cr_{0.9}Co_{0.1}O_{3-\delta}$	RT	0.21	143.6 ± 17.6	–	4.23 ± 0.14	170.5	148.9 ± 14.6	9.04 ± 0.54	9.3
$La_{0.8}Ca_{0.2}Cr_{0.9}Cu_{0.1}O_{3-\delta}$	RT	0.21	371.2 ± 36.2	–	4.33 ± 0.15	356.9	339.2 ± 16.2	9.85 ± 0.34	36.9
$La_{0.8}Ca_{0.2}Cr_{0.9}Fe_{0.1}O_{3-\delta}$	RT	0.21	99.8 ± 10.3	–	4.02 ± 0.12	154.3	133.6 ± 12.3	7.35 ± 0.42	12.9

The existence of partial pressure gradient across the membrane is another major factor affecting the mechanical properties of doped $LaCrO_3$ material. At constant temperature, formation of oxygen vacancy increases with reducing atmosphere (Fig. 1.20) and cause the lattice expansion. Reducing atmosphere also changes valence state of B-site cations

(Eq. (12) and (13)) resulting in the relaxation of the lattice by cation repulsion around oxygen vacancy and change in lattice volume [150]. The strain due to the change in lattice volume is known as chemically induced strain, ε_c [195].

Exposure to high oxygen partial pressure gradient further induces residual stress due to ε_c gradient across the OTM. For doped lanthanum chromite, the typical strain was observed to be 0.2-0.4% when oxygen partial pressure was reduced from 0.21 atm to 10^{-18} atm at 1000°C [111]. In reducing gas atmosphere, the Sr/Ca doping at A-site of $LaCrO_3$ leads to the formation of oxygen vacancies for charge compensation as shown in Eq. (15). However, in oxidizing atmosphere, the Cr^{3+} converts to Cr^{4+} (Eq. (14)). For instance, $La_{0.7}Ca_{0.3}CrO_{3-\delta}$ exhibits the δ =0.019 and 0.26 mole fraction of Cr^{4+} at 25°C in air while in reducing atmosphere (P_{O_2}= 10^{-18} atm) at 1000°C, the δ increases to 0.12 and Cr^{4+} mole fraction reduces to 0.06 [111]. For $La_{0.7}Ca_{0.3}Cr_{0.9}Ti_{0.1}O_{3-\delta}$ system, $\Delta\delta$, the difference in oxygen stoichiometry in air and reducing atmosphere (P_{O_2}=10^{-18} atm) is 0.073, the minimal among the available reports [111]. Therefore, Ti doping can be considered to minimize the strain induced due to the oxygen partial pressure gradient [111]. The variation in the oxygen vacancy formation or non-stoichiometry with the change in P_{O_2} can generate strain in the membrane due to expansion and contraction of lattice volume, respectively, in low and high P_{O_2} can contribute to the mechanical failure.

The expression below shows the relation between biaxial strain, elastic modulus, Poisson's ratio, deviation in oxygen non-stoichiometry and thickness of the membrane for a stack of *N* layers [199].

$$\varepsilon = \frac{\frac{\mathrm{E}_N L_N}{1-\vartheta_N}}{\sum_{j=1}^{N} \frac{E_j \mathrm{L}_j}{1-\vartheta_j}} \int_0^1 \varepsilon^{\delta} \left(\frac{y}{\mathrm{L}_N}\right) d(y/\mathrm{L}_N) \quad (26)$$

where ε, E_j, ϑ_j and L_j are the biaxial strain, Young's modulus, Poisson's ratio and thickness of a component j in the stack. $\varepsilon^{\delta}\left(\frac{y}{\mathrm{L}_N}\right)$ is the function which refers to the linear expansion of a volume element at position y resulting from local deviation in stoichiometry (δ). In case $j = N$, it is only one component i.e. membrane. In case of composite or dual phase membrane, $j \neq N$ and can be referred to the second phase, the equation provides that the difference in elastic modulus and Poisson's ratio of two phases or component can generate bi-axial strain at the interface. This can affect interfacial strength of the membrane.

In a dual phase OTM and/or an OTM in contact with intermediate and surface exchange layers, the difference in sintering behavior of different phases and layers during fabrication can lead to the formation of pores and cracks at the interface. This is due to difference in the linear shrinkage of two phases or layers during sintering. The differential shrinkage between the two different phases or components can generate stress, and form micro-cracks at the interface. For example, difference in sintering behavior causes formation of crack at the interface between YSZ and Ca-doped $LaCrO_3$ during co-firing at 1200-1500°C in air [200]. The cracks at the interface can grow and propagate through the interface and the porous adjacent layers, leading to mechanical failure during operation [201-202]. As discussed in section 1.4.2, thermal stress (Eq. (22) can be developed at the interfaces between the membrane and the adjacent layers (intermediate

and surface exchange) as well as between the perovskite and fluorite phases due to difference in their TEC. In addition, the temperature gradient due to inhomogeneous temperature distribution as well as thermal cycling during start-up and shut-down of the device can also generate stress according to Eq. (22). The thermal stress can also lead to pore and crack formation, origin of mechanical failure [144]. Therefore, an optimization of level and type of A and B-site dopants is needed to match shrinkage/TEC of one phase/layer to the other. This will minimize the stress in the bulk/interface, and increase the lifetime of OTM system. However, the available literature does not provide an in-depth study on mechanical behavior of bulk as well as interface of A and/or B-site doped lanthanum chromite based materials.

1.4.7. Oxygen flux/permeation

Oxygen permeation through a mixed ionic-electronic conductor involves three steps as shown in Fig. 1.27: surface exchange reaction at gas-solid interface I (higher P_{O_2} side), diffusion through membrane, and surface exchange reaction at solid-gas interface II (lower P_{O_2} side) [203-204].

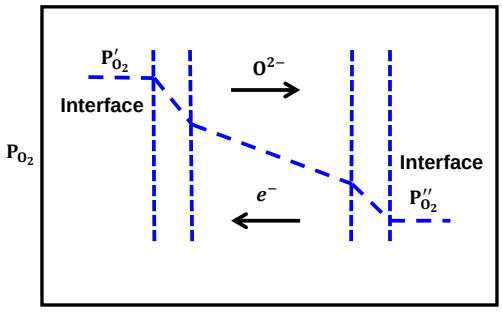

Fig. 1.27. Oxygen transport steps during oxygen permeation through a dense MIEC [204].

The following steps are involved at the different region as shown in Fig. 1.28:

Interface I: a) Oxygen adsorption (O_{ads}): $O_2(g) \rightarrow O_{ads}$ (27)

b) Oxygen incorporation (O_{inc}): $\frac{1}{2}O_2 + V_O^{\cdot\cdot} + 2e^- \rightarrow O_O^{\times}$ (28)

c) Charge transfer/ionization: $O_{inc} + 2e^- \rightarrow O^{2-}$ (29)

Membrane: d) Lattice and grain boundary diffusion of O_{inc} due to chemical potential gradient of oxygen ($P'_{O_2} \gg P''_{O_2}$)

e) Oxygen transport through oxygen vacancy ($V_O^{\cdot\cdot}$)

Interface II: f) Desorption of oxygen: $O^{2-} \rightarrow O_{des} + 2e^-$ (30)

g) Association of oxygen: $O_{des} + O_{des} \rightarrow O_{2_{ass}}$ (31)

h) Gas diffusion of associated oxygen molecules

Oxygen permeation through membrane is mainly dependent on surface/interfacial exchange on either side of the membrane and bulk diffusion within the membrane as shown in Fig. 1.27 and 1.28. L_c is a characteristic thickness value at which the oxygen flux is controlled by surface exchange kinetics as well as bulk diffusion [41]. The thickness of the membrane can be reduced to enhance the oxygen flux until it becomes less than L_c. The value for L_c can be determined by the ratio of the oxygen self-diffusivity and surface exchange coefficient. The oxygen flux of the membrane cannot be further improved by decreasing the thickness below L_c. However, the oxygen flux can significantly be increased by depositing a porous MIEC layer (surface exchange and intermediate) on the membrane which would enhance the surface kinetics and oxygen exchange at the interface [40-41, 43, 205].

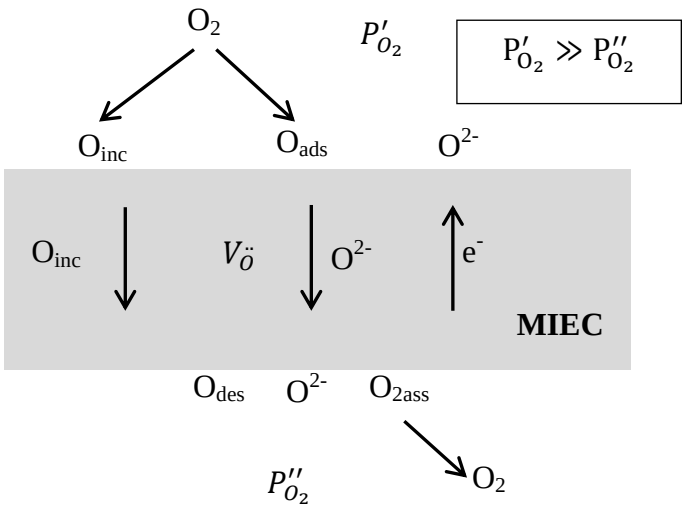

Fig. 1.28. Schematic of different steps involved in surface exchange for oxygen reduction and its diffusion in OTM.

The oxygen flux across the membrane can be written as (Wagner equation) [41]:

$$j_{O_2} = -\frac{RT}{4^2F^2L}\int_{\ln P'_{O_2}}^{\ln P''_{O_2}} \frac{\sigma_{el}\sigma_{ion}}{\sigma_{el}+\sigma_{ion}} d\ln P_{O_2} \quad (32)$$

where j_{O_2} corresponds to oxygen flux through unit area, σ_{el} and σ_{ion} are materials electronic and ionic conductivity respectively, R refers to ideal gas constant, T is absolute temperature, L is the membrane thickness, F refers to Faraday's constant, P'_{O_2} is feed oxygen partial pressure and P''_{O_2} is permeate side oxygen partial pressure. Depending on membrane thickness, operating temperature and oxygen partial pressure gradient, the limiting step is determined. Surface exchange reaction is dominant for oxygen transport for thin membrane but diffusion dominates for thicker membrane [41, 203]. Oxygen ions transports through the bulk of the perovskite lattice via oxygen vacancies once it is adsorbed on the surface (Fig. 1.28). Oxygen permeation flux increases with increase in

differential P_{O_2} (oxygen chemical potential gradient) and temperature because of decrease in oxygen ion migration energy [41, 203-204]. It is to note that, closed pores may be present in a dense membrane as a processing defect and the bulk diffusion path involves two more steps: distorted pathway and molecular gas diffusion through the pores as shown in Fig. 1.29 [206].

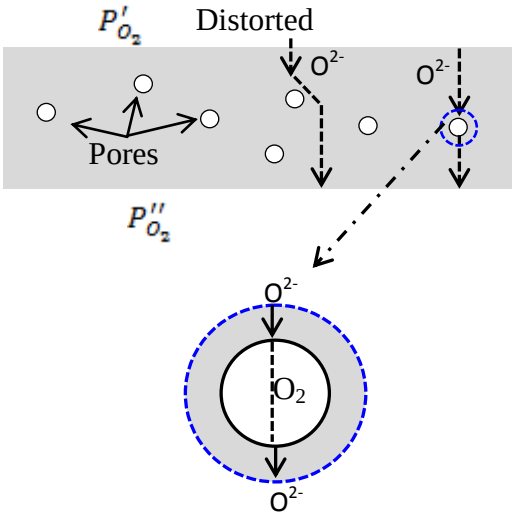

Fig. 1.29. Schematic of bulk diffusion path for OTM with closed pores [206].

As described in introduction section, undoped lanthanum chromite is predominantly electronic conductor and requires ionic conductivity or oxygen flux for the transport of oxygen ion in OTM. Doping of A-site (alkaline earth metals) and B-site (transition metals) is proposed to be useful for improving oxygen ionic conductivity via formation of oxygen vacancies. However, limited information is available for doped lanthanum chromites. Calcium doped lanthanum chromite has been investigated to a considerable extent [207-212]. Oxygen transport occurs predominately through diffusion of oxygen vacancies. Although cationic defects and anti-Frenkel defects are present in

calcium doped lanthanum chromite, their role on oxygen transport is negligible but yet to be confirmed [211]. At high P_{O_2} ($\geq$ 1atm) oxygen diffusion through grain boundaries affects oxygen permeation because of calcium enriched phase at grain boundaries [212].

The effect of calcium content on normalized oxygen flux for $La_{1-x}Ca_xCrO_{3-\delta}$ at 1000°C in the P_{O_2} range of 0.21-10^{-11} atm is shown in Fig. 1.30. Oxygen permeation increases with increase in oxygen vacancy concentration either by increase in calcium concentration or lowering P_{O_2} (Fig. 1.30) [211-212]. $La_{0.8}Sr_{0.2}CrO_3$ (1.3 mm thick) provides oxygen flux of 2×10^{-7} mol s^{-1} cm^{-2} at 850ºC and ΔP_{O_2} = 0.2 atm. Oxygen permeation is also dominated by oxygen vacancy diffusion in $(La_{0.75}Sr_{0.25})_{0.95}Cr_{0.5}Mn_{0.5}O_{3-\delta}$ [32]. The oxygen flux for $(La_{0.75}Sr_{0.25})_{0.95}Cr_{0.5}Mn_{0.5}O_{3-\delta}$ is determined as 1.3×10^{-9} mol s^{-1} cm^{-2} at 1000°C and 10^{-14} atm with the membrane thickness of 1mm. However, the oxygen permeation flux for $(La_{0.75}Sr_{0.25})_{0.95}Cr_{1-x}Fe_xO_{3-\delta}$ (x = 0.3-0.4) is higher than $(La_{0.75}Sr_{0.25})_{0.95}Cr_{0.5}Mn_{0.5}O_{3-\delta}$ due to higher oxygen vacancy concentration [33]. At 950ºC and ~10^{-18} atm, the oxygen flux for $(La_{0.75}Sr_{0.25})_{0.95}Cr_{0.7}Fe_{0.3}O_{3-\delta}$ and $(La_{0.75}Sr_{0.25})_{0.95}Cr_{0.6}Fe_{0.4}O_{3-\delta}$ (1mm thick) are ~$10^{-7.4}$ and ~$10^{-6.8}$ mol s^{-1} cm^{-2} respectively. The reason for increase in oxygen flux with increase in Fe doping level is due to higher oxygen vacancy concentration resulting into weakening of the metal-oxygen bonds [33] and higher mobility of oxygen ions.

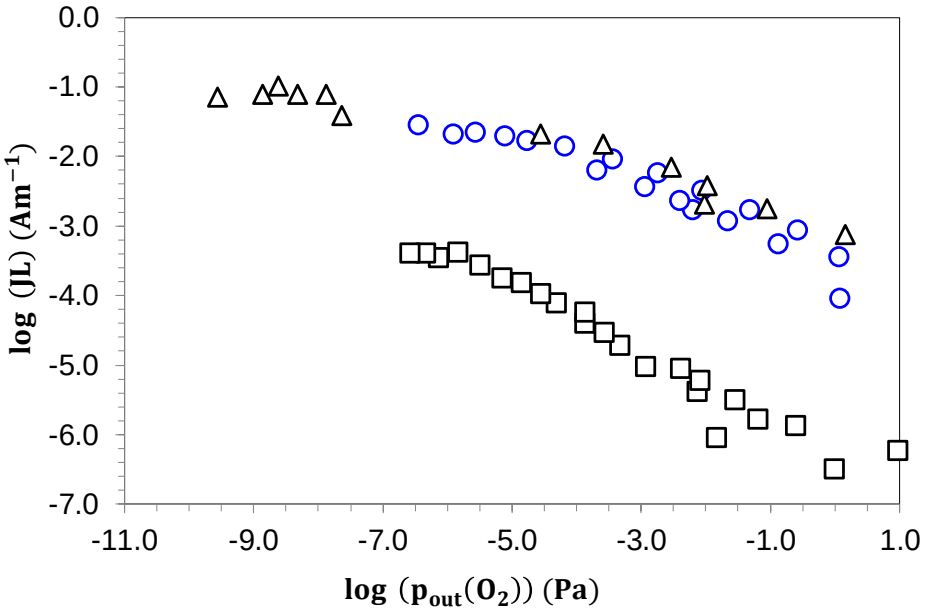

Fig. 1.30. Effect of calcium content on normalized permeation flux (JL), (○, Δ) $La_{0.75}Ca_{0.25}CrO_{3-\delta}$, (□) $La_{0.9}Ca_{0.1}CrO_{3-\delta}$, T = 1000°C (Reproduced from reference 212 with permission).

Fig. 1.31 shows the performance (oxygen permeation flux) of different single phase perovskites (chromites, cobaltites, manganites, and ferrites) based oxygen transport membrane as a function of temperature (700-1000°C) [32-33, 38, 213-219]. Predominantly, the compositions are doped with alkaline earth metals at A-site (Sr, Ca) and transition metals at B-site (Cr, Fe, Co, Mn, Al), which induces oxygen vacancies on partial substitution (Eq. (8), (12) and (13)). As shown in Fig. 1.31, it is difficult to compare the oxygen flux reported in literature due to the following reasons: a) the doping level varies from composition to composition, b) the oxygen flux measurements have been carried out under varying oxygen partial gradient; air is used as feed gas and different reducing gases ($He/N_2/H_2/CO/CH_4$) are used at the permeate side, c) the

membrane design (e.g. shape, thickness), and d) the fabrication conditions (e.g. sintering temperature and P_{O_2}) of the membrane varies from literature to literature for the same composition. Considering the above mentioned varying parameters, it is hard to visualize a specific trend. However, there are few general conclusions that can be made based on the available performance data as shown in Fig. 1.31.

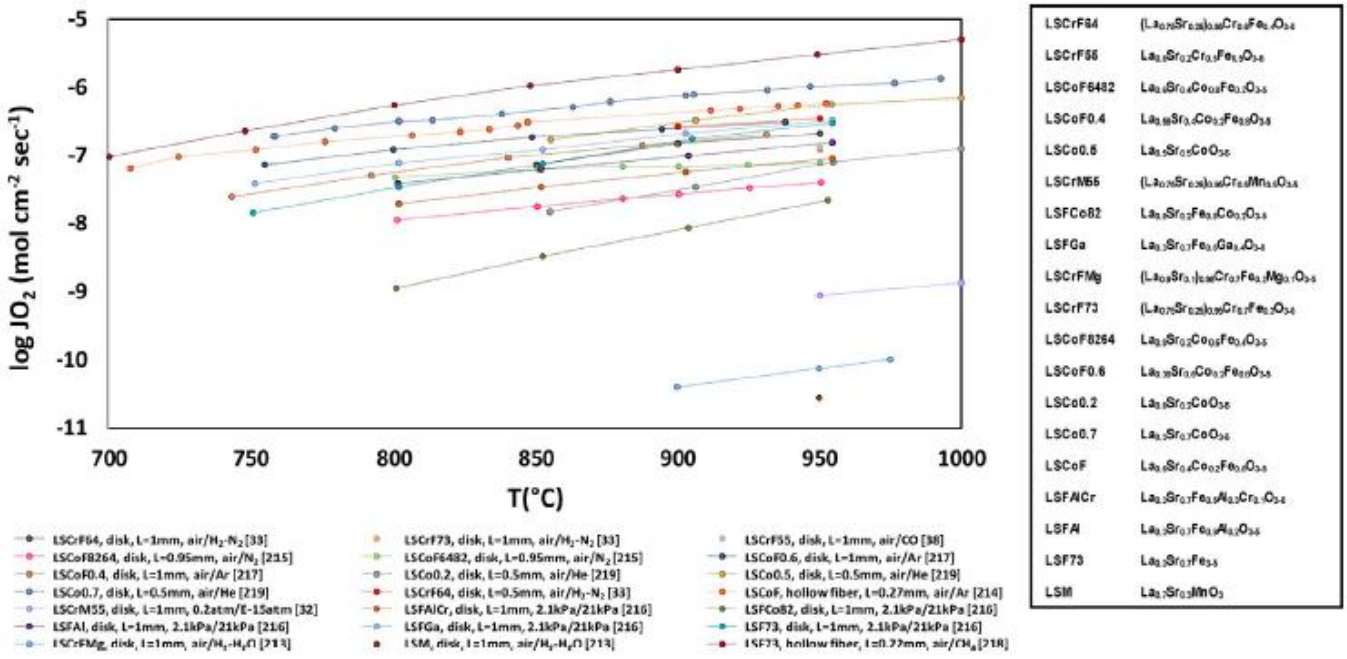

Fig. 1.31. Oxygen flux of various perovskite phase OTM (lanthanum chromites/manganites/ferrites/cobaltites) as a function of temperature (700-1000°C) [32-33, 38, 213-219].

The oxygen flux increases with increase in temperature due to increase in oxygen vacancies and faster kinetics. Also, as expected from Eq. 32, the flux increases with decrease in thickness for the same composition and operation conditions. For instance, the oxygen flux of $(La_{0.75}Sr_{0.25})_{0.95}Cr_{0.6}Fe_{0.4}O_{3-\delta}$ (LSCrF64) membrane increases from

~2.1×10^{-7} mol cm^{-2} sec^{-1} (d = 1 mm) to ~3.4×10^{-7} mol cm^{-2} sec^{-1} (d = 0.5 mm) at 950°C under air/H_2-N_2 gradient [33]. Furthermore, the flux increases with increase in dopant level due to increase in oxygen vacancies. For $(La_{0.75}Sr_{0.25})_{0.95}Cr_{1-x}Fe_xO_{3-\delta}$, the flux raised from ~$9.9\times10^{-8}$ mol cm^{-2} sec^{-1} (x = 0.3) to 2.1×10^{-7} mol cm^{-2} sec^{-1} (x = 0.4) at 950°C [33]. The flux also varies depending on the shape of the membrane. Generally, it is indicated from Fig. 1.31 that the compositions heavily doped with Co and Fe (cobaltites and ferrites) provides higher flux than Cr (chromites). This is because, Co and Fe exists in different valence state (+2/+3/+4), and induces higher oxygen vacancies (Eq. (12) and (13)) when oxygen partial pressure gradient is applied. However, as discussed before (in the introduction section, Table 1.4), the structural stability of the perovskite decreases when heavily doped with Co and Fe transition metals due to the change in valence state. Therefore, chromites are preferred.

To further enhance the performance/oxygen flux of lanthanum chromite as well as other materials based OTM, fluorite phase (ionic conductor) is added to the perovskite. Fig. 1.32 shows the performance of different dual phase (perovskite-fluorite) membrane in the temperature range of 600-1000°C [31, 37, 220-225]. Similar to single phase membranes, it is difficult to compare and observe a specific trend in the available performance data of dual phase membranes. In addition, there are two more varying parameter in case of dual phase membrane i.e. fluorite phase composition and the perovskite to fluorite ratio. The ionic conductivity, stability as well as the interaction of the perovskite phase varies depending on the fluorite phase composition and the ratio of perovskite to fluorite phase. On the other hand, in general, similar to single phase

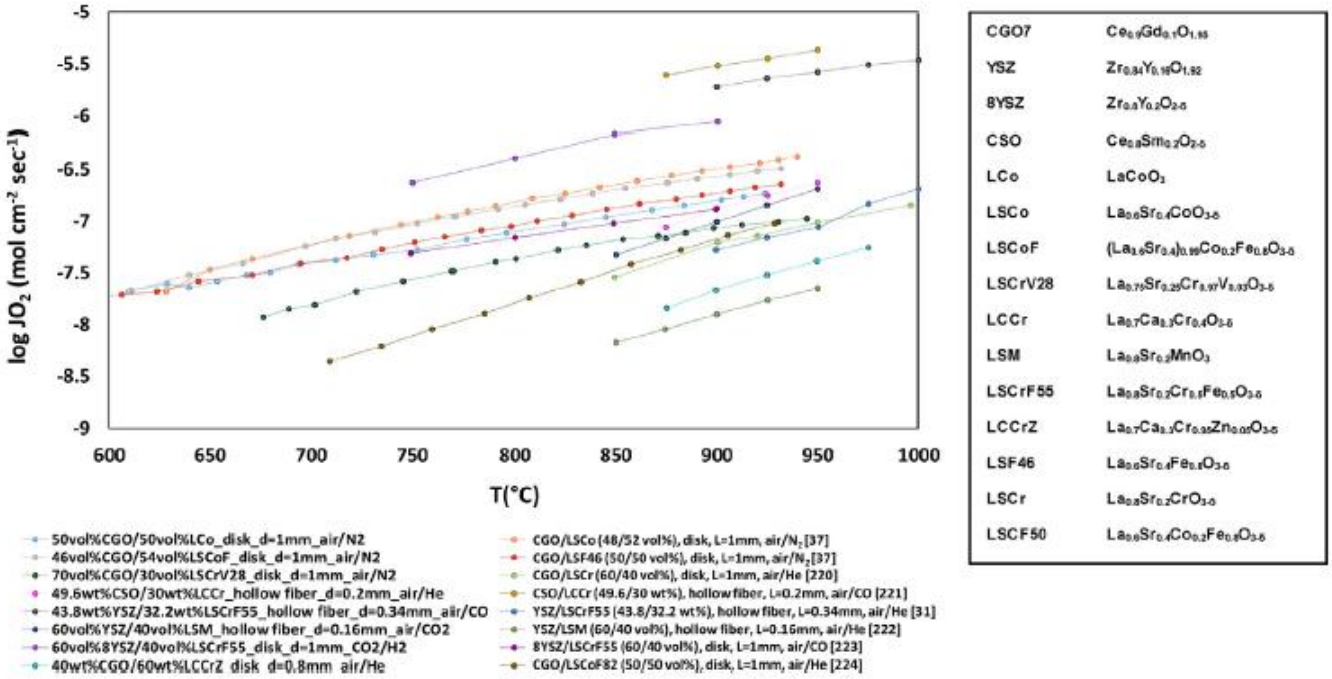

Fig. 1.32. Oxygen flux of various dual phase (perovskite-fluorite) OTM (lanthanum chromites/manganites/ferrites/cobaltites and YSZ/CGO/CSO) as a function of temperature (600-1000°C) [30, 36, 219-224].

perovskites (Fig. 1.31), the oxygen flux of dual phase membranes increase with increase in the temperature as well as doping level, and decrease in the membrane thickness as shown in the Fig. 1.32. Overall, lanthanum chromite based dual phase membrane (e.g. $Ce_{0.8}Sm_{0.2}O_{2-\delta}/La_{0.7}Ca_{0.3}Cr_{0.4}O_{3-\delta}$ and $Zr_{0.84}Y_{0.16}O_{1.92}/La_{0.8}Sr_{0.2}Cr_{0.5}Fe_{0.5}O_{3-\delta}$) shows higher performance than cobaltites, ferrites and manganites based membrane. This is probably due to less interaction of the chromites with fluorite phase, otherwise which can result into insulating secondary phase formation (e.g. $SrZrO_3$) and lower oxygen flux/performance. For instance, $La_{0.6}Sr_{0.4}Co_{0.2}Fe_{0.8}O_{3-\delta}$ interacts with 8YSZ to form $SrZrO_3$ at the interface in addition to $CoFe_2O_4$ and Co_3O_4 [226]. From Figs. 1.31 and 1.32,

it is also observed that the hollow fiber membrane (e.g. LSF and YSZ/LSCrM55) provides higher flux than disk shaped (planar) membrane because of higher surface area/volume ratios [221]. This is also due to the achieved lower wall thickness (0.1-0.4mm) in the hollow membrane design.

1.4.8. Chemical Stability

$LaCrO_3$–based perovskites should be stable in OTM operating conditions (P_{O_2} ~ 1-10^{-20} atm, T = 850-1000°C) for ≥ 40,000 h [227]. The stability of these oxides can be classified into three types namely bulk stability, surface/interface segregation, and interfacial stability.

1.4.8.1. *Bulk stability*

Although undoped $LaCrO_3$ is stable at OTM fabrication and operation temperature, it decomposes into vapor species depending on temperature and atmosphere [228-231]. Computational evaluation shows that $LaCrO_3$ vaporization starts in the temperature range of 1200-1400°C depending on the atmosphere: 1300°C in H_2 atmosphere and 1400°C in O_2 as well as CO atmosphere [229]. The weight loss due to vaporization increases from 8.0×10^{-4} % in O_2 to 0.03% in CO, and 0.09% in H_2 atmospheres at 1800°C [229]. The evolved vapor species are CrO_3, CrO_2, CrO, LaO, and O in O_2; Cr, CrO_2, CrO, and LaO in CO; and Cr, CrO_2, CrOH, and LaO in H_2 atmosphere [229]. Among these species, CrO_3 is predominant in air and O_2 atmospheres whereas Cr is predominant in CO and H_2 atmospheres. The computational evaluation for $LaCrO_3$ vaporization is also in agreement with that of experimental results [230]. Doped $LaCrO_3$,

in reality, is used as OTM which is exposed to gas atmospheres (P_{O_2}~ 0.21-10^{-22} atm) containing H_2, CO_2, CO, N_2, H_2O, S, and O_2. Bulk stability of the doped materials varies depending on type and level of dopants as well as temperature and oxygen partial pressure as discussed below.

1.4.8.1.1. *A-site dopants*

Lanthanum chromite is doped at A-site with alkaline earth metals (Sr and Ca). The stability of A-site doped $LaCrO_3$ depends on the solid solubility limit of the dopants [116, 232-235]. The solid solubility of dopants (Sr and Ca) in $La_{1-x}(Sr/Ca)_xCrO_3$ depends on temperature and atmosphere as shown in Fig. 1.33 along with dotted phase boundaries obtained from thermodynamic calculations. For example, the solid solubility limit for Sr is ~10 mol% at 1000°C in air and increases with reducing P_{O_2}(Fig. 1.33a). Above the solid solution limit, $SrCrO_4$ along with several unknown phases appear as shown in Fig. 1.33a [232]. While $SrCrO_4$ is common secondary phase, the remaining depends on the composition of the doped $LaCrO_3$ [122]. For example, Cr_2O_3 is found for A-site deficient, and $Sr_{2.67}(CrO_4)_2$ and La_2O_3 are found for A-site excess $(La_{0.7}Sr_{0.3})_xCrO_3$ ($0.95 \leq x \leq 1.05$) at 1000°C in air [122]. La_2CrO_6 phase is also found at <1000°C [122]. Thermodynamic assessment suggests the possible evolution of $La_{16}Cr_7O_{44}$ phase in air [232].

The solid solubility limit for Ca is ~30 mol% at 1000°C in air and increases with reducing P_{O_2} as shown in Fig. 1.33b [201]. Although, the figure shows that the solubility of Ca increases in lower P_{O_2}, one report in contrast shows that it decreases to ~20 mol% in 10^{-9} atm P_{O_2} at 1600°C [234]. The secondary phases in Ca-doped $LaCrO_3$ are $CaCrO_4$,

La_2CrO_6, $Ca_3(CrO_4)_2$ and $Ca_{10}(CrO_4)_7$ [235]. It is to be noted that solid solubility limit of $La_{1-x}Ca_xCrO_3$ (30 mol %) is higher than $La_{1-x}Sr_xCrO_3$ (10 mol %) at 1000°C in air. However, $CaCrO_4$ decomposes into $Ca_3(CrO_4)_2$ and liquid phase at ~1070°C. On the other hand, $SrCrO_4$ is more refractory than $CaCrO_4$ and decomposes at ~1250°C. Therefore, if $La_{1-x}(Sr/Ca)_xCrO_3$ is placed outside the single phase conditions (Fig. 1.33a and b), the second phase will precipitate faster in case of Ca-doped when compared to Sr-doped $LaCrO_3$ at the operating temperature of OTM (1000°C) [232, 235].

Apart from solid solubility limit, the reducing gas atmospheres also affect the chemical stability. In humidified H_2 atmosphere, the $Sr(OH)_2$, $Ca(OH)_2$, $Cr(OH)_2$, and LaH_2 may form while $SrCO_3$, $CaCO_3$, and Cr_2O_3 phases can form in CO and CO_2 containing atmospheres even at 800°C [116, 236]. Among these, hydroxyl compounds are volatile in the order of $Cr(OH)_2$>$Ca(OH)_2$>$Sr(OH)_2$ [116]. This means Sr-doped $LaCrO_3$ is more chemically stable than that of Ca-doped $LaCrO_3$. The melting point of the $CaCrO_4$ secondary phase decreases from ~1000°C in air to 850°C in CO_2 atmosphere to 640°C in ~3%H_2O containing 10% H_2 in N_2 atmosphere [122, 237]. Similarly, it is expected that the melting point of $SrCrO_4$ secondary phase also reduces to lower temperatures in reducing atmospheres. The appearance of liquid phase at lower temperature accelerates the precipitation of secondary phases.

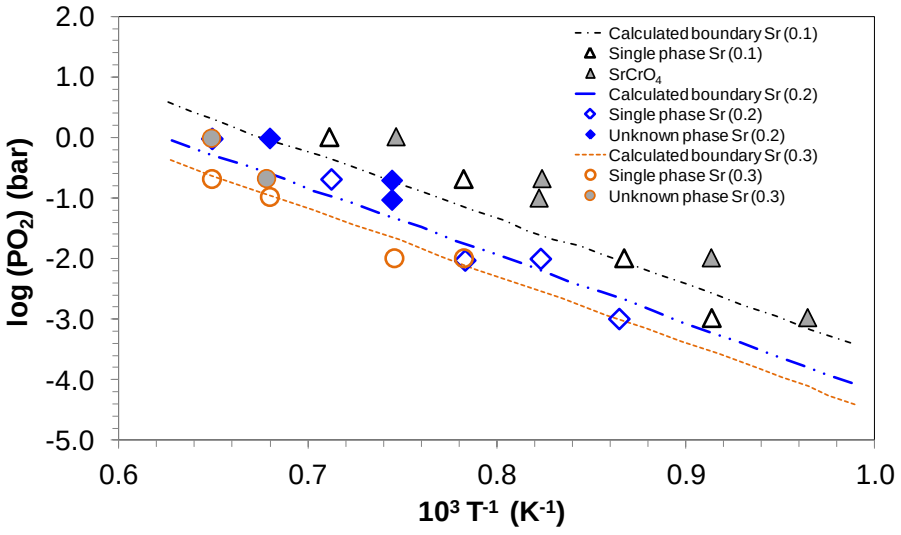

(a)

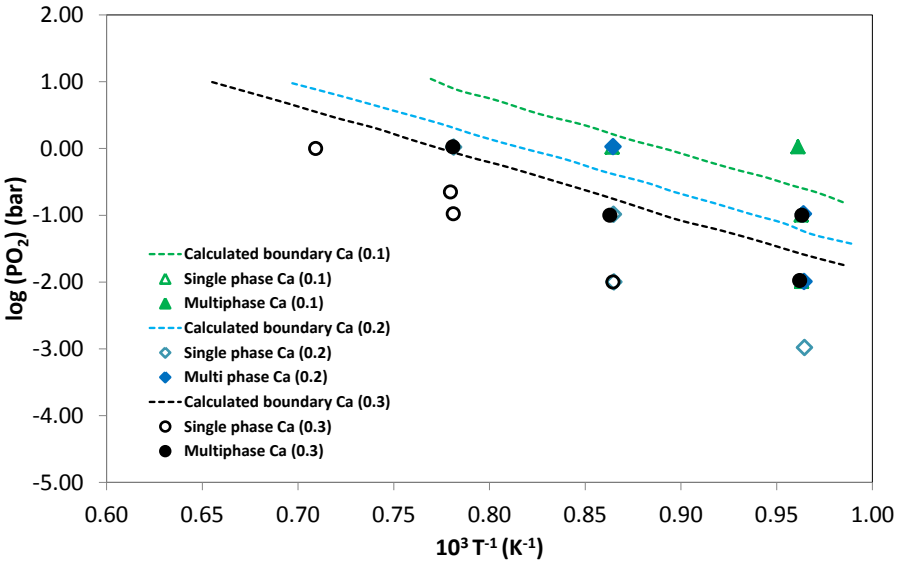

(b)

Fig. 1.33. Solid solubility limit of A-site (Sr, Ca) dopants in $LaCrO_3$ with PO_2 and temperature: a) Sr-dopant level, (b) Ca-dopant level [Reproduced from references 231,234 with permission].

1.4.8.1.2. A and *B-site dopants*

The information on the chemical stability of B-site doped $LaCrO_3$ is limited. Thermodynamic calculation shows that metallic phases appear as secondary phase due to the decomposition of the B-site doped $LaCrO_3$ [116]. For instance, Fe-doped lanthanum chromites decompose to Fe metal and the $LaCrO_3$ phase at 850°C and an oxygen partial pressure of 1.3×10^{-23} atm. At 850°C, the P_{O_2} for B-site doped $LaCrO_3$ decomposition to metal oxide and $LaCrO_3$ phase is calculated as 1.6×10^{-14} atm for Mg, 1.9×10^{-14} atm for Co, and 6.3×10^{-24} atm for Mn doping [113]. $La_{0.25}Sr_{0.75}Cr_{0.5}Mn_{0.5}O_{3-\delta}$ decomposes to $(LaSr)_2MnO_4$ and MnO in reducing atmosphere (~10^{-20} atm) at 900°C [141]. This is due to higher amount of oxygen vacancies formation for the charge balance of $Mn^{4+}\rightarrow Mn^{3+}$ and $Mn^{3+}\rightarrow Mn^{2+}$ in reducing gas atmosphere. Similarly, $La_{0.25}Sr_{0.75}Cr_{0.5}Fe_{0.5}O_{3-\delta}$ decomposes to $(LaSr)_2FeO_4$ and Fe due to the reduction of $Fe^{4+}\rightarrow Fe^{3+}$ and $Fe^{3+}\rightarrow Fe^{2+}$ under same conditions [141]. Precipitation of Ni has been observed in the grain boundaries of $La_{0.8}Ca_{0.2}Cr_{0.9}Ni_{0.1}O_3$ composition after annealing at 900°C in ~3% H_2O containing 10% H_2 (P_{O_2}~ 5.0×10^{-16} atm) [237]. Carbon deposition in the form of 5-20 nm film or soot has been observed for $A_{0.15}La_{0.85}Cr_{0.9}B_{0.1}O_3$ (A = Sr, Ca and B = Mn, Fe, Co, and Ni) samples treated in CH_4 containing gas atmosphere at 900°C [238].

1.4.8.2. *Surface Segregation*

Despite $LaCrO_3$ is stable in reducing atmosphere at ≤1000°C [228-229], surface segregation is often observed for doped $LaCrO_3$ [239-242]. The segregated phases are generally Sr or Ca enriched for A-site doped as well as simultaneous A- and B-site doped

$LaCrO_3$, and transition metal enriched for B-site dopants. For example, Sr-enriched segregation has been observed at the surface of $La_{0.75}Sr_{0.25}Cr_{0.5}Mn_{0.5}O_{3-\delta}$ annealed at $P_{O_2} \sim 10^{-3}$ atm for 10 h even at 600°C [241]. Sr-segregation concentration at the surface decreases with lowering P_{O_2} as evident by its absence in cathodic polarization of -2.5V and reappearance after subsequent anodic polarization of +2.0V in an *in-situ* XPS study during electrochemical investigation [241]. However, Sr and Ca segregation at surface is also observed in reducing atmospheres containing H_2, CH_4, and CO/CO_2. Co segregation has been reported for $LaCr_{0.9}Co_{0.1}O_3$ annealed at 1000°C and $\sim 10^{-16}$ atm for one night [241].

One of the driving forces for surface segregation is electric potential gradient induced kinetic de-mixing of cations as evident from the electrochemical studies [239, 241]. The driving forces for surface segregation without electrical potential gradient [241-242] may be the difference between the enthalpies of defect formation at the surface and in the bulk, and the chemisorption of gaseous species from the gas atmospheres, as observed in $SrTiO_3$ and $La_{0.7}Sr_{0.3}MnO_3$ [243-244]. This is supported by the observations of surface segregation in the doped $LaCrO_3$ even though the dopants concentrations are within solubility limits [242].

1.4.8.3. *Interface Stability*

Interface stability may be defined as the compatibility of $LaCrO_3$ perovskites with adjacent materials such as YSZ in dual phase composite OTM and perovskites/fluorites at surface exchange and intermediate layers. Undoped $LaCrO_3$ is compatible with YSZ but

doped $LaCrO_3$ reacts with YSZ during OTM fabrication and operation, resulting in electrically insulating zirconate phase's formation (e.g. $SrZrO_3$, $CrZrO_3$) [245]. It is shown that $CaCrO_4$ or other Ca-containing secondary phase needs to be precipitated from Ca-doped $LaCrO_3$ to form calcium zirconate ($CaZrO_3$). Ca from the secondary phase such as $CaCrO_4$ diffuses and reacts with YSZ resulting in $CaZrO_3$ phase at the interface [245]. $CaZrO_3$ phase formation will be favored in reducing atmosphere because the melting point of $CaCrO_4$ decreases in reducing atmosphere and the liquid phase enhances the Ca diffusion into the YSZ [245]. In corollary, the $SrCrO_4$ may need to be precipitated from Sr-doped $LaCrO_3$ prior to the formation of $SrZrO_3$. Since the melting point of $SrCrO_4$ is higher than that of $CaCrO_4$, Sr-doped $LaCrO_3$ is preferred for interface stability. Also, the formation of zirconate phases can be avoided by limiting the level of dopants to the lower end of solubility limit to inhibit $CaCrO_4$ or $SrCrO_4$ phase formation. It is noted that the lanthanum zirconate ($La_2Zr_2O_7$) phase formation, like in lanthanum manganite/YSZ interaction [246-248], is not favorable because the existence of La_2O_3 precipitates to interact with YSZ to form $La_2Zr_2O_7$ is unlikely, consistent with the experimental observation [116, 245].

1.5. Challenges

The challenges for the OTM development and commercial deployment are predominantly associated with fabrication, long term reliable operation and robust systems integration. Materials degradation arising from gas-solid and solid-solid interactions needs to be minimized. Basic scientific understanding of transport kinetics

and standardized method for oxygen flux/permeation evaluation also remain largely unknown. Above challenges are discussed below:

Fabrication cost: Fabrication of a flaw (crack and pore) free dense membrane is difficult due to poor sinterability of $LaCrO_3$ based perovskites (section 1.4.2). A-site excess and simultaneous A and B-site doping increases the density of $LaCrO_3$ if sintered at high temperature (1350-1600°C, Fig. 1.17 and 1.18). The fabrication temperature can be reduced to certain extent if sintered in controlled reducing P_{O_2} and/or high dopant level ($x \geq 0.3$). With increased dopant level and reduced P_{O_2}, the structural and chemical stability may be compromised as discussed in section 1.4.8. Difference in sintering behavior of the perovskite and fluorite phases can generate cracks at the interface of these phases. The flaws in the microstructure (bulk and interfaces) propagate and result into mechanical failure. Film deposition techniques have been applied (plasma spray, physical vapor deposition (sputtering and laser ablation), and electrochemical chemical vapor deposition) to avoid the high temperature sintering for obtaining dense $LaCrO_3$ based perovskites. Even though density can be achieved with controlled microstructure for the bulk membrane, high temperature (≥1300°C) annealing is required for strong interface. The installation, operation, and maintenance costs are very high for these deposition techniques compared to the conventional ceramic processing techniques such as wet chemical method. However, the parameters for the conventional techniques (wet chemical method) to deposit $LaCrO_3$ based perovskite are yet to be optimized.

Materials degradation: The OTM operating conditions (temperature, time, and atmosphere) also degrade the stability of materials due to reaction kinetics and solid-gas interaction as discussed in section 1.4.8. The perovskite phases can also react with the fluorite phase in dual phase membrane and form new compounds. The electrical conductivities of the secondary compounds are different than the bulk and affect the electrochemical activity for oxygen flux. Further, the bulk membrane may form interfacial compounds due to interaction between the membrane and the intermediate and surface exchange layers. The difference between the thermal expansion behavior of the primary and secondary compounds can lead to crack and pore formation. In addition, the porous microstructure of the intermediate and surface exchange layer can change due to atomic diffusion and grain growth. The gradient in P_{O_2} across the OTM as well as thermal cycling can also lead to mechanical failure. The lattice volume change can be mitigated by suitable B-site dopants to decrease the amount of oxygen vacancy.

The components of OTM devices are connected to other components (ceramic, metallic or alloy) in a balance of plant by sealants. The sealants for high temperature application are alumino-silicate based materials (glass and ceramic pastes). Silica evaporation from glass based sealants during operation can degrade not only sealant performance for preventing gas leakage but also the catalytic activity of the device due to deposition of silica vapor species at the electrochemically active areas (triple phase boundary) [156, 249].

Lack of fundamental understanding of transport kinetics and standardized method for oxygen flux/permeation evaluation: Electronic and ionic transport as well as the surface exchange kinetics depend on the defect chemistry and defect interactions. The transport and surface exchange kinetics are not much investigated despite the total electrical conductivity for lanthanum chromite based perovskites have been studied. The transference number for the doped lanthanum chromites need to be determined to effectively model defect chemistry and its correlation with the electrochemical activity. The desirable transference number is not known.

Different research groups use different methods to determine the oxygen flux and report as normalized value without detailing the experimental procedure and sample dimensions. As a result, the literature report cannot be compared for same composition for further improvement in materials development. Also, the information about oxygen flux is limited in literature. In most cases, the oxygen flux is determined by maintaining P_{O_2} gradient. In practice, the OTM will be exposed to the reducing atmospheres containing CO, CH_4, H_2, S, N, and other elements depending on the gas composition. The electrochemical behavior and oxygen flux not necessarily be same for all the gas compositions. It will depend on the redox behavior and microstructure of the OTM materials – a subject of further research.

Integration with a gasification or power generation system: To integrate in a gasification or power generation system, the OTM needs to be joined with the corresponding (ceramics and/or metal) components in the system. High temperature ceramic/glass/brazing seals are used at the joints with or without applied pressure. The

joining points are generally prone to mechanical failure because of high pressure (as high as ~400 atm), interfacial compounds due to interaction between the components, and generation of pores and cracks at the joining. The material development for joining the components as well the compatibility with the adjacent components needs to be studied.

1.6. Summary

The status of the lanthanum chromite based perovskites as mixed and ionic electronic conductor, for application in the active oxygen transport membrane, to separate oxygen from air has been reviewed. The tailoring of the required properties such as density, thermal expansion behavior, electrical conductivity, oxygen permeation, and thermo-chemo-mechano stability by tailoring the composition using dopants has been reviewed and discussed. Table 1.7 summarizes the properties of A and/or B-site doped lanthanum chromites.

The density of undoped lanthanum chromite is less than 60%. The poor sinterability is attributed to the evaporation of CrO_3 specie and its deposition as Cr_2O_3 at the inter-particle necks of $LaCrO_3$ during sintering process. A-site (Sr, Ca) and B-site dopants (Ni, Co, Cu, Mn, Fe) enhance densification of lanthanum chromite. More than 94% density can be obtained in Ca doped A-site excess as well in simultaneous A and B-site doped lanthanum chromite as shown in Table 1.7. Iron and nickel as the B-site dopant shows highest densification. However, it is dependent on dopant level and sintering temperature. Density increases with increasing doping level and sintering temperature.

Table 1.7. Summary - Properties of A and/or B-site doped lanthanum chromite materials [32-33, 38, 110, 112-115, 120, 123, 126, 128-131, 134, 139-142, 149, 183-185, 193-194].

Composition	**Relative Density (%)**	**Oxygen-Nonstoichiometry (Δδ) (T= 1000 °C PO_2 ~ 0.21-10^{-15} atm)**	**Thermal Expansion (×10^{-6} °C^{-1})**	**Electrical Conductivity (S cm^{-1})**	**Mechanical Property (Flexure Strength - MPa)**	**Oxygen-Flux (mol cm^{-2} sec^{-1})**
$LaCrO_3$	~50 (T~1450°C)	-	9.4 (air) (T=290-1050°C)	0.2-0.35 (air), 0.003-0.05 (H_2) (T~500-800°C)	-	-
A-site (Ca) doped $LaCrO_3$						
$La_{0.9}Ca_{0.1}CrO_{3-\delta}$	-	~0.0112	9 (air) (T=50-1000°C)	9.4-12.0 (air), 0.7-2.7 (H_2) (T~500-1000°C)	-	-
$La_{0.7}Ca_{0.28}CrO_3$	<60 (T~1550°C)	-			-	-
$La_{0.7}Ca_{0.3}CrO_{3-\delta}$	~68 (T=1600°C)	~0.07	9.7 (air) (T=50-1000°C)	30.2-37.1 (air), 2.2-4.3 (H_2) (T~500-850°C)	~220 (T= 1400°C)	-
$La_{0.7}Ca_{0.32}CrO_3$	>90 (T=1400°C)	-	-	-	-	-

$(La_{0.6}Ca_{0.4})_{1.02}CrO_3$	>95 (T=1350°C)	-	-	-	-	-
A-site (Sr) doped $LaCrO_3$						
$La_{0.9}Sr_{0.1}CrO_{3-\delta}$	-	~0.0114	10.7 (air) (T=50-1000°C)	7.3-8.5 (air), 0.4-2.1 (H_2) (T~500-800°C)	~80 (T= 600°C)	-
$(La_{0.85}Sr_{0.15})_{0.95}CrO_3$	~58 (T=1600°C	-	-	-	-	-
$La_{0.7}Sr_{0.3}CrO_{3-\delta}$	~65 (T=1400°C)	~0.082	11.1 (air) (T=50-1000°C)	37.2-39.8 (air), 3.9-4.8 (H_2) (T~500-800°C)	~98 (T= 1400°C)	-
$(La_{0.85}Sr_{0.15})_{1.02}CrO_3$	>90 (T=1600°C)	-	-	-	-	-
A-site (Sr,Ca) doped $LaCrO_3$						
$La_{0.75}Ca_{0.10}Sr_{0.15}CrO_3$	~84 (T=1400°C)	-	-	-	-	-
A-site (Ca/Sr) and B-site (Fe) doped $LaCrO_3$						
$La_{0.9}Ca_{0.1}Cr_{0.5}Fe_{0.5}O_3$	57.6 (T=1250°C)	-	-	3.0 (air) (T~727°C)	-	-
$La_{0.8}Ca_{0.2}Cr_{0.9}Fe_{0.1}O_{3-\delta}$	-	-	-	-	~154.3 (T= 25°C)	-
$La_{0.9}Sr_{0.1}Cr_{0.95}Fe_{0.05}O_3$	-	-	9.2 (air), 10.2 (H_2) (T=50-1000°C)	-	-	-
$La_{0.8}Sr_{0.2}Cr_{0.9}Fe_{0.1}O_{3-\delta}$	~84 (T=1400°C)	-	-	-	-	-

$La_{0.75}Sr_{0.25}Cr_{0.7}Fe_{0.3}O_{3-\delta}$	-	~0.1266			-	-
$(La_{0.75}Sr_{0.25})_{0.95}Cr_{0.7}Fe_{0.3}O_{3-\delta}$	95.2 (T=1700°C)	-	11.3 (air), 10.3 (CO/CO_2) (T=27-1097°C)	~31.6 (air), ~2.0 (10^{-18} atm) (T~900°C)	-	~1.0E-7 (T=950°C, disk, d= 1mm, air/H_2-N_2)
$(La_{0.75}Sr_{0.25})_{0.95}Cr_{0.6}Fe_{0.4}O_{3-\delta}$	-	-	11.1 (air), 10.5 (CO/CO_2) (T=27-1097°C)-	-	-	~1.5E-7 (T=900°C, disk, d=1mm, air/H_2-N_2)
$La_{0.8}Sr_{0.2}Cr_{0.5}Fe_{0.5}O_{3-\delta}$	~97 (T=1400°C)	-	-	~21.9 (air), ~6.4 (5%H_2-Ar) (T=800°C)	-	~1.2E-7 (T=950°C, disk, d=1mm, air/CO)
A -site (Ca/Sr) and B-site (Mn) doped $LaCrO_3$						
$La_{0.9}Ca_{0.1}Cr_{0.5}Mn_{0.5}O_3$	54.4 (T=1250°C)	-	-	2.2 (air) (T~727°C)	-	-
$La_{0.9}Sr_{0.1}Cr_{0.95}Mn_{0.05}O_3$	-	-	10.2 (air), 11.2 (H_2) (T=50-1000°C)	-	-	-
$La_{0.9}Sr_{0.1}Cr_{0.5}Mn_{0.5}O_3$	~78 (T=1475°C)	-	-	-	-	-
$La_{0.75}Sr_{0.25}Cr_{0.5}Mn_{0.5}O_{3-\delta}$	>94 (T=1600°C)	~0.1468	-	~38.6 (air), ~1.49 (5%H_2-Ar) (T=900°C)	-	-

$(La_{0.75}Sr_{0.25})_{0.95}Cr_{0.5}Mn_{0.5}O_{3-\delta}$	~94 (T=1600°C)	-	12.7 (air), 11.7 (CO/CO_2) (T=650-950°C)	20-35 ($0.21\text{-}10^{-12}$ atm) (T~750-1000°C)	-	~8.9E-10 (T=950°C, disk, d=1mm, ~0.2/E-15)
$La_{0.9}Sr_{0.1}Cr_{0.3}Mn_{0.7}O_3$	~95 (T=1475°C)	-	-	-	-	-
A -site (Ca/Sr) and B-site (Ni) doped $LaCrO_3$						
$La_{0.9}Ca_{0.1}Cr_{0.5}Ni_{0.5}O_3$	53.6 (T=1250°C)	-	-	23.3 (air) (T~727°C)	-	-
$La_{0.9}Sr_{0.1}Cr_{0.95}Ni_{0.05}O_3$	-	-	9.4 (air), 10.1 (H_2) (T=50-1000°C)	-	-	-
$La_{0.9}Sr_{0.1}Cr_{0.5}Ni_{0.5}O_3$	-	-	-	72.8 (air) (T~800°C)	-	-
$La_{0.85}Sr_{0.15}Cr_{0.95}Ni_{0.05}O_3$	~96.4 (T=1450°C)	-	10.3 (air) (T~50-1000°C)	-	-	-
A -site (Ca/Sr) and B-site (Co) doped $LaCrO_3$						
$La_{0.8}Ca_{0.2}Cr_{0.9}Co_{0.1}O_{3-\delta}$	-	-	-		~170.5 (T= 25°C)	-
$La_{0.85}Sr_{0.15}Cr_{0.95}Co_{0.05}O_3$	~91 (T=1450°C)	-	11.4 (air) (T~50-1000°C)	0.1-0.7 (air) (T~100-860°C)	-	-
$La_{0.9}Sr_{0.1}Cr_{0.95}Co_{0.05}O_3$	-	-	10.4 (air), 11.5 (H_2) (T=50-1000°C)	-	-	-

A -site (Ca/Sr) and B-site (Cu) doped $LaCrO_3$						
$La_{0.8}Ca_{0.2}Cr_{0.9}Cu_{0.1}O_{3-\delta}$	-	-	-	-	~356.9 (T= 25°C)	-
$La_{0.85}Sr_{0.15}Cr_{0.95}Cu_{0.05}O_3$	~94.5 (T=1450°C)	-	10.6 (air) (T~50-1000°C)	-	-	-
A -site (Ca/Sr) and B-site (Ti) doped $LaCrO_3$						
$La_{0.9}Sr_{0.1}Cr_{0.95}Ti_{0.05}O_3$	-	-	9.0 (air), 9.3 (H_2) (T=50-1000°C)	-	-	-
$La_{0.7}Sr_{0.3}Cr_{0.9}Ti_{0.1}O_{3-\delta}$	-	~0.048	-	-	-	-
$La_{0.7}Sr_{0.3}Cr_{0.7}Ti_{0.3}O_{3-\delta}$	-	~0.005	-	-	-	-

$La_{0.8}Sr_{0.2}Cr_{0.5}Fe_{0.5}O_{3-\delta}$ and $La_{0.85}Sr_{0.15}Cr_{0.95}Ni_{0.05}O_3$ are the best two compositions (Table 1.7) among doped $LaCrO_3$. But, the required sintering temperature is above 1350°C. Undoped lanthanum chromite changes room temperature orthorhombic to rhombohedral structure at ~260°C with a volume change. Strontium dopant (10 mol%) decreases the polymorphic transition temperature to ~42°C, eliminating the stress due to the change in lattice during thermal cycling. Calcium dopant (10 mol %) increases the polymorphic transition temperature to 307°C.

The thermal expansion coefficient (TEC) of the lanthanum chromite can be tuned virtually by maintaining the level of any dopant. For example, <20 mol% Sr/Ca doping and 5 mol% Ni/Mn/Fe doping is suitable to obtain TEC similar to 8YSZ (~10.3×10^{-6} $°C^{-1}$). The dopants also induce chemical expansion because of the presence of oxygen vacancy and different valance states of B-site cations. From Table 1.7, $La_{0.9}Sr_{0.1}Cr_{0.95}M_{0.05}O_3$ (Ni, Fe, Mn) composition shows TEC within the tolerable difference limit ($\pm1.0\times10^{-6}$ $°C^{-1}$) of fluorite phase (e.g. 8YSZ) in air and H_2 atmosphere (50-1000°C).

Undoped lanthanum chromite shows only electronic conduction. Ionic conductivity is induced in doped lanthanum chromites due to creation of oxygen vacancies. The dopants also increase the total (ionic and electronic) conductivity due to polaron hopping. The electrical conductivity value is varied for A-site dopants (strontium and calcium) depending on the dopant type and level. However, there is no significant variation. Nickel doping in the B-site shows the highest conductivity among others. However, Mn and Fe doping can induce mixed ionic-electronic conductivity. The role of

dopants on the electrochemical activity for oxygen permeation cannot be concluded due to limited knowledge. It is identified that $La_{0.9}Sr_{0.1}Cr_{0.5}Ni_{0.5}O_3$ composition shows the highest electrical conductivity as shown in Table 1.7.

Undoped lanthanum chromite is the most stable at the extreme OTM operating conditions. For the doped lanthanum chromite, strontium doping is more stable than calcium doping. Surface segregation is generally observed for ≥20 mol% dopant levels. Therefore, strontium is preferred A-site dopant at less than 20 mol% level. The stability for the B-site doping is not studied well. The solubility of the B-site dopants in the lanthanum chromite decreases in reducing atmosphere and tend to reduce to metallic form. Considering the positive role on the thermo-physical properties of the lanthanum chromite, B-site dopants can be used at lower level (≤30 mol %). However, cobalt doping should be avoided because it undesirably increases the TEC attributed to the change in valance state.

1.7. Overall objective and scope

Lanthanum chromite based perovskites have been considered as a promising candidate for OTM system. This is mainly due to its high thermo-chemical and redox stability at high temperature (>1000°C) in a wide range of oxygen partial pressure (0.21-10^{-22} atm). Despite having good electronic conductivity 0.6-1.0 S/cm at 1000°C and superior chemical stability in a wide temperature and PO_2 range, undoped $LaCrO_3$ is not suitable for OTM due to lack of ionic conduction and densification. To densify and obtain the desired thermal and electrical properties, dopants are introduced at A-site as well as B-site of lanthanum chromite. Sr and Ca are used as A-site dopants while

transition metals (Mn, Fe, Co, Ni and Ti) are considered for B-site dopants. A-site dopants are generally acceptor type and induce oxygen vacancy for ionic conduction. B-site dopants are introduced to maintain thermal and crystal structure stability, and to further increase the electrical conductivity and performance. To enhance the oxygen surface exchange and improve the overall oxygen flux, however, fluorite phase (YSZ/ScSZ) is added to the perovskites.

Based on the literature review, limited data exists on perovskite/fluorite based materials optimization and development for the oxygen transport membrane system. The literature search also shows lack of information pertaining to the interaction of perovskite and fluorite phases under oxidizing as well as reducing gas atmosphere required for long-term stable operation of the OTM device. Fundamental research needs to be conducted in the areas of the doping (type and level) effects on materials structure, phase transformation, properties, processing, electrochemical activity and stability (thermal, structure, chemical, microstructural and interfacial), in particular, for doped lanthanum chromites and/or mixed with fluorite phase, to fully exploit the material for active OTM application.

From the above discussions, it can be suggested that strontium as A-site dopant and transition metals (Mn, Ni and Fe) as B-site dopants can be considered for compositional design to achieve all the required properties simultaneously. From the thermo-mechanical stability point of view, titanium as B-site dopant can be considered because of reduced chemical expansion. In addition, Ti-based $La_{0.7}Sr_{0.3}Cr_{0.7}Ti_{0.3}O_{3-\delta}$ composition provides least oxygen-nonstoichiometry (δ) at 1000°C and P_{O_2}~1-10^{-15} atm

(Table 1.7). Overall, $La_{1-x}Sr_xCr_{1-y-z}M_yTi_zO_3$ (M = Ni, Fe, Mn; $x \leq 0.2$, y, $z \leq 0.3$) composition would be the best perovskite composition for OTM. For higher oxygen flux and performance, it is suggested to combine perovskite phase with fluorite phase (e.g. 8YSZ and 10ScSZ) to obtain higher ionic conductivity.

Due to the lack of information in literature (**Chapter 1**) and the above mentioned need/importance of perovskite/fluorite based materials development under simulating OTM fabrication (1400°C, ~ 0.21-10^{-10} atm) and operating (1000°C, ~ 0.21 – 10^{-16} atm) conditions, the objective of this research includes: (a) investigation of the structural, thermal, chemical, microstructural and interfacial stability of perovskites and perovskite–fluorite composites with varying Cr: M ratio, (b) develop understanding on the behavior of A and B-site doped single phase perovskites as well as their composites with YSZ/ScSZ/ScCeSZ under OTM processing and operating conditions, (c) relative stability and interactions of YSZ and ScSZ in perovskite under oxidizing and reducing atmosphere and (d) develop interaction/degradation mechanisms. Experimental approach considers examination of:

Chapter 2. Phase transformation, electrical conductivity and thermal expansion of lanthanum chromite

Chapter 3. Electrochemical determination of Gibbs energy of formation of lanthanum chromite using a composition-graded bielectrolyte

Chapter 4. Thermodynamic properties of $LaCrO_4$, La_2CrO_6, and $La_2Cr_3O_{12}$, and subsolidus phase relations in the system lanthanum-chromium-oxygen

Chapter 5. Manganese doped lanthanum-strontium chromite fuel electrode for solid oxide fuel cell and oxygen transport membrane systems

Chapter 6. Processing and electrochemical performance of manganese-doped lanthanum-strontium chromite in oxidizing and reducing atmospheres

Chapter 7. A new stable nickel and titanium co-doped lanthanum strontium chromite for high temperature electrochemical devices

Chapter 8. A comparative study on manganese-doped lanthanum-strontium chromite mixed with 8YSZ and 10ScSZ in oxidizing and reducing atmospheres

Chapter 9. Processing, interfacial stability and electrochemical performance of iron soped lanthanum strontium chromite in oxidizing and reducing atmosphere

Chapter 10. Effect of chromium: iron ratio and oxygen partial pressure on processing and stability of iron doped lanthanum strontium chromite

Chapter 11. Effect of chromium: iron ratio and oxygen partial pressure on processing and stability of iron doped lanthanum strontium chromite and scandia stablized zirconia

Chapter 12. Performance and post-test characterization of OTM system in experimental coal gasifier

1.8. References:

[1] A. Frassoldati, A. Cuoci, T. Faravelli, E. Ranzi, C. Candusso, D. Tolazzi, 1st International Conference on Sustainable Fossil Fuels for Future Energy – S4FE, 2009.

[2] H. Stadler, F. Beggel, M. Habermehl, B. Persigehl, R. Kneer, M. Modigell, P. Jeschke. Int. J. Greenhouse Gas Control 5 (2011) 7-15.

[3] V. White, R. Allam, E. Miller. 8th International Conference on Greenhouse Gas Emissions, Trondheim, Norway, 2006, 1-6.

[4] S. Walspurger, H.A.J. van Dijk. ECN-E-12-054 (2012) 28-34.

[5] D. Kang, R.S. Srinivasan, R.T. Thorogood, E.P. Foster EP. US Patent 5516359, 1996.

[6] M.F. Carolan, P. N. Dyer, US Patent 5712220, 1998.

[7] M.F. Carolan, P. N. Dyer. US Patent 5599383, 1997.

[8] A.G. Dixon, W.R. Moser, Y.H. Ma. Ind. Eng. Chem. Res. 33 (1994) 3015-24.

[9] H. Stadler, F. Beggel, M. Habermehl, B. Persigehl, R. Kneer, M. Modigell, P. Jeschke. Int J Greenhouse Gas Control 5 (2011) 7-15.

[10] S.S. Hashim, A.R. Mohamed, S. Bhatia. Ren. Sustain Energy Rev. 15 (2011) 1284-93.

[11] E.H. Shreiber, B. A.V. Hassel, R. Prasad. US Patent 7118612B2, 2006.

[12] Y. Zeng, Y. S. Lin, S.L. Swartz. J. Mem. Sci. 150 (1998) 87-98.

[13] B.C.H. Steele. Solid State Mater. Sci. 1 (1996) 684-91.

[14] S.P.S. Badwal, F.T. Ciacchi. Adv. Mater. 13 (2001) 993-96.

[15] L.L. Anderson, P.A. Armstrong, J.M. Repasky, V.E. Stein. International Pittsburgh Coal Conference, Pittsburgh, USA, 2011.

[16] S. Cooper, N. Frazier, P. Urane. Calvin College Department of Engineering 339/340 (2011) 1-63.

[17] W.P. Schmidt, K.W. Kovak, W.R. Licht, S.L. Feldman. Air Products and Chemicals Inc., 2000.

[18] Use of process analytics in cryogenic air separation plants, Chemical Industry case study, Siemens, p. 2

[19] R. Jafari. Iran International Zeolite Conference (IIZC), 2008.

[20] J. Da. Costa, S. Smart, J. Motuzas, S. Liu, D. Zhang. Project Number: 3-0510-0034. Report (2013) 1-13.

[21] P.N. Dyer, R. E. Richards , S.L. Russek , D.M. Taylor. Solid State Ionics 134 (2000) 21-33.

[22] B. Belaissaoui, Y.L. Moullec, H. Hagi, E. Favre. Sep. Purif. Tech. 125 (2014) 142-150.

[23] N.D. Paul, E.R. Robin, L.R. Steven, M.T. Dale. Solid State Ionics 134 (2000) 21-33.

[24] W. Lai, S.M. Haile. Phys. Chem. Chem. Phys. 10 (2008) 865-83.

[25] J.W. Stevenson, T.R. Armstrong, R.D. Carmeim, L.R. Pederson, L.R. Weber. J. Electrochem. Soc. 143 (1996) 2722-29.

[26] V.V. Kharton, A.A. Yaremchenko, A.V. Kovalevsky, A.P. Viskup, E.N. Naumovich, P.F. Kerko. J. Mem. Sci. 163 (1999) 307-17.

[27] X. Zhu and W. Yang, AIChE Journal 54 (2008) 665-672.

[28] J. Han, Y. Zeng, G. Xomeritakis, Y.S. Lin. Solid State Ionics 98 (1997) 63-72.

[29] J. Kim, Y.S. Lin. J. Mem. Sci. 167 (2000) 123-33.

[30] D.P. Fagg, I.P. Marozau, A.L. Shaula, V.V. Kharton, J.R. Frade. J. Solid State Chem. 179 (2006) 3347-56.

[31] J.J. Liu, T. Liu, W.D. Wang, J.F. Gao, C.S. Chen, J. Mem. Sci. 389 (2012) 435-440.

[32] V.V. Kharton, E.V. Tsipis, I.P. Marozau, A.P. Viskup, J.R. Frade, J.T.S. Irvine. Solid State Ionics 178 (2007) 101-13.

[33] M.F. Lü, E.V. Tsipis, J.C. Waerenborgh, A.A. Yaremchenko, V.A. Kolotygin, S. Bredikhin, V.V. Kharton. J. Power Sources 206 (2012) 59-69.

[34] X. Zhu, W. Yang. Mem. Sci. Tech. 14 (2011) 275-93.

[35] A. Yu. Zuev, A.I. Vylkov, D.S. Tsvetkov. Solid State Ionics 192 (2011) 220-224.

[36] T.A. Ramanarayanan, S.C. Singhal, and E.D. Wachsman. The Electrochemical Society Interface. Summer (2001) 1-27.

[37] J. Samson, M. Søgaard, P.V. Hendriksen. J. Mem. Sci. 470 (2014) 178-188.

[38] W. He, H. Huang, M. Chen, J.F. Gao, C.S. Chen. Solid State Ionics 260 (2014) 86-89.

[39] A. Julbe, D. Farrusseng, C. Guizard. Catal. Today 104 (2005) 102-113.

[40] H.J.M Bouwmeester, A.J. Burggraaf, in: A.J. Burggraaf, L. Cot (Eds.), Membrane Sci. Technol. Series, Amsterdam, Elsevier; 1996, pp. 435-510.

[41] J. Hong, P. Kirchen, A.F. Ghoniem. J. Mem Sci. 407 (2012) 407.

[42] N. Nagabhushana, J.A. Lane, G.M Christie, B.A. Van Hassel. US Patent 7556676, 2009.

[43] G.M. Christie, J.R. Wilson, B.A. Van Hassel. US Patent 090645 A2, 2011.

[44] M.F. Carolan, P.N. Dyer. US Patent 553447, 1996.

[45] M. Liu, A.V. Joshi, Y. Shen. US Patent 5240480, 1993.

[46] T. Nakamura, G. Petzow, L.J. Gauckler. Mater. Res. Bull. 14 (1979) 649-59.

[47] P. Dalach, D.E. Ellis, A.V. Walle. Phys. Rev. B 85 (2012) 014108.

[48] S.K. Mazumder, K. Acharya, C.L. Haynes, R. Williams, M.R.V. Spakovsky, D.J. Nelson, D.F. Rancruel, J. Hartvigsen, R.S. Gemmen. IEEE transactions on power electronics 19 (2004) 1263-78.

[49] D.J.L. Brett, A. Atkinson, N.P. Brandon, S.J. Skinner. Chem. Soc. Rev. 37 (2008) 1568-78.

[50] A.J Jacobson. Chem. Mater. 22 (2010) 660-74.

[51] A. Aguadero, L. Fawcett, S. Taub, R. Woolley, K.T. Wu, N. Xu, J.A. Kilner, S.J. Skinner. J. Mater. Sci. 47 (2012) 3925-48.

[52] J. Sunarso, S. Baumann, J.M. Serra, W.A. Meulenberg, S. Liu, Y.S. Lin, J.C. Diniz da Costa. J. Mem. Sci. 320 (2008) 13-41.

[53] Q. Jiang, S. Faraji, D.A. Slade, S.M.S. Williams. Mem. Sci. Tech. 14 (2011) 235-73.

[54] A.S. Mukasyan, C. Costello, K.P. Sherlock, D. Lafarga, A. Varma. Sep. Purif. Tech. 25 (2001) 117-26.

[55] V. V. M. Goldschmidt. Geochemische Verteilungsgesetze der Elemente. Tl. VIII (Skrifter utgitt av Det Norske Videnskaps - Akademi i Oslo, I. Matem.-Naturvid.Klasse. 1926): Untersuchungen über Bau und Eigenschaften von Krystallen.Dybwad Oslo, 1927.

[56] J. Richter, P. Holtappels, T. Graule, T. Nakamura, L.J. Gauckler. Monatsh Chem. 140 (2009) 985-99.

[57] R.A. De Souza, M. Martin. Monatsh Chem. 140 (2009) 1011-15.

[58] M. Cherry, M.S. Islam, C.R.A. Catlow. J. Solid State Chem. 118 (1995) 125-32.

[59] J.A. Kilner, R.J. Brook. Solid State Ionics 6 (1982) 237-52.

[60] Y.T. Suru, M. Shimazu, M. Shiono, M. Morinaga. Jap. J. Appl. Phys. 49 (2010) 045701.

[61] S. Taniguchi, M. Aniya. Int. Ferroelectrics 115 (2010) 18–24.

[62] H. Hayashi, H. Inaba, M. Matsuyama, N.G. Lan, M. Dokiya, H. Tagawa. Solid State Ionics 122 (1999) 1-15.

[63] M. Mogensen, D. Lybye, N. Bonanos, P.V. Hendriksen, F.W. Poulsen. Solid State Ionics 174 (2004) 279-86.

[64] H.U. Anderson. Solid State lonics 52 (1992) 33-41.

[65] H.U. Anderson, in: F.W. Poulsen, J.J. Bentzen, T. Jacobsen, E. Skou, M.J.L. Ostergard (Eds.), Proceedings of the 14th Riso International Symposium on Materials Science, Riso National Laboratory, Roskilde, 1993.

[66] J. Mizusaki. Solid State Ionics 52 (1992) 79-91.

[67] H. Yokokawa, N. Sakai, T. Kawada, M. Dokiya. Solid State Ionics. 52 (1992) 43-56.

[68] T. Nakamura, G. Petzow, L.J. Gauckler, Mat. Res. Bull. 14 (1979) 649.

[69] S. Gangopadhayay, T. Inerbaev, A.E. Masunov, D. Altilio, N. Orlovskaya. ACS Appl. Mater. Interfaces 7 (2009) 1512-19.

[70] C.H. Chen, H. Kruidhof, H.J.M. Bouwmeester, A.J. Burggraaf. J. Appl. Electrochem. 27 (1997) 71-75.

[71] M. Søgaard, P.V. Hendriksen, M. Mogensen. J. Solid State Chem. 180 (2007) 1489-1503.

[72] S.P. Jiang. J. Mater. Sci. 43 (2008) 6799-833.

[73] M. Khairy, P. Odier, Choisnet. J. de Phys. 47 (1986) C1-831.

[74] E.V. Tsipis, E.N. Naumovich, A.L. Shaula, M.V. Patrakeev, J.C. Waerenborgh, V.V. Kharton. Solid State Ionics 179 (2008) 57-60.

[75] R. Sayers, M. Rieu, P. Lenormand, F. Ansart, J.A. Kilner, S.J. Skinner. Solid State Ionics 192 (2011) 531-534.

[76] R. Sayers, J.E. Parker, C.C. Tang, S.J. Skinner. J. Mater. Chem. 22 (2012) 3536-43.

[77] N. Sakai, H. Yokokawa, T. Horita, K. Yamaji. Int. J. Appl. Ceram. Tech. 1 (2004) 23-30.

[78] J.GM. Furtado, R.N. Oliveira. Revista Matéria 13 (2008) 147-53.

[79] T. Horita. Fuel Cells Hyd. Energy (2009) 285-96.

[80] J.W. Fergus. Solid State Ionics 30 (2004) 1-15.

[81] P. Singh, N.Q. Minh. Int. J. Appl. Ceram. Tech. 1 (2004) 5-15.

[82] Z.G. Yang, J.W. Stevenson, P. Singh. Adv. Mater. Processes 161 (2003) 34-37.

[83] N. Xu, H. Zhao, X. Zhou, W. Wei, X. Lu, W. Ding, F. Li. Int. J. Hyd. Energy 35 (2010) 7295-301.

[84] J.M. Repasky, E.P. Foster, P.A. Armstrong, V.E. Stein, L.L. Anderson. Gasification Technologies Council, San Fransisco, California, USA, 2011.

[85] M.F. Carolan, C.M. Chen, C.F. Miller, E. Minford, J.J. Steppan, W.E. Waldron. ECS Trans 1 (2006) 335-43.

[86] J. Schwartz, R. Drnevich, P. Apte, A. Damle. DOE Annual Merit Review Meeting, 2003.

[87] N.H. Menzler, F. Tietz, S. Uhlenbruck, H.P. Buchkremer, D. Stöver. J. Mater. Sci. 45 (2010) 3109-35.

[88] L.R. Pederson, P. Singh, X.D. Zhou. Vacuum 80 (2006) 1066-83.

[89] R. Hui, Z. Wang, O. Kesler, L. Rose, J. Jankovic, S. Yick, R. Maric, D. Ghosh. J. Power Sources 170 (2007) 308-23.

[90] R. Maric, J. Roller, R. Neagu. J. Thermal Spray Tech. 20 (2011) 696-718.

[91] D. Beckel, A. Bieberle-Hütter, A. Harvey, A. Infortuna, U.P. Muecke, M. Prestat, J.L.M. Rupp, L.J. Gauckler. J. Power Sources 173 (2007) 325-45.

[92] G.Y. Meng, H.Z. Song, H.B. Wang, C.R. Xia, D.K. Peng. Thin Solid Films 409 (2002) 105-11.

[93] J.C. Boeker, P. Singh. US patent 4861345, 1989.

[94] P. Singh, R.J. Ruka. US Patent 5389456, 1995.

[95] A.J. Burggraaf, Y.S. Lin. US Patent 5, 1993.

[96] C. Keegan. Wincewicz, J.S. Cooper. J. Power Sources 140 (2005) 280-96.

[97] H. Itoh, M. Mori, N. Mori, T. Abe. J. Power Sources 49 (1994) 315-32.

[98] K.L. Choy. Prog. Mater. Sci. 48 (2003) 57-170.

[99] N. Sakai, S. Stùlen. J. Chem. Thermodyn. 27 (1995) 493-506.

[100] H. Hayashi, M. Watanabe, H. Inaba. Thermochimica Acta 359 (2000) 77-85.

[101] K. Oikawa, T. Kamiyama, T. Hashimoto, Y. Shimojyo, Y. Morii. J. Solid State Chem. 154 (2000) 524-29.

[102] T. Hashimotoa, N. Tsuzukia, A. Kishib, K. Takagic, K. Tsudac, M. Tanaka, K. Oikawa, K. Kamiyama, K. Yoshida, H. Tagawa, M. Dokiya. Solid State Ionics 132 (2000) 183-90.

[103] Y.S. Malghe, S.R. Dharwadkar, K. Krishnan, K.D.S Mudher. J. Thermal Anal. Calorimetry 95 (2009) 49-52.

[104] N.M. Sammes, R. Ratanaraj. J. Mater. Sci. 29 (1994) 4319-24.

[105] H. Hayashi, M. Watanabe, M. Ohuchida, H. Inaba, Y. Hiei, T. Yamamoto, M. Mori. Solid State Ionics 144 (2001) 301-13.

[106] N. Sakai, H. Fjellvâg, B.C. Hauback. J. Solid State Chem. 121 (1996) 202-13.

[107] R.D. Shannon. Acta Crystallogr. 32 A (1976) 751-767.

[108] H. E. Hoefer, W. F. Kock, J. Electrochem. Soc. 140 (1993) 2889.

[109] S. Tao and J. T. S. Irvine, Chem. Mater. 18 (2006) 5453-5460.

[110] N.M. Sammes, R. Ratnaraj. J. Mater. Sci. 30 (1995) 4523-26.

[111] T.R. Armstrong, J.W. Stevenson, L.R. Pederson, P.E. Raney. J. Electrochem. Soc. 143 (1996) 2919-25.

[112] M. Mori, Y. Hiei, T. Yamamoto. J. Am. Ceram. Soc. 84 (2001) 781-86.

[113] S. Gupta, M.K. Mahapatra, P. Singh. Mat. Res. Bull. 48 (2013) 3262-67.

[114] M. Mori, Y. Hiei, N.M. Sammes. Solid State Ionics 135 (2000) 743-48.

[115] M. Mori, Y. Hieia, N.M. Sammes. Solid State Ionics 123 (1999) 103-11.

[116] J. Sfeir. J. Power Sources 118 (2003) 276-85.

[117] H.C. Grahm, H.H. Davis. J. Am. Ceram. Soc. 54 (1971) 89-93.

[118] D.B. Meadowcroft, J.M. Wimmer. Am. Ceram. Soc. Bull. 58 (1979) 610.

[119] H. Yokokawa, N. Sakai, T. Kawada, M. Dokiya. J. Electrochem. Soc. 138 (1991) 1018-27.

[120] T. Wei, X. Liu, C. Yuan, Q. Gao, X. Xin, S. Wang. J. Power Sources 250 (2014) 152-159.

[121] R.M. German, P. Suri, S.J. Park. J. Mater. Sci. 44 (2009) 1-39.

[122] S. Simner, J. Hardy, J. Stevenson, T. Armstrong. J. Mater. Sci. 34 (1999) 5721-32.

[123] S. Simner, J. Hardy, J. Stevenson, T. Armstrong. J. Mater. Sci. 19 (2000) 863-865.

[124] L.A. Chick, J. Liu, J.W. Stevenson, T.R. Armstrong, D.E McCready. J. Am. Ceram. Soc. 80 (1997) 2109-20.

[125] B.F. Flandermeyer, M.M. Nasrallah, D.M. Sparlin, H.U. Anderson. High Temp. Sci. 20 (1985) 265.

[126] S.P. Simner, J.S. Hardy, J.W. Stevenson. J. Electrochem. Soc. 148 (2001) A351-60.

[127] S.P. Simner, J.S. Hardy, J.W. Stevenson, T.R. Armstrong, in: S.C. Singhal and M. Dokiya (Eds.), The Electrochemical Society Proceedings Series - SOFC-VI, Pennington, NJ, 1999.

[128] J.D. Carter, M.M. Nasrallah, H.U. Anderson. J. Mater. Sci. 31 (1996) 157-163.

[129] X. Ding, Y. Liu, L. Gao, L. Guo. J. Alloys Comp. 425 (2006) 318-322.

[130] K. Homma, F. Nakamura, N. Ohba, A.M. Sui, T. Hashimoto. J. Ceram. Soc. Japan 115 (2007) 81-84.

[131] A. Ruangvittayanon, S. Kuharuangrong. Suranaree J. Sci. Tech. 16 (2009) 319-323.

[132] G.M. Christie, P.H. Middleton, BCH Steele. J. Euro. Ceram. Soc. 14 (1994) 163-75.

[133] R. Koc, H.U. Anderson. J. Mater. Sci. 27 (1992) 5837-43.

[134] M. Mori, T. Yamamoto, H. Itoh, T. Watanabe. J. Mater. Sci. 32 (1997) 2423-31.

[135] J.B. Ong, M. Sayer, A. Mansingh. Can. J. Phys. 55 (1977) 1725-31.

[136] H.R.L. Martijn, J.M.B. Henny, V. Henk. J. Am. Ceram. Soc. 80 (1997) 2175-98.

[137] S. Stølen, E. Bakkenw, C.E. Mohn. Phys. Chem. Chem. Phys. 8 (2006) 429-47.

[138] M. Oishi, K. Yashiro, J.O. Hong, Y. Nigara, T. Kawada, J. Mizusaki. Solid State Ionics 178 (2007) 307-12.

[139] J. Mizusaki, S. Yamauchi, K. Fueki, A. Ishikawa. Solid State Ionics 12 (1984) 119-24.

[140] S. Onumaa, K. Yashiroa, S. Miyoshia, A. Kaimaia, H. Matsumotoa, Y. Nigaraa, T. Kawadaa, J. Mizusakia, K. Kawamurab, N. Sakaic, H. Yokokawa. Solid State Ionics 174 (2004) 287-93.

[141] M. Oishi, K. Yashiro, K. Sato, J. Mizusaki, T. Kawada. J. Solid State Chem. 181 (2008) 3177-84.

[142] I. Yasuda, T. Hikita. J. Electrochem. Soc. 140 (1993) 1699-704.

[143] W.L. Huang, Q. Zhu, W. Ge, H. Li. Comp. Mater. Sci. 50 (2011) 1800-05.

[144] S. Tanasescu, A. Orasanu, D. Berger, I. Jitaru, J. Schoonman. Int. J. Thermophysics 26 (2005) 543-557.

[145] J. Mizusaki, M. Hasegawa, K. Yashiro, H. Matsumoto, T. Kawada. Solid State Ionics 177 (2006) 1925-28.

[146] A. Zuev, L. Singheiser, K. Hilpert. Solid State Ionics 147 (2002) 1-11.

[147] K. Hilpert, R.W. Steinbrech, F. Boroomand, E. Wessel, F. Meschke, A. Zuev, O. Teller, H. Nickel, L. Singheiser. J. Euro. Ceram. Soc. 23 (2003) 3009-20.

[148] V. Vashooka, L. Vasylechkob, J. Zoselc, W. Grunerd, H. Ullmanna, U. Gutha. J. Solid State Chem. 177 (2004) 3784-94.

[149] S. Tao, J.T.S. Irvine. J. Electrochem. Soc. 151 (2004) A252-59.

[150] A. Atkinson, T.M.G.M Ramos. Solid State Ionics 129 (2000) 259-69.

[151] L. Deleebeeck, J.L. Fournier, V. Birss. Solid State Ionics 181 (2010) 1229-37.

[152] S. Miyoshi, J.O. Hong, K. Yashiro, A. Kaimai, Y. Nigara, K. Kawamura, T. Kawada, J. Mizusaki. Solid State Ionics 161 (2003) 209-217.

[153] SM Kelly. Recovery Act: oxy-combustion: oxygen transport membrane development DOE Presentation, http://www.netl.doe.gov/publications/proceedings/11/co2capture/presentations/3-Wednesday/24Aug11-Kelly-Praxair-OTM%20Development.pdf.

[154] N. Nagabhushana, J.A. Lane, G.M. Christie, B.A.V. Hassel. US Patent 7556676B2, 2009.

[155] A. Atkinson, B. Sun. Mater. Sci. Tech. 23 (2007) 1135-43.

[156] M.K. Mahapatra, K. Lu. Mater. Sci. Eng. R 67 (2010) 65-85.

[157] M.K. Mahapatra, K. Lu. J. Power Sources 195 (2010) 7129-39.

[158] M. Mori, T. Yamamoto, H. Itoh, H. Inaba, H. Tagawa. J. Electrochem. Soc. 145 (1998) 1374-81.

[159] A. Bieberle, L.J. Gauckler, in: H. Tuller, J. Schoonman, I. Riess (Eds.), Kluwer Academic Publishers, Dordrecht, 2000.

[160] D. Leea, I. Leea I, Y. Jeona, R. Songb. Solid State Ionics 176 (2005) 1021-25.

[161] H.J. Ko, J.J. Lee, S.H. Hyun. Solid State Lett. 13 (2010) B113-15.

[162] M. Filal, C. Petot, M. Mokchah, C. Chateau, J.L. Carpentier. Solid State Ionics 80 (1995) 27-35.

[163] V.V. Srdić, R.P. Omorjan. Ceram. Int. 27 (2001) 859-63.

[164] M.D. Mathews, B.R. Ambekar, A.K. Tyagi. Thermochimica Acta 309 (2002) 61-6.

[165] M.E. Hofer, W.F. Kock. J. Electrochem. Soc. 140 (1993) 2889-94.

[166] D.M. Bastidas, S. Tao, J.T.S. Irvine. J. Mater. Chem. 16 (2006) 1603.

[167] K.P. Ong, P. Wua. Appl. Phys. Lett. 90 (2007) 044109.

[168] W.Z. Zhu, S.C. Deevi. Mater. Sci. Eng. A 348 (2003) 227-43.

[169] S. Srilomsak, D.P. Schilling, H.U. Anderson. Ed. S.C. Singhal. Electrochemical Society, Pennington, NJ, 1989.

[170] K. Mori, H. Miyamoto, K. Takenobu, T. Matsudaira, in: B. Thorstensen, U. Bossel (Eds.), Proceedings of 2nd European Solid Oxide Fuel Cell Forum, Oslo, Norway, 1996.

[171] I. Yasuda, M. Hishinuma. Electrochem. 68 (2000) 526-30.

[172] K.J. Yoon, C.N. Cramer, J.W. Stevenson, O.A. Marina. Electrochem. Solid State Lett. 13 (2010) B101-05.

[173] K. Hilpert, R.W. Steinbrech, F. Boroomand, E. Wessel, F. Meschke, A. Zuev, O. Teller. J. Euro. Ceram. Soc. 23 (2003) 3009-20.

[174] S.P. Jiang, X.J. Chen, S.H. Chan, J.T. Kwok, K.A. Khor. Solid State Ionics 177 (2006) 149-57.

[175] S. He, H. Chen, R. Li, L. Ge, L. Guo, J. Power Sources 253 (2014) 187-192.

[176] J. Mizusaki, Y. Mima, S. Yamauchi, K. Fueki, H. Tagawa. J. Solid State Chem. 80 (1989) 102.

[178] D.P. Karim, A.T. Aldred. Phys. Rev. B 20 (1979) 2255-63.

[179] G.P. Triberis, M. Dimakogianni. J. Phys. Condens. Matter 21 (2009) 385406.

[180] W.Y. Howng, R.J. Thorn. J. Phys. Chem. Solids 41 (1980) 75-81.

[181] D.B. Meadowcroft. Brit. J. Appl. Phys. 2 (1969) 1225-33.

[182] S.P. Jiang, L. Liua, K.P. Ong, P. Wu, J. Li, J. Puc. J. Power Sources 176 (2008) 82-89.

[183] P.S. Devi, S.M. Rao. J. Solid State Chem. 98 (1992) 237-44.

[184] S. Mukherjee, M.R. Gonal, M.K. Patel, M. Roy, A. Patra, A.K. Tyagi. J. Am. Ceram. Soc. 95 (2012) 290-95.

[185] J. Mizusaki, M. Yoshihiro, S. Yamauchi, K. Fueki. J. Solid State Chem. 58 (1985) 257.

[186] H. Xiong, G.J. Zhang, J.Y. Zheng, Y.Q. Jia. Mater. Lett. 51 (2001) 61-67.

[187] G.J. Zhang, Y.R. Chen, R. Li, Y.Q. Jia, M.L. Liu, M.J. Jin. Mater. Chem. Phys. 63 (2000) 178-82.

[188] K.R. Poeppelmeier, M.E. Leonowicz, J.M. Longo. J. Solid State Chem. 44 (1982) 89-98.

[189] S. Tao, J.T.S. Irvine. Nature Mater. 2 (2003) 320-23.

[190] S. Zha, P. Tsang, Z. Cheng, M. Liu. J. Solid State Chem. 178 (2005) 1844-50.

[191] S. Tao, J.T.S. Irvine, J.A. Kilner. Adv. Mater. 17 (2005) 1734.

[181] S.P. Jiang, X.J. Chen, S.H. Chan, J.T. Kwok, K.A. Khor. Solid State Ionics 177 (2006) 177-149.

[192] K. Sasaki, J.P. Wurtz, R. Gschwend, M. Gödickemeier, L.J. Gauckler. J. Electrochem. Soc. 143 (1996) 143-530.

[193] S.W. Paulik, S. Baskaran, T.R. Armstrong. J. Mater. Sci. 33 (1998) 2397-404.

[194] Y.P. Fu, H.C. Wang. Int. J. Hydrogen Energy 36 (2011) 747-54.

[195] A. Atkinson, A. Selc. Solid State Ionics 134 (2000) 59-66.

[196] W. Acchar, C.R.C. Sousa, S.R.H. Mello-Castanho. Mater. Sci. Eng. A 550 (2012) 76-79.

[197] N. Nagendra, S. Bandopadhyay. J. Euro. Ceram. Soc. 23 (2003) 1361-68.

[198] N. Orlovskava, K. Kleveland, T. Grande, M.A. Einarsrud. J. Euro. Ceram. Soc. 20 (2000) 51-56.

[199] J.D. Carter, P.V. Hendriksen, M. Mogensen, Materials Department, Riso National Laboratory, Denmark, 1995.

[200] D.S. Smith, A. Smith. J. Mater. Sci. Lett. 5 (1986) 349-52.

[201] B.N. Sørensen, A. Horsewell. J. Am. Ceram. Soc. 84 (2001) 2051-59.

[202] B.N. Nguyen, B.J. Koeppel, S. Ahzi, M.A. Khaleel, P. Singh. J. Am. Ceram. Soc. 89 (2006) 1358-68.

[203] J. Sunarso, S. Baumann, J.M. Serra, W.A. Meulenberg, S. Liu, Y.S. Lind, J.C.D. Costa. J. Mem. Sci. 320 (2008) 13-41.

[204] Y.S. Lin, W. Wand, J. Han. AlChE J. 40 (1994) 786-98.

[205] D. Huiming, Z. Minyau, A. Benjamin. Solid State Ionics 74 (1994) 75-84.

[206] K. Zhang, J. Sunarso, Z. Shao, W. Zhou, C. Sun, S. Wanga, S. Liu. RSC Adv. 1 (2011) 1661-76.

[207] N. Sakai, T. Horita, H. Yokokawa, M. Dokiya, T. Kawada. Solid State Ionics 86-88 (1996) 1273-78.

[208] B.A. Van Hassel, T. Kawada, N. Sakai, H. Yokokawa, M. Dokiya. Solid State Ionics 66 (1993) 41-47.

[209] B.A. Van Hassel, T. Kawada, N. Sakai, H. Yokokawa, M. Dokiya. Solid State Ionics 66 (1993) 295-305.

[210] T. Kawada, T. Horita, N. Sakai, N. Yokokawa, M. Dokiya. Solid State Ionics 79 (1995) 201-7.

[211] D.K. Lee, H.I. Yoo. J. Electrochem. Soc. 147 (2000) 2835-43.

[212] N. Sakai, K. Yamaji, T. Horita, H. Yokokawa, T. Kawada, M. Dokiya, K.I. Hiwatashi, A. Ueno, M. Aizawad. J. Electrochem. Soc. 146 (1999) 1341-45.

[213] A.A. Yaremchenko, V.V. Kharton, V.A. Kolotygin, M.V. Patrakeev, E.V. Tsipis, J.C. Waerenborgh. J. Power Sources 249 (2014) 483-496.

[214] X. Tan, Y. Liu, K. Li. Ind. Eng. Chem. Res. 44 (2005) 61-66.

[215] Z. Taheri, K. Nazari, N. Seyed-Matin, A.A. Safekordi, B. Ghanbari, S. Zarrinpashne, R. Ahmadi. Reac. Kinet. Mech. Cat. 100 (2010) 459-469.

[216] A.A. Yaremchenko, V.V. Kharton, A.L. Shaula, M.V. Patrakeev, F.M.B. Marques. J. European Ceramic Society 25 (2005) 2603-2607.

[217] F.S. Küppers, S. Baumann, F. Tietz, H.J.M. Bouwmeester, W.A. Meulenberg. J. European Ceramic Society 34 (2014) 3741-3748.

[218] X. Tan, L. Shi, G. Hao, B. Meng, S. Liu. Sep. Purif. Tech. 96 (2012) 89-97.

[219] L.M. van der Haar. Universiteit Twente. Thesis, 2001, Chapter 2, pp. 23.

[220] J. Yi, Y. Zuo, W. Liu, L. Winnubst, C. Chen. J. Mem. Sci. 280 (2006) 849-855.

[221] T.F. Tian, W. Li, T. Liu, C.S. Chen. Solid State Ionics 225 (2012) 690-694.

[222] W. Li, J.J. Liu, C.S. Chen. J. Mem. Sci. 340 (2009) 266-271.

[223] W. Fang, Y. Zhang, J. Gao, C. Chen. Ceramics International 40 (2014) 799-803.

[224] J.H. Joo, G.S. Park, C.Y. Yoo, J.H. Yu. Solid State Ionics 253 (2013) 64-69
.
[225] T. Zhu, Z. Yang, M. Han. J. Mater. Sci. Technol. (2014) 1-5.

[226] F. Wang, M. Nishi, M. E. Brito, H. Kishimoto, K. Yamaji, H. Yokokawa, T. Horita, J. Power Sources 258 (2014) 281-289.

[227] E. Ivers-Tiffée, A. Weber, D. Herbstritt. J. Euro. Ceram. Soc. 21 (2001) 1805-11.

[228] E. Povoden, M. Chen, A.N. Grundy, T. Ivas, L.J. Gauckler. J. Phase Equil. Diff. 30 (2009) 12-27.

[229] S.A. Suvorov, A.P. Shevchik. Refractories and Industrial Ceramics 45 (2004) 94-99.

[230] D.H. Peck, M. Miller, D. Kobertz, H. Nickel, K. Hilpert. J. Am. Ceram. Soc. 79 (1996) 3266-72.

[231] K.T. Jacob, S. Gupta, P. Singh. J. Am. Ceram. Soc. 96 (2013) 3933-38.

[232] S. Miyoshi, S. Onuma, A. Kaimai, H. Matsumoto, K. Yashiro, T. Kawada, J. Mizusaki, H. Yokokaw. J. Solid State Chem. 177 (2004) 4112-18.

[233] D.H. Peck, M. Miller, K. Hilpert. Solid State Ionics 123 (1999) 59-65.

[234] D.H. Peck, M. Miller, K. Hilpert. Solid State Ionics 123 (1999) 47-57.

[235] S. Onuma, S. Miyoshi, K. Yashiro, A. Kaimai, K. Kawamura, Y. Nigara, T. Kawada, J. Mizusaki, N. Sakai, H. Yokokawa. J. Solid State Chem. 170 (2003) 68-74.

[236] H. Yokokawah, T. Horitaa, N. Sakaia, T. Kawadaa, M. Dokiyaa, Y. Takaib, M. Todokib. Thermochim. Acta 267 (1995) 129-138.

[237] G.M. Christie, P.H. Middleton, B.C.H. Steele. J. Euro. Ceram. Soc. 14 (1994) 163-75.

[238] J. Sfeir, P.A. Buffat, P.M. Ckli, N. Xanthopoulos, R. Vasquez, H.J. Mathieu, J.V. Herle, K.R. Thampi. J. Catal. 202 (2001) 229-44.

[239] J. Sfeir, J.V. Herle, A.J. McEvoy. J. Euro. Ceram. Soc. 19 (1999) 897-902.

[240] K. Rida, A. Benabbas, F. Bouremmad, M.A. Peńa, A. Martínez-Arias. Catal. Commun. 7 (2006) 963-68.

[241] A.K. Huber, M. Falk, M. Rohnke, B.G.L. Luerben, M. Amatib, J. Janek. Phys. Chem. Chem. Phys. 14 (2012) 751-58.

[242] M. Oishi, K. Yashiro, J.O. Hong, Y. Nigara, T. Kawada, J. Mizusaki. Solid State Ionics 178 (2007) 307-12.

[243] G. Horvath, J. Gerblinger, H. Meixner, J. Giber. Sensors Actuators B 32 (1996) 93-99.

[244] T.T. Fister, D.D. Fong, J.A. Eastman, P.M. Baldo, M.J. Highland, P.H. Fuoss, K.R. Balasubramaniam, J.C. Meador, P.A. Salvador. Appl. Phys. Lett. 93 (2008) 151904.

[245] J.D. Carter, C.C. Appel, M. Mogensen. J. Solid State Chem. 122 (1996) 407-15.

[246] M.K. Mahapatra, S. Bhowmick, N. Li, P. Singh. J. Euro. Ceram. Soc. 32 (2012) 2341-49.

[247] M. Keane, M.K. Mahapatra, A. Verma, P. Singh. Int. J. Hyd. Energy 37 (2012) 16776 -85.

[248] N. Li, M.K. Mahapatra, P. Singh. J. Power Sources 221 (2013) 57-63.

[249] P. Singh, S.D. Vora. Ceram. Eng. Sci. Proc. 26 (2005) 99-110.

CHAPTER 2: PHASE TRANSFORMATION, ELECTRICAL CONDUCTIVITY AND THERMAL EXPANSION OF LANTHANUM CHROMITE

2.1. Abstract

This paper addresses discrepancies pertaining to structural, thermal and electrical properties of lanthanum chromite. Experimental evidence is provided to support the hypothesis for poor densification in air as well as reduction in electrical conductivity in reducing atmosphere. Sintering condition for the synthesis of $LaCrO_3$ was optimized to 1450°C and 10h. Thermo-analytical (Differential scanning calorimetry - DSC) and high temperature X-ray diffraction (HT-XRD) studies show that orthorhombic lanthanum chromite transforms into rhombohedral structure at ~260°C and cubic structure above 1000°C. Co-existence of the structural phases and the variation in each polymorph with temperature in both air and 3%H_2-Ar atmosphere is reported. Presence and absence of Cr-rich phase at inter-particle neck are observed in oxidizing and reducing atmospheres respectively. The thermal expansion co-efficient was calculated to be 10.8±0.2 $\times 10^{-6}$/°C in the temperature range of RT-1400°C. Electrical conductivity of lanthanum chromite was found to be 0.11 S/cm in air. A decrease in electrical conductivity (0.02 S/cm at 800°C) of $LaCrO_3$, as observed in reducing atmosphere (3%H_2-Ar), corresponds to lattice volume change as indicated by peak shift in HT-XRD results.

2.2. Introduction

Lanthanum chromite ($LaCrO_3$) based perovskite oxides have been proposed for use as electrode materials in magnetohydrodynamic (MHD) power generators [1], oxygen sensors [2], and heating element in high temperature furnaces [3]. They have also been considered as

electrodes and interconnect materials in solid oxide fuel cells [4], and as oxygen transport membrane for air separation and oxy-fuel combustion with negligible greenhouse gas emission [5]. The diverse application of $LaCrO_3$ is attributed to its high melting point of ~2510ºC [6], good electrical conductivity of ~0.1 S/cm at 800ºC [7] and stability in both oxidizing (P_{O_2} = 0.21 atm) and reducing atmospheres (P_{O_2} = 10^{-22} atm) at 1000°C [8]. Optimization of the required properties, for specific applications, can be accomplished by doping of $LaCrO_3$ by alkaline earth metals (Sr, Ca) at A-site and transition metals at B-site (Mn, Ni, Fe, Co) [9].

Discrepancies in the structure and properties of undoped lanthanum chromite have been reported in the literature. Koehler et al. [10] have reported the anti-ferromagnetic to paramagnetic transition temperature for lanthanum chromite to be 47°C which is in disagreement with that of 14°C [11] and 27°C [12]. Various characterization methods used in these studies may be the reason of the variation in magnetic transition temperature [10-13]. $LaCrO_3$ has orthorhombic crystal structure at room temperature and rhombohedral at ~ 260 °C [11, 13, 14]. On the other hand, Oikawa et al. [15] reports the coexistence of orthorhombic and rhombohedral phase at the same transition temperature. It is also reported that the $LaCrO_3$ transforms to cubic structure at ≥1600°C [16-18]. In contrast, Momin et al. [19] found the cubic transition to be at 1027°C. The relative density of $LaCrO_3$ was reported to be ~50% at 1600°C [20, 21] and ~64 % at 1700°C when sintered in air [22]. It was proposed that the formation of CrO_3 volatile specie above 1000°C [23] and its condensation as Cr_2O_3 at the interparticle necks [24] during sintering results in the lower density of $LaCrO_3$. These studies, however, do not provide the evidence of Cr_2O_3 deposition in the microstructure. The volume expansion coefficient was reported to be 19.7×10^{-6} (25-267°C),

20.2 × 10^{-6} (277-1007°C), and 82.4 × 10^{-6}/°C (1027-1327°C), for the orthorhombic, hexagonal (rhombohedral) and cubic phases, respectively [19]. The same is obtained as 22.8 × 10^{-6}/°C (22-260°C) and 28.4 × 10^{-6}/ °C (260-740°C) for the orthorhombic and rhombohedral phases, respectively.[15] The thermal expansion coefficient of $LaCrO_3$ was measured to be 7.7 × 10^{-6}/°C, and 7.3 × 10^{-6} /°C, in the temperature range of -173-247°C and 257-867°C respectively, [25] in disagreement with the values of 4.6 × 10^{-6} /°C in 40-274°C temperature range and 9.4 × 10^{-6} /°C in 290-1052°C [18]. Electrical conductivity of $LaCrO_3$ is reported to be 0.1 S/cm at 800°C [7]. Ong et al. [26] found the conductivity as high as 0.34 S/cm at same temperature. These discrepancies can be attributed to the (a) sintering temperature and time as it can change the density of $LaCrO_3$, (b) La: Cr ratio due to evaporation and condensation of chromium vapor species and, (c) the amount of porosity that can affect the electrical conductivity. The different property measurement techniques can also result in discrepancy. Furthermore, experimental techniques involving the equilibration time for attaining uniform temperature and controlled environment can also affect the various property values.

Considering the above reasons for the causes of variation in the physical properties of $LaCrO_3$, this paper further investigates the structural changes and properties of $LaCrO_3$ using *in-operando* and *in-situ* characterization techniques. The possible reasons for the discrepancies in the reported literature are addressed by comparing the results of this study. Although the physical properties change with exposed atmosphere, the corresponding change in structure is not found in public domain as per author's knowledge. Accordingly, the change in structure and its relation to the electrical property has also been investigated with respect to exposed atmospheres.

2.3. Experimental

2.3.1. *$LaCrO_3$ synthesis*

$LaCrO_3$ was synthesized using lanthanum oxide (La_2O_3, 99.95%, Alfa Aesar, USA) and chromium oxide (Cr_2O_3, 99.9%, Sigma-Aldrich, USA) powders by solid state reaction technique. La_2O_3 and Cr_2O_3 powders were mixed using wet-ball milling in ethanol for 24h. After drying in air, the mixed powders were uniaxially pressed into cylindrical pellets at 287 MPa. Several sintering experiments were conducted in 1300-1650°C for period ranging from 5-24 h for the optimization of $LaCrO_3$ stoichiometry. X-ray diffraction (BRUKER-D8 ADVANCE, Bruker AXS Inc. Madison, WI) and energy dispersive spectroscopy (EDS) attached to scanning electron microscope (FEI - ESEM Quanta 250, Hillsboro, OH) techniques were used to identify the single phase $LaCrO_3$ and La: Cr ratio of the sintered samples to optimize sintering condition. An optimized sintering condition of 1450°C with 10 h dwell time was selected. The overall stoichiometry (La: Cr ratio = 1:1) was also confirmed by inductively coupled plasma (ICP) mass spectroscopy.

2.3.2. *Characterization*

The phase transition temperatures of $LaCrO_3$ were determined using differential scanning calorimeters (DSC; DSCQ100-TA for -80-350°C temperature range and STDQ600-TA for 100-1500°C range; TA Instruments, OH, USA) with 20°C/min heating rate. The same amount of $LaCrO_3$ powder (~10 mg) was used for both the DSC studies. The heat of transformation required for each phase transition was calculated using TA Instruments Universal Analysis 2000 software.

High temperature XRD (HT-XRD) studies of $LaCrO_3$ powder were performed in RT-1200^oC temperature range both in air and reducing gas atmosphere (3%H_2-Ar) to identify the change in crystal structure with temperature and exposed atmospheres. The heating and cooling rate of 5°C/min was used during the experiment with the holding time of 48 h at 1200°C and 1 h at remaining temperatures. The scan step was 0.02° using CuK_α radiation (λ = 1.5406 Å). The amount of different polymorphs of $LaCrO_3$ was calculated semi-quantitatively using ratio of intensity sum of the corresponding phase to that of all the phases.

A cylindrical bar (0.56cm × 0.33cm × 0.17cm) was cut from the sintered pellet to evaluate the thermal expansion coefficient (TEC) of the $LaCrO_3$ using dilatometer (NETZSCH - DIL 402 PC, NETZSCH Instruments, and Burlington, USA). The TEC measurement was carried out in the temperature range of RT-1400^oC in air with a heating rate of 3°C/min. Prior to the actual measurement; the dilatometer was calibrated using alumina (Al_2O_3) standard.

A thin cylindrical bar (0.56cm × 0.33cm × 0.17cm) was cut from the sintered pellet to determine the electrical conductivity of $LaCrO_3$ using standard four-probe DC technique in 100-1000°C in air and reducing gas atmosphere (3%H_2-Ar). The heating and cooling rates were 3°C/min. At least 30 minutes was elapsed to stabilize the temperature before collecting the data. Also, minimum of 4 days was provided at 950°C for the equilibration of 3% H_2-Ar gas atmosphere. The reliability of the experiment was initially confirmed by measuring the conductivity of well-studied YSZ.

Microstructure was investigated for sintered $LaCrO_3$ by scanning electron microscope. The sample used for electrical conductivity measurement was also studied to identify the effect of reducing atmosphere on the microstructure.

2.4. Results and Discussion

2.4.1. *Phase transition and Crystal structure*

The DSC profiles obtained for sintered $LaCrO_3$ to identify the phase transition temperatures are shown in Fig. 2.1. Fig. 2.1a shows two endotherms at ~15°C and at ~260°C while Fig. 2.1b shows endotherms at ~260°C and ~1300°C corresponding to structural phase transition. The endotherm at ~15°C corresponds to a magnetic order-disorder transition of $LaCrO_3$ [11] because of changes in the spin orientation of Cr^{3+} ions [27] leading from anti-ferromagnetic to paramagnetic state. The endotherms at ~260°C and ~ 1300°C correspond to the change in crystal structure and will be discussed in the subsequent paragraph. The measured heat of transformation required for the magnetic transition and the polymorphic transformations are 0.635J/g at~15°C, 1.768J/g at ~260°C, and 728.2J/g at ~ 1300°C. The above transformations were observed at the same temperature during the subsequent cycles. This suggests the reproducibility and reversibility of the magnetic and structural transition. The magnetic transformation temperature is in agreement with those determined using thermo-analytical techniques [11,13] but in disagreement with 47°C [10] and 27°C [12] determined using static magnetic susceptibility and neutron diffraction technique respectively.

HT-XRD patterns of the $LaCrO_3$ at different temperatures (RT-1200°C) in air are shown in Fig. 2.2a. The change in the crystal structure at 260°C and 1000°C is observed

(corresponding XRD patterns are shown for brevity). From the XRD pattern, $LaCrO_3$ is determined to be

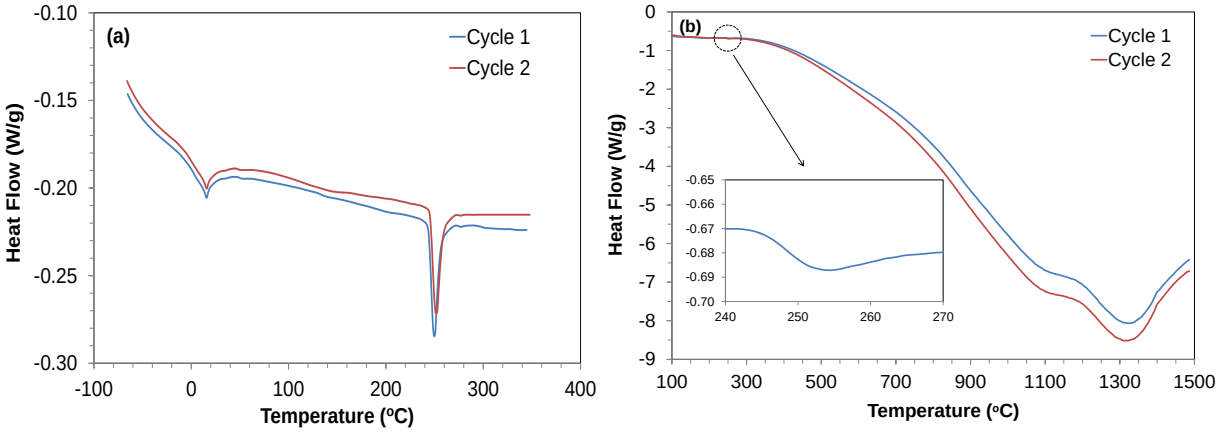

Fig. 2.1. DSC profiles of $LaCrO_3$: a) in -80°C to330°C range and b) in 100°C to1500°C

orthorhombic (JCPDS – 01-070-2694) at room temperature. The orthorhombic (O) structure changes to rhombohedral (JCPDS – 00-033-0702) at 260°C. This transition is marked by the disappearances of certain peaks (as indicated by asterisk in Fig. 2.2a) as well as peak splitting indicative of appearance of new polymorph in Fig. 2.2b. For example, the peak corresponding to $2\theta \rightarrow 32.5°$ splits at 260°C as shown in Fig. 2.2b, corresponding to rhombohedral (R) polymorph. It is also found that the $LaCrO_3$ coexists in both orthorhombic (~51%) and rhombohedral structure (~49%) at 260°C. With increase in temperature the splitted peaks start to combine at ~1000°C as shown in Fig 2.2b. Further merging of peaks at 1200°C (selected for brevity) indicates that the $LaCrO_3$ partially transforms into cubic (C) polymorph (JCPDS – 01-074-1961, Fig. 2.2b). The co-existence of orthorhombic (C) (~23%), rhombohedral (R) (~58%) and cubic (C) phase (~19%) was found at 1200ºC. With the temperature increase, the higher amount of cubic and rhombohedral polymorphs compare

to orthorhombic structure suggest that the orthorhombic polymorph is transforming into rhombohedral and cubic structure.

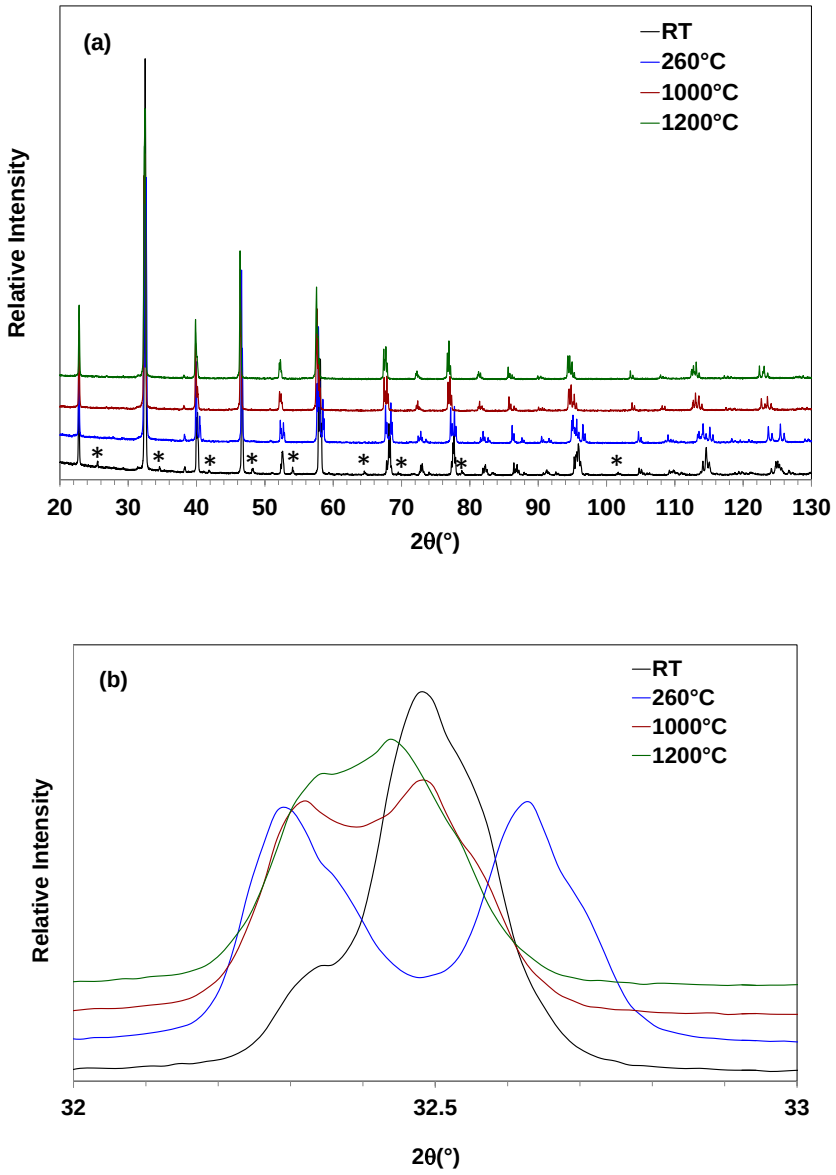

Fig. 2.2. (a) In-situ XRD patterns for undoped $LaCrO_3$ at RT, 260°C, 1000°C and 1200°C in air, (b) Magnified image of the HT-XRD for $LaCrO_3$ at RT, 260°C, 1000°C and 1200°C for 2θ = 32-33°

Similar XRD patterns features are observed in reducing gas atmosphere (3%H_2-Ar) as shown in Fig. 2.3a and b. The peak intensity, however, decreases in comparison with those in air as shown in Fig. 2.3b. Also, a slight peak shifting to the left is observed in reducing atmosphere. For instance, the peak corresponding to (042) plane at 58.13° appears at 58.09°

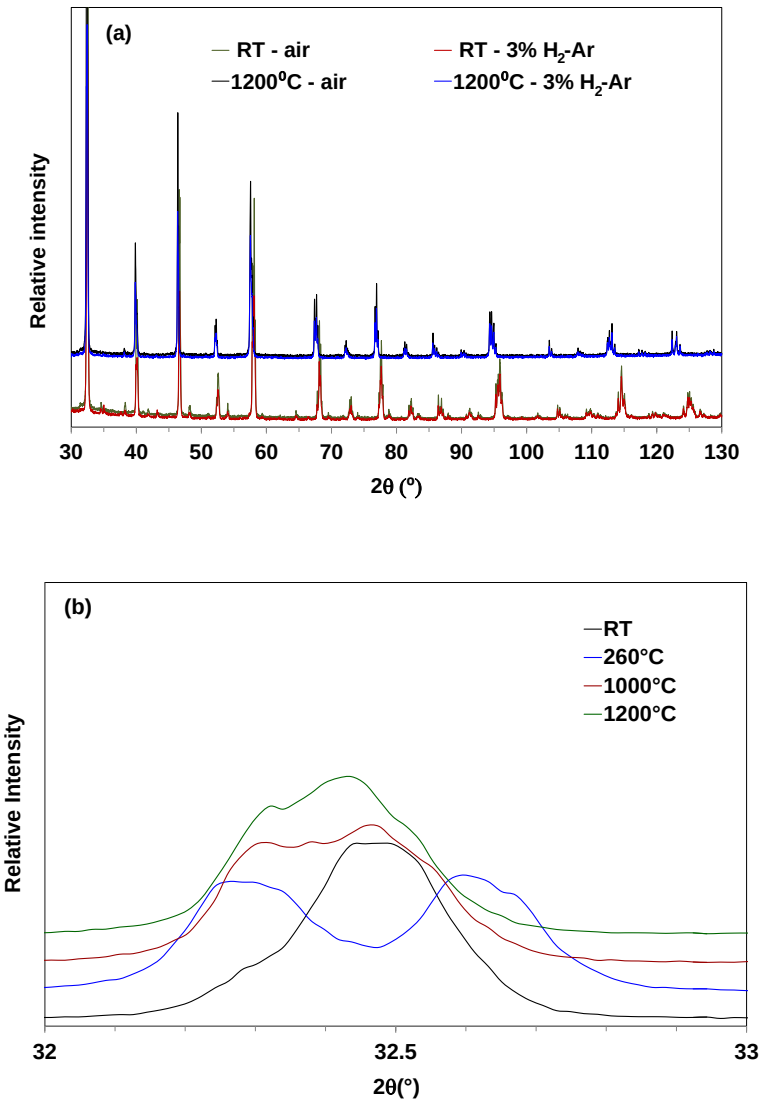

Fig. 2.3 (a) Comparison of HT-XRD patterns at RT and 1200°C in air and in reducing atmosphere (3% H_2-Ar) showing intensity variation. (b) Magnified image of the HT-XRD for

$LaCrO_3$ at RT, 260°C, 1000°C and 1200°C for 2θ = 32-33° in reducing atmosphere (3% H_2-Ar).

in reducing atmosphere as shown in Fig. 2.4 with the dotted lines. This suggests the increase in unit cell volume for the sample treated in 3%H_2-Ar and the values are given in Table 2.1. The change in lattice volume has not been calculated for the high temperatures due to limited accuracy in calculated phase quantity. The existence of Cr^{4+} ions in undoped $LaCrO_3$ is considered due to the inherent structural defects [28]. The change in lattice parameter is considered to be due to the change in valence state of Cr^{4+} to Cr^{3+} in reducing atmosphere which has bigger ionic radii ($r_{Cr^{3+}} > r_{Cr^{4+}}$). The calculated phase fraction of polymorphs (orthorhombic, rhombohedral and cubic) phase at different temperature in air and reducing atmosphere is shown in Fig. 2.5. Similar to air, the orthorhombic polymorph transforms into rhombohedral and cubic structure in reducing atmosphere.

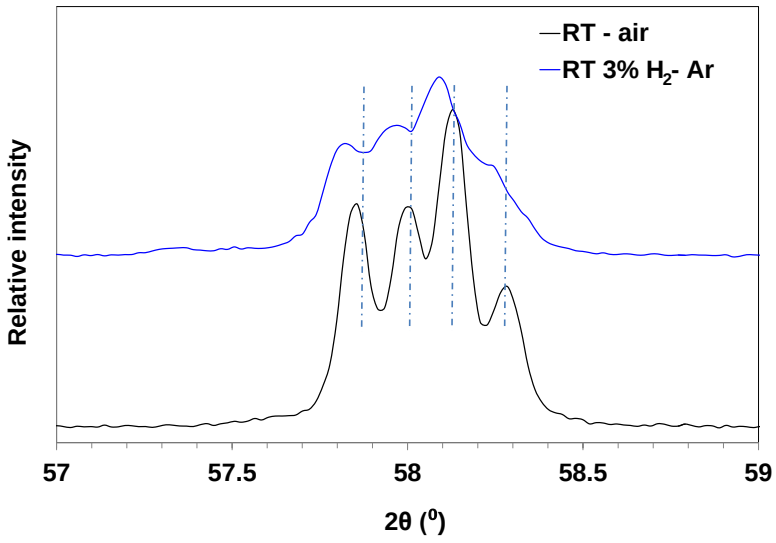

Fig. 2.4. Comparison of HT-XRD patterns showing peak shifting in reducing atmosphere (3% H_2-Ar) at RT.

The polymorphic transition temperatures obtained from HT-XRD are consistent with those found in DSC profiles (Fig. 2.1). The change in crystal structure corresponding to the endotherm at 1300°C was not determined due to the experimental limitation. The HT-XRD result confirms that the cubic transition initiates at ~1000°C and continues to 1200°C in agreement with Momin et al. [19] and Malghe et al. [29] but in disagreement with the transformation temperature ≥1600°C [16, 17, 18]. The DSC-endotherm at 1300°C is suggested to correspond to polymorphic transition to the cubic structure. The reversibility of the phase transition has also been confirmed by superimposing the XRD patterns during heating and cooling cycles (The patterns are not shown for brevity).

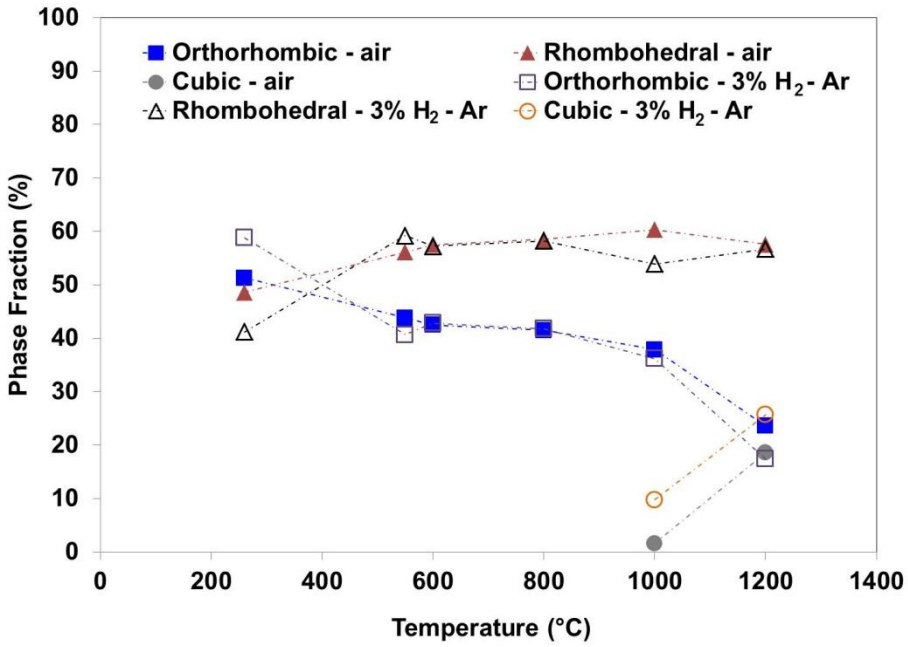

Fig. 2.5. Phase fraction (orthorhombic, rhombohedral and cubic) in the temperature range of RT-1200°C.

Table 2.1. Lattice parameters and unit cell volume of $LaCrO_3$ at room temperature in air and reducing atmosphere.

Composition ($LaCrO_3$)	a (Å)	b (Å)	c (Å)	Volume ($Å^3$)
Air	5.489±0.002	7.762±0.004	5.515±0.004	234.993±0.152
3%H_2-Ar	5.489±0.002	7.7676±0.003	5.5169±0.003	235.222±0.120

2.4.2. *Thermal expansion*

The thermal expansion of $LaCrO_3$, obtained from dilatometer, is shown in Fig. 2.6. A discontinuity at ~260°C is observed in the thermal expansion profile because of transformation from orthorhombic to rhombohedral structure, consistent with the DSC and HT-XRD results and in agreement with Sakai et al. [11] and Hayashi et al. [13]. Deviation from continuity in the thermal expansion curve, observed at ~ 1350°C, is consistent with DSC endotherm suggesting further change in crystal structure. It was found that the thermal expansion coefficients are 8.2±0.1/°C, 11.4±0.2/°C, and 7.3±1.4×10^{-6}/°C in the temperature range of RT-300°C, 300-1200°C and 1200-1400°C, respectively. The thermal expansion coefficient value is in close agreement with 7.7 × 10^{-6} /°C in the temperature range of -173-247°C [25]. A small variation can be attributed to the different temperature ranges considered in calculation. The results are in disagreement with 4.6×10^{-6} /°C in 40-274ºC temperature range.

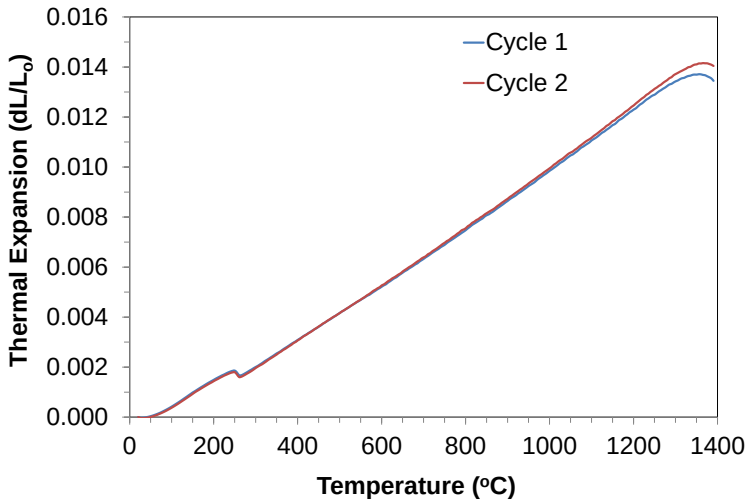

Fig. 2.6. Thermal expansion of $LaCrO_3$ from RT-1400ºC in air.

2.4.3. *Electrical conductivity*

The measured electrical conductivity is 0.11 S/cm at 800°C in agreement with 0.1 S/cm [7]. However, it decreases to 0.02 S/cm in Ar-3%H_2 atmosphere. This is considered to be due to the change in valence state of Cr^{4+} to Cr^{3+} during exposure to reducing gas atmosphere leading to reduction in the charge carrier concentration. This is also supported by an increase in lattice parameter in reducing atmosphere (Table 2.1). Fig. 2.7 shows the linear relationship between log σT and 1/T for electrical conductivity of $LaCrO_3$ in the temperature range of 100-1000°C in air and reducing gas (Ar-3%H_2) atmosphere. Reproducible results were obtained during both heating and cooling cycles. With increase in temperature, the conductivity increases due to increase in the lower thermal activated barrier. The above observation is consistent with the conductivity reported by Ruangvittayanon et al. [7] but in disagreement with Ong et al. [26]. The inset in the conductivity plot (Fig. 2.7) shows previously undocumented information related to the deviation from continuity at ~260°C

corresponding to the orthorhombic to rhombohedral transition of $LaCrO_3$. The activation energy was calculated to be 0.12eV and 0.34eV in air and reducing atmosphere (3%H_2-Ar).

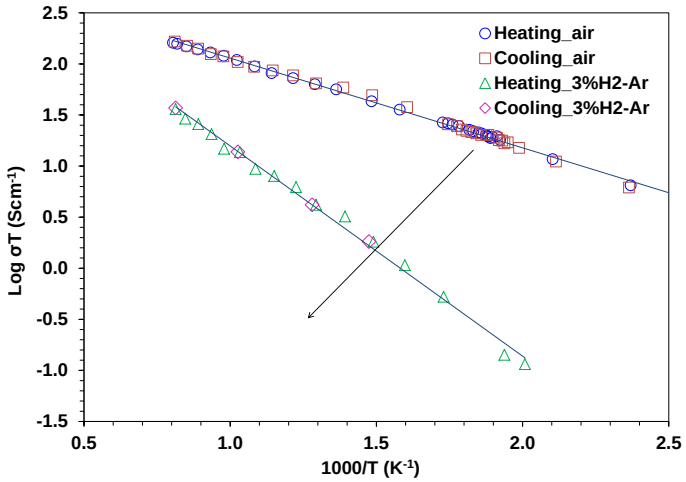

Fig. 2.7. Electrical conductivity of $LaCrO_3$ 100-1000°C in air and 3% H_2-Ar.

2.4.4. *Density and Microstructure*

The relative density of sintered $LaCrO_3$ pellet is ~52% in agreement with Mori et al. [21]. SEM images of the sintered $LaCrO_3$ show the porous microstructure (Fig. 2.9a). The grain size varies from 1.5 to 4.5µm with an average of 1.7 µm.

The observed lower density is attributed to chromium evaporation (CrO_3) as it is known to occur above 1000°C [23]. The vapor species of chromium evaporate from the bulk grains and condenses onto irregular contact (between grain boundaries) due to the surface energetics. As a result, the vapor species deposit as Cr_2O_3 at the particle necks and the neck growth continues without the mass-transport of the material from the bulk of the grains [30-32]. The Cr_2O_3 evaporation and condensation reactions are shown below [23]:

$$Cr_2O_3 + 3/2\ O_2 \rightarrow 2CrO_3\uparrow \text{ (evaporation)} \quad (1)$$

$2CrO_3\uparrow \rightarrow Cr_2O_3 + 3/2\ O_2$ (condensation) (2)

The chromia (Cr_2O_3) layer at the inter-particle neck inhibits further densification [30-32]. Based on EDS analysis, the deposition of chromium oxide is evident (La: Cr = 1 near the bulk surface, and La: Cr < 1 near the neck area) from the chromium enriched phase in the microstructures shown in Fig. 2.9b and c. After the electrical conductivity measurement in reducing gas atmosphere (Ar-3%H_2), microstructural analysis of the treated sample are shown in Figure 2.9d and e. The extensive surface rearrangement (compared to air) may attribute to the intensity decreases in the corresponding XRD pattern (Fig. 2.4) [33]. The samples also did not show the formation of chromium enriched phases.

This study provides experimental evidence to support the hypothesis for reduced densification in air and decreased electrical conductivity in reducing atmosphere for undoped $LaCrO_3$. Presence of chromium oxide in the microstructure (Fig. 2.8b and c) validates chromium oxide evaporation-condensation attributing to poor densification of $LaCrO_3$. Peak shift in the XRD pattern of $LaCrO_3$ in 3%H_2-Ar atmosphere confirms the change in the valence state of Cr^{4+} to Cr^{3+} resulting in lower electrical conductivity. HT-XRD patterns confirm the orthorhombic transformation to rhombohedral polymorph at ~ 260°C and to cubic polymorph at ~1000°C. Consistency of phase transformation temperatures has been confirmed by different complimentary techniques (DSC, Dilatometer, HT-XRD, and electrical conductivity).

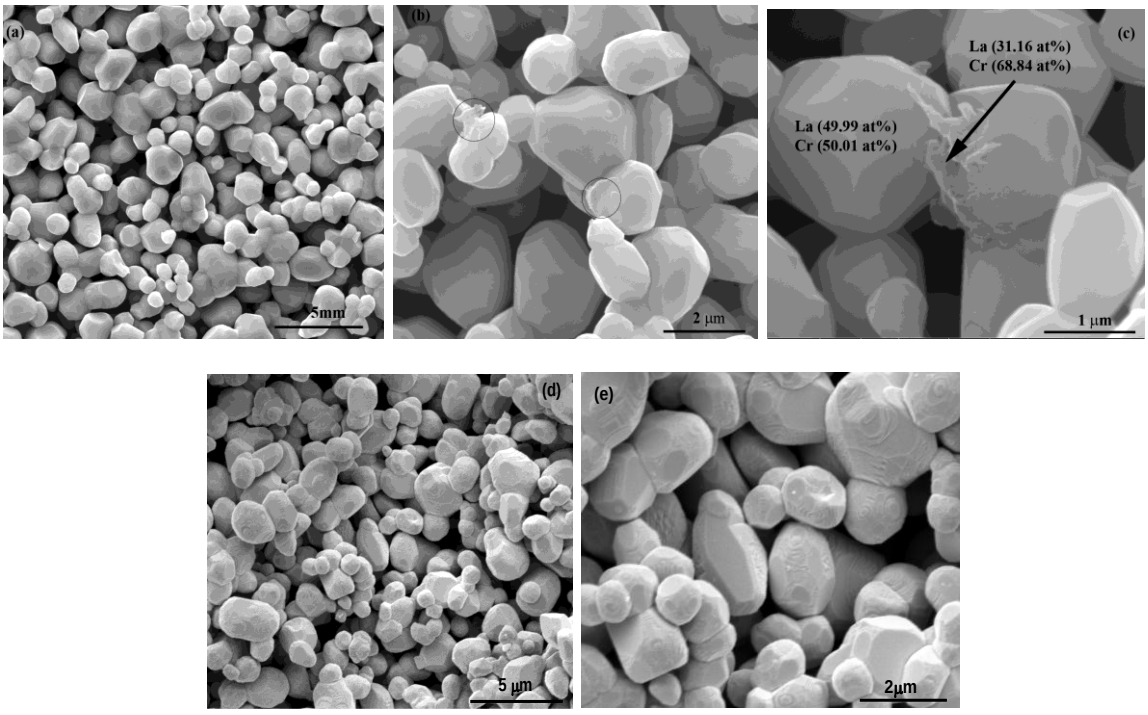

Fig. 2.8. SEM images of $LaCrO_3$: a) lower magnification–air, b) and c) higher magnifications–air, d) lower magnification–3% H_2-Ar, e) higher magnification–3% H_2-Ar.

2.5. Conclusions

$LaCrO_3$ has been synthesized and its structure and properties have been investigated in oxidizing (air) and reducing (3%H_2-Ar) atmospheres. Transition from orthorhombic to rhombohedral structure at 260°C has been confirmed by HT-XRD, DSC, dilatometer, and 4-probe DC conductivity studies. HT-XRD shows the coexistence of orthorhombic and rhombohedral phases at 260°C along with transformation to cubic phase above 1000°C. This study suggests that the disagreement in magnetic and polymorphic transition temperatures, as reported in literature, arises due to the use of different characterization techniques. Decrease in electrical conductivity in reducing atmosphere is corroborated to reduction of chromium ions in lanthanum chromite as supported by increase in lattice volume.

2.6. References

[1] J.B. Heywood, G.J. Womack: J.B. Heywood, G.J. Womack (Eds.), Open-Cycle MHD Power Generation. New York, 1969.

[2] S.M. Khetre, H.V. Jadhav, S.R. Bamane, Rasayan J. Chem. 2 (2009) 174-178.

[3] A.M. Azad, R. Sudha , O.M. Sreedharan, J. Less Common Metals 166 (1990) 57-62.

[4] J. Sfeir, J. Power Sources 118 (2003) 276-285.

[5] A.S. Mukasyan, C. Costello, K.P. Sherlock, D. Lafarga, A. Varma, Separation and purification technology 25 (2001) 117-126.

[6] R. Berjoan, Rev. Int. Hautes Temp. Refract 13 (1976) 119-35.

[7] A. Ruangvittayanon, S. Kuharuangrong, Suranaree J. Sci. Technol. 16 (2009) 319-323.

[8] T. Nakamura, G. Petzow, L. Gauckler, Mater. Res. Bull. 14 (1979) 649–659.

[9] X. Ding, Y. Liu, L. Gao, L. Guo, J. Alloys and Comp. 425 (2006) 318-322.

[10] W.C. Koehler, E.O. Wollan, J. Phys. Chem. Solids 2 (1957) 100-106.

[11] N. Sakai N, S. Stolen, J. Chem. Thermodyn. 27 (1995) 493-506.

[12] K.P. Bansal, S. Kumari, B.K. Das, G.C. Jain, J. Mater. Sci. 18 (1983) 2095-2100.

[13] H. Hayashi, M. Watanabe, H. Inaba, Thermochimica Acta. 359 (2000) 77-85.

[14] T. Hashimoto, K. Komazaki, S. Wang, Proceeding of the Institute of Natural Sciences, Nihon University 38 (2003) 265-276.

[15] K. Oikawa, T. Kamiyama, T. Hashimoto, Y. Shimojyo, and Y. Morii, J. Solid State Chemistry 154 (2000) 524-529.

[16] J. S. Ruiz, A. M. Anthony, and M. Foex, C.R. Acad. Sci. Paris B. 264 (1967) 1271.

[17] S. Geller, P.M. Raccah, Phys. Rev. B. 2 (1970) 1167.

[18] H.E. Hofer and W.F. Kock, J. Electrochem. Soc. 140 (1993) 2889-2894.

[19] A.C. Momin, E.B. Mirza, M.D. Mathews, J. Mater. Sci. Lett. 10 (1991) 1246-1248.

[20] M. Mori, Y. Hiei, N.M. Sammes, Solid State Ionics 135 (2000) 743-748.

[21] M. Mori, Y. Hiei, N.M Sammes, Solid State Ionics 123 (1999) 103-111.

[22] M.M. Sammes, R. Ratnaraj, J. Mater. Sci. 29 (1994) 4319-4324.

[23] D.B. Meadowcroft, J.M. Wimmer, Amer. Ceram. Soc. Bull. 58 (1979) 610-615.

[24] S. Simner, J. Hardy, J. Stevenson, T. Armstrong T, J. Mat. Sci. 34 (1999) 5721-5732.

[25] B. Gildu, H. Fjellvag, A. Kjekshus, Acta Chim. Scand. 48 (1994) 37-45.

[26] K.P. Ong, P. Wu, App. Phys. Lett. 90 (2007) 044109-3.

[27] Y. Du, Z.X. Cheng, X.L. Wang, S.X. Dou, J. Appl. Phy. 108 (2010) 093914-9.

[28] J. B. Webb, M. Sayer, A. Mansingh. J Phys. 55 (1977) 77-217.

[29] Y.S. Malghe, S.R. Dharwadkar, K. Krishnan, K.D. Singh Mudher, J. Thermal Analysis and Calorimetry 95 (2009) 49-52.

[30] H. Yokokawa, N. Sakai, T. Kawada and M. Dokiya, J. Electrochem. Soc. 138 (1991) 1018-1027.

[31] N.Q. Minh, T. Takahashi. Science and Technology of Ceramic Fuel Cells. New York, 1995, pp. 183-184.

[32] S. Simner, J. Hardy, J. Stevenson, T. Armstrong, J. Mat. Sci. 34 (1999) 5721-5732.

[33] H. Chen, Mat. Chem Phys. 43 (1996) 116-125.

CHAPTER 3: ELECTROCHEMICAL DETERMINATION OF GIBBS ENERGY OF FORMATION OF $LaCrO_3$ USING A COMPOSITION-GRADED BIELECTROLYTE

3.1. Abstract

Presented are new measurements of the standard Gibbs free energy of formation of rhombohedral $LaCrO_3$ from component oxides La_2O_3 and Cr_2O_3 in the temperature range from 875 to 1175 K, using a bielectrolyte solid state cell incorporating single crystal CaF_2 and composition-graded solid electrolyte $(LaF_3)_y{\cdot}(CaF_2)_{1-y}$($y$=0 to 0.32). The results can be represented analytically as $\Delta G^{o}_{f(ox)}$ (±2270) / J mol^{-1} = –72329 + 4.932 (T / K). The measurements were undertaken to resolve serious discrepancies in the data reported in the literature. A critical analysis of previous electrochemical measurements indicates several deficiencies that have been rectified in this study. The enthalpy of formation obtained in this study is consistent with calorimetric data. The standard enthalpy of formation of orthorhombic $LaCrO_3$ from elements at 298.15 K computed from the results of this study is $\Delta H^{o}_{f(298\&15)}$ / kJ mol^{-1} = – 1536.2 (±7). The standard entropy of orthorhombic $LaCrO_3$ at 298.15 K is estimated as 99.0 (±4.5) J mol^{-1}K^{-1}.

3.2. Introduction

Solid-oxide fuel cells (SOFC) and oxygen transport membranes (OTM) are examples of key emerging solid-state electrochemical technologies for efficient utilization of conventional fossil fuels, carbon capture and reuse, and syngas production. The technologies also find applications in oxygen generation, life support system, and resource utilization as applicable to deep space missions. The component materials for high temperature systems

largely vary from advanced doped mixed ionic and electronic conducting perovskites as electrodes to ionic conducting oxides with fluorite structure as electrolytes and electronically conducting perovskites as interconnects and bi-polar separators. Although the electrical and electrochemical performance of these materials remains acceptable under short term test conditions, long term structural and chemical stability has remained an issue.

Lanthanum chromite ($LaCrO_3$) based perovskites have been considered as a promising candidate material for electrodes as well as interconnects for high temperature solid oxide fuel cells [1] and oxygen transport membranes [2]. This is mainly because of its high melting point (2773 K) [3], electrical conductivity and thermo-physical stability in both oxidizing ($P_{O_2} = 0.21$ atm) and reducing ($P_{O_2} = 10^{-22}$atm) atmospheres at high temperature [1, 4, 5]. Optimization of the required properties can be achieved by doping of pure $LaCrO_3$ by alkaline earth metals (Sr, Ca, Mg) at A-site and transition metals (Mn, Ni, Fe, Co) at B-site [6]. Physical, chemical and thermal properties of $LaCrO_3$ has been investigated and reported by several researchers over many years [1, 4, 7-9]. However, thermodynamic properties of $LaCrO_3$ are still not very well understood and there is a serious lack of consistency in the data reported literature [10-15]. Accurate thermodynamic properties of $LaCrO_3$ along with other physical and chemical properties is therefore of technical interest and importance for the design of $LaCrO_3$-based materials possessing desirable electrochemical properties.

Adiabatic calorimetry was used by Korobeinikova et al. [16] to measure the heat capacity (C_P) of $LaCrO_3$ in the temperature range from 340 to 900 K. Differential scanning calorimetry was used for C_P determination by Hofer et al. [17] (480–610 K) and Satoh et al. [18] (77–280 K). Laser flash calorimetry was used by Sakai et al. [19] (100–1000 K) for C_P

measurement. Sakai and Stolen [20] reported the heat capacity of $LaCrO_3$ in the temperature range from 298.15 to 1000 K using adiabatic shield calorimetry. The measured heat capacity exhibits anomalies corresponding to the magnetic order-disorder transition from antiferromagnetic state at ~288 K and structural phase transition at ~538 K. Values reported by Korobeinikova et al. [16] are considerably higher and those of Sakai et al. [19] significantly lower than the data reported by other investigators. The data of Sakai and Stolen [20] appear to be the most reliable. Unfortunately, none of the heat capacity measurements extent to sufficiently low temperature for an accurate evaluation of standard entropy at 298.15 K. Cheng et al. [15] has measured the enthalpy of formation of $LaCrO_3$ by drop solution calorimetry using molten lead borate as solvent.

Chen et al. [10] used a solid state cell based on MgO-stabilized ZrO_2 to determine the Gibbs free energy formation of $LaCrO_3$ at 1273 K. The solid electrolyte $(MgO)ZrO_2$ exhibits significant electronic conductivity at the low oxygen chemical potential associated with the working electrode consisting of $Cr+LaCrO_3+La_2O_3$. Electronic conductivity gives rise to electrochemical oxygen permeability, transporting oxygen from the reference electrode ($Cr+Cr_2O_3$) at higher potential to the working electrode at lower oxygen potential. The oxygen flux through the electrolyte causes polarization of both electrodes and lowers EMF. Consequently, the Gibbs free energy of formation of $LaCrO_3$ derived from the measurement is expected to be significantly less negative than the true value. A better solid electrolyte for the cell would have been Y_2O_3-doped ThO_2.

Measurement of the standard Gibbs free energy of formation for $LaCrO_3$ was the endeavor of Azad et al. [11], Chen et al. [12] and Dudek et al. [13], who used a solid state cell based on CaF_2 as the electrolyte operated in an oxygen containing gas atmosphere. Azad

et al. [11], and Chen et al. [12] used pure oxygen gas at ambient pressure, whereas Dudek et al. [13] used dry argon gas in which oxygen partial pressure was 8×10^{-4} atm. The cell used can be represented as;

$$(-)\ \mathrm{Pt}, \mathrm{O_2}, \mathrm{La_2O_3} + \mathrm{LaF_3} | \mathrm{CaF_2} | \mathrm{LaF_3} + \mathrm{LaCrO_3} + \mathrm{Cr_2O_3}, \mathrm{O_2}, \mathrm{Pt}\ (+) \qquad \text{(I)}$$

The temperature ranges of electromotive force (EMF) measurement and the results obtained by the three groups of investigators are summarized in Table 3.1. Unfortunately; the phases present at the reference and/or the working electrode are not thermodynamically stable under the operating conditions. At the reference electrode, La_2O_3 and LaF_3 would have reacted to form non-stoichiometric oxyfluoride $LaO_{1-x}F_{1+2x}$ [21-23]. Below ~1007 K, $LaCrO_3$ could have been oxidized to $LaCrO_4$ in pure oxygen. Further, there is significant solubility of LaF_3 in CaF_2. Diffusion of La^{3+} ions into CaF_2 may have affected the EMF of the solid state cell.

Peck et al. [14] determined the Gibbs energy of formation of $LaCrO_3$ using Knudsen-cell mass-spectrometry in the temperature range from 1887 to 2333 K. As indicated in Table 3.1, their results are in gross conflict with the data from the solid-state electrochemical cells. Surface depletion of the volatile component is a cause for concern in the measurement of the vapor pressure over solid materials. Peck et al. [14] used a large orifice with a diameter of 0.3 mm. Because of the discordant results on Gibbs energy of formation of $LaCrO_3$ documented above and summarized in Table 3.1, new measurements were undertaken to resolve the conflicts.

Table 3.1. Comparison of the reported values for the standard Gibbs free energy formation of $LaCrO_3$.

Gibbs free energy of formation for $LaCrO_3$	Temperature range	References
$\Delta G^{o}_{f,ox(LaCrO_3)}(\pm 1{,}500)/\text{J mol}^{-1} = -30{,}100$	1273 K	Chen et al. [10]
$\Delta G^{o}_{f,ox(LaCrO_3)}(\pm 400)/\text{J mol}^{-1} = -44{,}450 + 2.12\ (T/\text{K})$ $\Delta G^{o}_{f,ox(LaCrO_3)}/\text{J mol}^{-1} = -42{,}637.4$ (at 855 K)	855 – 1073 K	Azad et al. [11]
$\Delta G^{o}_{f,ox(LaCrO_3)}/\text{J mol}^{-1} = -94{,}758 + 85.3\ (T/\text{K})$ $\Delta G^{o}_{f,ox(LaCrO_3)}/\text{Jmol}^{-1} = -21{,}826.5$ (at 855 K)	700 – 885 K	Chen et al. [12]
$\Delta G^{o}_{f,ox(LaCrO_3)}(\pm 380)/\text{J mol}^{-1} = -42{,}290$	1273 K	Dudek et al. [13]
$\Delta G^{o}_{f,ox(LaCrO_3)}(\pm 1{,}100)/\text{J mol}^{-1} = -74{,}700 - 2.02\ (T/\text{K})$	1887 – 2333 K	Peck et al. [14]

A solid state electrochemical technique was chosen because of its higher inherent accuracy. The cell was redesigned to avoid problems encountered with cell I used earlier. The reference electrode was changed from a mixture of La_2O_3 and LaF_3 to a mixture of CaO and CaF_2 in the new design to avoid the formation of oxyfluoride. The oxygen partial pressure in the gas phase over the electrodes was reduced by using an $Ar+O_2$ gas mixture to avoid the oxidation of $LaCrO_3$ to $LaCrO_4$. A bielectrolyte combination consisting a single crystal pellet CaF_2 coupled to a polycrystalline composition-graded pellet of $(LaF_3)_y{\cdot}(CaF_2)_{(1-y)}$ was used to minimize the diffusive flux of La^{3+} ions from LaF_3 in the working electrode into the solid electrolyte. The new cell can be represented as:

y=0 y=0.32

Au, O_2 ($P_{O_2} = 0.01$) , CaO + CaF_2 || CaF_2 || $(LaF_3)_y{\cdot}(CaF_2)_{(1-y)}$ || $LaCrO_3$ + Cr_2O_3

+ LaF_3, O_2 ($P_{O_2} = 0.01$) , Au (II)

with the right-hand electrode positive. To prevent grain boundary diffusion of CaO from the CaO + CaF_2 reference into the solid electrolyte, a single crystal of CaF_2 is placed adjacent to it. Composition graded solid electrolyte $(LaF_3)_y \cdot (CaF_2)_{(1-y)}$ is placed in contact with CaF_2 single crystal such that y = 0 at the contact surface. The value of y = 0.32 at the other extremity of the graded electrolyte in contact with the measuring electrode containing pure LaF_3 as one of the components. This composition corresponds closely to the saturation solubility of LaF_3 in CaF_2. A similar arrangement was used earlier [24] for measurement of the Gibbs energy of formation of $LaGaO_3$.

2.6. Experimental

2.6.1. *Materials*

Optical-grade single crystals of CaF_2, obtained from Harshaw Chemical Company, were in the form of disks 1.5 cm in diameter and 0.2 cm thick. Ultra-pure anhydrous powders of CaF_2, LaF_3, CaO, La_2O_3 and Cr_2O_3 were supplied by Johnson Matthey Ltd. Moisture and other volatile impurities were removed from the powders by heating to 1273 K in dry inert gas. To prepare $LaCrO_3$, stoichiometric amounts of La_2O_3 and Cr_2O_3 were first ball-milled, then pelletized at 150 MPa and subsequently reacted at 1673 K for ~ 40ks. To ensure completeness of the reaction, the pellet was reground, repelletized and reacted again at the same temperature for a similar period. Powder X-ray diffraction (XRD) confirmed the formation of green colored $LaCrO_3$. At room temperature, $LaCrO_3$ has an orthorhombic unit cell (space group *Pnma*) with a = 0.5511, b = 0.7758 and c = 0.5479 nm. Above 540 (±10)

K, structure changes to rhombohedral (space group *R*3*c*), with lattice parameters a = 0.5561 and c = 1.3567 nm in the hexagonal setting.

The fluoride phase in equilibrium with $LaCrO_3$ and Cr_2O_3 could be either LaF_3 or $LaO_{1-x}F_{1+2x}$. For the correct design of the solid state cell, it is important to know the equilibrium fluoride phase. The oxyfluoride LaOF was prepared by solid state reaction. Mixed in equimolar ratio were fine powders of La_2O_3 and LaF_3. The homogenized mixture was compressed into pellets and reacted in a pre-purified argon gas atmosphere first at 1275 K for 36 ks and subsequently at 1475 K for 18 ks to complete the reaction,

$$^1/_3\, LaF_3 + {}^1/_3\, Ln_2O_3 \rightarrow LaOF \qquad (1)$$

The high purity Ar gas (99.999 %) used in the experiments was further purified by passing through anhydrous $Mg(ClO_4)_2$ and over P_2O_5 to remove moisture, and then through Cu turnings at 750 K and Ti granules at 1150 K to remove residual oxygen. After heat treatment, the pellets were pulverized. The formation of LaOF was confirmed by XRD. The oxyfluoride has cubic structure at high temperature and rhombohedral or tetragonal structure at low temperature depending on composition. Rapid quenching into chilled mercury retained the high-temperature form of LaOF. The lattice parameter of the cubic phase at room temperature is a = 0.5765 nm. The lattice parameters of the rhombohedral LaOF (space group $R\bar{3}m$) with two formulae units per unit cell are a = 0.7133 nm and α = 33.0°. In separate experiments, LaOF and LaF_3 were equilibrated at different temperatures with an equimolar mixture of $LaCrO_3$ and Cr_2O_3 for periods up to ~120 ks. The fluoride phase in equilibrium with $LaCrO_3$ and Cr_2O_3 was identified by XRD as LaF_3 in the temperature range from 875 to 1175 K. LaF_3 crystallized in tysonite-type structure, space group $P\bar{3}c1$, with

lattice parameters a = 0.7186 nm and c = 0.7351 nm. EDS was unable to detect any appreciable solid solubility of Cr_2O_3 in $LaCrO_3$.

Although ideally a composition-graded solid electrolyte $(LaF_3)_y{\cdot}(CaF_2)_{(1-y)}$ with linear variation in composition (y) is advantageous, in practice it is difficult to prepare such a structure. In the current study, pellets were prepared in which the composition was varied in steps of 8 mol. %. Homogeneous solid solutions of CaF_2 containing 8, 16, 24, 28 and 32 mol % LaF_3 were first prepared by solid state diffusion. Well-mixed fine powders (d < 1μm) of CaF_2 and LaF_3 in the required proportions was pelletized and heat-treated at 1475 K for ~400 ks under pre-purified Ar gas to synthesize homogeneous solid solutions. Prepared by repeated consolidation of layers, each having a uniform composition, was the functionally graded solid electrolyte. A measured quantity of CaF_2 powder was pressed in a steel die at 150 MPa, solid solution having the next composition (8 mol. %. LaF_3) was then placed over it and consolidated again at the same pressure. The procedure was repeated with successive compositions of the solid solution until the graded structure visualized in Fig. 3.1 was obtained for use in cell II. After final compaction at 200 MPa, the composite pellet was sintered under pre-purified Ar gas at 1375 K for ~300 ks. A glove box was used for processing of the solids containing lanthanum oxide to prevent contamination by moisture or carbon dioxide.

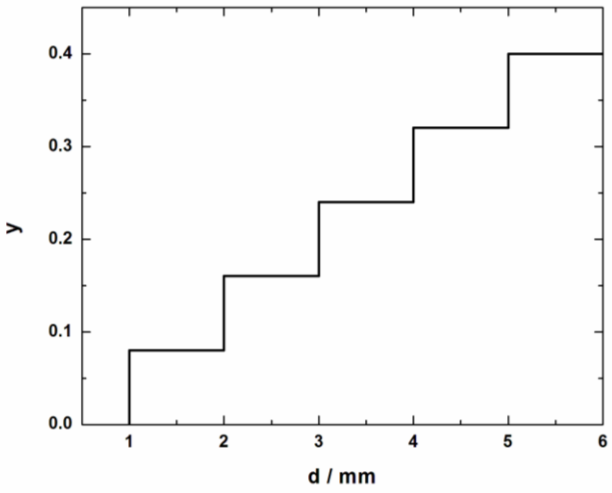

Fig. 3.1. Profile of composition-graded solid electrolyte, $(LaF_3)_y \cdot (CaF_2)_{1-y}$ with *y* varying from 0 to 0.32 in the steps of 0.08.

Argon-oxygen gas mixture containing 1% oxygen was used to provide gas atmosphere around the electrodes. The high purity mixture, obtained from a commercial source, was completely dehydrated before use in the solid state cell by passing it through towers containing silica gel and anhydrous magnesium perchlorate, and finally over boats containing anhydrous phosphorus pentoxide.

2.6.2. *Procedure*

Prepared by heating a compacted equimolar mixture of CaO and CaF_2 under dry $Ar+O_2$ mixture at 1273 K was the reference electrode of cell II. The working electrode was prepared in a similar way using an equimolar mixture of $Cr_2O_3 + LaCrO_3 + LaF_3$. Mixing of the fluoride and oxide phases at the electrodes was required to generate the equilibrium fluorine potential at each electrode under the oxygen-containing gas phase. The mean particle sizes of the powders used for the preparation of the electrodes were in the range from 2 to 9 μm.

Shown in Fig. 3.1 is a line sketch of the apparatus used in this study. The contraption is basically the same as that used earlier for the measurement of the Gibbs energy of formation of $LaGaO_3$ [24]. On either side of the bielectrolyte assembly were spring-loaded the electrode pellets, with thin gold gauze placed between the electrolyte and each electrode. Gold wires attached to the gold gauze were connected to a digital voltmeter with high-impedance ($10^{16}\,\Omega$). The reference electrode was placed in contact with single crystal CaF_2. In contact with the composition-graded electrolyte was placed the working electrode. A rigid system consisting of a closed-end alumina tube and an alumina rod attached to a water-cooled brass cap was used to hold the pellets together. Good contact between pellets was ensured by springs attached to the brass cap that applied a small compressive force. Gold foils, inserted between the electrode pellets and the alumina rod and tube, prevented contact between them. The cell assembly was mounted inside a vertical outer alumina tube; the ends of the tube were closed with water-cooled brass caps. Then the tube was evacuated, leak-tested and refilled with dry $Ar+O_2$ gas mixture. The alumina tube enclosing the cell was suspended in a vertical resistance furnace such that the electrodes were in the constant-temperature zone (±1 K). A Kanthal shield was placed between the alumina tube and the furnace. The shield was earthed to avoid induced EMF on cell leads from furnace winding. The cell was operated under dry $Ar+O_2$ gas mixture at ambient pressure, flowing at 2.5 mL s^{-1}. A mass flow controller was used to set the flow rate. A trace of water vapor in the gas were found produce tiny specks of CaO on the surface of CaF_2, rendering it either translucent or opaque. Moisture degradation also affected the composition-graded electrolyte.

The reversible EMF of cell II was measured in the temperature range from 875 to 1175 K. The temperature of the cell was measured by a Pt/Pt-13%Rh thermocouple

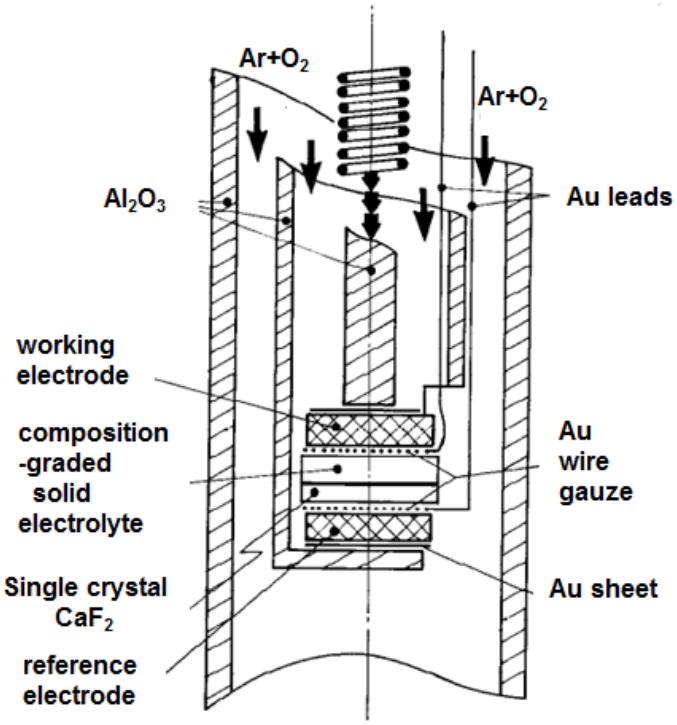

Fig. 3.2. Schematic diagram of the apparatus used for the EMF measurement.

calibrated against the melting point of gold. Temperatures recorded in this study are based on the ITS-90 scale. The time taken to attain constant EMF varied from ~30 ks at 875 K to ~10 ks at 1175 K. The electrochemical reversibility of the cell was checked by microcoulometric titration in both directions. A small direct current of ~15μA is passed through the cell for ~0.6 ks using an external potential source. The EMF was then monitored as a function of time. The EMF was found to return gradually to the steady value before each titration. Infinitesimally displaced from equilibrium were the chemical potentials at each electrode during each titration. Return of the EMF to the same value after successive displacements in opposite directions confirmed the attainment of equilibrium at each electrode. Moderate change in the flow rate of $Ar+O_2$ mixture through the cell in the range from 1.5 to 4.5 mL s^{-1} did not affect the EMF. The EMF was reproducible on cycling temperature confirming

thermal reversibility of the cell. After each run, the cell was cooled and the electrode pellets were examined by XRD and energy dispersive X-ray spectroscopy (EDS). The phase composition of the electrodes was not altered during EMF measurements.

2.7. Results and Discussion

2.7.1. *Interpretation of the EMF of the Solid State Cell*

The cubic fluoride solid solution $La_yCa_{1-y}F_{2+y}$ has excess fluoride ions in interstitial sites as in solution of YF_3 in CaF_2 [25] resulting in enhanced ionic conductivity relative to pure CaF_2. Since the transport number of fluoride ions is greater than 0.99 in pure CaF_2 and $La_yCa_{1-y}F_{2+y}$ [26-27] under the experimental conditions used in this study, the EMF of a solid-state cell (E) incorporating these electrolytes is given by;

$$\eta F E = \mu_{F_2}^{'} - \mu_{F_2}^{''} \qquad (2)$$

where η = 2 is the number of electrons associated with the electrode reactions, and F = 96485.3 C mol^{-1} is the Faraday constant. The chemical potentials of fluorine at the two electrodes are represented by $\mu_{F_2}^{'}$ and $\mu_{F_2}^{''}$, with $\mu_{F_2}^{'} > \mu_{F_2}^{''}$. It has been demonstrated in an earlier study [28] that the EMF of a cell incorporating the composition-graded solid electrolyte $La_yCa_{1-y}F_{2-y}$ obeys the Nernst equation. Both experiment and theoretical analysis show that the chemical potentials of the neutral form of the mobile species at the electrodes determine the EMF of a cell that incorporates a composition-graded electrolyte, when there is only one mobile ion with transport number close to unity [29-33]. Measurable diffusion potential is not generated by the concentration gradient of relatively immobile ions.

2.7.2. *Gibbs Energy of Formation of $LaCrO_3$*

Plotted in Fig. 3.3 is the reversible EMF of cell II, which shows a small increase with temperature. The equation obtained from linear least-squares regression analysis is:

$$E\ (\pm 1.03)\ /\ \text{mV} = 545.15 + 7.42\text{x}10^{-3}(T\ /\ \text{K}) \qquad (3)$$

The uncertainty limit represents two times the standard deviation. At the working electrode on the right-hand side of cell II, the electrochemical reaction can be written as:

$$^2/_3\ LaF_3 + {}^1/_3\ Cr_2O_3 + {}^1/_2\ O_2 + 2\ e^- \rightarrow {}^2/_3\ LaCrO_3 + 2\ F^- \qquad (4)$$

At the reference electrode on the left-hand side of the cell, the corresponding reaction is:

$$CaO + 2\ F^- \rightarrow\ CaF_2 + {}^1/_2\ O_2 + 2\ e^- \qquad (5)$$

Since the gas atmosphere is the same over both electrodes, oxygen partial pressures are equal on both sides of the cell. The EMF of cell II is then related to the standard Gibbs energy change for the virtual cell reaction;

$$^2/_3\ LaF_3 + {}^1/_3\ Cr_2O_3 + CaO \rightarrow {}^2/_3\ LaCrO_3 + CaF_2 \qquad (6)$$

$$\Delta G^{\circ}_{(6)}\ (\pm 200)\ /\ \text{J mol}^{-1} = -\ 2\text{F}E$$

$$= -\ 105198 - 1.432\ (T\ /\ \text{K}) \qquad (7)$$

For the exchange reaction,

$$CaF_2 + {}^1/_3\ La_2O_3 \rightarrow CaO + {}^2/_3\ LaF_3 \qquad (8)$$

the standard Gibbs energy change, computed from data in the thermodynamic compilation of Knacke et al. [34], can be represented by the equation,

$$\Delta G^{\circ}_{(8)}\ (\pm 1500)\ /\ \text{J mol}^{-1} = 56979 + 4.72\ (T\ /\ \text{K}) \qquad (9)$$

in the temperature range from 850 to 1200 K. The reaction that represents the formation of rhombohedral $LaCrO_3$ from Cr_2O_3 and La_2O_3 with corundum and A-rare earth structures, respectively, can be obtained by combining reactions (6) and (8):

$^{1}/_{2}$ La_2O_3 (A-rare earth) + $^{1}/_{2}$ Cr_2O_3 (corundum) → $LaCrO_3$ (rhombohedral) (10)

$\Delta G^{o}_{(10)}$ (±2270) / J mol^{-1} = –72329 + 4.932 (T / K) (11)

in the temperature range from 875 to 1175 K. Lack of precision in the thermodynamic data for oxides and fluorides of calcium and lanthanum reported in the literature [34] is the main cause for the relatively large uncertainty limit associated with reaction (11). As more precise data for these compounds become available, accuracy of data for $LaCrO_3$ from the EMF measurements reported here will be enhanced.

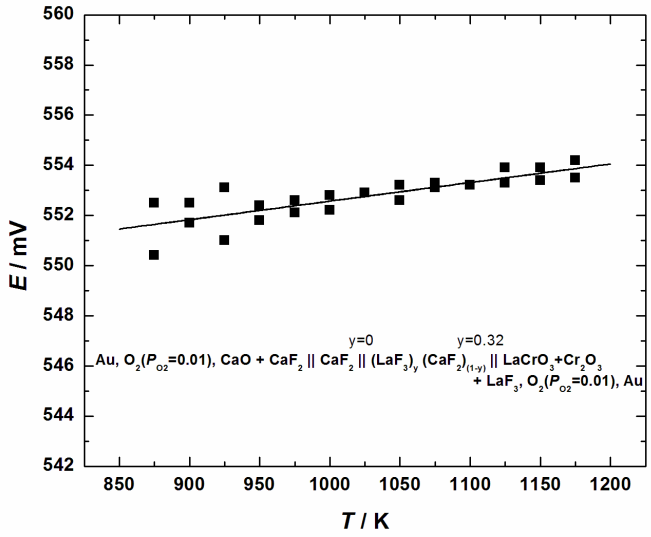

Fig 3.3. Variation of the EMF of cell-II as a function of temperature.

The standard Gibbs energy of formation of $LaCrO_3$ obtained in this study is compared with the value reported by earlier investigators [10-14] in Fig. 3.4. The values obtained in this study are markedly more negative than the data from earlier electrochemical measurements [10-13]. Chen et al. [10] used $(MgO)ZrO_2$ as the solid electrolyte to measure the oxygen chemical potential of a three-phase electrode consisting of $Cr+LaCrO_3+La_2O_3$ relative to $Cr+Cr_2O_3$ as the reference at 1273 K. As indicated in the introduction solid electrolyte

(MgO)ZrO_2 exhibits significant electronic conductivity at the low oxygen chemical potential associated

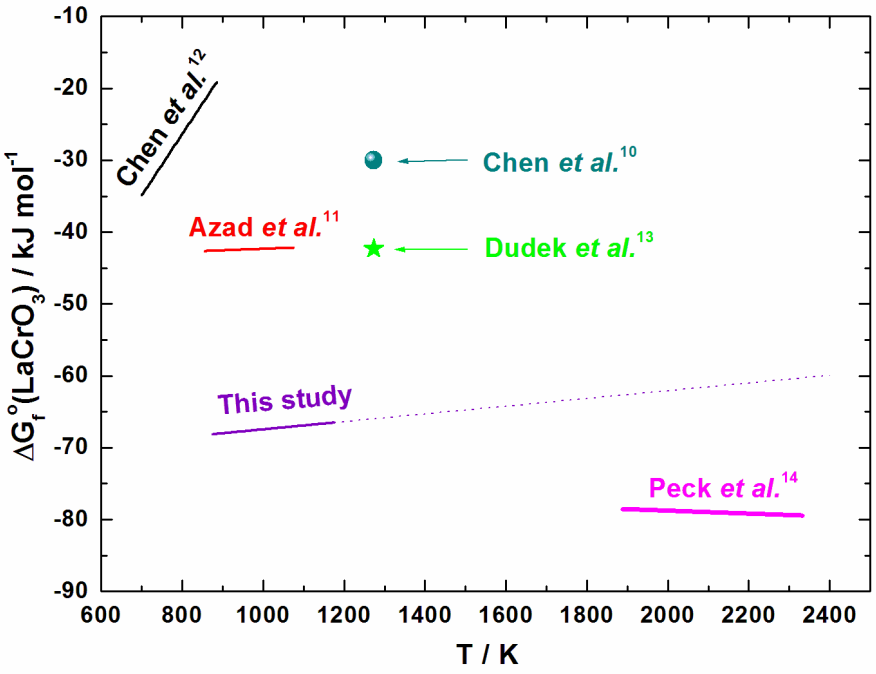

Fig. 3.4. Standard Gibbs free energy of formation of $LaCrO_3$ as a function of temperature: comparison of the results obtained in this study with data reported in the literature.

with the working electrode. Hence it is not surprising that Gibbs energy of formation derived from their measurement is significantly less negative than other data. Azad et al. [11], Chen et al. [12] and Dudek et al. [13] used solid-state cells based on CaF_2 as the electrolyte. Their reference electrodes were made from a mixture of LaF_3 and La_2O_3 in approximately equal mass ratio. At high temperature, this would have resulted in a single-phase nonstoichiometric oxyfluoride $LaO_{1-x}F_{1+2x}$ characterized by x = 0.182 (or X_{LaF_3} = 0.625), in which activity of La_2O_3 would have been substantially less than unity. The cell EMF is related to the ratio of fluorine partial pressures, which in turn is related to the ratio of activities of La_2O_3 at the two electrodes. Because of the formation of the oxyfluoride, their measured EMF would have

been considerably reduced resulting in a less negative value for the Gibbs energy of formation of $LaCrO_3$. The difference between the results of Azad et al. [11] and Chen et al. [12], who used almost identical electrochemical cells, is a cause of concern. Chen et al. [12] attribute the large difference to the possible formation of LaOF at the reference electrode (La_2O_3 + LaF_3) used by Azad et al. [11]. Azad et al. [11] prepared their electrodes in air. Chen et al. [12] have suggested that LaF_3 reacted with moisture present in air to form LaOF. Since their own electrodes were prepared in static oxygen atmosphere, they argued that their reference electrode is free of LaOF. In fact, LaOF can form both by hydrolysis of LaF_3 and by solid-state reaction between La_2O_3 and LaF_3. Both Azad et al. [11] and Chen et al. [12] did not examine their electrodes carefully after EMF measurements. It is likely that both measurements were affected by the formation of the oxyfluoride phase. A more plausible reason for the difference in their results is related to size of particles of $LaCrO_3$ used in the two studies. Chen et al. [12] synthesized nano-size $LaCrO_3$ powder using a sol-gel route, whereas Azad et al. [11] prepared micron-size $LaCrO_3$ by solid-state reaction. Because of the surface energy contribution, the Gibbs energy of nano-size $LaCrO_3$ would be much higher than that of the corresponding micron-size material, as shown for example by studies on the Gibbs energy of formation of $MgAl_2O_4$ as a function of particle size [35]. The size effect is probably the main reason for the difference in the Gibbs energy of formation of $LaCrO_3$ obtained by Azad et al. [11] and Chen et al. [12] using almost identical cells.

At temperatures below ~1007 K, $LaCrO_3$ can be oxidized to $LaCrO_4$ in the presence of oxygen gas at ambient pressure. The instability of $LaCrO_3$ would have biased the EMF measurements of Azad et al. [11] (855–1073 K), Chen et al. [12] (700–885 K). Azad et al. [11] have reported, but not explained, rapid decrease in EMF at temperatures beyond 1073 K,

which may have been caused by the slow decomposition of $LaCrO_4$ formed at lower temperatures. Devoid of this complication is the measurement of Dudek et al. [13] at 1273 K.

Further, there is significant solubility of LaF_3 in CaF_2 which may affect the EMF of cells based on pure CaF_2. With the formation of oxyfluoride at the reference electrode, the activity of LaF_3 at this electrode would be reduced. The unbalanced diffusive flux of La^{3+} ions into CaF_2 electrolyte from the two electrodes can affect the EMF. It can therefore be concluded that the similar cells used by Azad et al. [11], Chen et al. [12] and Dudek et al. [13] were ill-designed for the measurement of the Gibbs energy of formation of $LaCrO_3$. The data obtained from these studies are unreliable.

The Gibbs energy of formation of $LaCrO_3$ obtained from Knudsen-cell mass-spectrometric measurements of Peck et al. [14] are more negative than the results of this study extrapolated. This indicates the possibility of surface depletion of the volatile component Cr_2O_3 at their sample surface. Because of the low value of diffusion coefficient in solids, flux of chromium to the sample surface may not be rapid enough to match the rate of vaporization from the surface. The large orifice diameter (0.3 mm) of the Knudsen cell used by Peck et al. [14] argues against the attainment of solid–vapor equilibrium inside the cell.

$LaCrO_3$ is reported to exhibit small cation nonstoichiometry at high temperatures. The maximum excess Cr in $LaCrO_3$ is reported as 0.38 at % in air at 1773 K [36]. At the same temperature, Ilieve et al. [37] claim to have prepared single phase samples containing 0.76 and 1.28 at % excess Cr in pure oxygen. The measurements of Chen et al. [10] and Peck et al. [14] relate to Cr-deficient $LaCrO_3$ saturated in La_2O_3, while all other thermodynamic measurements [11-13] including this study are conducted on Cr-rich $LaCrO_3$ saturated in

Cr_2O_3. However, the narrow non-stoichiometric range cannot explain the large differences in the integral molar properties of $LaCrO_3$.

2.7.3. *Oxygen Potential for the decomposition of $LaCrO_3$*

When the oxygen potential over $LaCrO_3$ is reduced sufficiently, the compound will decompose according to the reaction;

$$2\ LaCrO_3 \rightarrow La_2O_3 + 2\ Cr + {}^3/_2\ O_2 \qquad (12)$$

The standard free energy change for this reaction can be obtained by combining results obtained in this study for $LaCrO_3$ with the free energy formation of Cr_2O_3 (ΔG_f^o (± 900) / J mol^{-1} = –115940 + 250.35(T / K) [38]. The oxygen potential for the decomposition according to the reaction (12) is given by;

μ_{O_2} (±3100) / J mol^{-1} = RT ln P_{O_2} = – 840400 + 173.48(T / K)

The stability domain of $LaCrO_3$ as a function of log P_{O_2} and reciprocal of temperature is shown in Fig. 3.5.

2.7.4. *Enthalpy and Entropy of Formation of $LaCrO_3$*

The enthalpy of formation of rhombohedral $LaCrO_3$ from La_2O_3 and Cr_2O_3 at an average temperature of 1025 K is given by the temperature-independent term on the right-hand side of Eq. (11): $\Delta H^o_{f(ox)}$ / kJ mol^{-1} = – 72.33 (±3.3). The corresponding value from the EMF study of Azad et al. [11] is –22.2 (±5) kJ mol^{-1} and Chen et al. [12] is –47.4(±6) kJ mol^{-1}. Using heat capacity data of Sakai and Stolen [20] for $LaCrO_3$, Ziemniak et al. [39] for Cr_2O_3 and Knacke et al. [34] for La_2O_3, the enthalpy of formation of orthorhombic $LaCrO_3$ from oxides at 298.15 K is –73.15 (±3.5) kJ mol^{-1}. The small enthalpy and entropy of phase

transition of $LaCrO_3$ is incorporated in the thermal data of Sakai and Stolen [20] used in the assessment. The enthalpy of formation from oxides at 298.15 K is in reasonable agreement with the calorimetric value of –70.06 (±2.79) kJ mol^{-1} at 298.15 K reported by Cheng et al. [15]. The standard enthalpy of formation of orthorhombic $LaCrO_3$ from the elements at 298.15 K computed from the results of this study using data for Cr_2O_3 ($\Delta H^{o}_{f(298\&15)}$ / kJ mol^{-1} = – 1131.21) from Ziemniak et al. [39] and La_2O_3 ($\Delta H^{o}_{f(298\&15)}$ / kJ mol^{-1} = – 1794.94) from Knacke et al. [34] is $\Delta H^{o}_{f(298\&15)}$ / kJ mol^{-1} = – 1536.2(±6).

The entropy of formation of rhombohedral $LaCrO_3$ from oxides at 1025 K is related to the temperature-dependent term in Eq. (11); $\Delta S^{o}_{f(ox)}$ / J $mol^{-1}K^{-1}$ = – 4.93 (±3.4). Using heat capacity data for reactants and products, [20, 34, 39] the corresponding value for orthorhombic $LaCrO_3$ at 298.15 K is: $\Delta S^{o}_{f(ox)}$ / J mol^{-1} K^{-1} = – 5.81 (±3.4). The small negative entropy of formation from component oxides is consistent with the negative volume change ($\Delta V^{o}_{f(ox)}$ / mL mol^{-1} = 3.74) for the formation reaction at room temperature. From the entropy of formation, the standard entropy of orthorhombic $LaCrO_3$ at 298.15 K, can be estimated as 99.0 (±4.5) J $mol^{-1}K^{-1}$. Standard entropies of Cr_2O_3 ($S^{o}_{298\&15}$ / J $mol^{-1}K^{-1}$ = 82.3) from Ziemniak et al. [39] and La_2O_3 ($S^{o}_{298\&15}$ / J $mol^{-1}K^{-1}$ = 127.32) at 298.15 K from Knacke et al. [34] were used for this estimation. An accurate measurement of the heat capacity of $LaCrO_3$ at very low temperatures would be beneficial for an independent assessment of its entropy.

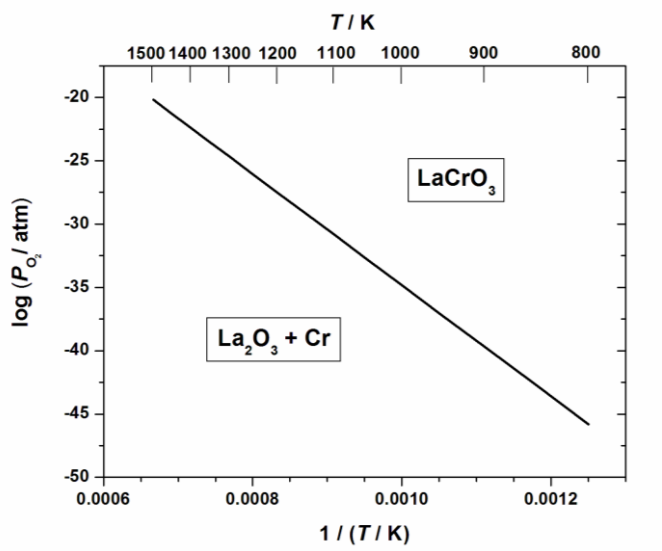

Fig. 3.5. The stability domain of $LaCrO_3$ as a function of log P_{O_2} and reciprocal of absolute temperature.

2.8. Conclusion

An advanced version of the solid-state cell incorporating a single crystal CaF_2 and composition-graded $(LaF_3)_y{\cdot}(CaF_2)_{1-y}$ as electrolytes was used for the determination of the standard Gibbs free energy of formation of rhombohedral $LaCrO_3$ from component oxides in the temperature range from 875 to 1175 K. The cell was designed to overcome the faults in earlier electrochemical measurements. The results obtained in this study, $\Delta G^{o}_{f(ox)}$ (±2270) / J mol^{-1} = –72329 + 4.932 (T / K), are consistent with the calorimetric enthalpy of formation from component oxides and bridge the large gap between divergent electrochemical and mass-spectrometric measurements reported in the literature. For formation of orthorhombic $LaCrO_3$ from the elements at 298.15 K, the standard enthalpy change computed from the results of this study is $\Delta H^{o}_{f(298\&15)}$ / kJ mol^{-1} = – 1536.2(±7). The standard entropy of orthorhombic $LaCrO_3$ at 298.15 K is obtained as 99.0 (±4.5) J mol^{-1} K^{-1}. Results obtained in

this study supersede earlier data and permit more accurate characterization of interface reactions and vapor transport in solid oxide fuel cells and oxygen transport membranes using either pure or doped $LaCrO_3$.

2.9. References

[1] J. Sfeir. J. Power Sources. 118 (2003) 276-285.

[2] A. S. Mukasyan, C. Costello, K. P. Sherlock, D. Lafarga, and A. Varma. Separation and Purification Technology 25 (2001) 117-126.

[3] M. Foëx. C.R. Acad. Sci. Paris 260 [8] 6389-6392 (1965).

[4] J. G. M. Furtado, and R. N. Oliveira. Revista Matéria. 13 (2008) 147-153.

[5] S. Tanasescu, D. Berger, D. Neiner, and N. Totir. Solid State Ionics 157 (2003) 365-370.

[6] X. Ding, Y. Liu, L. Gao, and L. Guo. J alloys and compounds 425, 318-322 (2006).

[7] S. P. Jiang, L. Liua, K. P. Ong, P. Wu, J. Li, and J. Puc. J Power Sources 176 (2008) 82-89.

[8] H. Hayashi, M. Watanabe, and H. Inaba. Thermochimica Acta 359 (2000) 77-85.

[9] J. W. Fergus. Solid State Ionics 30 (2004) 1-15.

[10] S. Chen, Z. Hai, F. Li, and G. Zhou. Zhongguo Xitu Xuebao. 5 [3] (1987) 19-24.

[11] A. M. Azad, R. Sudha and O. M. Sreedharan. J. Less-Common Metals, 166 (1990) 57-62.

[12] Z. Chen, X. Xing, W. Yuan, X. Huang, and H. Li. 25 [5] (2006) 562-66.

[13] M. Dudek, G. Rog, and A. Kozlowska-Rog. Polish J. Chem., 81 (2007) 23-29.

[14] D. H. Peck, M. Miller, D. Kobertz, H. Nickel, and K. Hilpert. J. Am. Ceram. Soc. 79 [12] (1996) 3266-72.

[15] J. Cheng, A. Navrotsky, X. D. Zhou and H. U. Anderson. J. Mater. Res. 20 [1] (2005) 191-200.

[16] A. V. Korobeinikova and A. Reznitskii. High Temp. 14 [4] (1976) 805-806.

[17] H. E. Hofer and W. F. Kock, J. Electrochem. Soc. 140 [10] (1993) 2889-2894.

[18] H. Satoh, S. Koseki, M. Takagi, W. Y. Chung, and N. Kamegashira. J. Alloys Compd. 259 (1997) 176-182.

[19] K. Oikawa, T. Kamiyama, T. Hashimoto, Y. Shimojyo, and Y. Morii. J. Solid State Chem. 154 (2000) 524-529.

[20] N. Sakai and S. Stolen, J. Chem. Thermodyn. 27(1995) 493.

[21] W. H. Zachariasen. ActaCryst. 4 (1951) 231-236.

[22] D. B. Shinn and H.A. Eick. Inorg. Chem. 8 [2] (1969) 232-235.

[23] K. Niihara and S. Yajima. Bull. Chem. Soc. Jpn. 45 [1] (1972) 20-23.

[24] K. T. Jacob, N. Dasgupta, H. Näfe, and F. Aldinger. J. Mater. Res., 15 [12] (2000) 2836-2845.

[25] R. W. Ure Jr. J. Chem. Phys. 26 [6] (1957) 1363-1373.

[26] J. Delect, R.J. Heus, and J.J. Egan. J. Electrochem.Soc.125 [5] (1978) 755-58.

[27] K. Ono, T. Fujimura, and J. Moriyama. J. Jpn. Inst. Met. 42 [5] (1978) 469-74.

[28] K. T. Jacob, N. Dasgupta, and Y. Waseda. J. Am. Ceram.Soc. 81 [7] (1998) 1926-1930.

[29] S. Mukhopadhyay and K.T. Jacob. J. Electroanal. Chem. 395 (1995) 107-115.

[30] S. Mukhopadhyay and K.T. Jacob. J. Electrochem. Soc. 140 [9] (1993) 2629-2635.

[31] S. Mukhopadhyay and K.T. Jacob. Metall. Mater. Trans. A. 25A (1994)173-181.

[32] S. Mukhopadhyay and K.T. Jacob, "Application of Composition Gradient Solid Electrolytes in Sensors and Thermodynamic Measurements": pp. 106-26 in Proc. Second

International Symposium on Ionic and Mixed Conducting Ceramics, Edited by T.A. Ramanarayanan, W.L. Worrell and H.L. Tuller, The Electrochemical Society, Pennington, U.S.A., 1994.

[33] K. T. Jacob and S. Mukhopadhyay. J. Electrochem.Soc., 142 (1995) 161-165.

[34] O. Knacke, O. Kubaschewski, and K. Hesselmann (eds.), "Thermochemical Properties of Inorganic Substances",Vols. I and II, 2nd Ed. Springer-Verlag, Berlin, FRG, 1991.

[35] K. T. Jacob, K. P. Jayadevan, R. M. Mallya, and Y. Waseda. Adv. Mater. 12 (2000) 440-444.

[36] C. P. Khattack and D. E. Cox. Mater. Res. Bull. 12 (1972) 463-472.

[37] M. N. Iliev, A. P. Litvinchuk, V. G. Hadjiev, Y. Q. Wang, J. Cmaidalka, R. L. Meng, Y. Y. Sun, N. Kolev, and M. V. Abrashev. Phys. Rev. B 74 (2006) 214301-7.

[38] K. T. Jacob. J. Electrochem. Soc. 124 (1977) 1827-1831.

[39] S. E. Ziemniak, L. M. Anovitz, R. A. Castelli and W. D. Porter. J. Chem. Thermodynamics 39 (2007) 1474-1492.

CHAPTER 4: THERMODYNAMIC PROPERTIES OF $LaCrO_4$, La_2CrO_6 AND $La_2Cr_3O_{12}$, AND SUB-SOLIDUS PHASE RELATIONS IN THE SYSTEM La–Cr–O

4.1. Abstract

In the system La–Cr–O, there are three ternary oxides ($LaCrO_4$, $La_2Cr_3O_{12}$ and La_2CrO_6) that contain Cr in higher valence states V or VI. On heating $LaCrO_4$ decomposes to $LaCrO_3$, $La_2Cr_3O_{12}$ to a mixture of $LaCrO_4$ and Cr_2O_3, and La_2CrO_6 to $LaCrO_3$ and La_2O_3 with loss of oxygen. The oxygen potentials corresponding to these decomposition reactions are determined as a function of temperature using solid-state cells incorporating yttria-stabilized zirconia as the electrolyte. Measurements are made from T = 840 K to the decomposition temperature of the ternary oxides in pure oxygen. The standard Gibbs free energies of formation of the three ternary oxides are derived from the electromotive force (EMF) of the three cells. The standard enthalpy of formation and standard entropy of the three ternary oxides at 298.15 K are estimated. Sub-solidus phase relations in the system La–Cr–O are computed from thermodynamic data and displayed as isotherm sections at several temperature intervals. The decomposition temperatures in air are T_d = 880 K for $La_2Cr_3O_{12}$, T_d = 936 K for $LaCrO_4$ and T_d = 1056 K for La_2CrO_6.

4.2. Introduction

Magnetohydrodynamic (MHD) power generators [1], oxygen sensors [2], and heating elements in high temperature furnaces [3] are few applications where lanthanum chromite ($LaCrO_3$) based perovskite oxides have been proposed for use. High-temperature solid-state electrochemical devices such as solid-oxide fuel cells (SOFC) [4] and oxygen transport membranes (OTM) [5] are emerging advanced technologies for clean and efficient energy. A

material with good electrical conductivity and stable in both oxidizing and reducing atmospheres at high temperature is required for these applications. Lanthanum chromite ($LaCrO_3$) based materials meet these requirements in the oxygen partial pressure (p_{O_2}) range from (0.21 to 10^{-22}) atm at T = 1273 K [6]. At lower temperatures and high oxygen partial pressures, chromites can be oxidized to chromates. This study explores thermodynamic stability domain of lanthanum chromite with respect to oxidation.

$LaCrO_4$ forms as an intermediate phase during the growth of $LaCrO_3$ thin films on yttria-stablized zirconia (YSZ) and stainless steel substrates using spray pyrolysis [7] and RF magnetron sputtering [8] techniques. During synthesis of $LaCrO_3$ from La_2O_3 and $Cr_2(CO_3)_3$ in air at T = 1073 K, both $LaCrO_4$ and La_2CrO_6 containing Cr in higher valence states are formed as secondary phases. There is a third stable lanthanum chromate, $La_2Cr_3O_{12}$, reported in the literature [9-10]. Since thermodynamic data on these compounds are not available from any source, their standard Gibbs energies of formation have been determined as a function of temperature using a solid-state electrochemical cells incorporating Y_2O_3-stabilized ZrO_2 as the solid electrolyte.

4.3. Experimental

4.3.1. *Materials*

$LaCrO_4$ was prepared by pyrolysis of $La(CH_3COO)(CrO_4).2H_2O$ precursor in air at T = 873 K for (~4) ks, following the procedure outlined by Furusaki et al. [11]. The precursor was obtained by heat treatment in air at T = 673 K of the residue obtained by evaporation of an equimolar solution of lanthanum acetate ($La(CH_3COO)_3.1.5H_2O$) and chromium trioxide (CrO_3). The evaporation was done at $T \approx 350$ K using a rotary evaporator. The formation of the dark green $LaCrO_4$ by combustion of the acetate moiety in the precursor was confirmed

by X-ray diffraction (XRD). It had a monazite-type monoclinic structure, space group $P2_1/n$. The lattice parameters calculated from the XRD pattern were a = 0.7041 nm, b = 0.7241 nm, c = 0.6705 nm and β = 104.95°. The CrO_4^{3-} tetrahedra in $LaCrO_4$ have C_1 symmetry with different Cr–O bond lengths. The orthochromate is one of the few stable oxides containing Cr(V) ion having d^1 electronic configuration. The valence state of Cr has been characterized by Raman spectroscopy [12] and X-ray photoelectron spectroscopy [13]. The electron binding energies (E_B) and and Auger parameters (α) of Cr(V) and La(III) indicate that the Cr–O bond in CrO_4 tetrahedra have a strong covalent character, with electron transfer from oxygen to Cr(V); La–O bond in $LaCrO_4$ is more ionic than in $LaCrO_3$. $LaCrO_4$ is an n-type semiconductor with activation energy of (~18) kJ mol^{-1}, conforming to a band model [14].

It was difficult to prepare single phase La_2CrO_6, although a mixture containing La_2CrO_6 and La_2O_3 can be readily obtained by heating a mixture of La_2O_3 and Cr_2O_3 in the molar ratio 3:1 in pure dry oxygen gas at T = 1073 K. The XRD pattern of La_2CrO_6, obtained by subtracting the known pattern of La_2O_3 from that of the mixture, can be indexed on a orthorhombic unit cell with lattice parameters a = 0.4397 nm, b = 0.4235 nm, c = 1.375 nm. La_2CrO_6 decomposes to a mixture of La_2O_3 and $LaCrO_3$ when heated in air above T = 1073 K.

Lanthanum chromate heptahydrate ($La_2Cr_3O_{12}.7H_2O$) was prepared from a solution containing dissolved La_2O_3 and H_2CrO_4 in the appropriate ratio in a Teflon-lined autoclave heated to $T \approx 435$ K and then cooled very slowly. The heptahydrate crystals were filtered out and washed in acetone. Thermogravimetric analysis (TGA) indicated the loss of water in two main steps during heating. Five molecules of H_2O were lost between (325 and 400) K and the remaining two between (425 and 650) K in air. Anhydrous crystalline $La_2Cr_3O_{12}$ was

prepared by isothermal annealing at T = 750 K in pure oxygen. Residual moisture in high purity oxygen gas used in this study was removed by passing the gas through a tower packed with anhydrous magnesium perchlorate and then over anhydrous phosphorus pentoxide. In air $La_2Cr_3O_{12}$ decomposes to Cr_2O_3 and $LaCrO_4$ when heated above T = 923 K.

4.3.2. *Solid-state electrochemical measurements*

The reversible EMF of the following cells was measured as a function of temperature:

Pt, $LaCrO_4$+$LaCrO_3$ / (Y_2O_3) ZrO_2 / O_2 (0.1 MPa), RuO_2, Pt (I)

Pt, $La_2Cr_3O_{12}$+$LaCrO_4$+Cr_2O_3 / (Y_2O_3) ZrO_2 / O_2 (0.1 MPa), RuO_2, Pt (II)

Pt, La_2CrO_6+$LaCrO_3$+La_2O_3 / (Y_2O_3) ZrO_2 / O_2 (0.1 MPa), RuO_2, Pt (III)

According to the convention used here, the right-hand side electrodes are positive. Yttria-stabilized zirconia, (Y_2O_3) ZrO_2, used as the solid electrolyte, was in the form of a closed-end tube separating reference and working electrode compartments. A leak test was performed on the (Y_2O_3) ZrO_2 tube before use to ensure the absence of physical permeability. The apparatus used for the measurements and the procedure employed are similar to those described elsewhere [15-16]. Hence, only a brief description and essential points are given here.

Pure oxygen gas at a pressure p = 0.1 MPa, used as the reference electrode, was passed inside the (Y_2O_3) ZrO_2 tube over a RuO_2 electrode. At low temperatures, RuO_2 is a better catalyst than Pt for the conversion of oxygen molecules to oxygen ions. The RuO_2 electrode was made by inserting few drops of aqueous solution of $RuCl_3$ inside (Y_2O_3) ZrO_2 tube and drying the solution to get a deposit of $RuCl_3$ against inside flat surface of the tube. This procedure was repeated thrice. The tube was then heated at (~1100) K for (0.3) ks. By this treatment, an adherent porous film of RuO_2 was formed. A Pt mesh, spot welded to a Pt

wire, was placed over the RuO_2 electrode and pressed down by an alumina tube. The top end of (Y_2O_3) ZrO_2 tube was closed tightly with the brass cap with O-ring seals. The working electrode, consisting of a mixture of oxides, was compacted in a (Y_2O_3) ZrO_2 crucible. The crucible was placed in an outer quartz tube closed at one end and provided with a side arm. The top end of the quartz tube was tapered into cone shape. The (Y_2O_3) ZrO_2 tube was inserted through the cone and pressed down against the working electrode mixture with a Pt wire inserted between them. The gap between the quartz cone and (Y_2O_3) ZrO_2 tube was closed with De Khotinsky cement, with the Pt lead passing through it. The quartz tube was then evacuated through the side arm and flame sealed under vacuum. During measurements at high temperature, equilibrium oxygen potential was established inside the quartz tube by decomposition of an oxide phase present at the working electrode. An excess of the phase that decomposed was taken at the working electrode. For example, in cell I the molar ratio of $LaCrO_4$ to $LaCrO_3$ was 1.5:1. In cell II, the ratio of $La_2Cr_3O_{12}$ $LaCrO_4$:Cr_2O_3 was 1.5:1:1, and in cell III the ratio of La_2CrO_6:$LaCrO_3$:La_2O_3 was 1.5:1:1.

Using microcoulometric titration in each direction, the reversibility of the EMF was confirmed. The EMF was stable for periods in excess of (~40) ks at constant temperature. Essentially the same EMF was generated when the cell temperature was approached from higher and lower values. The measured EMF was independent of oxygen gas flow rate at the reference electrode in the range from (0.8 to 3.6) $ml \cdot s^{-1}$. After cooling, the electrodes were inspected using optical and scanning electron microscope and XRD. On the examination, no extraneous side reactions were detected. However, a small change in the relative concentrations of the oxide phases was observed, consistent with the expected partial

decomposition of one phase to establish equilibrium oxygen partial pressure inside the evacuated quartz tube.

4.4. Results and Discussion

4.4.1. *Electromotive force of Solid-State Cell*

The reversible EMF of cells I, II and III is plotted as a function of temperature in Fig. 4.1 and are shown in Table 4.1. The EMF decreases linearly with temperature. The decrease results from the increasing oxygen partial pressure at the working electrode with temperature, while the oxygen pressure at the reference electrode remains constant. The linear least-squares regression analysis gives the following expressions for EMF:

$$E_{\mathrm{I}} \pm 0.92 \,/\, (\mathrm{mV}) = 444.27 + 0.4409\,(T/\mathrm{K}) \quad (1)$$

$$E_{\mathrm{II}} \pm 1.02 \,/\, (\mathrm{mV}) = 418.30 + 0.4415\,(T/\mathrm{K}) \quad (2)$$

$$E_{\mathrm{III}} \pm 1.16 \,/\, (\mathrm{mV}) = 499.98 + 0.4397\,(T/\mathrm{K}) \quad (3)$$

The quoted uncertainty limit corresponds to twice the standard deviation (2σ) obtained from regression analysis. The cell I was operated on the temperature range (840–1020) K, cell II in the range (840–960) K and cell III in the range (840–1140) K. The cells register zero EMF when the oxygen partial pressure at both electrodes became equal. The high temperature limit for each cell was indicated when the cell registered small negative value of EMF, signaling a pressure above atmospheric at the working electrode. The low temperature limit for EMF measurements was set by sluggish cell response.

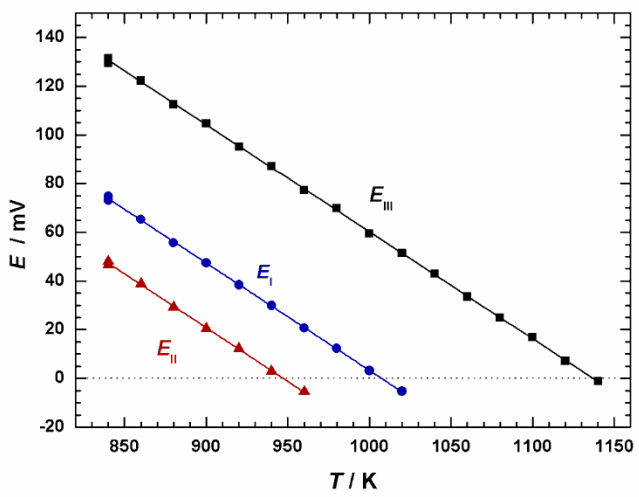

Fig. 4.1. Temperature dependence of the reversible EMF of solid-state cells: —●— (blue online), cells I; –▲– (red online), cell II; and —■— (black online), cell III.

Table 4.1. Values of the each Cell EMF as a function of temperature along with uncertainty estimates obtained from the least-squares regression analysis

***T* (K)**	**E_1 (mV)**	**E_{II} (mV)**	**E_{III} (mV)**
840	73.2 (±3)	46.7 (±4)	129.6 (±4)
860	65.2 (±3)	38.9 (±4)	122.2 (±4)
880	55.7 (±3)	29.3 (±4)	112.6 (±4)
900	47.5 (±3)	20.6 (±4)	104.7 (±4)
920	38.4 (±3)	12.3 (±4)	95.1 (±4)
940	29.9 (±3)	3.0 (±4)	87.2 (±4)
960	20.6 (±3)	-5.4 (±4)	77.3 (±4)
980	12.3 (±3)	-	70.0 (±4)
1000	3.2 (±3)	-	59.5 (±4)
1020	-5.3 (±3)	-	51.5 (±4)
1040	-	-	42.9 (±4)
1060	-	-	33.5 (±4)
1080	-	-	24.9 (±4)
1100	-	-	16.9 (±4)
1120	-	-	7.2 (±4)
1140	-	-	-1.2 (±4)

4.4.2. *Gibbs Energy of Formation of $LaCrO_4$, $La_2Cr_3O_{12}$ and La_2CrO_6*

The oxygen chemical potential determining reaction at the working electrode of cell I is,

$$LaCrO_3 + 1/2\,O_2 \rightarrow LaCrO_4 \quad (4)$$

The standard Gibbs free energy change for this reaction and the associated oxygen chemical potential can be calculated from the EMF using the Nernst equation:

$$\Delta G^{\circ}_{r(4)} \pm 180\ /(\mathrm{J \cdot mol^{-1}}) = -2FE_I = 0.5RT\ \ln p_{O_2} = -85731 + 85.096(T/\mathrm{K}) \quad (5)$$

Generally, three condensed phases are required to define oxygen potential in a ternary system at constant temperature. However, in this case, two phases are sufficient because their compositions are related. The La to Cr ratio in the two compounds is the same. This composition constraint reduces one degree of freedom. The oxygen potential defined by the equilibrium between the $LaCrO_3$ and $LaCrO_4$ will prevail in the adjoining three phase fields containing these two phases [17].

The enthalpy of oxidation of $LaCrO_3$ to $LaCrO_4$ at the average experimental temperature T_{av} = 930 K is (–85.73 ± 0.77) kJ·mol^{-1}. Recently, the standard Gibbs energy of formation of $LaCrO_3$ from component oxides La_2O_3 and Cr_2O_3 has been determined in the temperature range (875 to 1175) K using a bi-electrolyte solid state cell [18]. For the reaction,

$$1/2\,La_2O_3 + 1/2\,Cr_2O_3 \rightarrow LaCrO_3 \quad (6)$$

$$\Delta G^{\circ}_{r(6)} \pm 2270\ /(\mathrm{J \cdot mol^{-1}}) = -72329 + 4.932\ (T/\mathrm{K}) \quad (7)$$

Combining equations (4) and (6), formation of $LaCrO_4$ from stable binary oxides Cr_2O_3, La_2O_3 and O_2 gas can be written as:

$$1/2\,La_2O_3 + 1/2\,Cr_2O_3 + 1/2\,O_2 \rightarrow LaCrO_4 \quad (8)$$

$$\Delta G^{\circ}_{r(8)} \pm 2300/(\mathrm{J \cdot mol^{-1}}) = -158060 + 90.028\ (T/\mathrm{K}) \quad (9)$$

The oxygen potential at the working electrode of cell II is determined by the reaction,

$$2\mathrm{LaCrO_4} + 1/2\,\mathrm{Cr_2O_3} + 5/4\,\mathrm{O_2} \rightarrow \mathrm{La_2Cr_3O_{12}} \quad (10)$$

for which standard Gibbs free energy change can be computed from the EMF;

$$\Delta G^{\circ}_{r(10)} \pm 490/(\mathrm{J \cdot mol^{-1}}) = -5\mathrm{F}E_{\mathrm{II}} = 1.25\,\Delta\mu_{\mathrm{O_2}} = -201800 + 213.038\,(T/\mathrm{K}) \quad (11)$$

Combining equations (8) and (10), the free energy of formation of $La_2Cr_3O_{12}$ from stable binary oxides (Cr_2O_3 and La_2O_3) and O_2 gas can be calculated. For the reaction,

$$\mathrm{La_2O_3} + 3/2\,\mathrm{Cr_2O_3} + 9/4\,\mathrm{O_2} \rightarrow \mathrm{La_2Cr_3O_{12}} \quad (12)$$

$$\Delta G^{\circ}_{r(12)} \pm 4600/(\mathrm{J \cdot mol^{-1}}) = -517920 + 393.094\,(T/K) \quad (13)$$

The oxygen potential defining reaction at the working electrode for cell III is;

$$\mathrm{LaCrO_3} + 1/2\,\mathrm{La_2O_3} + 3/4\,\mathrm{O_2} \rightarrow \mathrm{La_2CrO_6} \quad (14)$$

and the standard Gibbs free energy change for this reaction is computed as:

$$\Delta G^{\circ}_{\mathrm{r(14)}} \pm 340/(\mathrm{J \cdot mol^{-1}}) = -3\mathrm{F}E_{\mathrm{III}} = 0.75\Delta\mu_{\mathrm{O_2}} = -144723 + 127.279(T/\mathrm{K}) \quad (15)$$

Combining equations (6) and (14), the free energy formation for La_2CrO_6 from stable binary oxides (Cr_2O_3, La_2O_3) and O_2 gas can be written as:

$$\mathrm{La_2O_3} + 1/2\,\mathrm{Cr_2O_3} + 3/4\,\mathrm{O_2} \rightarrow \mathrm{La_2CrO_6} \quad (16)$$

$$\Delta G^{\circ}_{16} \pm 2300/(\mathrm{J \cdot mol^{-1}}) = -217052 + 132.211\,(T/K) \quad (17)$$

The oxygen chemical potentials corresponding to reactions (4), (10) and (14), derived from the EMF of the three cells, are plotted as a function of temperature in Fig. 4.2. Also shown is the oxygen chemical potential for the three-phase field ($LaCrO_4$ + $La_2Cr_3O_{12}$ + La_2CrO_6). The lines have similar positive slope. Also plotted is oxygen chemical potential for fixed values of oxygen partial pressure ($RT \ln p_{O_2}$), which have either zero or negative slope. Intersection of these two sets of lines defines the equilibrium decomposition temperature at the defined oxygen partial pressures. The decomposition temperatures of the three ternary

oxides at different oxygen partial pressures are listed in Table 4.2. The decomposition temperature of $LaCrO_4$ in air obtained in this study (T_d = 936 K) compares with the value of T_d = 953 ±10 K reported by Carter et al. [19] using DTA and TGA. Carter et al. [19] studied the decomposition on heating and did not determine the temperature for formation of $LaCrO_4$ on cooling. During the decomposition of $LaCrO_4$ to $LaCrO_3$, oxygen coordination around La atoms change from (9 to 12) and around Cr atoms from tetrahedral to octahedral. The major structural rearrangement during decomposition is probably linked to high activation energy and slow kinetics. Thus, the decomposition temperature reported by Carter et al. [19] may not be considered as the equilibrium decomposition temperature.

Table 4.2. Decomposition temperature of the ternary oxides $LaCrO_4$, $La_2Cr_3O_{12}$ and La_2CrO_6 at different partial pressures of oxygen

Oxygen partial pressure p_{O_2} (atm)	Decomposition temperature of $LaCrO_4$ (K)	Decomposition temperature of $La_2Cr_3O_{12}$ (K)	Decomposition temperature of La_2CrO_6 (K)
1	1007 (±3)	947 (±3)	1137 (±4)
0.21	936 (±3)	880 (±3)	1056 (±4)
10^{-2}	822 (±3)	773 (±3)	927 (±4)
10^{-4}	695 (±3)	653 (±3)	7834)

4.4.3. *Thermodynamic properties of $LaCrO_4$, $La_2Cr_3O_{12}$ and La_2CrO_6 at 298.15 K*

There is no heat capacity data available for the ternary oxides $LaCrO_4$, $La_2Cr_3O_{12}$ and La_2CrO_6 reported in the literature. Therefore, thermodynamic properties of these compounds

at T = 298.15 K cannot be rigorously derived from the current measurements. However, following the suggestion of Kubaschewski and Alcock [20] the change in heat capacity (ΔC_P) for reactions involving a gas phase such as,

$$a\,A_2O_3 + b\,B_2O_3 + c\,O_2 \rightarrow A_{2a}B_{2b}O_{3(a+b)+2c} \quad (18)$$

can be approximated as:

$$\Delta C_P/(\mathrm{J\cdot mol^{-1}\cdot K^{-1}}) = 12.552c \quad (19)$$

The constant value for ΔC_P may be used in the absence of heat capacity data on reactants and products to estimate properties at T = 298.15 K

The enthalpy of formation of $LaCrO_4$ from binary oxides Cr_2O_3 and La_2O_3 and O_2 gas according to reaction (8) at the mean temperature T = 930 K can be obtained from the results of this study: $\Delta H^{\circ}_{r(8)} \pm 3.4$ / ($\mathrm{kJ\cdot mol^{-1}}$) = −158.06 .The corresponding value at T = 298.15 K can be estimated as −162.025 ± 3.6 $\mathrm{kJ\cdot mol^{-1}}$ using the ΔC_P approximation. Using enthalpy of formation of Cr_2O_3 ($\Delta H^{o}_{f(298\&15)}$/ ($\mathrm{kJ\cdot mol^{-1}}$) = −1131.21) from Ziemniak et al. [21] and La_2O_3 ($\Delta H^{o}_{f(298\&15)}$/ ($\mathrm{kJ\cdot mol^{-1}}$) = −1794.94) from Knacke et al. [22], the standard enthalpy of formation of $LaCrO_4$ from the elements at T = 298.15 K can be calculated as $\Delta H^{o}_{f(298.15)}$± 6 ($\mathrm{kJ\cdot mol^{-1}}$) = −1625.1. The entropy change for reaction (8) at T = 930 K is $\Delta S^{\circ}_{r(8)} \pm 3.4$ / ($\mathrm{J\cdot mol^{-1}\cdot K^{-1}}$) = – 90.028; the corresponding value at T = 298.15 K can be computed as – 97.17 ± 3.5 / ($\mathrm{J\cdot mol^{-1}\cdot K^{-1}}$) using the ΔC_P approximation. Using standard entropies of Cr_2O_3 ($S^{o}_{298\&15}$/ ($\mathrm{J\cdot mol^{-1}\cdot K^{-1}}$) =−82.3) from Ziemniak et al. [21] and La_2O_3 ($S^{o}_{298\&15}$($\mathrm{J\cdot mol^{-1}\cdot K^{-1}}$) = −127.32) and O_2 ($S^{o}_{298\&15}$/ ($\mathrm{J\cdot mol^{-1}\cdot K^{-1}}$) = −205.15) from Knacke et al. [22], the standard entropy of $LaCrO_4$ at T = 298.15 K can be estimated as $S^{o}_{298\&15} \pm 4.2$ / ($\mathrm{J\cdot mol^{-1}\cdot K^{-1}}$) = 110.2.

Using an analogous procedure, from the enthalpy of formation of $La_2Cr_3O_{12}$ according to reaction (12) at the mean temperature T = 900 K ($\Delta H^{\circ}_{r(12)}$ ± 6.9 / (kJ·mol^{-1}) = −517.92) its standard enthalpy of formation from elements can be evaluated as $\Delta H^{o}_{f\,(298.15)}$± 14.2 / (kJ·mol^{-1}) = −4026.7 and. From the entropy change at T = 900 K, $\Delta S^{\circ}_{r(12)}$ ± 6.8 / (J·mol^{-1}·K^{-1}) = −393.1), the standard entropy at T = 298.15 K can be estimated as $S^{o}_{298.15}$ ± 8.8 / (J·mol^{-1}·K^{-1}) = 288.1.

Similarly, using the enthalpy of formation of La_2CrO_6, according to reaction (16) at the mean temperature T = 990 K, the standard enthalpy of formation from elements at T = 298.15 K can be appraised as $\Delta H^{o}_{f\,(298.15)}$ ± 6.9 / (kJ·mol^{-1}) = −2684.1 and. The standard entropy at T = 298.15 K can be assessed as $S^{o}_{298.15}$ ± 4.0 / (J·mol^{-1}·K^{-1}) = 178.8.

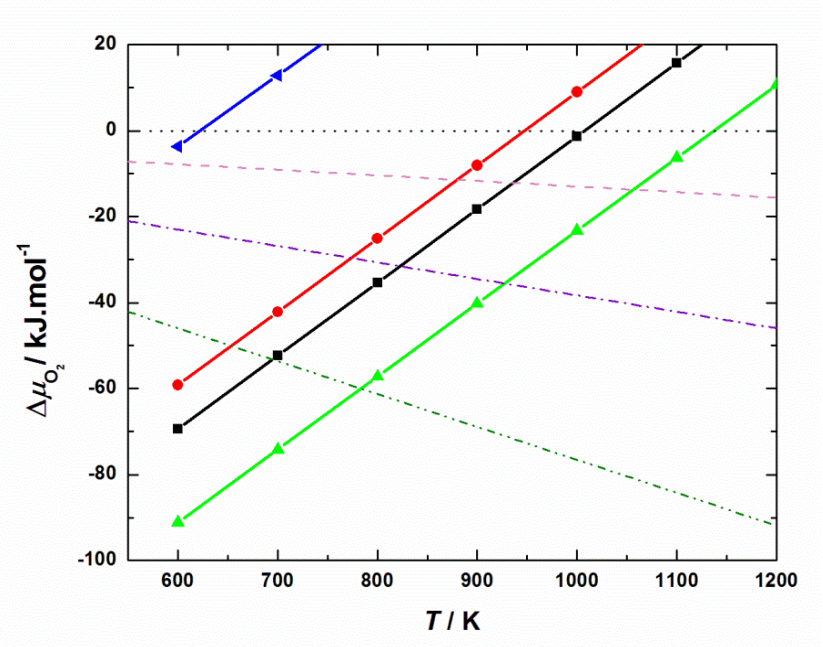

Fig. 4.2. Oxygen chemical potentials corresponding to the decomposition reactions of ternary oxides as a function of temperature: —■— (black online), $LaCrO_4$; —●— (red online), $La_2Cr_3O_{12}$; and —▲— (green online), La_2CrO_6. Also shown is oxygen potential for the

oxidation of $LaCrO_4$ to a mixture of La_2CrO_6 and $La_2Cr_3O_{12}$: −◀− (blue online). The variation of oxygen potential as a function of temperature for constant values of oxygen partial pressure is also plotted: ···· (p_{O_2} = 1 atm), - - - - (p_{O_2} = 0.21 atm), - · - · - (p_{O_2} = 10^{-2} atm) and - · · - · · - (p_{O_2} = 10^{-4} atm).

4.4.4. *Sub-solidus phase relation in system La–Cr–O*

Using thermodynamic data for ternary oxides – results of this study on three oxides ($LaCrO_4$, $La_2Cr_3O_{12}$ and La_2CrO_6) with Cr in higher valence state, and our previous study on $LaCrO_3$ – sub-solidus phase relations for the system La–Cr–O are computed at different temperatures using free energy minimization procedure. The results are shown in Fig. 4.3 and 4.5 to 4.8. Below T = 947 K, all the four ternary oxides are stable. As shown in Fig. 4.3, for T < 622 K only the two ternary oxides ($La_2Cr_3O_{12}$ and La_2CrO_6) containing hexavalent Cr is in equilibrium with pure O_2 at ambient pressure; $LaCrO_4$ does not coexist with O_2. This can be demonstrated by plotting the Gibbs energy change or oxygen chemical potential for the reaction:

$$4LaCrO_4 + O_2 \rightarrow La_2CrO_6 + La_2Cr_3O_{12} \qquad (20)$$

as a function of temperature. As seen from Fig. 4.2, the standard Gibbs free change for the reaction is negative below T = 622 K. Thus, the phase mixture of $La_2Cr_3O_{12}$ and La_2CrO_6 is more stable than $LaCrO_4$ in equilibrium with pure oxygen at 0.1 MPa. Eight three-phase fields involving solids are present below T = 622 K; La+Cr+La_2O_3, Cr+La_2O_3+$LaCrO_3$, Cr+$LaCrO_3$+Cr_2O_3, La_2O_3+$LaCrO_3$+La_2CrO_6, $LaCrO_3$+Cr_2O_3+$LaCrO_4$, $LaCrO_3$+$LaCrO_4$+La_2CrO_6, La_2CrO_6+$LaCrO_4$+$La_2Cr_3O_{12}$ and $LaCrO_4$+Cr_2O_3+$La_2Cr_3O_{12}$. The validity of the tie line connecting $LaCrO_3$ and La_2CrO_6 in Fig. 4.3 can be tested by considering the exchange reaction:

$$La_2O_3 + 3LaCrO_4 \rightarrow LaCrO_3 + 2La_2CrO_6 \quad (21)$$

The standard Gibbs free change for the reaction is plotted in Fig. 4.4 as a function of temperature. The negative Gibbs free energy confirms the tie line connecting $LaCrO_3$ and La_2CrO_6 is energetically favored compared to the line connecting La_2O_3 and $LaCrO_4$. Similarly the validity of tie line linking $LaCrO_4$ and Cr_2O_3 shown in Fig. 4.3 can be tested by examining the free energy change associated with the exchange reaction:

$$2La_2Cr_3O_{12} + 5LaCrO_3 \rightarrow 9LaCrO_4 + Cr_2O_3 \quad (22)$$

The standard free change for the reaction plotted in Fig. 4.4 indicates that $La_2Cr_3O_{12}$ is in equilibrium with $LaCrO_3$. There are no intermetallic compounds in the binary system La–Cr. [23] Cr is almost insoluble in solid La and the solid solubility of La in Cr is negligible at sub-solidus temperatures.

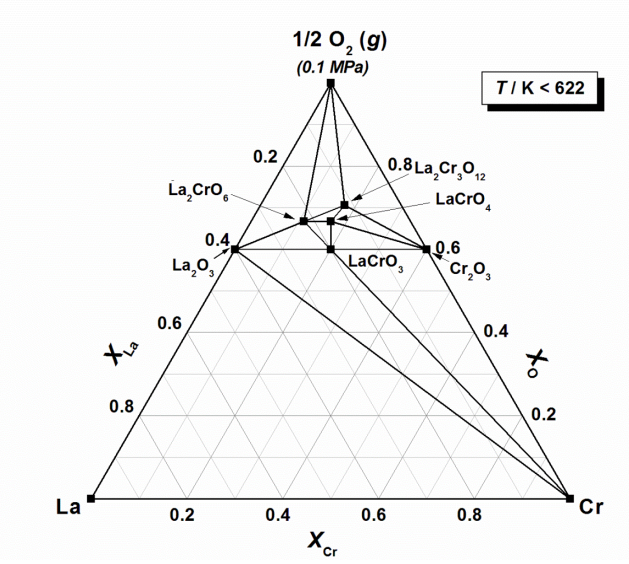

Fig. 4.3. Sub-solidus phase relations of the system La–Cr–O for temperatures below T = 622 K.

At temperatures above T = 622 K, $LaCrO_4$ also exists in equilibrium with O_2. Thus, three ternary oxides, $LaCrO_4$, $La_2Cr_3O_{12}$ and La_2CrO_6, can coexist with pure oxygen as demonstrated in Fig. 4.5. The upper temperature limit for phase relations displayed in Fig.

4.5 is set by the decomposition of $La_2Cr_3O_{12}$. Above T = 947 K, $La_2Cr_3O_{12}$ decomposes to a mixture of $LaCrO_4$ and Cr_2O_3 in pure oxygen and the phase relations in the temperature range from (947 to 1007) K are as shown in Fig. 4.6. $LaCrO_4$ decomposes to $LaCrO_3$ at T =

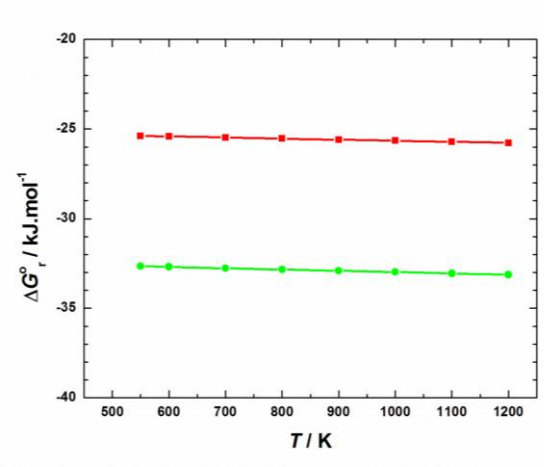

Fig. 4.4. Plot of the standard Gibbs energy change for exchange reactions involving oxide phases as a function of temperature for identifying tie lines: —●— (green online), reaction (21); and —■— (red online), reaction (22).

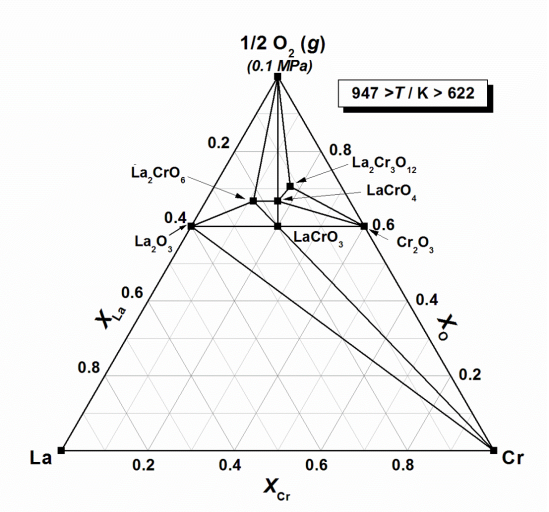

Fig. 4.5. Sub-solidus phase relations of the system La–Cr–O for temperature range from (622 to 947) K.

1007 K and phase relations in the temperature range (1137 < T (K) < 1007) are as shown in Fig. 4.7. Furthermore, at T = 1137 K, La_2CrO_6 decomposes to $LaCrO_3$ and La_2O_3 and the phase relations are shown in Fig. 4.8 for temperatures higher than T = 1137 K. La melts at T = 1193 K and there is a eutectic at T = 1124 K, where a liquid containing 3.44 at % Cr in equilibrium with solids La and Cr [23]. This will introduce additional phase fields involving liquid alloys and La_2O_3. The saturation solubility of Cr in the liquid at T = 1200 K (x_{Cr} = 0.042) and 1600 K (x_{Cr} = 0.11) are identified in Fig. 4.8 and the boundary of the two phase field involving liquid alloy and La_2O_3 are shown by the dotted lines.

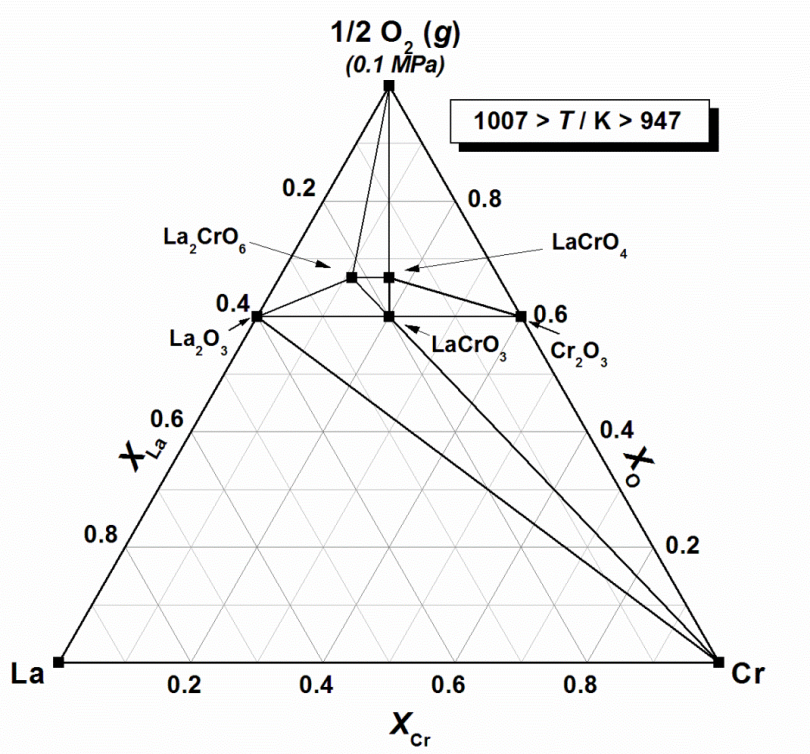

Fig. 4.6. Sub-solidus phase relations of the system La–Cr–O in the temperature range from (947 to 1007) K.

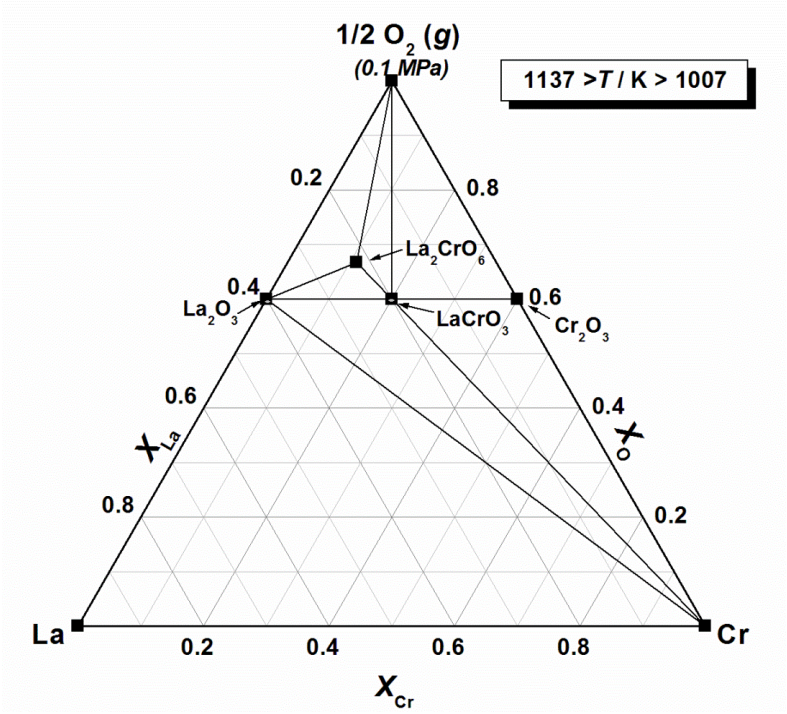

Fig. 4.7. Sub-solidus phase relations of the system La–Cr–O for temperature range from (1007 to 1137) K.

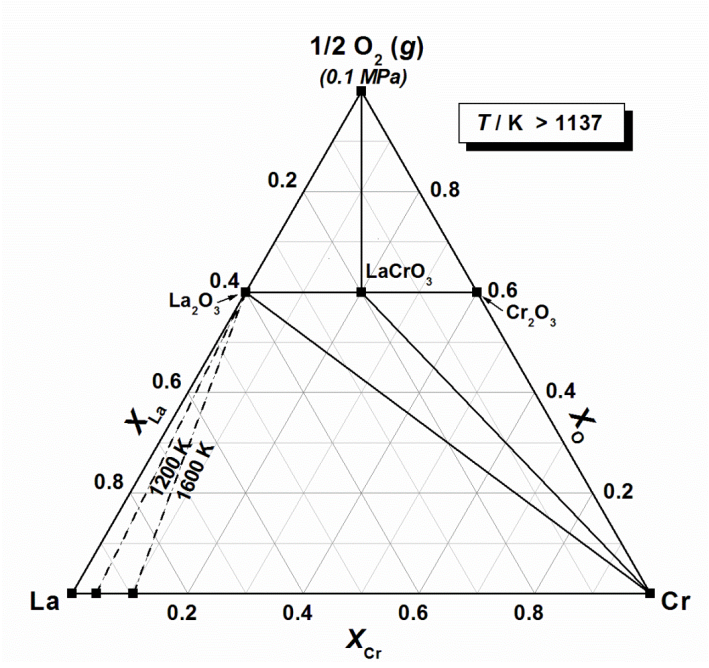

Fig. 4.8. Phase relations of the system La–Cr–O for temperature above T = 1137 K.

4.5. Conclusion

Three solid-state electrochemical cells based on $(Y_2O_3)\,ZrO_2$ as the solid electrolyte were designed to measure the standard Gibbs free energy of formation of $LaCrO_4$, $La_2Cr_3O_{12}$ and La_2CrO_6, containing Cr in higher valence states of V and VI. For the formation of ternary oxides from their component binary oxides (Cr_2O_3, La_2O_3) and O_2 gas, the derived Gibbs energies of formation in the temperature range from T = 840 K to the decomposition temperature in pure oxygen gas can be represented by the equations,

$LaCrO_4$: $\Delta G^{\circ}_{\mathrm{f(ox)}} \pm 2300/(\mathrm{J \cdot mol^{-1}}) = -158060 + 90.028\ (T/\mathrm{K})$

$La_2Cr_3O_{12}$: $\Delta G^{\circ}_{\mathrm{f(ox)}} \pm 4600/(\mathrm{J \cdot mol^{-1}}) = -517920 + 393.094\ (T/K)$

La_2CrO_6: $\Delta G^{\circ}_{\mathrm{f(ox)}} \pm 2300/(\mathrm{J \cdot mol^{-1}}) = -217052 + 132.211\ (T/K)$.

Thermodynamic properties of these compounds at T = 298.15 K are estimated using an approximate value for ΔC_P. The standard enthalpy of formation from elements at T = 298.15 K for $LaCrO_4$, $La_2Cr_3O_{12}$ and La_2CrO_6 are –1625.1 (±6), –4026.7 (±14.2) and –2684.1 (± 6.9) $kJ{\cdot}mol^{-1}$ respectively. The standard entropy of $LaCrO_4$, $La_2Cr_3O_{12}$ and La_2CrO_6 at 298.15 K are 110.2 (±4.2), 288.1 (±8.8) and 178.82 (±4.0) $kJ{\cdot}mol^{-1}{\cdot}K^{-1}$, respectively. Using the thermodynamic data for ternary oxides, sub-solidus phase relations in the system La–Cr–O are computed in different temperature intervals.

4.6. References

[1] J.B. Heywood, G.J. Womack: J.B. Heywood, G.J. Womack (Eds.), Open-Cycle MHD Power Generation. New York, 1969.

[2] S.M. Khetre, H.V. Jadhav, S.R. Bamane, Rasayan J.Chem. 2 (2009) 174–178.

[3] A.M Azad, R. Sudha, O.M. Sreedharan, J. Less Common Metals. 166 (1990) 57–62.

[4] J. Sfeir, J. Power Sources 118 (2003) 276–285.

[5] A.S. Mukasyan, C. Costello, K.P. Sherlock, D. Lafarga, A. Varma, Sep. Purif. Technol. 25 (2001) 117–126.

[6] T. Nakamura, G. Petzow, L. Gauckler, Mater. Res. Bull. 14 (1979) 649–659.

[7] Y. Jiang, J. Gao, M. Liu, Y. Wang, G. Meng, Mater. Lett. 61 (2007) 1908–1911.

[8] M. Chi, N. Browning, N. Orlovskaya, J Solid State Electrochem. 10 (2006) 659–662.

[9] D.L. Hoang, A. Dittmar, M. Schneider, A. Trunschke, H. Lieske, K.-W. Brzezinka, K. Witke, Thermochim. Acta 400 (2003) 153–163.

[10] I. Bueno, C. Parada, R. Saez Puche, Solid State Ionics 63–65 (1993) 707–713.

[11] A. Furusaki, H. Konno, R. Furuichi, Nippon Kagaku Kaishi (1992) 612–618.

[12] Y. Aoki, H. Konno, H. Tachikawa, M. Inagaki, Bull. Chem. Soc. Jpn. 73 (2000) 1197.

[13] H. Konno, H. Tachikawa, A. Furusaki, R. Furuichi, Anal. Sci. 8 (1992) 641–646.

[14] Y. Aoki, H. Konno, H. Tachikawa, J. Mater. Chem.11 (2001) 1214–1221.

[15] K.T. Jacob, D. Prusty, J. Alloys Compd. 507 (2010) L–17–20.

[16] K.T. Jacob, G. Rajitha, G.M. Kale, J. Alloys Compd. 481 (2009) 228–232.

[17] S.V. Varamban, K.T. Jacob, Mater. Sci. Eng. B. B49 (1997) 100-109.

[18] K.T. Jacob, S. Gupta, P. Singh, J. Am Cer. Soc. to be submitted.

[19] J.D. Carter, H.U. Anderson, M.G. Shumsky, J. Mater. Sci. 31 (1996) 551-57.

[20] O. Kubaschewski, C.B. Alcock, Metallurgical Thermo-Chemistry, 5th ed., Pergamon Press, Oxford, 1979.

[21] S.E. Ziemniak, L.M. Anovitz, R.A. Castelli, W. D. Porter, J. Chem. Thermodyn. 39 (2007) 1474–1492.

[22] O. Knacke, O. Kubaschewski, K. Hesselmann (Eds.), Thermochemical Properties of Inorganic Substances, Springer-Verlag Publishing, Heidelberg and Verlag Stahleisen mbH, Dusseldorf, 1991.

[23] E.M. Savitskii, V.F. Terekhova, A.V. Kholopov, Russ. Inorg. Chem. 5 (1960) 362–363.

CHAPTER 5: MANGANESE DOPED LANTHANUM-STRONTIUM CHROMITE FUEL ELECTRODE FOR SOLID OXIDE FUEL CELL AND OXYGEN TRANSPORT MEMBRANE SYSTEMS

5.1. Abstract

$(La_{0.75}Sr_{0.25})_{0.95}Cr_{0.7}Mn_{0.3}O_3$ (LSCM) mixed with 8YSZ has promising attributes to function as fuel electrode and electrolyte membrane in high temperature electrochemical devices including solid oxide fuel cell as well as oxygen transport membrane systems. In this study, electrochemical performance of the symmetrical cells of the configuration LSCM/8YSZ//8YSZ//LSCM/8YSZ is investigated under simulating device operating conditions. Role of temperature (850-950°C) and bias (0-0.8V) is evaluated on the electrochemical impedance of the symmetrical cells in oxidizing (air) and reducing atmosphere (Ar-3%H_2-3%H_2O). Higher performance is obtained in oxidizing when compared to reducing atmosphere. Bulk, surface and the electrode/electrolyte interfaces are examined during post-test characterization of the tested cells. No electrode delamination as well as no interface layer or compound formation is identified in the bulk and/or interface in both oxidizing and reducing atmosphere.

5.2. Introduction

Increasing energy demand and the drive for reducing the global environmental issues such as global warming and harmful gas emissions (NO_x and SO_x) calls for clean, sustainable and efficient advanced technologies. Solid oxide fuel cells (SOFC) and oxygen transport membrane (OTM) systems are the potential alternate clean energy solutions for conversion of chemical energy into electricity and heat as well efficient fuel combustion with

almost no emissions (1-6). OTM system is also beneficial for syngas production, which can be further processed to obtain liquid fuel for transportation using Fischer–Tropsch process [1]. However, there are few challenges in the stable performance of these systems due to instability of their material exposed to fuel atmosphere.

Ni-YSZ is considered as the state of art material for fuel side electrode due to its high electro-catalytic activity and mixed electronic and ionic conductivity [5-6]. However, carbon formation and large volume change during redox cycling are the major challenges of this fuel electrode (7). Currently, A and B-site doped lanthanum chromite based perovskites are being investigated as they are stable in fuel atmosphere at high temperatures [8-9]. Manganese doped lanthanum-strontium chromite is considered as one of the promising fuel electrode as it provides the combination of high electrical conductivity and electrochemical activity as well as good thermal expansion match with the state of the art electrolyte (8YSZ) [1-4, 10-15]. The electrode polarization resistance for $La_{0.75}Sr_{0.25}Cr_{0.5}Mn_{0.5}O_{3-\delta}$ is demonstrated as 0.2 Ω cm^2 when exposed to 97%H_2-3%H_2O at 900°C, similar to Ni/YSZ cermets (16). The conductivity of $La_{0.75}Sr_{0.25}Cr_{0.5}Mn_{0.5}O_3$ is found to be 38 S cm^{-1} at 900°C which does not change for oxygen partial pressure (PO_2) above 10^{-10} atm [15]. In addition, the thermal expansion coefficient (TEC) of $La_{0.75}Sr_{0.25}Cr_{0.5}Mn_{0.5}O_3$ is measured as 9.3×10^{-6} K^{-1} in the temperature range of 65-955°C, comparable to 8YSZ (10.3×10^{-6} K^{-1}). However, $La_{0.75}Sr_{0.25}Cr_{0.5}Mn_{0.5}O_{3-\delta}$ with higher Mn-doping level tends to destabilize when exposed to reducing atmosphere. For instance, $(La,Sr)_2MnO_4$ and MnO secondary phases are identified for $La_{0.75}Sr_{0.25}Cr_{0.5}Mn_{0.5}O_{3-\delta}$ at 900°C and 10^{-20} atm [17].

In this study, therefore, we evaluate the electrochemical performance of LSCM with lower Mn concentration and when mixed with 8YSZ in order to improve the oxygen ions

conduction. The testing is performed in oxidizing (air) as well as reducing atmosphere (Ar-3%H_2-3%H_2O) in the device operating temperature range i.e. 850-950°C. The effect of bias variation is also studied on the electrochemical behavior and stability of the composite.

5.3. Experimental

5.3.1. *LSCM and 8YSZ composite based symmetric cell fabrication*

LSCM powder was arranged from Praxair Inc. Afterwards, the LSCM powder was mixed with 8YSZ in the 50: 50 weight ratios and LSCM/8YSZ paste was prepared utilizing ink vehicle (Fuel Cell Materials). LSCM/8YSZ working and counter electrode with the thickness of ~20 µm and diameter ~10 mm were screen-printed on both sides of 8YSZ electrolyte (thickness ~200 µm; Fuel Cell Materials). The electrode layers were dried and sintered at ~1200°C with the heating rate of 3°C/min for 2 h in air. Platinum paste (Electro-Science Laboratories Inc.) was utilized to attach platinum screen current collector and platinum wires to each electrode layer. Curing of the platinum paste was obtained at ~900°C for 1 h in air atmosphere. Subsequently, LSCM/8YSZ//8YSZ//LSCM/8YSZ symmetric cells were installed in a tubular alumina reaction chamber in the furnace. Multi-channel potentiostat (VMP2, Bio-Logic) were used for electrochemical cell measurement.

5.3.2. *Electrochemical testing*

Symmetrical cells of configuration LSCM/8YSZ//8YSZ//LSCM/8YSZ were heated in the temperature range of 850-950°C and exposed to oxidizing (air) and reducing gas (Ar-3%H_2-3%H_2O) atmosphere with a flow rate of 300 sccm. Bias varying from 0-0.8 V was applied using the potentiostat. Electrochemical impedance was measured in the frequency range of 100 mHz - 200 kHz utilizing a 10 mV alternating current. Experiments were

repeated to ensure reproducibility. Post-test characterization of the tested symmetrical cells was conducted using the SEM-EDS.

5.4. Results and Discussion

5.4.1. *Electrochemical measurements and post-test observations*

Measurements at different temperatures (850°C, 900°C and 950°C), bias (0 V, 0.3 V, 0.5 V and 0.8V) and varying gas compositions (air and Ar-3%H_2-3%H_2O) were performed in order to evaluate the different electrochemical behavior and stability of the LSCM/8YSZ composite based symmetrical cells. Fig. 5.1 and 5.2 shows nyquist plots of impedance spectra obtained from the symmetrical cell (LSCM/8YSZ//8YSZ//LSCM/8YSZ) testing in the temperature range of 850-950°C with bias varying from 0-0.8V in oxidizing (air) and reducing atmosphere (Ar-3%H_2-3%H_2O) respectively. High frequency intercept represents ohmic resistance, while non-ohmic contributions are represented by the semicircle diameter [18]. In reducing atmosphere, two semicircles are observed and correspond to the ion transfer through the microstructure and/or electrochemical kinetics of the electrode material (high frequency) and charge transfer at the interface (low frequency) [19-20]. However, the two electrode arcs get merged in oxidizing atmosphere [19]. From the impedance spectra's in Fig. 5.1 and 5.2, it is identified that the performance increases with increase in temperature and bias. Similar trend is obtained in oxidizing as well as reducing atmosphere as shown in Fig. 5.1 and 5.2. However, higher performance is achieved for the cell tested in air when compared to Ar-3%H_2-3%H_2O. Fig. 5.3 shows non-ohmic resistance of the symmetrical cell of configuration LSCM/8YSZ//8YSZ//LSCM/8YSZ as a function of temperature (850-950°C) with varying bias (0-0.8V). The non-ohmic resistance increases with increase in temperature and bias in oxidizing and reducing atmosphere.

Fig. 5.4 shows the comparison of non-ohmic resistance of the tested cells in the temperature range of 850-950°C at 0 V and 0.5 V. In oxidizing atmosphere, lower resistance is measured when compared to reducing atmosphere. It increases from ~7.9 to 9.5 $\Omega.cm^2$ when gas is switched from air to Ar-3%H_2-3%H_2O respectively under no bias (0 V) at 950°C. Under the constant bias of 0.5 V and 950°C, the resistance increases from ~5.6 (air) to 7.8 $\Omega.cm^2$ (Ar-3%H_2-3%H_2O). The trend in resistance changes for 0.3 V and 0.8 V is similar to those observed at 0 V and 0.5 V. The plots are omitted for brevity. The difference in the non-ohmic resistance corresponds to the electrode kinetics that gets affected by the variation in oxygen partial pressure and/or H_2 adsorption/desorption on the surface when gas atmosphere is changed from to air and Ar-3%H_2-3%H_2O [20].

After the electrochemical testing on the LSCM/8YSZ based symmetrical cells, the tested cells were first visually examined to confirm on the electrode integrity with the 8YSZ electrolyte. No delamination of the electrode layers was identified on the examination. Subsequently, the tested symmetrical tested cells were characterized to understand the degradation behavior in oxidizing and reducing atmosphere. No interface layer or compound formation is identified during the surface/interface/bulk analysis of the tested cells using SEM-EDS. This is shown in Fig. 5.5. No microstructural changes are observed in the air as well as Ar-3%H_2-3%H_2O tested symmetrical cells as shown in Fig. 5.5. This corresponds to the stability of LSCM/8YSZ composite in oxidizing and reducing atmosphere required for OTM and SOFC systems.

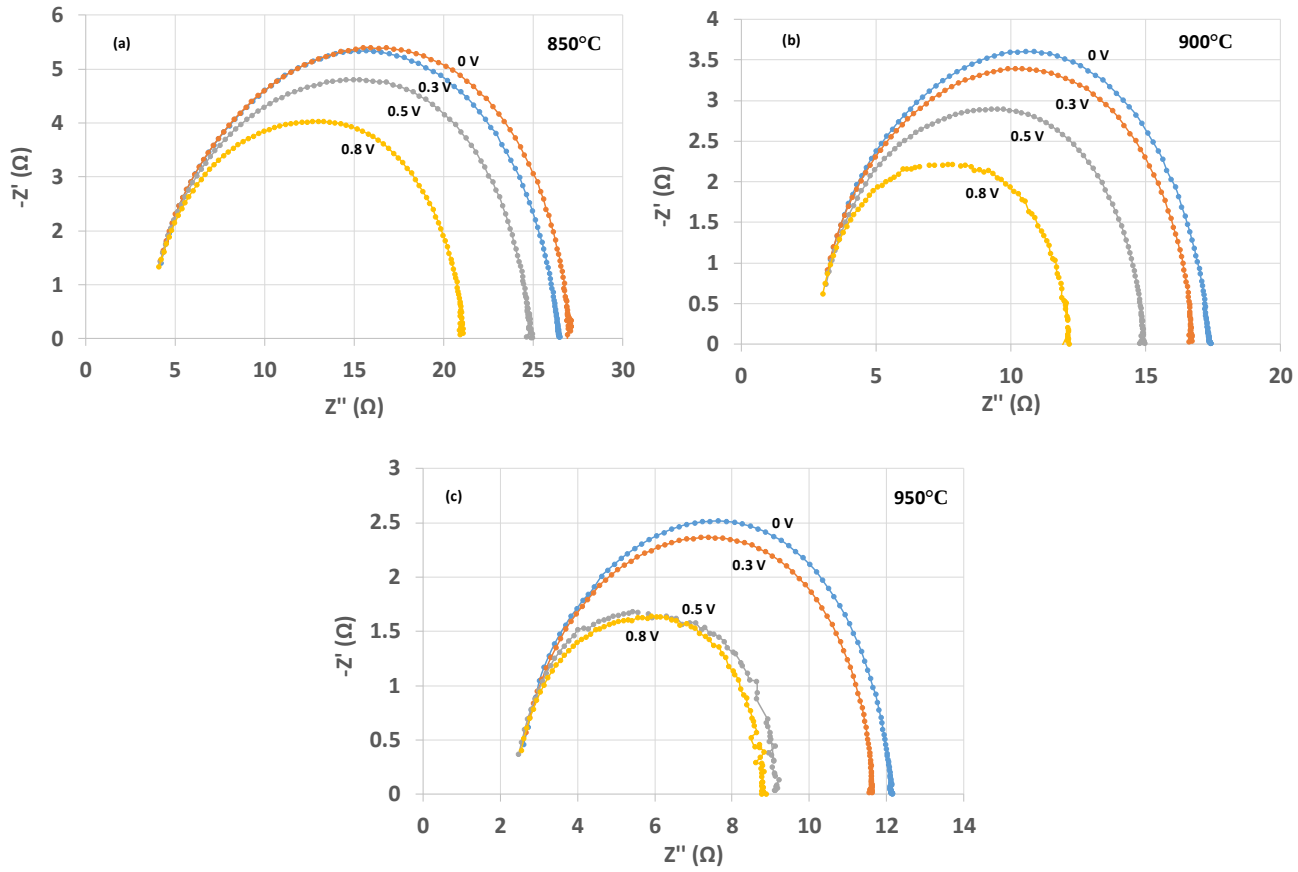

Fig. 5.1. Nyquist plots of impedance spectra acquired from symmetrical cell testing of configuration LSCM/8YSZ//8YSZ//LSCM/8YSZ in oxidizing atmosphere (air): (a) 850°C, (b) 900°C and (c) 950°C.

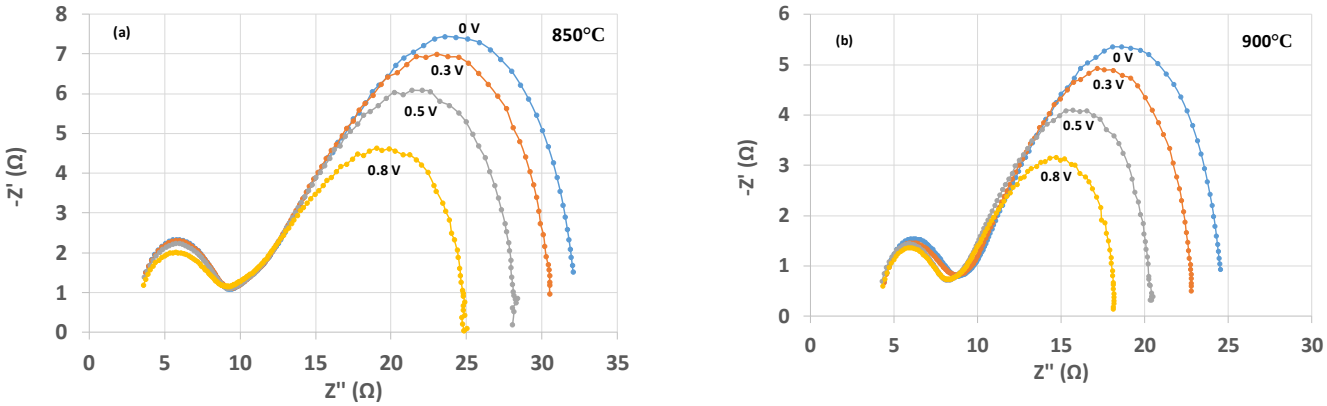

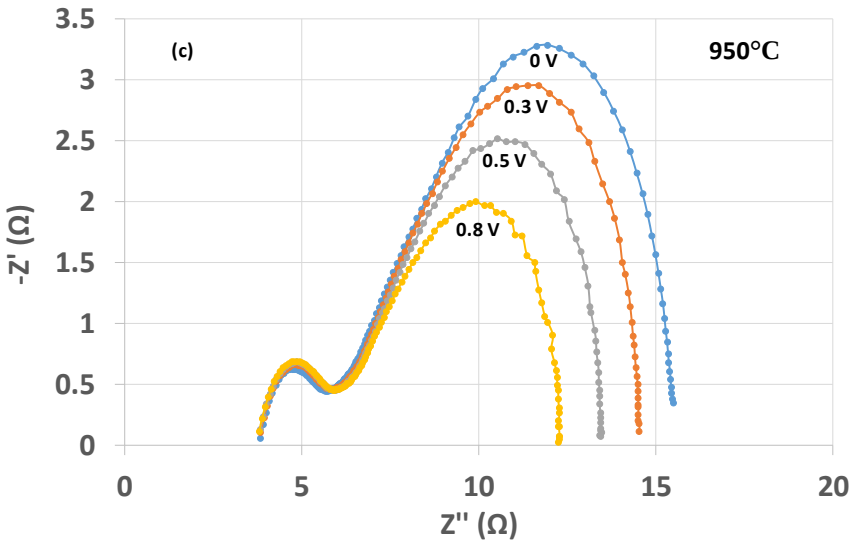

Fig. 5.2. Nyquist plots of impedance spectra acquired from symmetrical cell testing of configuration LSCM/8YSZ//8YSZ//LSCM/8YSZ in reducing atmosphere (Ar-3%H_2-3%H_2O): (a) 850°C, (b) 900°C and (c) 950°C.

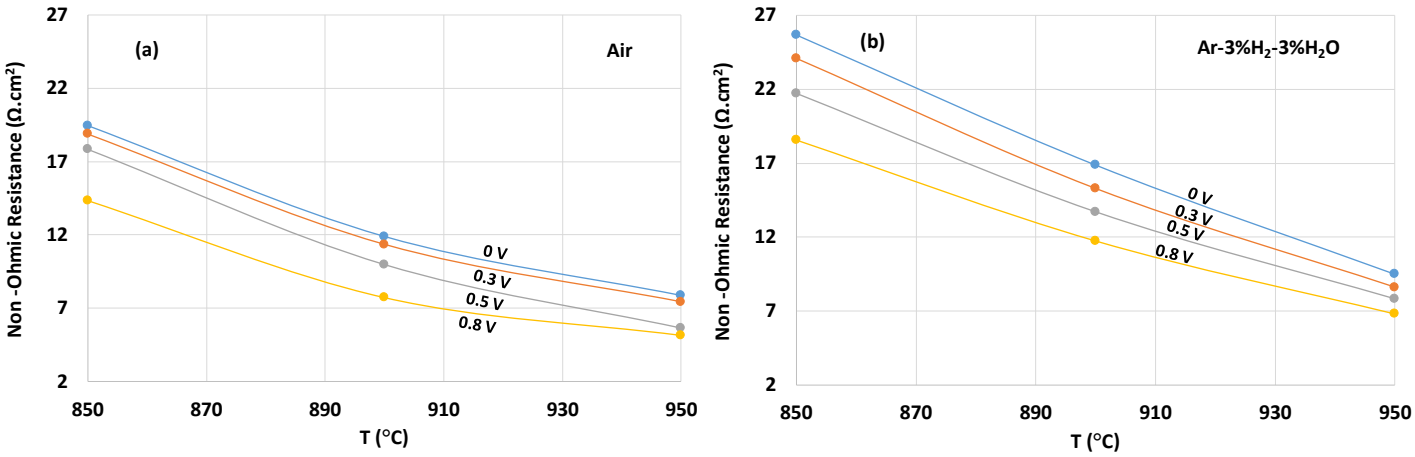

Fig. 5.3. Non-ohmic resistance of symmetrical cell of configuration LSCM/8YSZ//8YSZ//LSCM/8YSZ: (a) Air and (b) Ar-3%H_2-3%H_2O.

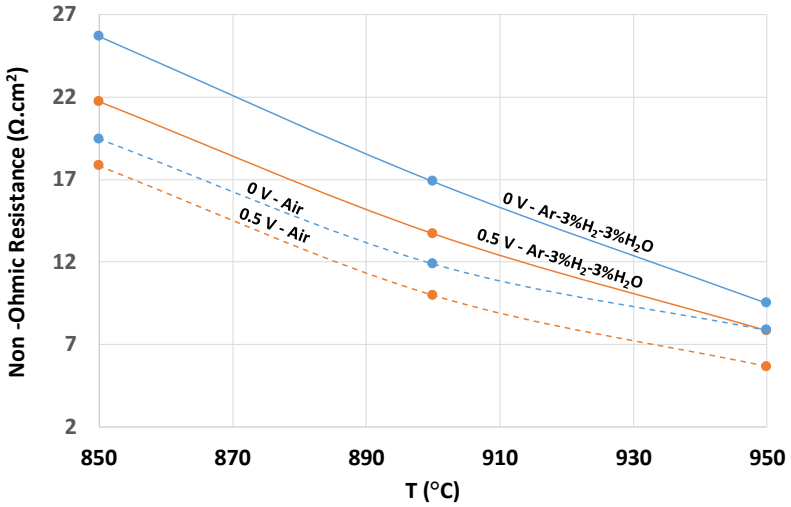

Fig. 5.4. Comparison of non-ohmic resistance of symmetrical cell of configuration LSCM/8YSZ//8YSZ//LSCM/8YSZ at 950°C under constant bias of 0 V and 0.5 V in air and Ar-3%H_2-3%H_2O.

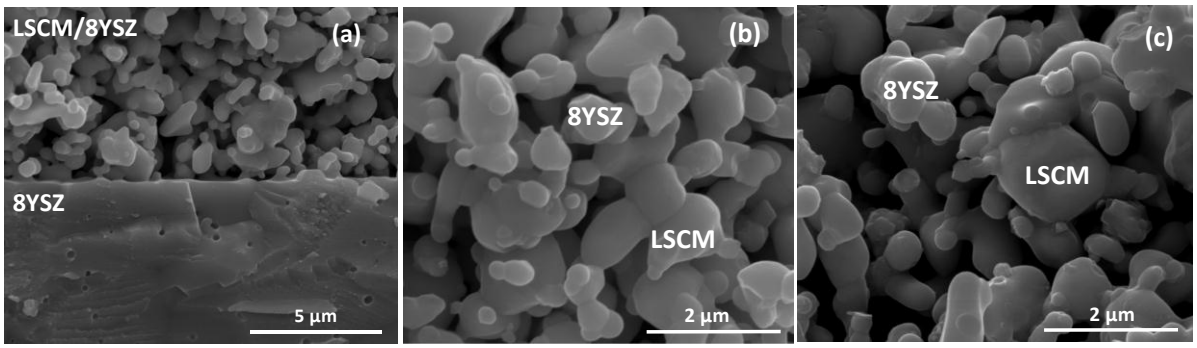

Fig. 5.5. SEM micrographs of post-tested symmetrical cells of configuration LSCM/8YSZ//8YSZ//LSCM/8YSZ: (a) Electrode/electrolyte interface, (b) Anode side electrode surface in air and (c) Anode side electrode surface in Ar-3%H_2-3%H_2O.

5.5. Conclusions

LSCM/8YSZ composite based symmetrical cells of the configuration LSCM/8YSZ//8YSZ/LSCM/8YSZ are synthesized in air atmosphere at ~1200°C. Electrochemical performance of the cells has been measured in the operating temperature range of 850-950°C and the bias varying from 0 V to 0.5 V in oxidizing and reducing atmosphere. Higher performance is achieved in air when compared to Ar-3%H_2-3%H_2O. Using, SEM-EDS, no interface reaction between the electrode and electrolyte is identified in the post-tested cells. In addition, no secondary phase formation is observed at the surface as well as in the bulk.

5.6. References

[1] S. Gupta, M. K. Mahapatra and P. Singh, MSE: R: Reports 90 (2015) 1-36 http://dx.doi.org/10.1016/j.mser.2015.01.001.

[2] S. Gupta, M. K. Mahapatra and P. Singh, Mater. Res. Bull. 48 (2013) 3262-3267.

[3] K. T. Jacob, S. Gupta and P. Singh. J. Am. Ceram. Soc. 96 (2013) 3933-3938.

[4] K. T. Jacob, S. Gupta and P. Singh. J. Am. Ceram. Soc. 96 (2013) 3272-3278.

[5] J. Sfeir. J. Power Sources 118 (2003) 276–285.

[6] A. Atkinson, S. Barnett, R. J. Gorte, J.T.S. Irvine, A. J. McEvoy, M. Moguensen, S. C. Singhal and J. Vohs. Nat. Mater. 3 (2004) 17–27.

[7] V. B. Vert, F. V. Melo, L. Navarrete and J. M. Serra. Appl. Catal. B: Environ. 115 (2012) 346–356.

[8] P. Duran, J. Tartaj, F. Capel and C. Moure. J. Eur. Ceram. Soc. 24 (2004) 2619–2629.

[9] A. S. Mukasyan, C. Costello, K. P. Sherlock, D. Lafarga and A. Varma, Sep. and Purif. Technol. 25 (2001) 117–126.

[10] V. V. Kharton, E. V. Tsipis, I. P. Marozau, A. P. Viskup, J. R. Frade and J. T. S. Irvine. Solid State Ionics 178 (2007) 101–113.

[11] T. Norby, R. Hildrum, M. Seiersten, R. Glenne, P. A. Osborg and O. Dyrlie, Proceedings of the European Solid Oxide Fuel Cell Forum I, Switzerland, 1994.

[12] V. A. Kolotygin, E. V. Tsipis, A. L. Shaula, E. N. Naumovich, J. R. Frade, S.I. Bredikhin and V.V. Kharton. J. Solid State Electrochem. 15 (2011) 313–327.

[13] J. G. M. I. Furtado and R. N. Oliveira. Revista Matéria 13 (2008) 147–153.

[14] T. Nakamura, G. Petzow and L. Gauckler. Mater. Res. Bull. 14 (1979) 649–659.

[15] S. Tao and J. T. S. Irvine. J. Electrochem. Soc. 151 (2004) A252–259.

[16] S. Tao and J. T. S. Irvine. Nat. Mater. 2 (2003) 320-323.

[17] M. Oishi, K. Yashiro, K. Sato, J. Mizusaki and T. Kawada. J. Solid State Chem. 181, (2008) 3177–3184.

[18] M. Keane, M. K. Mahapatra, A. Verma, P. Singh. Int. J. Hydrogen Energy 37 (2012) 16776 -16785.

[19] D. M. Bastidas, S. Tao and J. T. S. Irvine. J. Mat. Chem. 16 (2006) 1603-1605.

[20] P. Blennow, K. K. Hansen, L. R. Wallenberg and M. Mogensen, Solid State Ionics 180 (2009) 63-70.

CHAPTER 6: PROCESSING AND ELECTROCHEMICAL PERFORMANCE OF MANGANESE-DOPED LANTHANUM-STRONTIUM CHROMITE IN OXIDIZING AND REDUCING ATMOSPHERES

6.1. Abstract

This study reports the role of oxygen partial pressure (PO_2) on the microstructural changes and compound formation during the exposure of $(La_{0.75}Sr_{0.25})_{0.95}Cr_{0.7}Mn_{0.3}O_3$ (LSCM73) to 1400°C to emulate oxygen transport membrane device fabrication. Results of electrochemical testing of LSCM73+8YSZ//8YSZ//LSCM73+8YSZ symmetrical cells, is also reported at 950°C with time for 80h in oxidizing (air) and reducing atmospheres (Ar-3%H_2-3%H_2O). Our results from elevated temperature exposure studies show a decrease in the density during exposure to reducing atmospheres due to the absence of liquid phase assisted sintering and inability to form $SrCrO_4$. Formation of rhombohedral structure and $MnCr_2O_4$ spinel phase is evident in air whereas Mn_3O_4 phase formation occurs along with lattice transformation to cubic structure at lower PO_2. Our experimental results are in agreement with LSCM73 phase diagram constructed using Thermo-Calc. Stable electrochemical performance is obtained in air and in reducing atmosphere, non- ohmic resistance increases with time which is attributed to Sr-segregation on LSCM73 surface and interaction between LSCM/8YSZ. No delamination of the electrode layer is observed in both oxidizing and reducing atmosphere.

6.2. Introduction

The world energy council projects primary energy demand to increase dramatically in the future as population grows and developing nations elevate their living standards.

Finding an effective and timely solution to the emerging global climate change and related environmental issues are universally recognized as the major challenge of this decade. High temperature (≥650°C) solid-state electrochemical devices such as oxygen transport membrane (OTM) enables clean and efficient utilization of fossil fuels via oxy-combustion [1-2]. The technology can be adapted globally to enhance energy efficiency, reduce carbon foot print and extend the fuel reserve for future [1-4]. OTM system is also advantageous for tonnage oxygen production and syngas production which can be further processed for hydrogen production via water gas shift reaction [3]. The syngas can also be converted into liquid fuels for transportation via Fischer-Tropsch process [5].

Oxygen transport membrane system consist of three layers i.e. air electrode (surface exchange layer), oxygen transport membrane and fuel electrode (intermediate layer) [6]. Oxygen molecules from air dissociate into oxygen ions at the air electrode, migrate through the membrane, and recombine with the electron to form oxygen molecule on the fuel side [7]. The driving force for the selective oxygen transport is the existence of oxygen partial pressure gradient. Air and fuel electrodes are used to enhance surface exchange kinetics and improve the oxygen flux performance of OTM system [7]. Wide spread implementation of the aforesaid, however, remains critically limited by the current unfavorable economics, unproven reliability and lack of longevity.

Chemical/structural/redox stability and high ionic as well as electronic conductivity have been identified as one of the key requirements for oxygen transport membrane and fuel electrode [8-9]. Ni-YSZ is conventionally used as the fuel electrode for SOFC due to its excellent electro-catalytic activity, electronic and ionic conductivity and thermal expansion match with the electrolyte. However, carbon deposition, volume change

during redox cycling and susceptibility to sulphur poisoning are the limitations of Ni-YSZ [10]. To overcome the limitations of Ni-YSZ, mixed ionic and electronic conducting perovskites with/without fluorite phase are being considered as an alternative SOFC anode and membrane/fuel electrode for OTM device [11-12]. This paper focuses on materials development for oxygen transport membrane (OTM) system. However, the results can also be utilized for the development of SOFC fuel electrode.

Lanthanum chromite based perovskites have been studied extensively as an oxygen transport membrane and fuel electrode [13-26]. This is due to its high chemical and structural stability at high temperatures in oxidizing as well as reducing atmospheres. Lanthanum chromite is commonly doped with alkaline earth metal at A-site and transition metal at B-site for improving its electrical conductivity, electrochemical performance, thermal expansion coefficient and densification. The dopants, on the other hand, have also been found to deteriorate the structural and thermo-chemical stability of these materials specifically in reducing atmosphere ($\leq 10^{-10}$ atm). A review article is recently published on the effect of A and B-site dopants on the structure-thermal-electrical-mechanical properties of lanthanum chromite based materials for oxygen transport membrane by Gupta et al. [16].

$La_{0.75}Sr_{0.25}Cr_{1-x}Mn_xO_3$ (LSCMx) is being investigated for fuel side electrode and oxygen transport membrane (OTM) as it provides the combination of high electrochemical activity, high electrical conductivity and good thermal expansion match with 8YSZ [16-19, 25-30]. LSCMx is also identified as promising fuel electrode for direct utilization of hydrocarbon fuels [27]. The electrode polarization resistance for $La_{0.75}Sr_{0.25}Cr_{0.5}Mn_{0.5}O_{3-\delta}$ (LSCM55) is 0.2 Ω cm^2 at 900°C in 97%H_2-3%H_2O, comparable to Ni/YSZ cermets [30]. The conductivity of $La_{0.75}Sr_{0.25}Cr_{0.5}Mn_{0.5}O_3$ is 38 S cm^{-1} at 900°C and remains same for

PO_2 values above 10^{-10} atm [29-30]. However, further lowering of PO_2 to ~10^{-21} atm, the conductivity decreases to 1.5 S cm^{-1} [29-30]. The thermal expansion coefficient (TEC) of LSCM55 is 9.3×10^{-6} K^{-1} in air in the temperature range of 64-956°C. The TEC is comparable to 8YSZ (10.3×10^{-6} K^{-1}), a most commonly used oxygen ion conducting fluorite phase [31].

For lanthanum chromite based materials, density increases with decreasing oxygen partial pressure [32-33]. Because, the vapor pressure of CrO_3 significantly decreases in reducing atmospheres. Subsequently, Cr_2O_3 deposition at the inter-particle necks is inhibited resulting in higher densification [32-33]. The sintering behavior of A-site doped lanthanum chromite based materials is well known in the literature [16].

As mentioned above, these materials are further doped at B-site to improve the structural-thermal-electrical properties as required for OTM system. However, the sintering behavior of simultaneously A-site and B-site doped $LaCrO_3$ is not investigated in the literature. In this study, we report the sintering and electrochemical behavior of manganese-doped lanthanum-strontium chromite, which is one of the most promising candidates for oxygen transport membrane and fuel electrode. However, LSCMx with higher Mn-doping level destabilizes in reducing atmosphere. For example, $(La,Sr)_2MnO_4$ and MnO secondary phases have been detected for LSCM55 when exposed to 900°C and 10^{-20} atm [34]. Formation of Mn-Cr-O spinel ($MnCr_2O_4$) has also been indicated in LSCM55 [35]. In reducing atmosphere, the spinel phase reduces to MnO [35-36]. The results exhibit that LSCMx with high Mn doping level (LSCM55) is not stable in reducing atmosphere [16, 35-36]. Furthermore, it is identified in the recently published review article that B-site (e.g. Mn) doping level is good to be restricted (≤30 mol.%) from stability point of view [16].

However, in the reported literature, LSCMx is not investigated with higher Cr: Mn ratio or lower Mn doping level under OTM processing and operating conditions. Therefore, a composition with lower concentration of Mn i.e. $(La_{0.75}Sr_{0.25})_{0.95}Cr_{0.7}Mn_{0.3}O_{3-\delta}$ (LSCM73) is chosen for this study. A-site deficient composition is chosen for this study to avoid the Sr-segregation which is likely to occur in lanthanum strontium manganite/chromite based materials [16, 37]. Furthermore, A-site deficiency is found to be beneficial to avoid the interaction of lanthanum strontium manganite/chromite based materials with stabilized zirconia fluorite phase to form insulating phase such as $La_2Zr_2O_7$ and $SrZrO_3$ [16, 38]. Sintering behavior and microstructure analysis of LSCM73 is examined under simulating OTM fabrication conditions (~1400°C and PO_2 ~ 0.21-10^{-10} atm). On the other hand, electrochemical impedance measurement is performed at lower temperature under simulating anodic OTM operation conditions (~950°C and ~10^{-17} atm).

6.3. Experimental

6.3.1. *$(La_{0.75}Sr_{0.25})_{0.95}Cr_{0.7}Mn_{0.3}O_{3-\delta}$ synthesis*

LSCM73 powder was obtained from Praxair Inc. The particle size distribution of the powder was D_{50} = 1.34μm. The powder was uniaxially pressed into cylindrical pellets. Subsequently, LSCM73 powder was also mixed with 0.5%$SrCrO_4$ to understand the effect of $SrCrO_4$ on densification and validate our results and hypothesis. The pellets were bisque fired at 1100°C for 4h and then, sintered in air, N_2 (~10^{-5} atm) and Ar-3%H_2-3%H_2O (~10^{-10} atm) atmosphere at 1400°C with 10h dwell time. Samples were cooled in the flowing gas environment to ensure the maintenance of the oxygen pressure during cooling.

6.3.2. *Characterization*

Density of all the samples was measured using Archimedes principle. The microstructural analysis was conducted using scanning electron microscope (FEI - ESEM Quanta 250, Hillsboro, OH). Energy dispersive spectroscopy (EDS) attached to the SEM was used for elemental compositional analysis.

X-ray diffraction (BRUKER-D8 ADVANCE, Bruker AXS Inc. Madison, WI) technique was used to determine the crystal structure of LSCM73 and secondary compounds, if any, sintered in different gas atmospheres. The scan step was 0.02° using CuK_{α} radiation (λ = 1.5406 Å).

6.3.3. *Symmetric cell fabrication*

LSCM73 is predominantly electronic conductor, and therefore mixed with 8YSZ for ionic conduction in 50:50 weight ratios for the fabrication of symmetrical cell and testing. LSCM73+8YSZ paste was prepared using ink vehicle (Fuel Cell Materials). LSCM73+8YSZ working and counter electrodes (thickness: ~20 µm, diameter: 10 mm) were screen-printed on both sides of 200 µm thick $(ZrO_2)_{0.92}(Y_2O_3)_{0.08}$(YSZ) electrolyte (Fuel Cell Materials). After drying at room temperature, the electrodes were sintered at 1200°C (heating rate of 3°C/min) for 2 h in air. Lower sintering temperature (1200°C) was chosen for fabrication of the cell to obtain porous electrode layer as well as to avoid secondary phase's formation that were observed at 1400°C. No secondary phases are identified in the as-sintered symmetrical cells. Platinum screen current collector (Alfa Aesar, 50 mesh) and platinum wires (Alfa Aesar, 0.25 mm) were attached to each electrode using platinum paste (Electro-Science Laboratories Inc.). The platinum paste was cured in air at 900°C for 1 h (3°C/min). The electrochemical active area of the cell electrode was calculated to be 0.8 cm^2. As-assembled

symmetric cells of configuration LSCM73+8YSZ //8YSZ//LSCM73+8YSZ were installed in a tubular alumina reaction chamber placed in the constant temperature zone of a furnace. The leads from a multi-channel potentiostat (VMP2, Bio-Logic) were attached to the assembled symmetric cell.

6.3.4. *Electrochemical testing*

The symmetrical cells were heated to 950°C (3°C/min) in flowing air and Ar-3%H_2-3%H_2O with flow rate maintained at 300sccm. 3% water vapor was introduced in the Ar-3%H_2 gas stream through a water bubbler at room temperature. Using the potentiostat, a pre-determined constant bias of 0.5V was applied for 80 h. The impedance was measured (at four hour intervals) in the frequency range from 100 mHz to 200 kHz using a 10 mV alternating current. To ensure reproducibility, experiments were repeated several times at the imposed voltage condition. Post-test characterization of the symmetrical cells was performed using SEM-EDS (FEI - ESEM Quanta 250).

6.4. Results and Discussion

6.4.1. *Crystal Structure*

Fig. 6.1 shows the XRD pattern of LSCM73 bisque-fired at 1100°C in air and sintered at 1400°C in air, N_2, and Ar-3%H_2-3%H_2O atmosphere. Extra peaks corresponding to the $SrCrO_4$ (JCPDS 073-1082) are identified in the bisque-fired sample in agreement with SrO-Cr_2O_3-La_2O_3 phase diagram [39]. The width of the peaks appears to increase likely due to the diminution of the perovskite grain size with decreasing in the PO_2 as is indicated in the next section 6.4.2. The crystal structure for LSCM73 is rhombohedral (JCPDS 75-9872). However, the peaks splitting corresponding to the rhombohedral phase decreases with decrease in PO_2. And, it almost disappears in case of the samples sintered in

Ar-3%H_2-3%H_2O attributing to less distortion of the lattice and higher symmetry phase formation. The possible higher symmetry phase is cubic (JCPDS 074-1961) after rhombohedral [36]. This is consistent with the co-existence of cubic and rhombohedral phase for LSCM73 when sintered in N_2. But, in Ar-3%H_2-3%H_2O, predominantly cubic phase is identified corresponding to disappearance of the peaks splitting and phase transformation to the higher symmetry phase. In future, a detailed study will be investigated for in-depth understanding of the phase transformation as a function of PO_2.

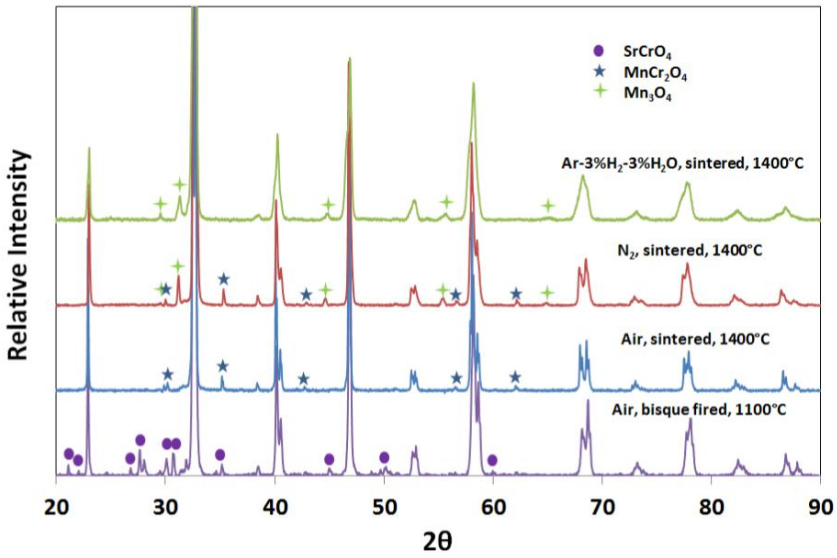

Fig. 6.1. XRD pattern of LSCM73 bisque-fired (1100°C) in air and sintered (1400°C) in air, N_2 and Ar-3%H_2-3%H_2O.

In case of air and N_2 atmosphere, new peaks are identified as Mn-Cr-O spinel phase (marked by blue five pointed star) i.e. $MnCr_2O_4$ (JCPDS 075-1614) as shown in Fig. 6.1. The peaks disappearance corresponding to $MnCr_2O_4$ is observed for the samples sintered in Ar-3%H_2-3%H_2O atmosphere. However, presence of new peaks (marked by green four pointed star) is observed for the samples sintered in lower oxygen partial pressure (N_2 and Ar-3%H_2-3%H_2O). The peaks are identified as Mn_3O_4 (JCPDS 086-2337) in reducing gas

atmospheres [36, 40]. Co-existence of $MnCr_2O_4$ and Mn_3O_4 is observed for the samples sintered in N_2 (~10^{-5} atm) atmosphere. However, in Ar-3%H_2-3%H_2O atmosphere, only Mn_3O_4 peaks are identified.

6.4.2. *Sintering behavior and Microstructural Analysis*

Fig. 6.2 shows the density of LSCM73 as a function of oxygen partial pressure (PO_2) sintered at 1400°C for 10h. The density of bisque fired sample is ~48% which increases to ~68% for air sintered sample. However, it decreases to ~56% with decrease in PO_2 for the sample sintered in Ar-3%H_2-3%H_2O. Also, the average grain size decreases from 3.0μm (air) to 1.2μm (N_2) to 0.6μm (Ar-3%H_2-3%H_2O) with decrease in PO_2. Fig. 6.3 shows the polished surface SEM microstructures of the samples sintered in air, N_2 (~10^{-5} atm) and Ar-3%H_2-3%H_2O (~10^{-10} atm) gas atmosphere. In oxidizing atmosphere (air), secondary phases have been observed predominantly at grain boundaries as marked in Fig. 6.3a. Elemental analysis reveals that the secondary phases mainly consist of Mn and Cr with small amount of La and Sr as shown in Table 6.1. Fig. 6.4 shows the elemental mapping of air sintered sample with enriched Mn and Cr phases. These phases are $MnCr_2O_4$ spinel as confirmed from XRD. The spinel formation decreases with decrease in PO_2. However, a new Mn-rich phase is observed in the samples sintered in reducing atmosphere, and it increases with decreasing oxygen partial pressure as shown in Fig 6.3b and c. This is also observed in the elemental mapping (Fig. 6.5) of LSCM73 sintered in Ar-3%H_2-3%H_2O. Table 6.2 shows the SEM-EDS elemental analysis of Mn-rich phase and bulk. The phase is identified as Mn_3O_4 using XRD in Fig 6.1.

It is known that densification of Sr-doped $LaCrO_3$ is assisted by liquid phase ($SrCrO_4$) sintering [41]. The reaction (1) is favored at an oxygen partial pressure of 0.21 atm.

$SrO\,(s) + 1/2Cr_2O_3\,(s) + 3/4O_2 \leftrightarrow SrCrO_4\,(s)$ (1)

Gibb's free energy formation for $SrCrO_4$ are −158 and −50 kJ mol^{-1} at PO_2 ~ 0.21 and 10^{-5} atm (900°C) respectively. With decreasing oxygen partial pressure, the Gibb's free energy for the formation of $SrCrO_4$ increases, and becomes positive at 900°C for the partial pressures less than $10^{-7.2}$ atm. For example, the free energy for $SrCrO_4$ formation is +75 kJ mol^{-1} at ~10^{-10} atm 900°C [42]. In addition, according to SrO-Cr_2O_3-La_2O_3 system, $SrCrO_4$ phase is unstable at low oxygen partial pressure (~10^{-9} atm) at 1600°C [39].

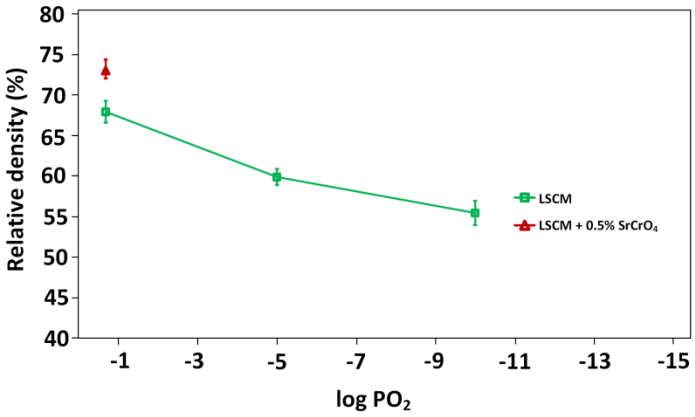

Fig. 6.2. Relative density of sintered LSCM73 in air (0.21 atm), N_2 (10^{-5} atm) and Ar-3%H_2-3%H_2O (10^{-10} atm).

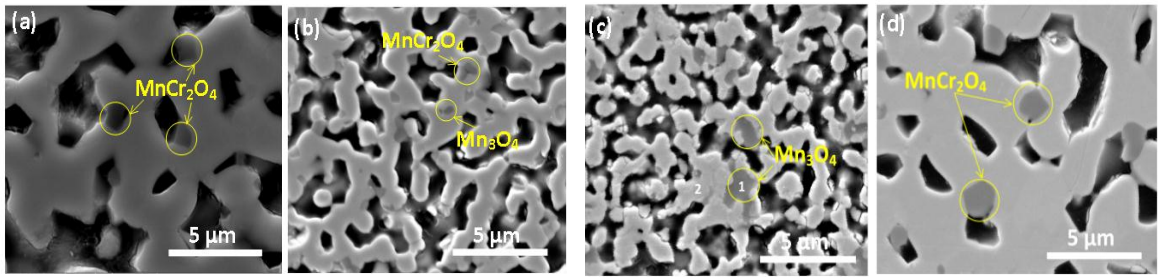

Fig. 6.3. Polished surface SEM micrographs of sintered LSCM73 in a) air, b) N_2, c) Ar-3%H_2-3%H_2O, and d) air (with 0.5% $SrCrO_4$).

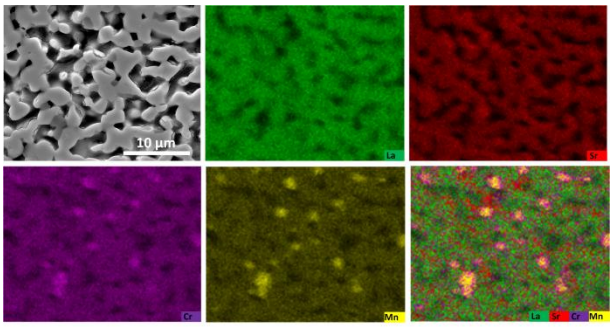

Fig. 6.4. Elemental mapping of polished surface SEM micrographs of sintered LSCM73 in air.

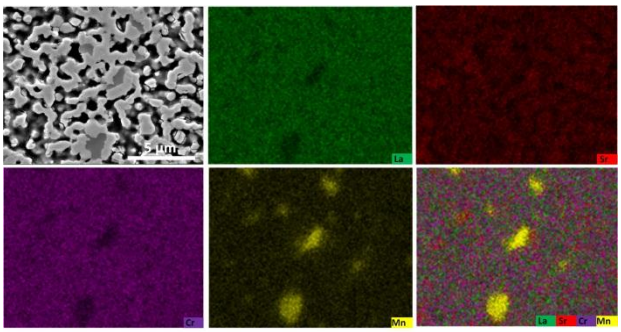

Fig. 6.5. Elemental mapping of polished surface SEM micrographs of sintered LSCM73 in Ar-3%H_2-3%H_2O atmosphere.

In case of A-site doped $La_{0.7}Sr_{0.3}CrO_3$, $SrCrO_4$ phase exolution occurs at ~800°C and melts at 1256°C [43]. The $SrCrO_4$ liquid phase re-dissolves into the perovskite at high temperature and assists densification. Similarly, in case of A and B-site doped LSCM73, the $SrCrO_4$, which is present in the bisque fired sample liquefies and re-dissolves into the lattice at high temperature resulting in higher densification. Higher grain growth is also achieved for the samples sintered in air due to the liquid phase assisted sintering. However, the grain growth and density decrease on lowering PO_2. Lower densification with decreasing oxygen partial pressure is associated with decreasing $SrCrO_4$ and subsequent liquid phase sintering. To validate our hypothesis, 0.5% of $SrCrO_4$ is added to LSCM73 and sintered in air under

same conditions. The results show higher densification for LSCM73+0.5%$SrCrO_4$ when compared to LSCM73 sintered sample as shown in Fig. 6.2. The SEM micrograph of the sintered LSCM73+0.5%$SrCrO_4$ sample is shown in Fig. 6.3d. Highest density (~73%) is achieved for LSCM73 when mixed with 0.5% $SrCrO_4$ and sintered in air. This corresponds to the higher amount of liquid phase formation [44].

On the other hand, chromium evaporation is likely to occur for lanthanum chromite based materials in the form of CrO_3 and it condenses as Cr_2O_3 (Eq. 2) at the grain boundaries (irregular contacts) due to the surface energetics [13].

$$4CrO_3 \rightarrow 2Cr_2O_3 + 3O_2 \quad (2)$$

Manganese is soluble in Cr_2O_3 up to a limit of 1.6% of the cation sites at 1000°C [45]. Manganese tends to diffuse and react with Cr_2O_3 to form $MnCr_2O_4$ (Eq. 3), preferentially at the grain boundaries of LSCM73 as shown in Fig. 6.4a and d. Thermodynamically, the spinel phase formation is favorable at 1400°C with the Gibbs free energy of formation for $MnCr_2O_4$ to be -40.1kJ/mol [46].

$$MnO + Cr_2O_3 \rightarrow MnCr_2O_4 \quad (3)$$

The formation of spinel phase is also in agreement with Mn-Cr-O phase diagram [36]. According to the phase diagram, the cubic spinel phase forms at 1400°C in air. With decrease in PO_2, the Cr-evaporation and condensation with the formation of Cr_2O_3 decreases. Subsequently, the formation of $MnCr_2O_4$ also decreases with decrease in oxygen partial pressure. This is in agreement with our observation in the SEM micrographs of LSCM73 in air (Fig. 6.3a), N_2 (Fig. 6.3b) and Ar-3%H_2-3%H_2O (Fig. 6.3c). On the other hand, Mn_3O_4 phase is observed in the samples sintered in N_2 (~10^{-5} atm) and Ar-3%H_2-3%H_2O (~10^{-10} atm) gas atmosphere. However, the formation of Mn_3O_4 increases with decrease in PO_2. In

the literature, it is given that $MnCr_2O_4$ dissociates into MnO in reducing gas atmosphere [35-36]. However, no experimental or theoretical evidence is provided. Furthermore, if the spinel

Table 6.1. SEM-EDS elemental analysis of LSCM73 sintered in air.

Element	**La (at. %)**	**Sr (at. %)**	**Cr (at. %)**	**Mn (at. %)**
Area 1 (Mn-Cr-spinel)	8.1±1.0	2.7±4.3	51.6±1.1	37.6±4.6
Area 2 (Bulk)	37.8±0.1	16.4±0.4	31.7±0.2	13.7±0.3

Table 6.2. SEM-EDS elemental analysis of LSCM73 sintered in Ar-3%H_2-3%H_2O.

Element	**La (at. %)**	**Sr (at. %)**	**Cr (at. %)**	**Mn (at. %)**
Area 1 (Mn-oxide)	10.2±3.0	5.6±4.3	11.4±2.3	70.8±3.9
Area 2 (Bulk)	35.4±0.9	16.4±2.2	32.9±0.4	15.3±0.3

phase dissociates into MnO and Cr_2O_3 in reducing atmosphere, the appearance of Cr_2O_3 should be detected like MnO using XRD or SEM. The presence of Cr_2O_3 is not identified in the literature as well as in our study. The formation of $MnCr_2O_4$ is dependent on Cr_2O_3 (Eq. 3). According to our study, in reducing atmosphere, we propose that Mn diffuses into the condensed Cr_2O_3 until it is consumed to form $MnCr_2O_4$. Afterwards, Mn diffuses at the outer surface and exits in the lattice as MnO. During cooling, the temperature and PO_2 decreases to the region where MnO is not stable and it forms Mn_3O_4 in agreement with our XRD results [40].

The exolution of MnO phase in LSCM73 in reducing gas atmosphere can also be explained based on the oxygen exchange defect reactions. It is known that Mn can exist in three valence states i.e. $Mn^{2+}/Mn^{3+}/Mn^{4+}$ in LSCM [34]. Due to the existence of disproportionate Mn valence state, oxygen vacancies exist in the lattice of LSCM73 for the charge compensation. At lower PO_2, the transition of $Mn^{4+} \rightarrow Mn^{3+}$ and $Mn^{3+} \rightarrow Mn^{2+}$ results in higher amount of oxygen vacancies formation for charge neutrality. The oxygen exchange between LSCM73 and gas phase can be represented as shown below [34]:

$$\frac{1}{2}O_2 + V_O^{\cdot\cdot} + 2Mn_{Mn}^{\times} = O_O^{\times} + 2Mn_{Mn}^{\cdot} \quad (4)$$

$$\frac{1}{2}O_2 + V_O^{\cdot\cdot} + 2Mn_{Mn}^{\prime} = O_O^{\times} + 2Mn_{Mn}^{\times} \quad (5)$$

where $Mn_{Mn}^{\times}$ refers to Mn^{3+} on Mn^{3+} sites, $Mn_{Mn}^{\cdot}$ refers to Mn^{4+} on Mn^{3+} sites, $Mn_{Mn}^{\prime}$ refers to Mn^{2+} on Mn^{3+} sites, and $V_O^{\cdot\cdot}$ refers to oxygen vacancy with two positive charges.

We postulate that LSCM73 perovskite lattice structure destabilizes due to the existence of higher amount of oxygen vacancies and Mn^{2+} (0.830 Å) with higher ionic radii than Mn^{3+} (0.645Å). Therefore, in reducing atmosphere, Mn^{2+} does not retain in the $A^{3+}B^{3+}O_3^{2-}$ perovskite lattice of LSCM73 and exolve as MnO. Oishi et al. [34] have reported similar exolution of MnO from LSCM55 lattice when exposed to $PO_2 \sim 10^{-20}$ atm at 900°C.

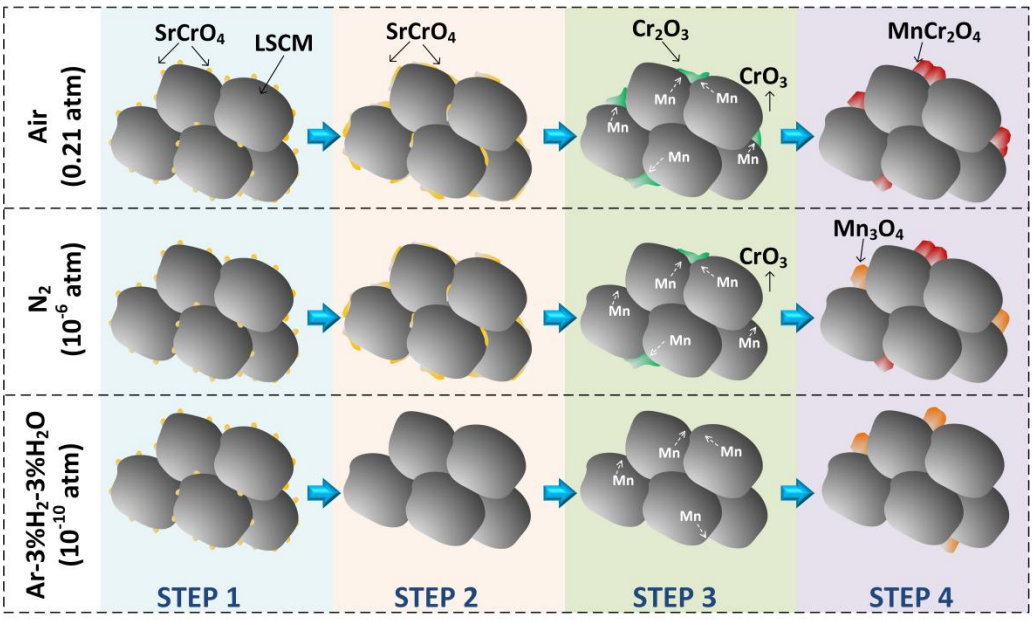

Fig. 6.6. Schematic of sintering steps for LSCM73 sintered in air, N_2 and Ar-3%H_2-3%H_2O.

Mechanism and the sintering behavior of LSCM73 in air, N_2 and Ar-3%H_2-3%H_2O gas atmosphere are shown in Fig. 6.6. In step 1, the starting material is same for the three cases i.e. bisque fired (at 1100°C) LSCM73 with the existence of $SrCrO_4$ (indicated by yellow color). In step 2, the $SrCrO_4$ melts (indicated by yellow color) at ~1256°C in case of air and N_2 atmosphere. However, due to the positive Gibbs free energy of formation in reducing atmosphere, $SrCrO_4$ is unstable for the samples sintered in Ar-3%H_2-3%H_2O (~10^{-10} atm). It is hypothesized that the $SrCrO_4$ would dissociate into SrO and Cr_2O_3 and dissolve back into the lattice when heating up to the sintering temperature. During Step 3, the evaporated CrO_3 condenses and deposits in the form of Cr_2O_3 (indicated by green color), preferentially at the grain boundaries due to higher surface energy. And, Mn diffuses at the outer surface and reacts with Cr_2O_3 to form $MnCr_2O_4$ spinel (indicated by red color). However, as explained above, the CrO_3 evaporation and condensation as Cr_2O_3 decreases

(step 3) in reducing atmosphere. Therefore, the availability of Cr_2O_3 to react with Mn to form $MnCr_2O_4$ decreases with decrease in PO_2. Consequently, Mn diffuses at the outer surface and exists as Mn_3O_4 in the lattice. As a result, both $MnCr_2O_4$ and Mn_3O_4 exist for the sample sintered in N_2 atmosphere as shown in the step 4. In Ar-3%H_2-3%H_2O atmosphere with least PO_2 (~ 10^{-10} atm) among the three cases, there is no $MnCr_2O_4$ formation due to the absence of Cr_2O_3 (step 3) and therefore, Mn comes out as Mn_3O_4 (indicated by orange color) in step 4.

6.4.3. *Thermodynamic Calculations*

To support our experimental results and hypothesis on the sintering behavior of LSCM73, we performed thermodynamic calculations using the CALculation of PHAse Diagram (CALPHAD). The CALPHAD approach was pioneered by Kaufman [47] to model complex phase equilibria in multicomponent systems. Its theoretical basis is thermodynamic description of individual phases. The thermodynamic database was developed using Thermo-Calc [48]. Thermo-Calc is a program developed by KTH Royal Institute of Technology in the 1970s. For over 40 years, Thermo-Calc has been at the forefront of scientific software and databases for calculations involving computational thermodynamics [47, 49].

The customized thermodynamic database for La-Sr-Cr-Mn-O-H-S system was adopted in the current investigations, which is able to simulate the phase equilibria of perovskite at various gas conditions including the gas species like H_2O, O_2, SO_2, H_2S, etc. It is a combined database with the La-Sr-Cr-Mn-O database [46, 50-51] and SSUB database [52]. It has the Gibbs energy description of all the phases we are interested in the current work, including the perovskite and spinel phases. It is expanded by adding Cr on the basis of

the La-Sr-Mn-O thermodynamic database, which was initially developed to consider the Cr poisoning effect to LSM.

In the current work, the phase stabilities of LSCM73 were examined at different oxygen partial pressures at 1400°C in comparison with the experimental observations. According to our thermodynamic calculations and Fig. 6.7, LSCM73 will form spinel in air, with the decrease of the oxygen partial pressure, phases like MnO and SrO will form. The theoretical predictions are in agreement with our experimental results at 1400°C. Spinel phase co-exists with perovskite phase in air (0.21 atm). However, at lower PO_2 (~10^{-5} atm), three phase co-exists as shown in our experimental observations i.e. perovskite, spinel and MnO. With further decrease in PO_2, only MnO phase co-exists with perovskite as shown in Fig. 6.7 which is also in agreement with our experimental results. As mentioned in the previous section, during cooling, it is to be noted that the temperature and PO_2 reduces to the region where MnO is not stable and it forms Mn_3O_4 [40]. This is in agreement with our XRD results.

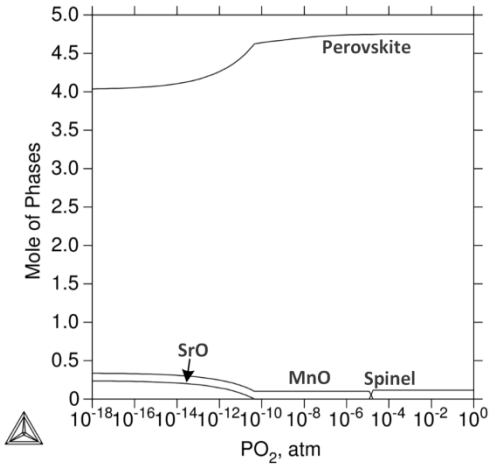

Fig. 6.7. Relationship between the phase stabilities of LSCM73 at 1400°C and oxygen partial pressure.

6.4.4. *Electrochemical measurements and post-test observations*

Fig. 6.8a and b shows electrochemical performance of the symmetrical cell (LSCM73+8YSZ//8YSZ//LSCM73+8YSZ) at 950°C and 0.5 V in air and Ar-3%H_2-3%H_2O respectively. Ohmic resistance is represented by high frequency intercept, while the semicircle diameter represents sum of the non-ohmic contributions [53]. In case of reducing atmosphere (Ar-3%H_2-3%H_2O), two semicircles are observed corresponding to the charge (ion) transfer at the electrolyte/electrode interface and electrochemical kinetics involved with electrode material (e.g. adsorption and/or diffusion processes to/from the interface) [54-55]. However, the two electrode arcs merged in oxidizing atmosphere (air) [41]. Fig. 6.9 shows comparison plot of ohmic and non-ohmic resistances as a function of time for the cell tested at 0.5 V in air and Ar-3%H_2-3%H_2O. In case of oxidizing atmosphere, ohmic and non-ohmic resistances increase with time, but there is no significant variation observed especially after 20h as shown in Fig 6.8a and 6.9. This corresponds to higher stability of LSCM73 in oxidizing atmosphere. On the other hand, in reducing atmosphere, the ohmic resistance almost stabilizes with increase in time as shown in Fig. 6.9. However, non-ohmic resistance continuously increases with time. The non-ohmic resistance for the tested cell is ~12.0 $\Omega.cm^2$ (0h) and increases to ~24.9 $\Omega.cm^2$ (80h) in Ar-3%H_2-3%H_2O at 950°C when bias of 0.5V is applied. Resistance of the tested cell increases when exposed to reducing gas atmosphere as shown in Fig. 6.9.

Symmetrical cells (LSCM73+8YSZ//8YSZ//LSCM73+8YSZ) before and after testing are analyzed. No changes are identified with the naked eye. In addition, no delamination of the porous electrode layers is observed after manual removal of Pt mesh along with Pt wires. Bulk electrode and electrode/electrolyte interfaces are examined for microstructural changes

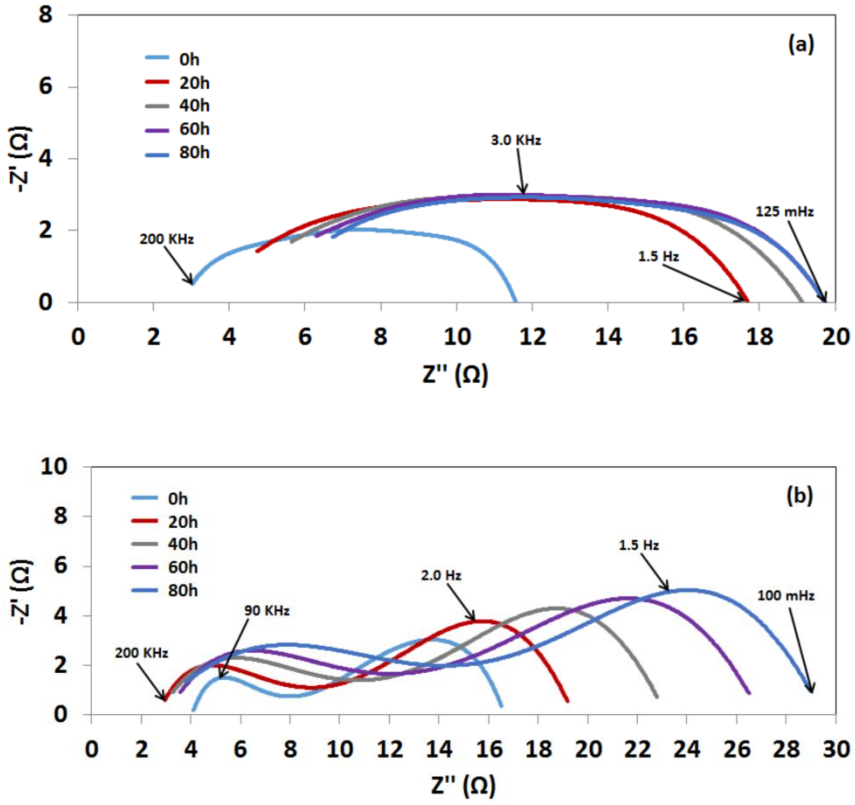

Fig. 6.8. Nyquist plots of impedance spectra obtained from the symmetrical cell of configuration LSCM73+8YSZ//8YSZ//LSCM73+8YSZ tested at 950°C with 0.5 V from 0 to 80 h: a) in air, and b) in Ar-3%H_2-3%H_2O. For clarity, only five spectra are shown.

and reaction products formation. Fig. 6.10a shows the interface of LSCM73+8YSZ (anode) and 8YSZ (electrolyte). There is no interface layer or compound formation observed at the interface in air. Furthermore, when compared to as-sintered cell (Fig. 6.10b), no changes are identified in the microstructure of the tested cell in air (Fig. 6.10c). However, in Ar-3%H_2-3%H_2O, surface morphology of LSCM73 phase is significantly modified as shown in Fig. 6.10d. Nano-size particles segregation is observed on the anode surface of the tested cell as shown in Fig. 6.10d. Surface compositional analysis is performed using SEM-EDS at ~20 different points. It is observed that the average Sr: La ratio is higher for the symmetrical cell

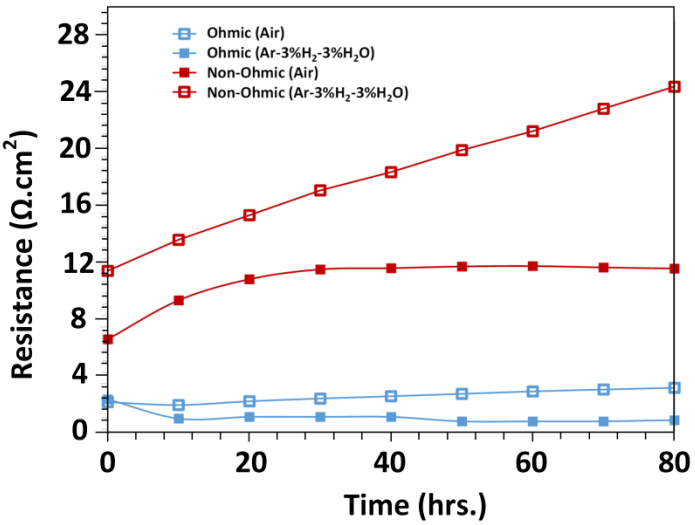

Fig. 6.9. Comparison plots of resistance (ohmic and non-ohmic) changes with time (80h) for the symmetrical cell of configuration LSCM73+8YSZ//8YSZ//LSCM73+8YSZ tested at 0.5 V in air and Ar-3%H_2-3%H_2O.

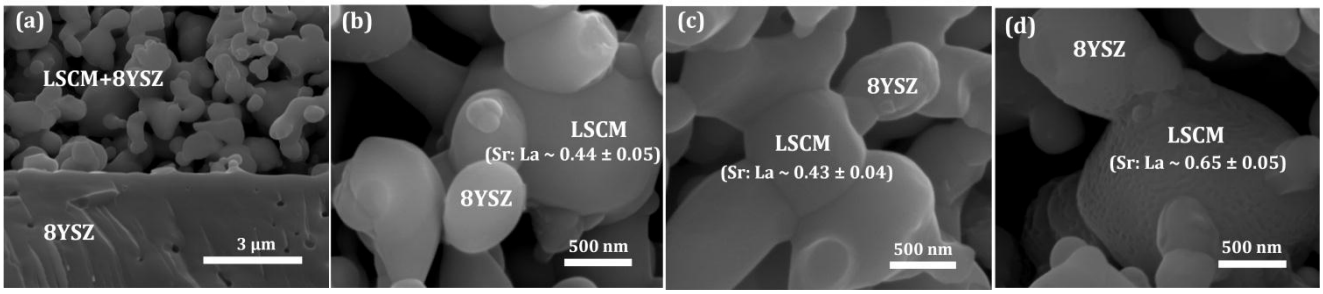

Fig. 6.11. SEM micrographs of the symmetrical cell of configuration LSCM73+8YSZ//8YSZ//LSCM73+8YSZ (anode surface): a) LSCM73+8YSZ and 8YSZ interface b) as-sintered in air, c) tested in air, and d) tested in Ar-3%H_2-3%H_2O.

tested in Ar-3%H_2-3%H_2O (Sr: La ~ 0.65±0.05) when compared to those tested air (Sr: La ~ 0.44±0.05) which matches with as-sintered cell (Sr: La ~ 0.43±0.04). This corresponds to the Sr-segregation in case of the cell tested in reducing atmosphere. Sr enrichment on lanthanum strontium manganite surface is reported earlier after heat treatment (1000°C) in nitrogen

atmosphere (humid) at low partial pressure of oxygen [56]. Hu et al. [50] have observed similar surface morphological changes attributing to Sr-segregation in $(La_{0.8}Sr_{0.2})_{0.98}MnO_3$ (LSM) after electrochemical cell testing in air (with 50% water vapor) at 850°C for 100h. Consequently, the resistance of the LSM based symmetrical cells increased [57]. Similarly, it is postulated that the SrO segregation on LSCM73 surface results in the increase of resistance with time when tested in Ar-3%H_2-3%H_2O. Figure 6.11a and b shows electrode-electrolyte interface after removable of LSCM73 layer from the cells tested in air and Ar-3%H_2-3%H_2O respectively. Ridges and lip formations along with the reaction zone (indicated by yellow circles) are observed at the contact of LSCM/8YSZ and attributes to an interaction between electrode and electrolyte in Ar-3%H_2-3%H_2O unlike air. Similar interactions are reported between LSM/8YSZ by Keane [58] and Li et al. [59] resulting into an increase in the polarization resistance under the applied bias. However, less interaction is identified in this study for LSCM-8YSZ system when compared to LSM-8YSZ.

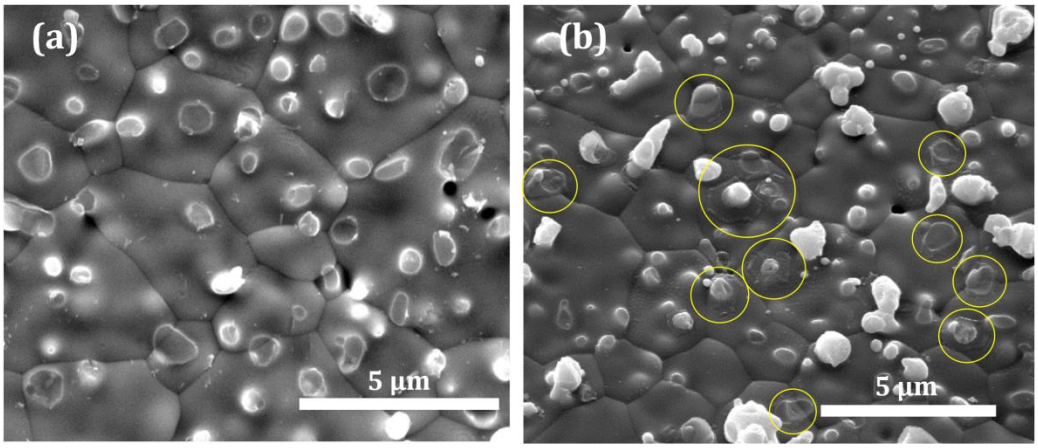

Fig. 6.12. SEM micrograph of the anode-side electrolyte interface after testing and removing LSCM73 layer: a) air and b) Ar-3%H_2-3%H_2O.

6.5. Conclusions

$(La_{0.75}Sr_{0.25})_{0.95}Cr_{0.7}Mn_{0.3}O_3$ (LSCM73) experiences enhanced densification in air during sintering at 1400°C when compared to reducing atmosphere. Spinel phase formation ($MnCr_2O_4$) has been observed when sintered in air (0.21 atm) and N_2 (~10^{-5} atm) whereas Mn_3O_4 phase formation is observed at lower oxygen partial pressure (~10^{-5} and ~10^{-10} atm). Thermodynamic calculations as well as construction of phase diagram, developed using Thermo-Calc software, supports experimental observations. The crystal structure of the sintered LSCM73 shows rhombohedral lattice structure in air and its transformation to cubic in reducing atmosphere. Stable and superior performance of the symmetric cell of configuration LSCM73+8YSZ//8YSZ//LSCM73+8YSZ, during electrochemical testing at 950°C, is attributed to surface and interface stability and lack of Sr segregation in oxidizing atmospheres when compared to exposure to reducing atmospheres.

6.6. References

[1] T. Faravelli, E. Ranzi, C. Candusso, A. Frassoldati, A. Cuoci and D. Tolazzi. Simplified kinetic schemes for oxy-fuel combustion. 1st International Conference on Sustainable Fossil Fuels for Future Energy, 2009.

[2] H. Stadler, F. Beggel, M. Habermehl, B. Persigehl, R. Kneer, M. Modigell, P. Jeschke. Int. J. Greenhouse Gas Control 5 (2011) 7–15.

[3] L.L. Anderson, P.A. Armstrong, J.M. Repasky, and V.E. Stein, "Enabling Clean Coal Power Generation: ITM Oxygen Technology. Proceedings of the 28th Annual International Pittsburgh Coal Conference, Pittsburgh, PA, USA, 2011.

[4] M.J. Shin, J.H. Yu. Int. J. Hydrogen. Energy 35 (2010) 7512-7518.

[5] G.A. Mills. Liquid Fuels from syngas – progress report. Department of chemical engineering, University of Delaware, Newark 116-117.

[6] N. Nagabhushana, J.A. Lane, G.M. Christie, B.A.V. Hassel. Composite oxygen ion transport membrane. US Patent 7556676B2, 2009.

[7] H.J.M. Bouwmeester, A.J. Burggraaf, in: A.J. Burggraaf AJ, Cot L (Eds.). Fundamentals of inorganic membrane science and technology. Membrane Science and Technology Series 4, Elsevier, Amsterdam, 1996, pp. 435–510.

[8] J. Sfeir. J. Power Sources 118 (2003) 276–285.

[9] A. Atkinson, S. Barnett, R.J. Gorte, J.T.S. Irvine, A.J. McEvoy, M. Moguensen, S.C. Singhal, J. Vohs. Nat. Mater. 3 (2004) 17–27.

[10] V.B. Vert, F.V. Melo, L. Navarrete, J.M. Serra. Appl. Catal. B: Environ. 115 (2012) 346–356.

[11] P. Duran, J. Tartaj, F. Capel, C. Moure. J. Eur. Ceram. Soc. 24 (2004) 2619–2629.

[12] A.S. Mukasyan, C. Costello, K.P. Sherlock, D. Lafarga, A. Varma. Sep. and Purif. Technol. 25 (2001) 117–126.

[13] S. Gupta, M.K. Mahapatra, P. Singh. Mat. Res. Bull. 48 (2013) 3262-67.

[14] K.T. Jacob, S. Gupta, P. Singh. J. Am. Ceram. Soc. 96 (2013) 3933-38.

[15] K.T. Jacob, S. Gupta, P. Singh. J. Am. Ceram. Soc. 96 (2013) 3272-3278.

[16] S. Gupta, M.K. Mahapatra, P. Singh. MSE: R: Reports 90 (2015) 1-36.

[17] V.V. Kharton, E.V. Tsipis, I.P. Marozau, A.P. Viskup, J.R. Frade, J.T.S. Irvine. Solid State Ionics 178 (2007) 101-113.

[18] S. Gupta, P. Singh. ECS Transactions 66 (2015) 117-123.

[19] V.A. Kolotygin, E.V. Tsipis, A.L. Shaula, E.N. Naumovich, J.R. Frade, S.I. Bredikhin, V.V. Kharton. J. Solid State Electrochem. 15 (2011) 313-327.

[20] J.J. Liu, T. Liu, W.D. Wang, J.F. Gao, C.S. Chen. J. Mem. Sci. 389 (2012) 435-440.

[21] T. Wenyi, Z. Qin, Y. Han, Z. Xiufang, L. Hongyi. Int. J. Hydrogen Energy 37 (2012) 7398-7404.

[22] W. He, H. Huang, M. Chen, J.F. Gao, C.S. Chen. Solid State Ionics 260 (2014) 86-89.

[23] W. Tan, Q. Zhong, D. Xu, H. Yan, X. Zhu. Int. J. Hydrogen Energy 36 (2013) 16656-16664.

[24] W. Fang, Y. Zhang, J. Gao, C. Chen. Ceramics International 40 (2014) 799-803.

[25] G.M. Christie, J.R. Wilson, B.A.V. Hassel. Catalyst containing oxygen transport membrane. US Patent 090645A2, 2011.

[26] N. Nagabhushana, J.A. Lane, G.M. Christie, B.A.V. Hassel. Composite for oxygen ion transport membrane. EP 2054355B1, 2012.

[27] M. Van den Bossche, R. Matthews, A. Lichtenberger, S. McIntosh. J. Electrochem. Soc. 157 (2010) B392-B399.

[28] T. Nakamura, G. Petzow, L. Gauckler. Mater. Res. Bull. 14 (1979) 649–659.

[29] S. Tao, J.T.S. Irvine. J. Electrochem. Soc. 151 (2004) A252–259.

[30] S. Tao, J.T.S. Irvine. Nature Mater. 2 (2003) 320-323.

[31] M. Filal, C. Petot, M. Mokchah, C. Chateau, J.L. Carpentier. Solid State Ionics 80 (1995) 27-35.

[32] H. Yokokawa, N. Sakai, T. Kawada, M. Dokiya. J. Electrochem. Soc.138 (1991) 1018-27.

[33] M. Masashi, T. Yamamoto, T. Ichikawa, T. Takeda. Solid State Ionics 148 (2002) 93–101.

[34] M. Oishi, K. Yashiro, K. Sato, J. Mizusaki, T. Kawada. J. Solid State Chem. 181 (2008) 3177–3184.

[35] S. Tao, J.T.S. Irvine. Chem. Mater. 18 (2006) 5453-5460.

[36] I.H. Jung. Solid State Ionics 177 (2006) 765-777.

[37] W. Lee, Z. Cai, and B. Yildiz. 45 (2012) 405-412.

[38] Y.J. Leng, S.H. Chan, K.A. Khor, S.P. Jiang. J. Applied Electrochem. 34 (2004) 409-415.

[39] D.H. Peck, M. Miller, K. Hilpert. Solid state Ionics 123 (1999) 59-65.

[40] S. Fritsch and A. Navrotsky. J. Am. Cer. Soc. 1996;79:1761-68.

[41] M. Mori, Y. Hiei, N.M. Sammes. Solid State Ionics 123 (1999) 103-111.

[42] T. Zhang, R.K. Brow, W.G. Fahrenholtz, S.T. Reis. J. Power Sources 205 (2012) 301–306.

[43] S. Simner, J. Hardy, J. Stevenson, T. Armstrong. J. Mater. Sci. 34 (1999) 5721-32.

[44] R.M. German, S. Farooq, C.M. Kipphut. Mater. Sci. Eng. A 215 (1988) 215-224.

[45] D.J. Young. Tech. & Eng. 350 (2008) 350-351.

[46] E. Povoden-Karadeniz. Thermodynamic Database of the La-Sr-Mn-Cr-O Oxide System and Applications to Solid Oxide Fuel Cells, Diss., Eidgenössische Technische Hochschule ETH Zürich, Nr. 18139, 2008.

[47] L. Kaufman, H. Bernstein. Computer Calculation of Phase Diagrams with Special Reference to Refractory Metals. New York: Academic Press, 1970.

[48] J.O. Andersson, T. Helander, L.H. Hoglund, P.F. Shi and B. Sundman. CALPHAD 26 (2002) 273-312.

[49] N. Saunders, A.P. Miodownik. CALPHAD (Calculation of Phase Diagrams): A Comprehensive Guide, Oxford, New York: Pergamon, XVI, 1998:479.

[50] A.N. Grundy, B. Hallstedt, L.J. Gauckler. Calphad-Computer Coupling of Phase Diagrams and Thermochemistry 28 (2004) 191-201.

[51] E. Povoden-Karadeniz, M. Chen, T. Ivas, A.N. Grundy, L.J. Gauckler. J. Mat. Res. 27 (2012) 1915-1926.

[52] Lehrstuhl für Theoretische Hüttenkunde, Rheinisch-Westfälische Technische Hochschule Aachen, Thermodynamic Properties of Inorganic Materials, Vol. IV, 1999.

[53] M. Keane, M.K. Mahapatra, A. Verma, P. Singh. Int. J. Hydrogen Energy 37 (2012) 16776-16785.

[54] D.M. Bastidas, S. Tao, J.T.S. Irvine. J. Mat. Chem. 16 (2006) 1603-1605.

[55] P. Blennowa, K. Kent. K.K. Hansen, L.R. Wallenberg, M. Mogensen. Electrochimica Acta 52 (2006) 1651–1661.

[56] C. Knöfel, M. Chen, M. Mogensen. Fuel Cells (2011) 669-677.

[57] B. Hu, M. Keane, M.K. Mahapatra, P. Singh. J. Power Sources 248 (2014)196-204.

[58] M. Keane, M.K. Mahapatra, A. Verma, P. Singh. Int. J. Hydrogen. Energy 37 (2012) 16776-16785.

[59] N. Li, M. Keane, M.K. Mahapatra, P. Singh. Int. J. Hydrogen. Energy 38 (2013) 6298-6303.

.

CHAPTER 7: A NEW STABLE NICKEL AND TITANIUM CO-DOPED LANTHANUM STRONTIUM CHROMITE FOR HIGH TEMPERATURE ELECTROCHEMICAL DEVICES

7.1. Abstract

Effects of nickel and titanium co-doping of the chromite perovskite $La_{0.85}Sr_{0.15}Cr_{1-2y}Ni_yTi_yO_{3-\delta}$ ($0.05 \leq y \leq 0.3$) on the electrical conductivity, chemical stability, microstructure, density, thermal expansion and electrochemical performance have been investigated for high temperature electrochemical devices. Density and the electrical conductivity increased with nickel concentration. Sr-segregation on the surface of $La_{0.85}Sr_{0.15}Cr_{1-2y}Ni_yTi_yO_{3-\delta}$ has been observed for $y \geq 0.2$ and associated with reduction in the electrical conductivity. For $y = 0.1$, $La_{0.85}Sr_{0.15}Cr_{1-2y}Ni_yTi_yO_{3-\delta}$ showed the highest electrical conductivity in air and reducing atmosphere (PO_2 ~10^{-24} atm). The conductivity of $La_{0.85}Sr_{0.15}Cr_{1-2y}Ni_yTi_yO_{3-\delta}$ ($y = 0.1$) in reducing atmosphere (3.58 S cm^{-1} at 950°C) also remains higher than the most widely investigated compositions such as $(La_{0.75}Sr_{0.25})_{0.95}Cr_{0.5}Mn_{0.5}O_{3-\delta}$ (2.81 S cm^{-1}) and $(La_{0.75}Sr_{0.25})_{0.95}Cr_{0.7}Fe_{0.3}O_{3-\delta}$ (1.41 S cm^{-1}). Smaller deviation in the oxygen stoichiometry is similarly observed for $La_{0.85}Sr_{0.15}Cr_{0.8}Ni_{0.1}Ti_{0.1}O_{3-\delta}$ ($\delta = 0.011$) when compared to $La_{0.75}Sr_{0.25}CrO_{3-\delta}$ ($\delta = 0.091$), $La_{0.75}Sr_{0.25}Cr_{0.5}Mn_{0.5}O_{3-\delta}$ ($\delta = 0.175$) and $La_{0.75}Sr_{0.25}Cr_{0.5}Fe_{0.5}O_{3-\delta}$ ($\delta = 0.148$) at 1000°C and ~10^{-24} atm. Thermal expansion coefficient (TEC) of $La_{0.85}Sr_{0.15}Cr_{0.8}Ni_{0.1}Ti_{0.1}O_{3-\delta}$ ($11.3 \pm 0.14 \times 10^{-6}$/°C) matches closely with 8YSZ ($10.9 \pm 0.17 \times 10^{-6}$/°C). Highest electrochemical performance is obtained for our new composition $La_{0.85}Sr_{0.15}Cr_{0.8}Ni_{0.1}Ti_{0.1}O_{3-\delta}$ when mixed with 8YSZ in both oxidizing and reducing atmosphere, in comparison with $(La_{0.75}Sr_{0.25})_{0.95}Cr_{0.7}Mn_{0.3}O_{3-\delta}$ and

$(La_{0.8}Sr_{0.2})_{0.95}Cr_{0.7}Fe_{0.3}O_{3-\delta}$. No degradation is identified in the post-tested LSCNT0.1 based symmetrical cells.

7.2. Introduction

High temperature (≥650°C) solid-state electrochemical systems such as oxygen transport membrane (OTM), solid-oxide fuel cells (SOFC) and solid oxide electrolysis cells (SOEC) for power generation and clean combustion respectively are a select few technologies which can be adapted in near term to enhance the chemical to electrical energy conversion efficiency, reduce carbon foot print and extend the fuel reserve for future energy security and environmental sustainability [1-2]. Although progress in the OTM, SOFC and SOEC technologies along with technical challenges have been reported [1-5], development of stable materials along with performance improvement remains topic of research interest [6-8].

Chemical/structural/redox stability and high electrical conductivity/performance have been identified as key requirements for OTM, SOEC and SOFC electrode [3]. To improve the surface exchange kinetics and performance of oxygen transport membrane, porous air and fuel electrodes are also utilized for OTM system [9]. Perovskites and/or perovskite-fluorite composites are currently being developed for OTM system [8-16]. However, thermal-chemical-structural stability, high thermal expansion coefficient, lower conductivity and electrochemical performance in reducing atmosphere are challenges with the current existing materials [8-16]. For instance, lanthanum cobaltite ($LaCoO_{3-\delta}$) obtain high thermal expansion coefficient (20×10^{-6} K^{-1}) and decomposes into La_2CoO_4 and CoO at 1000°C and oxygen partial pressure of $<10^{-7}$ atm [8]. Similarly, lanthanum ferrite ($LaFeO_{3-\delta}$) provides high thermal expansion coefficient (23.8×10^{-6} K^{-1}) for T > 600°C and

decomposes into La_2O_3 and Fe metal at 1000°C and in reducing atmosphere ($<10^{-17}$ atm) [8][8].

LSM-YSZ is the state of the art material for SOFC cathode and SOEC anode [17-20]. However, LSM-YSZ tends to degrade with time under SOFC/SOEC operating conditions. Furthermore, delamination of the LSM based electrodes has been identified after testing [17-19]. Cation migration, interfacial reaction and porosity formation at the interface of LSM and 8YSZ phase are some of the major challenges with the current state of the art material [17-18]. Insulating interfacial reaction compounds such as lanthanum and/or strontium zirconate formation results in lower cell performance [17-19]. On the other hand, Ni-YSZ is conventionally used as the SOFC anode and SOEC cathode due to its high electro-catalytic activity, electronic and ionic conductivity. However, carbon deposition, stability, volume change during redox cycling and susceptibility to sulphur poisoning are the limitations of Ni-YSZ [6-7].

To overcome the limitations of the above mentioned materials such as $LaCoO_{3-\delta}$, $LaFeO_{3-\delta}$, LSM-YSZ and Ni-YSZ, lanthanum chromite-based perovskites have been considered as a promising candidate for SOFC/SOEC electrode [21-22], interconnect [23] and also OTM [5,8]. Lanthanum chromite based materials have also been proposed for use as electrode materials in magnetohydrodynamic (MHD) power generators, oxygen sensors and heating element in high temperature furnaces [24-25]. The potential of various lanthanum chromite based materials as OTM is demonstrated in detail in the recently published review article by Gupta et al. [8]. This is mainly due to its high thermo-chemical stability at high temperature (>1000°C) in a wide range of oxygen partial pressure ($0.21\text{-}10^{-22}$ atm) [26]. For instance, $(La,Sr)(Cr,Mn)O_{3-\delta}$ (LSCM) and $(La,Sr)(Cr,Fe)O_{3-\delta}$ (LSCF) have

been extensively investigated for OTM and air/fuel side electrode as it provides the combination of high electrochemical activity, good chemical compatibility with adjacent materials and structural stability [7, 27-33]. However, the properties (conductivity, thermal expansion coefficient and stability) of these materials degrade in reducing atmosphere. This is considered to be due to change in the valence state or disproportional existence of transition metal (M = Mn/Fe) into $M^{2+}/M^{3+}/M^{4+}$ at B-site, and charge compensation via oxygen vacancy formation. These materials also destabilize in reducing atmosphere. For example, $(La,Sr)_2MnO_4$ and MnO secondary phases in $(La_{0.75}Sr_{0.25})_{0.95}Cr_{0.5}Mn_{0.5}O_{3-\delta}$ and $(La,Sr)_2FeO_4$ in $(La_{0.75}Sr_{0.25})_{0.95}Cr_{0.5}Fe_{0.5}O_{3-\delta}$ have been detected at 900°C and ~10^{-20} atm [34].

The abovementioned description leaves the research community with a need of new improved material for high temperature electrochemical devices. Therefore, this study focuses on the development of new improved lanthanum chromite based material that can be utilized for various applications ranging from oxygen transport membrane system (as electrolyte and/or electrode) for oxy-combustion or syngas production to solid-oxide fuel/electrolysis cells (as interconnect and/or electrode) for clean and efficient power generation. Based on a literature review [8], among the transition metal dopants, Ti enhances the stability of lanthanum chromite based materials due to smaller change in its valence state and/or deviation from oxygen stoichiometry in reducing atmosphere [34-36]. Ni doping increases the electrical conductivity because of increase in Cr^{4+} ions to maintain charge neutrality [37-38]. It also increases the density of lanthanum chromite, a requirement for OTM and SOFC interconnect application [38-39]. The importance of Ni and Ti co-doping at the B-site of lanthanum strontium chromite is also listed in our recently published review

article [8]. To exploit the advantages of Ni and Ti doping, we have investigated the role of simultaneous Ni and Ti doping on the electrical, structural, thermal and electrochemical properties of $La_{0.85}Sr_{0.15}Cr_{1-2y}Ni_yTi_yO_{3-\delta}$ (y = 0.05, 0.1, 0.2 and 0.3) in oxidizing and reducing atmosphere as well as compared our results with the most investigated lanthanum chromite based compositions i.e. LSCM and LSCF.

7.3. Experimental

7.3.1. *Material Synthesis*

$La_{0.85}Sr_{0.15}Cr_{0.9}Ti_{0.1}O_{3-\delta}$ (LSCT0.1), $La_{0.85}Sr_{0.15}Cr_{0.9}Ni_{0.05}Ti_{0.05}O_{3-\delta}$ (LSCNT0.05), $La_{0.85}Sr_{0.15}Cr_{0.8}Ni_{0.1}Ti_{0.1}O_{3-\delta}$ (LSCNT0.1), $La_{0.85}Sr_{0.15}Cr_{0.6}Ni_{0.2}Ti_{0.2}O_{3-\delta}$ (LSCNT0.2), and $La_{0.85}Sr_{0.15}Cr_{0.4}Ni_{0.3}Ti_{0.3}O_{3-\delta}$ (LSCNT0.3) were synthesized by solid state reaction technique using lanthanum oxide (La_2O_3, 99.95%, Alfa Aesar, USA), chromium oxide (Cr_2O_3, 99.9%, Sigma-Aldrich, USA), strontium oxide (SrO, 99.5%, Alfa Aesar, USA), titanium oxide (TiO_2, 99.99%, Sigma-Aldrich, USA) and/or nickel oxide (NiO, 99.99%, Sigma-Aldrich, USA) powders. La_2O_3, Cr_2O_3, SrO, TiO_2 and/or NiO powders were mixed using wet-ball milling in ethanol for 48h followed by drying in air. The mixed powders were uniaxiallly pressed into cylindrical pellets. The pellets were sintered at 1450°C for 24h with a heating and cooling rate of 3°C/min.

7.3.2. *Characterization*

X-ray diffraction (BRUKER-D8 ADVANCE, Bruker AXS Inc. Madison, WI) technique was used to confirm the formation of single compound and to determine the crystal structure of $La_{0.85}Sr_{0.15}Cr_{1-2y}Ni_yTi_yO_{3-\delta}$ (LSCNTy) ($0.05 \leq y \leq 0.3$). The scan step was 0.02° using CuK_α radiation (λ = 1.5406 Å).

Density of all the sintered samples LSCT0.1 and LSCNTy ($0.05 \leq y \leq 0.3$) were measured using Archimedes principle. The microstructural analysis was conducted using scanning electron microscope (FEI - ESEM Quanta 250, Hillsboro, OH). Energy dispersive spectroscopy (EDS) attached to the SEM was used for elemental analysis.

X-ray photoelectron spectroscopy (XPS) was used for surface analysis of LSCNT0.3 to confirm the Sr-segregation on the surface. The measurements were performed using a monochromated Al Kα x-ray source, which provides enhanced resolution (Kratos, AXIS 165, and U.K.). All spectra were referenced to the C 1s binding energy at 284.6 eV. Pass energies of 160 eV and 20 eV were used for survey and high resolution spectra, respectively. Angle-resolved XPS (ARXPS) was performed at 0° and 60°. CasaXPS 2.3.15 software was used for spectra analysis.

A rectangular bar (0.56cm × 0.33cm × 0.17cm) was cut from the sintered pellet to measure the thermal expansion coefficient (TEC) of the LSCT0.1 and LSCNTy ($0.05 \leq y \leq 0.3$) samples using dilatometer (NETZSCH - DIL 402 PC, NETZSCH Instruments, and Burlington, USA). The TEC measurement was carried out in the temperature range of 200-1300°C in air with a heating rate of 3°C/min. Similarly, the TEC of $(La_{0.75}Sr_{0.25})_{0.95}Cr_{0.7}Mn_{0.3}O_{3-\delta}$ (LSCM73) and $(La_{0.8}Sr_{0.2})_{0.95}Cr_{0.7}Fe_{0.3}O_{3-\delta}$ (LSCF73) compositions were also measured for comparison. The dilatometer was calibrated using alumina (Al_2O_3) standard prior to the actual measurement.

Electrical conductivity of the LSCT0.1 and LSCNTy ($0.05 \leq y \leq 0.3$) bar samples (configuration similar to that of the TEC measurement) were measured using standard four-probe DC technique in the temperature range of 500-950°C in air and reducing (Ar-3%H_2) gas atmosphere. The equilibrium oxygen partial pressure were calculated based on Ar-3%H_2

gas mixture containing 1ppm H_2O (impurity level in the certified gas mixture) or 3%H_2O (RT humidification) The heating and cooling rates were 3°C/min. At least 30 minutes was elapsed to stabilize the temperature before collecting the data. In addition, for the equilibration of Ar-3%H_2 gas atmosphere, minimum of 2 days was provided at 950°C. By measuring the conductivity of well-studied YSZ, the reliability of the experiment was initially confirmed.

Thermogravimetric analysis (TGA, Perkin Elmer, CT, and USA) was performed on selected samples to determine the oxygen non-stoichiometry (δ) at 1000°C in oxidizing (PO_2~0.21 atm) and reducing gas atmosphere (PO_2~10^{-24} atm).

7.3.3. *Symmetric cell fabrication*

Among all the studied compositions, highest electrical conductivity is obtained for LSCNT0.1 in addition to the good thermal expansion match with 8YSZ. Therefore, LSCNT0.1 composition is chosen for symmetrical cell testing. However, it is predominantly electronic conductor and therefore mixed with 8YSZ for ionic conduction in the weight ratio of 50:50 for the cell fabrication and testing. 25 mm diameter symmetric button cells (LSCNT0.1+8YSZ//8YSZ//LSCNT0.1+8YSZ) consisting of 200 μm thick $(ZrO_2)_{0.92}(Y_2O_3)_{0.08}$(YSZ) electrolyte (Fuel Cell Materials) and 25 μm thick LSCNT0.1+8YSZ electrode were fabricated for electrochemical testing. Concentric circular electrodes were applied on both sides of the electrolyte disc by screen printing technique using 105 mesh screen. Electrodes were subsequently sintered in air for 2 h in the temperature range of 1200-1300°C. The electrochemical active area of the cell electrode was calculated to be 0.8 cm^2. Platinum screen current collector (Alfa Aesar, 50 mesh) with platinum wires (Alfa Aesar, 0.25 mm) were attached to each electrode using platinum contact

paste (Electro-Science Laboratories Inc.). Sintering of the current collector was performed in air for 1 h at 900°C. Likewise, LSCM73 and LSCF73 composition based symmetric cells were fabricated for performance comparison with LSCNT0.1. The symmetrical cell configurations corresponding to LSCM73 and LSCF73 were LSCM73+8YSZ//8YSZ//LSCM73+8YSZ and LSCF73+8YSZ//8YSZ//LSCF73+8YSZ respectively. A 25 mm diameter alumina tube was used to support the symmetric cell assembly, and the leads from a multi-channel potentiostat (VMP2, Bio-Logic) were attached to the assembled button cell. A type K (chromelealumel) thermocouple was placed within 5 mm of the cell to monitor the operating temperature.

7.3.4. *Electrochemical testing*

The cells were heated to 950°C at 3°C/min in flowing air and Ar-3%H_2-3%H_2O with flow rate maintained at 300sccm. Using the potentiostat, a pre-determined constant voltage of 0.5V was applied for 80 h and the impedance measurement was performed at two-hour intervals using a 10 mV alternating current in the frequency range from 100 mHz to 200 kHz. Experiments were repeated several times at the imposed voltage condition to ensure reproducibility. Post-test microstructural analysis of the symmetrical cells was performed using SEM-EDS.

7.4. Results and Discussion

7.4.1. *Crystal structure*

Fig. 7.1 shows the XRD patterns of the sintered samples. It is to be noted that no secondary phase has been detected for the studied compositions. The crystal structure of un-doped $LaCrO_3$ is orthorhombic (JCPDS – 01-070-2694) and in agreement with reported literature [24-25, 40]. However, in case of LSC0.15 ($La_{0.85}Sr_{0.15}CrO_3$), the small peaks

corresponding (e.g. ~33.1° and 41.5°) to orthorhombic phase disappear and major peaks (e.g. ~32.3° and 40.1°) get split as shown in Fig. 7.1. XRD pattern of LSC0.15 matches with rhombohedral structure (JCPDS – 00-033-0702). It is known that Sr-doping at A-site stabilizes the rhombohedral structure of $LaCrO_3$ at room temperature [41].

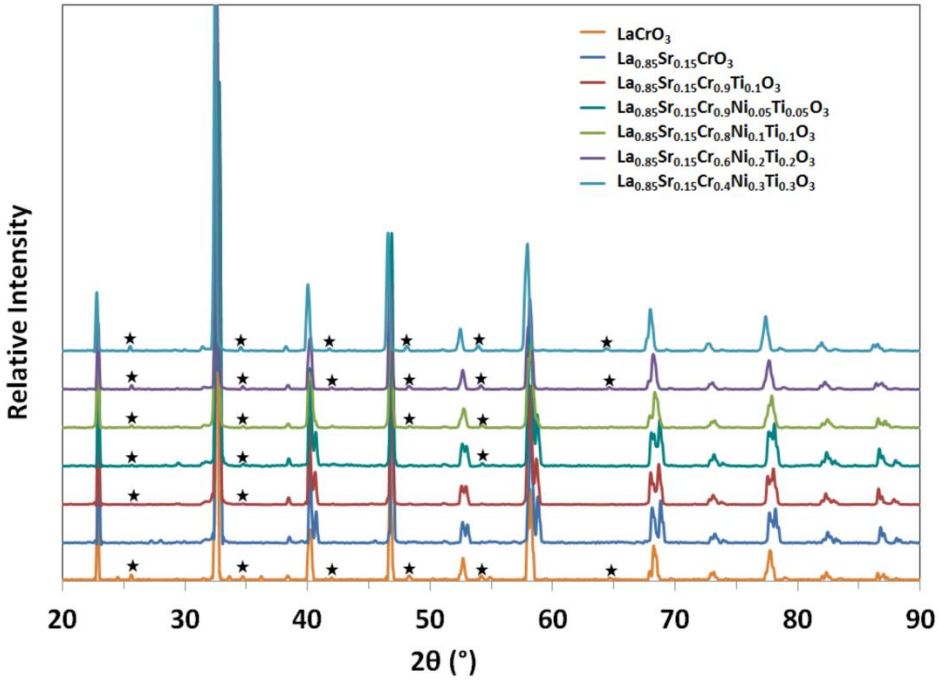

Fig. 7.1. XRD patterns (2θ = 20–90°) of sintered $LaCrO_3$, LSC0.15, LSCT0.1, LSCNT0.05, LSCNT0.1, LSCNT0.2 and LSCNT0.3.

On Ti-doping at B-site (LSCT0.1), new peaks start to appear which matches with the orthorhombic phase peaks in un-doped $LaCrO_3$ as indicated by asterisk in Fig. 7.1. This corresponds to the existence of orthorhombic structure along with the rhombohedral phase in Ti-doped sample, LSCT0.1. The results are in agreement with $La_{1-x}Sr_xCr_{1-x}Ti_xO_3$ ($0 < x \leq 0.2$) compositions reported by Mori et al. [42]. The intensity and the appearance of new Bragg's planes (asterisk marks) corresponding to the orthorhombic phase increases with increase in the dopant concentration. This indicates that both orthorhombic and

rhombohedral phases exist for LSCNTy ($0.05 \leq y \leq 0.3$) samples. The existence of orthorhombic phase for Ni-doped $LaCrO_3$ and $La_{1-x}Sr_xCrO_3$ has also been reported earlier [39-40, 43]. In addition to the new peaks appearance, the peak splitting corresponding to rhombohedral phase starts to disappear with higher dopant level. No peak splitting has been observed for y>0.05 except the appearance of few shoulder peaks aside of the major peaks (e.g. ~58.2° and 68.6°) which starts to disappear with the dopant level increase. This is shown in Fig. 7.1 and 7.2. Small shift in the peaks (e.g. ~58.2° and 68.6°) are also observed as the amount of dopant increases (shown by dashed lines in Fig. 7.2), suggesting an increase in lattice volume. An increase in the B-site cation ionic radii of a perovskite decreases tolerance factor due to octahedral (BO_6) tilting and results into lower symmetry crystal structure (orthorhombic) [44]. The increase in orthorhombic phase and the lattice volume with higher doping level is associated with larger ionic radii of Ni^{2+} (0.690 Å) when compared to Cr^{3+} (0.615 Å) and Ti^{4+} (0.605 Å).

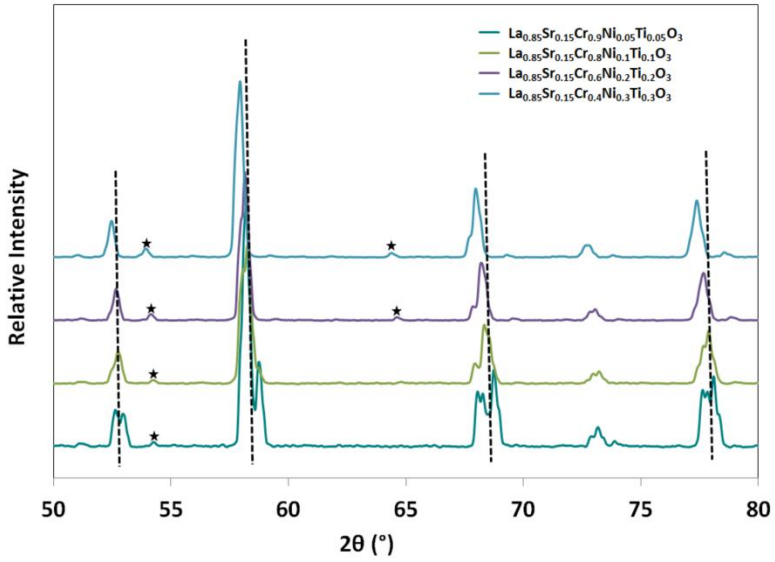

Fig. 7.2. Peaks shift in the XRD patterns (2θ = 50–80°) of sintered LSCNT0.05, LSCNT0.1, LSCNT0.2 and LSCNT0.3.

7.4.2. *Density and Microstructural Analysis*

The relative density of LSCT0.1 is very low as shown in Fig. 7.3. On partial substitution of Ni at B-site with titanium, the densification of LSCNTy ($0.05 \leq y \leq 0.3$) is enhanced. The density of the LSCNTy increases with Ni-dopant concentration as shown in Fig. 7.3. Highest relative density of ~66.8% (±1.3) is obtained for the composition of LSCNT0.3.

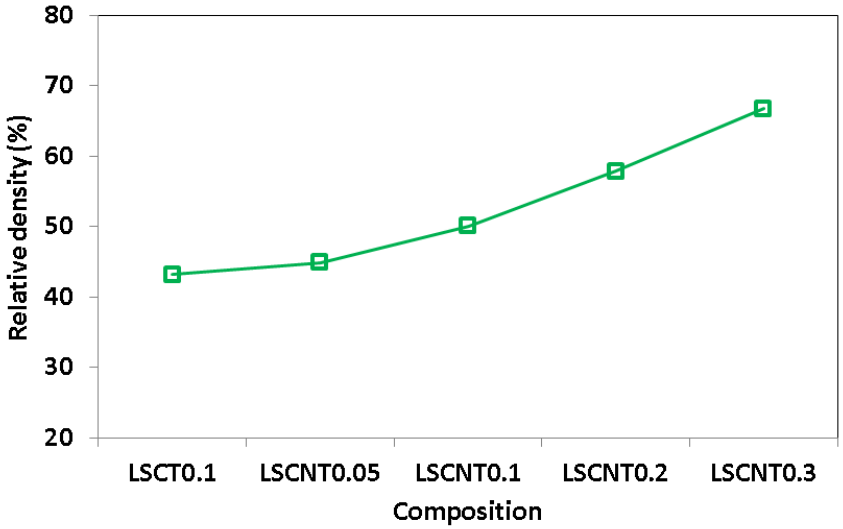

Fig. 7.3. Relative density of the sintered LSCT0.1, LSCNT 0.05, LSCNT0.1, LSCNT0.2 and LSCNT0.3.

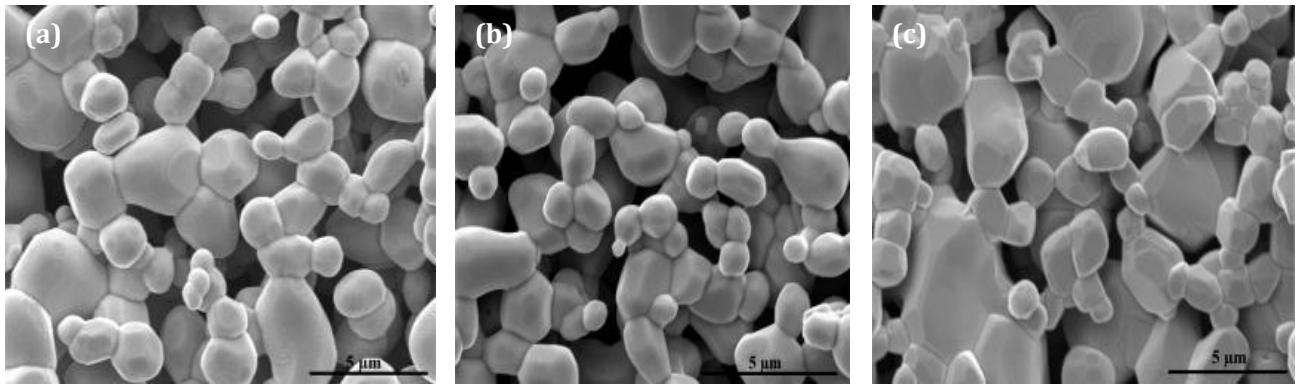

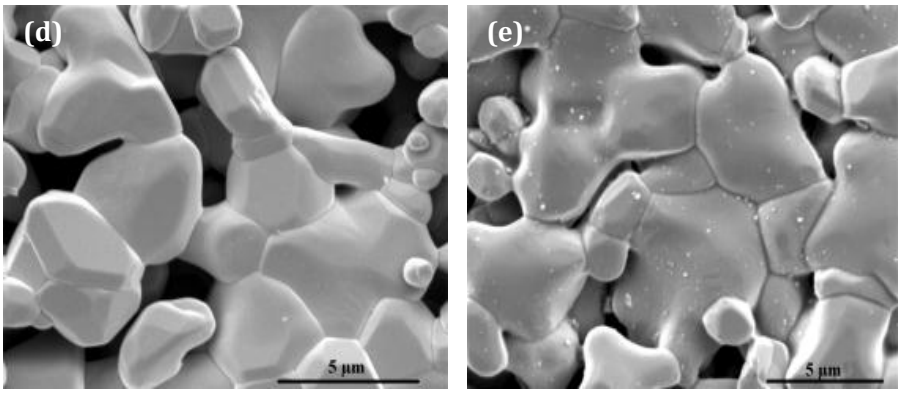

Fig. 7.4. SEM micrograph of a) LSCT0.1, b) LSCNT0.05, c) LSCNT0.1, d) LSCNT0.2, and e) LSCNT0.3.

Fig. 7.4 shows the micrographs of the sintered samples. The porous microstructure supports the low density of the samples (Fig. 7.3). The average grain sizes of LSCT0.1, LSCNT0.05, LSCNT0.1, LSCNT0.2, and LSCNT0.3 are ~1.7µm, 1.8µm, 3.2µm, 3.5µm, and 4.4µm, respectively. It is indicated that the grain size increases with increase in Ni-dopant concentration and density. Appearance of small white spots is observed only for LSCNT0.2, and LSCNT0.3. EDS spot analysis at ~ 20 points suggests that the white spots are enriched with strontium (10.8±0.3 at. %) compared to the bulk grains (5.4±0.2 at. %).

XPS analysis confirms the enrichment of strontium at the surface for LSCNT0.3 sample. Angle resolved measurement is performed as higher take-off angle is more sensitive to the surface. Fig. 7.5 shows the XPS spectra (0° and 60°) with Sr 3d doublet separation of 1.7eV. The Sr 3d photoelectron spectrum corresponds to the perovskite lattice (bulk) at lower binding energy (132±0.1eV for $3d_{5/2}$ and 133.7±0.1eV for $3d_{3/2}$) and surface at higher binding energy (133.7±0.1eV for $3d_{5/2}$ and 135.4±0.1eV for $3d_{3/2}$). The binding energy matches closely with the literature [45-46]. Sr-segregation (SrO) at the surface contributes to the surface spectrum with higher binding energy [45-47]. The $Sr_{surface}/Sr_{lattice}$ ratio varies from

0.19 to 0.25 as the XPS angle changes from 0° to 60. In addition, higher Sr/La ratio (0.27) than the actual prepared composition (0.18) further supports Sr-segregation at the surface.

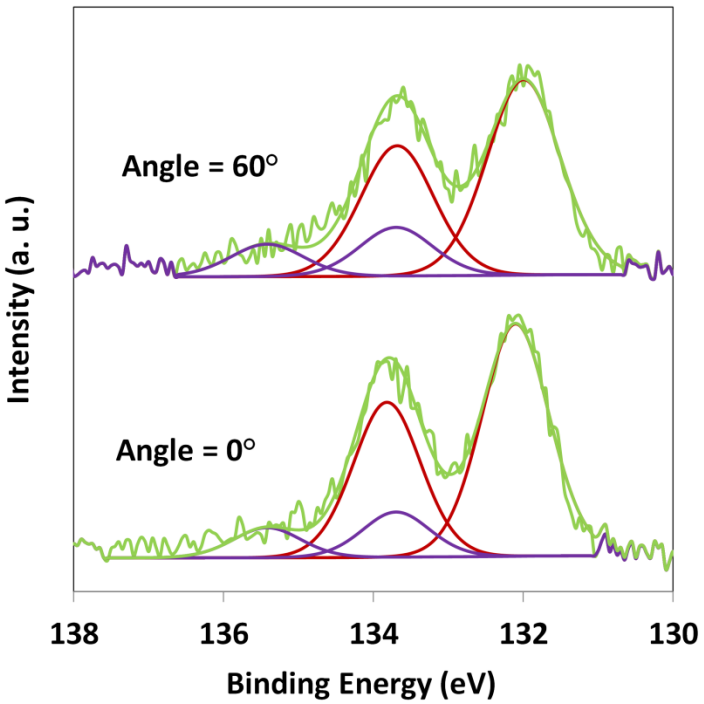

Fig. 7.5. Angle resolved X-ray Sr 3d photoelectron spectra of LSCNT0.3.

It is known that the surface composition and structure depends on the transition metal doping concentration [48]. Also, the surface free energies changes based on different dopants as well as their ionic radii. The surface segregation occurs to reduce the free energy of the system. The lattice strain induced by higher doping level and larger cation (nickel) size promotes the surface segregation for LSCNTy (y≥0.2) [49-50].

7.4.3. *Electrical conductivity*

The electrical conductivities of the studied compositions have been plotted with respect to temperature in log σT vs. 1/T plots in Fig. 7.6 and 7.7. Fig. 7.6 shows the conductivity in air while Fig. 7.7 shows the conductivity in reducing atmosphere (PO_2~10^{-24}

atm). Reproducible results were obtained during both heating and cooling cycles. With increase in temperature, the conductivity increases due to lower thermal activation barrier. Electrical conductivity values of the sintered LSCT0.1 and LSCNTy ($0.05 \leq y \leq 0.3$) samples at 900°C in air and reducing atmosphere (PO_2~10^{-24} atm) are given in Table 7.1. Since the samples are porous, the conductivities (σ_{corr}) for the corresponding dense samples have also been calculated (Table 7.1) using general effective media model which is described somewhere else [51].

The conductivity increases with introduction of nickel dopant at B-site of LSCT0.1 followed by decrease with further increase in dopant concentration ($y \geq 0.2$). However, the conductivities decrease in Ar-3%H_2 atmosphere for all the compositions when compared to air. However, highest conductivity has been obtained for LSCNT0.1 both in air and reducing atmosphere among the studied compositions.

In oxidizing atmosphere, oxygen loss has not been detected in the samples from TGA conducted in air at 1000°C. This implies that change in the valence state of Cr^{3+} to Cr^{4+} leads to the charge balance required for Sr^{2+} substitution on La^{3+} site as it does in case of $La_{1-x}Sr_xCrO_{3-\delta}$ [52] along with Ti^{4+}. On nickel doping, higher number of Cr^{4+} formation occurs due to the further charge balance required for the substitution of Ni^{2+} on Cr^{3+} site [8, 37]. For the nickel doped samples (LSCNTy), therefore, the conductivity increases due to the increase in the Cr^{4+} formation required for the charge neutrality resulting in large number of charge carriers for conduction [37].

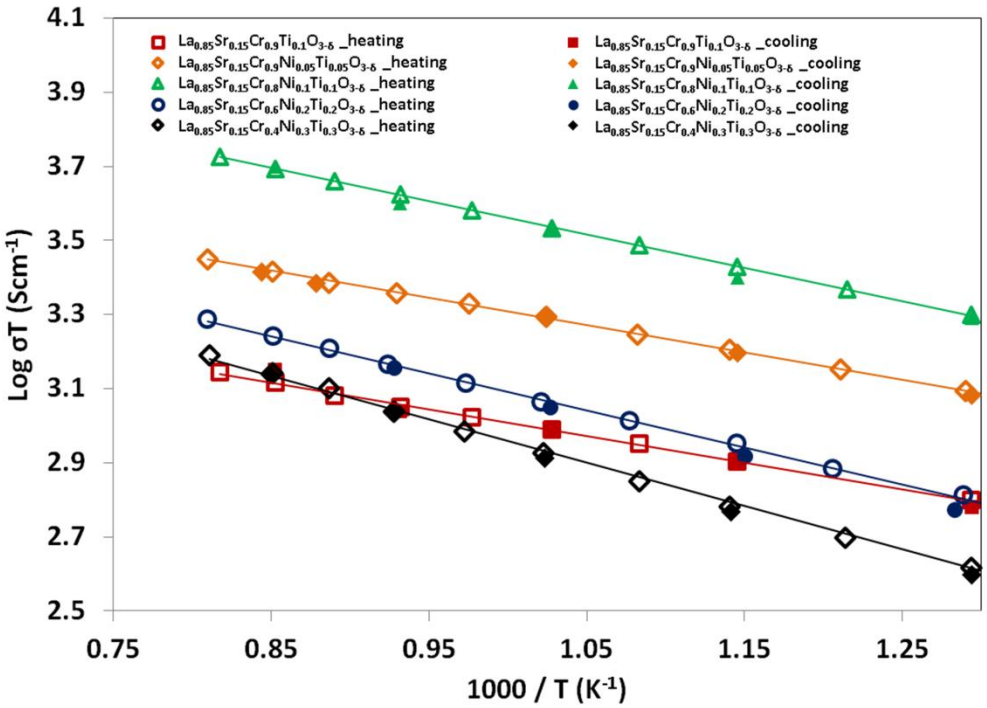

Fig. 7.6. Electrical conductivity of LSCT0.1 and LSCNTy ($0.05 \leq y \leq 0.3$) in the temperature range of 500–950°C in air.

For high concentration of dopants ($y \geq 0.2$), the Sr-segregation at the surface increases the band gap for electronic conduction. Consequently, the electrical conductivity decreases [53]. Furthermore, the physical properties of transition metal doped perovskites are dependent on the dopant amount, structure and surface segregation [48]. The electrical conductivity of the perovskites varies with change in charge carrier concentration as well as doping level [54]. A heavy doping (~25%) induces strain and distortion into the lattice of the doped perovskites [54]. Heavy doping also promotes lower symmetry in the lattice structure (orthorhombic) as shown in Fig. 7.1. This is associated with the distortion of octahedra (BO_6) which enhances scattering of charge carriers and decreases electrical conductivity [44]. Therefore, in case of LSCNT0.2 and LSCNT0.3, the higher dopant concentration (≥20 mol%) may also result into the decrease in conductivity.

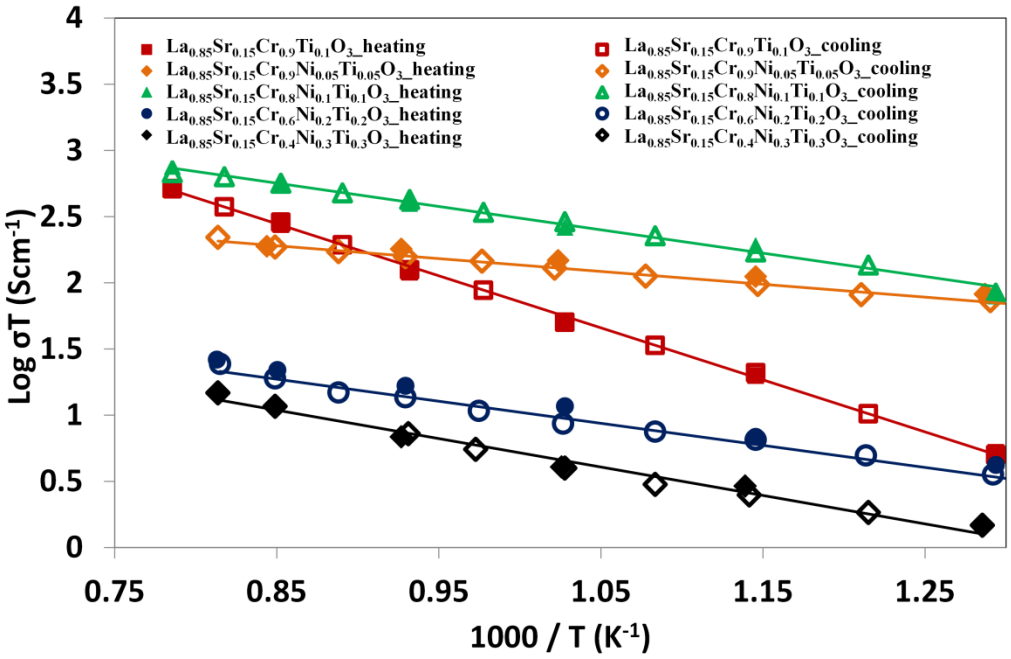

Fig. 7.7. Electrical conductivity of LSCT0.1 and LSCNTy ($0.05 \leq y \leq 0.3$) in the temperature range of 500–950°C in PO_2~10^{-24} atm.

Table 7.1. Electrical conductivity (σ) of LSCT0.1 and LSCNTy ($0.05 \leq y \leq 0.3$) at 900°C in air and (PO_2~10^{-24} atm).

Composition	σ (air) (S cm^{-1})	σ_{corr} (air) (S cm^{-1})	σ (~10^{-24}atm) (S cm^{-1})	σ_{corr} (~10^{-24}atm) (S cm^{-1})
$La_{0.85}Sr_{0.15}Cr_{0.9}Ti_{0.1}O_3$	1.12	7.45	0.24	1.55
$La_{0.85}Sr_{0.15}Cr_{0.9}Ni_{0.05}Ti_{0.05}O_3$	2.22	12.3	0.16	0.84
$La_{0.85}Sr_{0.15}Cr_{0.8}Ni_{0.1}Ti_{0.1}O_3$	4.21	16.5	0.48	1.84
$La_{0.85}Sr_{0.15}Cr_{0.6}Ni_{0.2}Ti_{0.2}O_3$	1.49	3.94	0.02	0.05
$La_{0.85}Sr_{0.15}Cr_{0.4}Ni_{0.3}Ti_{0.3}O_3$	1.18	2.27	0.01	0.02

* σ_{corr} refers to porosity corrected conductivity values.

In reducing atmosphere (PO_2~10^{-24} atm), oxygen vacancy is generated as confirmed by the oxygen loss (δ) detection for the samples from the TGA conducted at 1000°C. The δ values for $La_{0.85}Sr_{0.15}Cr_{1-2y}Ni_yTi_yO_{3-\delta}$ are 0.009, 0.011, and 0.015, respectively, for LSCT0.1, LSCNT0.1 and LSCNT0.3. It is reported that the valence state of Ti^{4+} does not change and stable in H_2 atmosphere [42]. Our results also indicate no change in the valence state of titanium cation from Ti 2p XPS spectra analysis with a binding energy of 457.6±0.1eV for $2p_{3/2}$ and 463.4±0.1eV for $2p_{1/2}$ which corresponds to Ti^{4+} valence state [55-57]. This implies that charge neutrality required for substituting Sr^{2+} on La^{3+} and Ni^{2+} on Cr^{3+} site is maintained predominantly by the oxygen vacancies formation in the reducing gas atmosphere [8]. Subsequently, the charge carriers for conduction decreases with oxygen vacancies formation. The cationic defects can also form defect clusters with the oxygen vacancies ($V_O^{\cdot\cdot}$) by electrostatic force. Formation of oxygen vacancies also induces tensile strain in the lattice. Combined effect of defect cluster and lattice strain increases the electronic band gap [49-50]. Subsequently, the conductivity decreases in the reducing atmosphere.

As discussed in the introduction, higher conductivity and stability are two important factors for OTM and SOEC/SOFC electrode/interconnect which usually tend to degrade in reducing atmosphere. In the literature, the lanthanum chromite based materials with various dopants (Mn, Fe, Co and Ti) at B-site have been investigated widely to overcome the challenge. On comparison with some of the promising lanthanum chromite based materials with 92-99% relative density [22, 32]; $(La_{0.75}Sr_{0.25})_{0.95}Cr_{0.5}Mn_{0.5}O_{3-\delta}$ (2.81 S cm^{-1}), $(La_{0.75}Sr_{0.25})_{0.95}Mn_{0.5}Cr_{0.1}Ti_{0.4}O_{3-\delta}$ (1.58 S cm^{-1}), $(La_{0.75}Sr_{0.25})_{0.95}Mn_{0.5}Ti_{0.5}O_{3-\delta}$ (1.51 S cm^{-1}), $(La_{0.75}Sr_{0.25})_{0.95}Cr_{0.7}Fe_{0.3}O_{3-\delta}$ (1.41 S cm^{-1}), and $(La_{0.75}Sr_{0.25})_{0.95}Cr_{0.6}Fe_{0.4}O_{3-\delta}$ (0.54 S cm^{-1}), the conductivity of Ni and Ti co-doped $La_{0.85}Sr_{0.15}Cr_{0.8}Ni_{0.1}Ti_{0.1}O_{3-\delta}$ (3.58 S cm^{-1}) is highest

at 950°C in reducing atmosphere (~10^{-16} atm) as shown in Table 7.2. Also, the deviation from oxygen stoichiometry (1000°C and ~10^{-24} atm) for $La_{0.85}Sr_{0.15}Cr_{0.8}Ni_{0.1}Ti_{0.1}O_{3-\delta}$ (0.011) is less than $La_{0.75}Sr_{0.25}CrO_{3-\delta}$ (0.091), $La_{0.75}Sr_{0.25}Cr_{0.5}Mn_{0.5}O_{3-\delta}$ (0.175) and $La_{0.75}Sr_{0.25}Cr_{0.5}Fe_{0.5}O_{3-\delta}$ (0.148) [34]. This corresponds to the higher stability of LSCNT0.1 in reducing gas atmosphere required for the above mentioned applications.

Table 7.2. Comparison of electrical conductivity (σ) of various doped lanthanum chromite based perovskites at 950°C and 10^{-16} atm.

Composition	σ (S cm^{-1})	References
$La_{0.85}Sr_{0.15}Cr_{0.8}Ni_{0.1}Ti_{0.1}O_3$	~3.58	This work
$(La_{0.75}Sr_{0.25})_{0.95}Cr_{0.5}Mn_{0.5}O_{3-\delta}$	~2.81	[7]
$(La_{0.75}Sr_{0.25})_{0.95}Mn_{0.5}Cr_{0.1}Ti_{0.4}O_{3-\delta}$	~1.58	[7]
$La_{0.75}Sr_{0.25}Cr_{0.5}Mn_{0.5}O_{3-\delta}$*	~1.60	[13, 15, 17, 19]
$(La_{0.75}Sr_{0.25})_{0.95}Mn_{0.5}Ti_{0.5}O_{3-\delta}$	~1.51	[7]
$(La_{0.75}Sr_{0.25})_{0.95}Cr_{0.7}Fe_{0.3}O_{3-\delta}$	~1.41	[18]
$(La_{0.75}Sr_{0.25})_{0.95}Cr_{0.6}Fe_{0.4}O_{3-\delta}$	~0.54	[18]

* The measurement is taken at 900°C and ~10^{-21} atm.

7.4.4. *Thermal expansion coefficient*

Thermal expansions of LSCT0.1 and LSCNTy ($0.05 \leq y \leq 0.3$) have been measured in the temperature range of 200–1300°C as shown in Fig. 7.8. Yttrium-stabilized zirconia (8YSZ) is one of the most common oxygen ion conductive materials which are used as a fluorite phase for ionic conduction in SOFC and OTM [58]. The thermal expansion

behaviour of 8YSZ has also been included in the Fig. 7.8 and Table 7.3 for comparison. The thermal expansion coefficient (TEC) of LSCT0.1 is 13.1±0.18 × 10^{-6}/°C which is higher than the TEC of 8YSZ (10.9±0.17 × 10^{-6}/°C). However, the thermal expansion coefficient of LSCNT0.1 matches closely with 8YSZ (10.9±0.17 × 10^{-6}/°C).

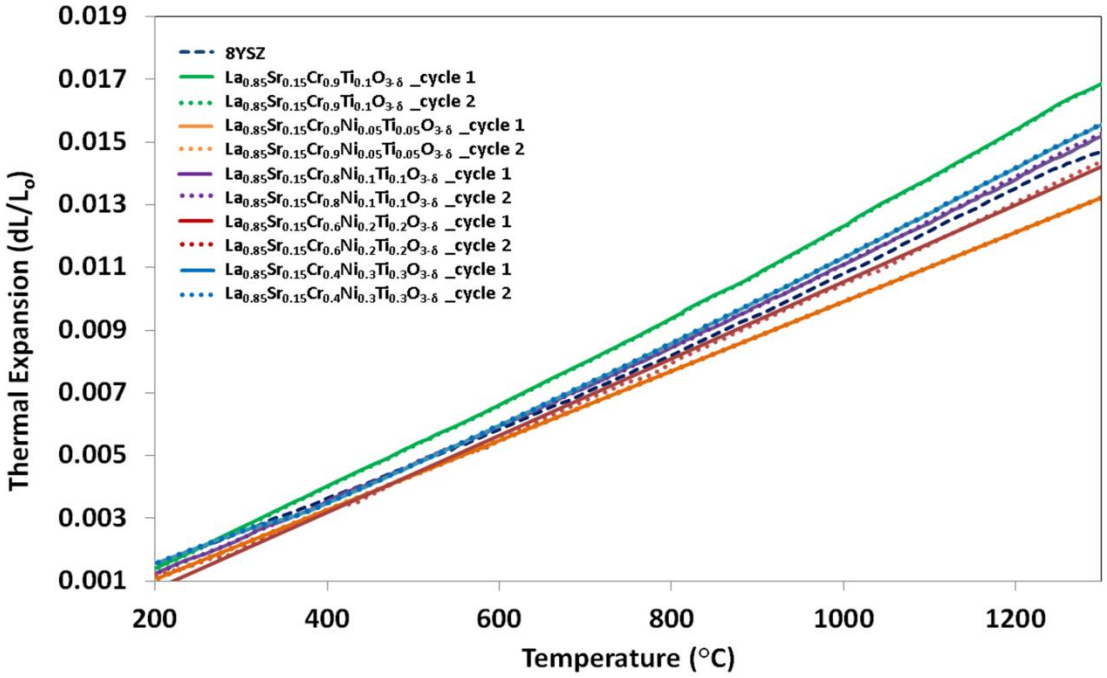

Fig. 7.8. Thermal expansions of LSCT0.1 and LSCNTy (0.05 ≤ y ≤ 0.3) in the temperature range of 200–1300°C in air.

Fig. 7.8 shows that co-doping of Ni-dopant at B-site results in lowering the thermal expansion close to 8YSZ. This could be due to the increase in the interatomic bond strength on Ni-doping [59]. Table 7.3 provides the TEC value of all A-site (Sr) and B-site (Ni/Ti) co-doped lanthanum chromite samples. The thermal expansion coefficient of LSCNT0.05 is

Table 7.3. Thermal expansion coefficient of 8YSZ, LSCT0.1 and LSCNTy ($0.05 \leq y \leq 0.3$) in the temperature range of 200-1300°C in air.

Composition	Thermal Expansion Coefficient ($\times 10^{-6}$/°C)
8YSZ	10.9±0.17
$La_{0.85}Sr_{0.15}Cr_{0.9}Ti_{0.1}O_3$	13.1±0.18
$La_{0.85}Sr_{0.15}Cr_{0.9}Ni_{0.05}Ti_{0.05}O_3$	9.9±0.21
$La_{0.85}Sr_{0.15}Cr_{0.8}Ni_{0.1}Ti_{0.1}O_3$	11.3±0.14
$La_{0.85}Sr_{0.15}Cr_{0.6}Ni_{0.2}Ti_{0.2}O_3$	11.5±0.21
$La_{0.85}Sr_{0.15}Cr_{0.4}Ni_{0.3}Ti_{0.3}O_3$	12.1±0.25

Table 7.4. Comparison of thermal expansion coefficient of 8YSZ, LSCNT0.1, LSCM73 and LSCF73 in the temperature range of 200-1300°C in air.

Composition	Thermal Expansion Coefficient ($\times 10^{-6}$/°C)
8YSZ	10.9±0.17
LSCNT0.1	11.3±0.14
LSCM73	11.8±0.12
LSCF73	11.7±0.11

$9.9(\pm 0.21) \times 10^{-6}$/°C which increases with increase in Ni-doping level for LSCNTy ($0.1 \leq y \leq 0.3$). The reason is attributed to increase in the lattice volume due to the high ionic radii of Ni^{2+} (0.690 Å) when compared to Cr^{3+} (0.615 Å) and Ti^{4+} (0.605 Å), in agreement with XRD results. Table 7.4 shows the TEC comparison of the best composition of this study i.e. LSCNT0.1 with the most studied compositions (LSCF73 and LSCM73) in the literature and 8YSZ. The closest thermal expansion match of 8YSZ is found with LSCNT0.1 when compared to LSCF73 and LSCM73.

7.4.5. *Electrochemical measurements and post-test characterization*

Fig. 7.9a and b shows typical impedance spectra exhibited by the symmetrical cell of configuration LSCNT0.1+8YSZ//8YSZ//LSCNT0.1+8YSZ at 950°C and 0.5 V in air and Ar-3%H_2-3%H_2O respectively. The semicircle in the impedance plane represents the contributions from electrolyte resistance (ohmic), oxygen surface exchange and migration through the microstructure, as well as gas-phase oxygen transport. The high frequency intercept represents ohmic resistance, while the sum of non-ohmic contributions is represented by the semicircle diameter [60]. In case of reducing atmosphere (Ar-3%H_2-3%H_2O), two semicircles are observed corresponding to the ion transfer through the microstructure (high frequency) and charge transfer at the interface (low frequency) [61]. However, the two electrode arcs are merged in oxidizing atmosphere (air) [61]. Fig 7.10a and b shows ohmic and non-ohmic resistances as a function of time for the cells tested at 950°C under the bias of 0.5 V in air and Ar-3%H_2-3%H_2O respectively. In case of oxidizing atmosphere, the resistance change is mostly due to increase in ohmic resistance as shown in Figs. 7.9a and 7.10a. There is no significant change observed in the non-ohmic resistance of the tested cell in air. The non-ohmic resistance increases from ~0.20 $\Omega.cm^2$ (0 h) to ~0.26 $\Omega.cm^2$ (80 h) in air at 950°C. As shown in Figs. 7.9a and 7.10a, the LSCNT0.1+8YSZ composite demonstrates low polarization resistance and stable performance in air atmosphere as required for OTM/SOFC/SOEC air electrode. Furthermore, no interfacial reaction resulting in lanthanum/strontium zirconate formation is identified in case of LSCNT0.1+8YSZ composite unlike LSM/8YSZ [17-18].

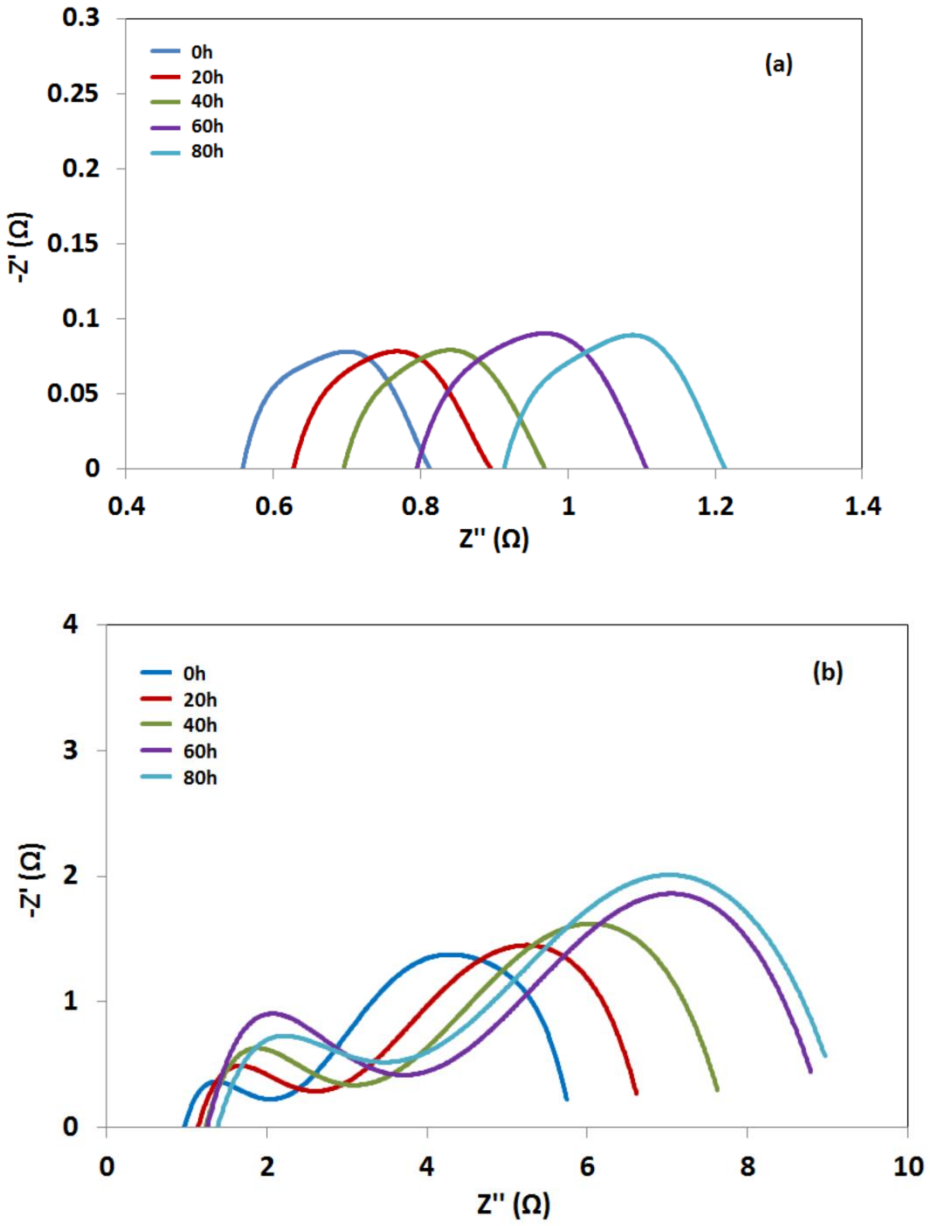

Fig. 7.9. Nyquist plots of impedance spectra obtained from the symmetrical cell of configuration LSCNT0.1+8YSZ//8YSZ//LSCNT0.1+8YSZ tested at 950°C with 0.5 V from 0 to 80 h: a) in air, and b) in Ar-3%H_2-3%H_2O. For clarity, only five spectra are shown.

In reducing atmosphere, there is no significant change observed in the ohmic resistance for 80h. The non-ohmic resistance for the tested cell is ~3.9 Ω.cm^2 (0 h), and increased to ~6.6 Ω.cm^2 (80 h) in Ar-3%H_2-3%H_2O at 950°C. Fig. 7.11a (air) and b (Ar-

3%H_2-3%H_2O) shows non-ohmic resistance comparison of new LSCNT0.1 composition based symmetrical cell (LSCNT0.1+8YSZ//8YSZ//LSCNT0.1+8YSZ) with extensively investigated LSCM based symmetrical cell (LSCM73+8YSZ//8YSZ //LSCM73+8YSZ) and LSCF based symmetrical cell (LSCF73+8YSZ//8YSZ //LSCF73+8YSZ) under the same electrochemical testing conditions (0.5V and 950°C) for 80h. The non-ohmic resistance of LSCM73 based cell increases from ~7.1 $\Omega.cm^2$ to ~12.1 $\Omega.cm^2$ in air and ~11.9 $\Omega.cm^2$ to ~24.9 $\Omega.cm^2$ in Ar-3%H_2-3%H_2O. On the other hand, the non-ohmic resistance of LSCF73 based composition increases from ~2.4 $\Omega.cm^2$ to ~4.5 $\Omega.cm^2$ and ~3.3 $\Omega.cm^2$ to ~9.7 $\Omega.cm^2$ in air and Ar-3%H_2-3%H_2O respectively. However, the non-ohmic resistance of LSCNT0.1 based cell increased only from ~0.20 $\Omega.cm^2$ to ~0.26 $\Omega.cm^2$ and ~3.9 $\Omega.cm^2$ to ~6.6 $\Omega.cm^2$ in air and Ar-3%H_2-3%H_2O respectively. Resistance of the tested cell increases with decrease in PO_2 or when exposed to reducing gas atmosphere. However, highest performance and significantly lower resistance is obtained for LSCNT0.1 based composition cell when compared to LSCM73 and LSCF73 in both oxidizing and reducing gas atmosphere. This is shown in Fig. 7.11. This corresponds to higher stability of LSCNT0.1 based symmetrical cell.

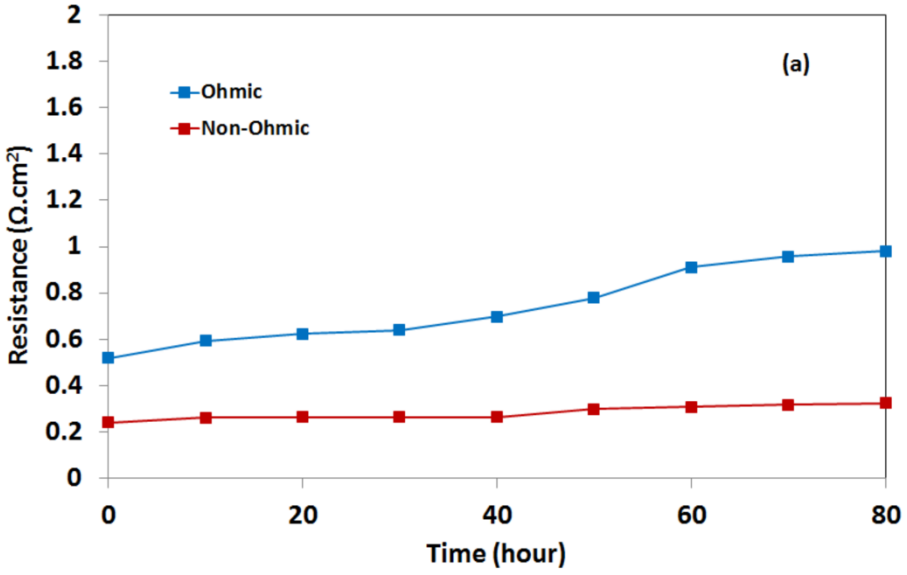

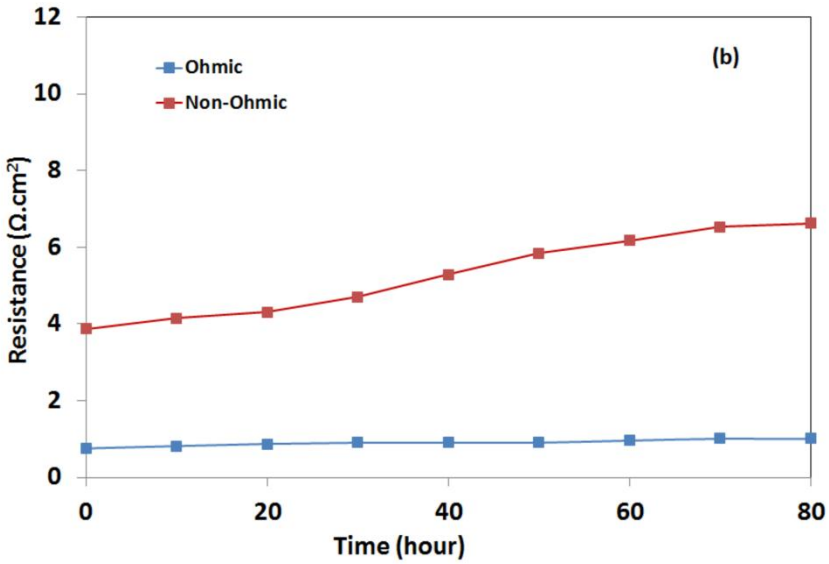

Fig. 7.10. Plots of resistance (ohmic and non-ohmic) changes with time for the symmetrical cell of configuration LSCNT0.1+8YSZ//8YSZ//LSCNT0.1+8YSZ tested at 0.5 V: a) in air, and b) Ar-3%H_2-3%H_2O.

After completion of the electrochemical tests, microstructures of the tested symmetrical cells were examined to understand the degradation behavior of the tested cells as shown in Fig. 7.12. When compared to as-sintered cell (Fig. 7.12a), there is no significant change observed in the microstructure of tested LSCNT0.1 based symmetrical cells both in air and Ar-3%H_2-3%H_2O as shown in Figs. 7.12b and c respectively. Similarly, when compared to as-sintered cell (Figs. 7.12d and g), no microstructural changes are observed in case of the LSCF73 and LSCM73 based symmetrical cells when tested in air as shown in Figs. 7.12e and h respectively. However, surface morphology of LSCF phase is modified in case of the LSCF73 based cell tested in Ar-3%H_2-3%H_2O (Fig. 7.12f). This probably contributes to the cell performance degradation with time in reducing atmosphere. Similarly, LSCM surface modification is identified in case of the LSCM73 based symmetrical cell tested in reducing gas atmosphere. Segregation of nano-particles is observed on the LSCM

phase of the anode surface of the tested cell as shown in Fig. 7.12i. At ~20 different points, surface elemental analysis is performed using SEM-EDS. The average Sr: La ratio is found to be higher for the symmetrical cell tested in Ar-3%H_2-3%H_2O (Sr: La ~ 0.65±0.05) than those tested in air (Sr: La ~ 0.44±0.05) which is comparable with the as-sintered cell (Sr: La ~ 0.43±0.04). This corresponds to the Sr-segregation in case of the cell tested in reducing atmosphere. Similar surface morphological changes corresponding to Sr-segregation are observed for $(La_{0.8}Sr_{0.2})_{0.98}MnO_3$ (LSM) after electrochemical cell testing with the exposure of 50% water vapor in air at 850°C for 100h [19]. Therefore, likewise LSM, it is possible that Sr-segregation on LSCM73 surface results in degradation of the cell and higher resistance. However, in case of LSCNT0.1 based symmetrical cells, no surface modification and/or interfacial reaction are identified corresponding to its higher stability and performance when compared to LSCF73 and LSCM73.

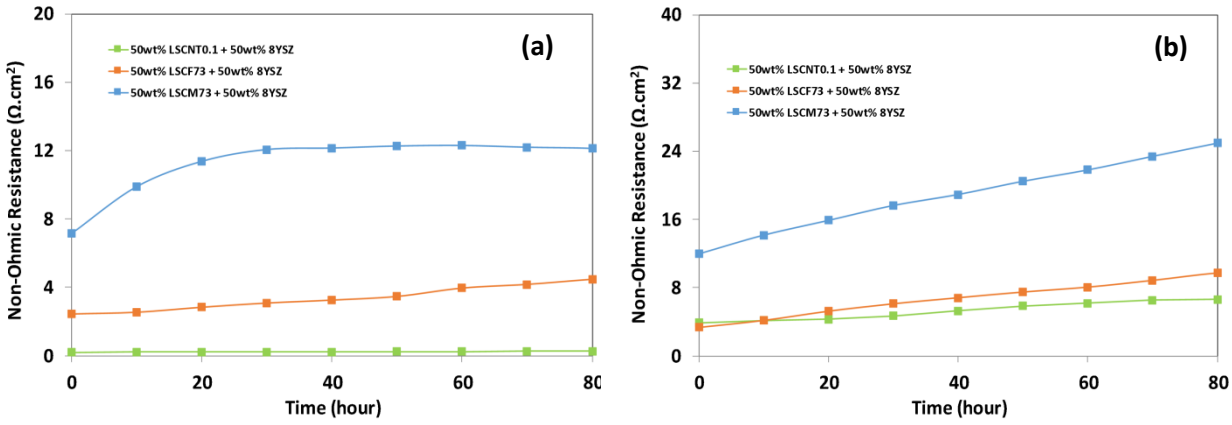

Fig. 7.11. Comparison plots of non-ohmic resistance changes with time for the symmetrical cell of configurations: LSCNT0.1+8YSZ//8YSZ//LSCNT0.1+8YSZ, LSCF73+8YSZ//8YSZ//LSCF73+8YSZ and LSCM73+8YSZ//8YSZ//LSCM73+8YSZ tested at 0.5 V: a) in air, and b) Ar-3%H_2-3%H_2O.

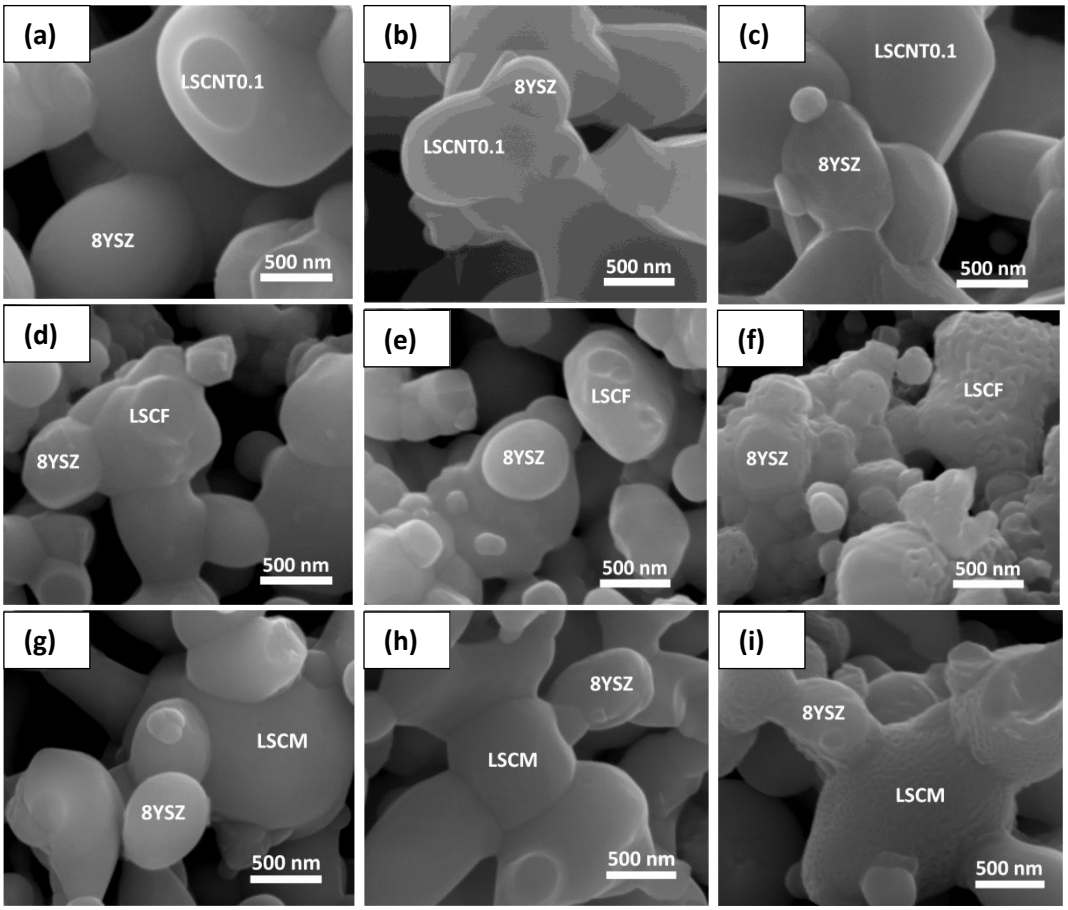

Fig. 7.12. SEM micrographs of the tested symmetrical cell (anode surface): LSCNT0.1+8YSZ//8YSZ//LSCNT0.1+8YSZ - a) as-sintered, b) in air, c) in Ar-3%H_2-3%H_2O; LSCF73+8YSZ//8YSZ//LSCF73+8YSZ - d) as-sintered, e) in air, and f) in Ar-3%H_2-3%H_2O; LSCM73+8YSZ//8YSZ//LSCM73+8YSZ - g) as-sintered, h) in air, and i) in Ar-3%H_2-3%H_2O.

7.5. Conclusion

Ni and Ti co-doped $La_{0.85}Sr_{0.15}Cr_{1-2y}Ni_yTi_yO_{3-\delta}$ ($0.05 \leq y \leq 0.3$) perovskites have been synthesized. The electrical conductivity of LSCNT0.1 is highest among the compositions studied as well as when compared to LSCF and LSCM based compositions. Sr-segregation decreases the electrical conductivity in air for $y \geq 0.2$ while oxygen vacancy formation and

association of defects/defect clustering and lattice strain decreases the conductivity in reducing atmosphere. The thermal expansion coefficient of LSCNT0.1 closely matches with 8YSZ. Using electrochemical testing, it is shown that $La_{0.85}Sr_{0.15}Cr_{0.8}Ni_{0.1}Ti_{0.1}O_{3-\delta}$ based symmetrical cells obtain higher and stable performance when compared to widely investigated $(La_{0.75}Sr_{0.25})_{0.95}Cr_{0.7}Mn_{0.3}O_{3-\delta}$ and $(La_{0.8}Sr_{0.2})_{0.95}Cr_{0.7}Fe_{0.3}O_{3-\delta}$ compositions. Unlike LSCM73 and LSCF73, no degradation has been observed for LSCNT0.1 based symmetrical cells during the post-test characterization of the cells. Higher electrochemical performance and stability of a newly co-doped lanthanum strontium chromite based composition (LSCNT0.1 + 8YSZ) are demonstrated in both oxidizing and reducing atmosphere for high temperature electrochemical devices.

7.6. References

[1] A. Atkinson, S. Barnett, R.J. Gorte, J.T.S. Irvine, A.J. McEvoy, M. Moguensen, S.C. Singhal, J. Vohs. Nat. Mater. 3 (2004) 17–27.

[2] J.C.R. Morales, D.M. Lo´pez, J.C. Va´zquezc, J.T.S. Irvine. RSC Advances 1 (2011) 1403-1414.

[3] J. Sfeir. J. Power Sources 118 (2003) 276–285.

[4] P. Duran, J. Tartaj, F. Capel, C. Moure. J. Eur. Ceram. Soc. 24 (2004) 2619–2629.

[5] A.S. Mukasyan, C. Costello, K. P. Sherlock, D. Lafarga, A. Varma. Sep. and Purif. Technol. 25 (2001) 117–126.

[6] V.B. Vert, F.V. Melo, L. Navarrete, J.M. Serra, Appl. Catal. B: Environ. 115 (2012) 346–356.

[7] V.V. Kharton, E.V. Tsipis, I.P. Marozau, A.P. Viskup, J.R. Frade, J.T.S. Irvine. Solid State Ionics 2007, 178, 101–113.

[8] S. Gupta, M.K. Mahapatra, P. Singh. Mater. Sci. Eng. R 90 (2015) 1–36.

[9] H.J.M. Bouwmeester, A.J. Burggraaf, in: A.J. Burggraaf, L. Cot (Eds.). Membrane Science and Technology Series, Elsevier, Amsterdam, 1996, pp. 435–510.

[10] J. Richter, P. Holtappels, T. Graule, T. Nakamura, L.J. Gauckler. Monatshefte Chem. 140 (2009) 985–999.

[11] M. Cherry, M.S. Islam, C.R.A. Catlow. J. Solid State Chem. 118 (1995) 125–132.

[12] J.A. Kilner, R.J. Brook. Solid State Ionics 6 (1982) 237–252.

[13] Y.T. Suru, M. Shimazu, M. Shiono, M. Morinaga, Jpn. J. Appl. Phys. 49 (2010) 045701.

[14] J.W. Stevenson, T.R. Armstrong, R.D. Carmeim, L.R. Pederson, L.R. Weber. J. Electrochem. Soc. 143 (1996) 2722–2729.

[15] J. Kim, Y.S. Lin. J. Membr. Sci. 167 (2000) 123–133.

[16] J.J. Liu, T. Liu, W.D. Wang, J.F. Gao, C.S. Chen. J. Membr. Sci. 389 (2012) 435–440.

[17] M. Keane, M.K. Mahapatra, A. Verma, P. Singh. Int. J. Hydrogen Energy 37 (2012) 16776 – 16785.

[18] N. Li, M. Keane, M.K. Mahapatra, P. Singh. Int. J. Hydrogen Energy 38 (2013) 6298 – 6303.

[19] B. Hu, M. Keane, M.K. Mahapatra, P. Singh, J. Power Sources 248 (2014) 196 – 204.

[20] B. Hu, M.K. Mahapatra, M. Keane, H. Zhang, P. Singh. J. Power Sources 268 (2014) 404 – 413.

[21] T. Norby, R. Hildrum, M. Seiersten, R. Glenne, P.A. Osborg, O. Dyrlie. Proceedings of the European Solid Oxide Fuel Cell Forum I, Switzerland, 1994.

[22] V.A. Kolotygin. E.V. Tsipis, A.L. Shaula, E.N. Naumovich, J.R. Frade, S.I. Bredikhin, V.V. Kharton. J. Solid State Electrochem. 15 (2011) 313–327.

[23] J.G.M.I. Furtado, R.N. Oliveira. Revista Matéria. 13 (2008) 147–153.

[24] S. Gupta, M.K. Mahapatra, P. Singh. Mater. Res. Bull. 48 (2013) 3262– 3267.

[25] K.T. Jacob, S. Gupta, P. Singh. J. Am. Ceram. Soc. 96 (2013) 3933–3938.

[26] T. Nakamura, G. Petzow, L. Gauckler. Mater. Res. Bull. 14 (1979) 649–659.

[27] S. Tao, J.T.S. Irvine. J. Electrochem. Soc. 151 (2004) A252–259.

[28] J. Liu, B. Madsen, Z. Ji, S. Barnett. Electrochem. Solid State Lett. 5 (2002) A122–124.

[29] S. Zha, P. Tsang, Z. Cheng, M. Liu. J. Solid State Chem. 175 (2005) 844–1850.

[30] D.M. Bastidas, S. Tao, J.T.S. Irvine. J. Mater. Chem. 16 (2006) 1603–1605.

[31] S. Tao, J.T.S. Irvine, Nat. Mater. 2 (2003) 320–323.

[32] M.F. Lu, E.V. Tsipis, J.C. Waerenborgh, A.A. Yaremchenko, V.A. Kolotygin, S. Bredikhin, V.V. Kharton. J. Power Sources 206 (2012) 59–69.

[33] S. Tao, J.T.S. Irvine. Chem. Mater. 18 (2006) 5453–5460.

[34] M. Oishi, K. Yashiro, K. Sato, J. Mizusaki, T. Kawada. J. Solid State Chem. 181 (2008) 3177–3184.

[35] Y. Takahashi, A. Kawahara, T. Suzuki, M. Hirano, W. Shin. Solid State Ionics 181 (2010) 300–305.

[36] A. Atkinson, T.M.G.M. Ramos. Solid State Ionics 129 (2000) 259–269.

[37] H. Xiong, G.J. Zhang, J.Y. Zheng, Y.Q. Jia. Mater. Lett. (2001) 61–67.

[38] S.P. Simner, J.S. Hardy, J.W. Stevenson. J. Electrochem. Soc. 148 (2001) A351–A360.

[39] A. Ruangvittayanon, S. Kuharuangrong. Suranaree J. Sci. Technol. 16 (2001) 319–323.

[40] H.E. Hofer, W.F. Kock. J. Electrochem Soc. 140 (2003) 2889–2894.

[41] H. Hayashi, M. Watanabe, M. Ohuchida, H. Inaba, Y. Hiei, T. Yamamoto, M. Mori. Solid State Ionics 144 (2001) 301–313.

[42] M. Mori, Y. Hiei. J. Am. Ceram. Soc. 84 (2001) 2573–2578.

[43] W. Kobsiriphat, B.D. Madsen, Y. Wang, M. Shah, L.D. Marks, S.A. Barnett. J. Electrochem. Soc. 157 (2010) B279–284.

[44] M.R. Levy. Ph.D. Thesis, University of London, 2005.

[45] Z. Cai, M. Kubicek, J. Fleig, B. Yildiz. Chem. Mater. 24 (2012) 1116–1127.

[46] J.E. Elshof, H.J.M. Bouwmeester. H. Verweij. Solid State Ionics 89 (1996) 81–92.

[47] P. Decorse, E. Quenneville, S. Poulin, M. Meunier, A. Yelon. J. Vac. Sci. Technol. A 19 (2001) 910-915.

[48] H. Dulli, P.A. Dowben, S.H. Liou, E.W. Plummer. Phy. Rev. B 62 (2000) R14629-14632.

[49] W. Lee, J.W. Han, Y. Chen, Z. Cai, B. Yildiz. J. Am. Chem. Soc. 135 (2013) 7909−7925.

[50] W. Jung, H.L. Tuller. Energy Environ. Sci. 5 (2012) 5370–5378.

[51] D.S. Mclachlan, M. Blaszkiewicz, R.E. Newnham. J. Am. Cer. Soc. 73 (1990) 2187-2203.

[52] I. Yasuda, M. Hishinuma. Solid State Ionics 80 (1995) 141-150.

[53] Y. Chen, W. Jung, Z. Cai, J.J. Kim, H.L. Tuller, B. Yildiz, Energy Environ. Sci. 5 (2012) 7979-7988.

[54] S.P. Jiang, L. Liu, K.P. Ong, P. Wu, J. Li, J. Puc. J. Power Sources 176 (2008) 82-89.

[55] S.M. Mukhopadhyay, T.C.S. Chen. J. Appl. Phys. 74 (1993) 872-876.

[56] T. Chakroborty, S. Ray, M. Itoh. Phys. Rev. B 83 (2011) 144407-144410.

[57] J.L. Jou, C.M. Lei, Y.W. Xu, W.C.V. Yeh. Chinese J. Phy. 50 (2012) 926-931.

[58] M. Filal, Petot, M. Mokchah, C. Chateau, J.L. Carpentier. Solid State Ionics 80 (1995) 27- 35.

[59] X. Ding, Y. Liu, L. Gao, L. Guo. J. Alloys and Compd. 425 (2006) 318-322.

[60] M. Keane, M.K. Mahapatra, A. Verma, P. Singh. Int. J. Hydrogen Energy 37 (2012) 16776-16785.

[61] D.M. Bastidas, S. Tao, J.T.S. Irvine. J. Mat. Chem. 16 (2006) 1603-1605.

CHAPTER 8: A COMPARATIVE STUDY ON MANGANESE-DOPED LANTHANUM-STRONTIUM CHROMITE MIXED WITH 8YSZ AND 10ScSZ IN OXIDIZING AND REDUCING ATMOSPHERES

8.1. Abstract

This paper reports a comparative study of LSCM perovskite mixed with 8YSZ and 10ScSZ for the application of oxygen transport membrane system. Role of oxidizing and reducing atmosphere is also reported on processing and electrochemical performance of the composites. Higher density is obtained when LSCM is mixed with 10ScSZ when compared to 8YSZ in oxidizing as well as reducing atmosphere. Both LSCM/8YSZ and LSCM/10ScSZ show higher density in Ar-3%H_2-3%H_2O atmosphere than air. An interaction between LSCM and 8YSZ/10ScSZ and $SrZrO_3$ formation is identified in both the cases in reducing atmosphere. $MnCr_2O_4$ formation is found only in LSCM/8YSZ composite in Ar-3%H_2-3%H_2O. On comparison with LSCM/8YSZ//8YSZ/LSCM/8YSZ, low polarization resistance and higher performance is obtained for the symmetrical cell of configuration LSCM/10ScSZ//8YSZ/LSCM/10ScSZ. Unlike LSCM/8YSZ composite, no significant changes are identified in the polarization resistance of LSCM/10ScSZ cell for 80h. Post-test characterization show Sr-segregation on the surface of LSCM in case of LSCM/8YSZ cell; attributing to its significant performance degradation in reducing atmosphere.

8.2. Introduction

Perovskite-fluorite based oxygen transport membranes (OTM) are currently being developed for wide range of industrial applications including syngas production which can be further processed to liquid fuel for transportation [1-4]. OTM's also finds application in the power plants for clean and efficient energy production via oxy-combustion with minimal gas emissions [1-5]. The membranes can also easily be incorporated in the integrated gasification combined cycle (IGCC) and coal gasification fuel cell (CGFC) systems for efficient power generation along with CO_2 capture [1-5].

During the operation of oxygen transport membrane, one side of OTM is exposed to air and the other side to fuel (e.g. H_2, CO, CH_4) [1, 6]. Due to the oxygen partial difference across the membrane, oxygen selectively permeates through the membrane and gets separated on the fuel side as required for the above mentioned applications. $(Ln,A)(B)O_{3-\delta}$ (Ln = rare earth metals, A = Sr, Ca and B = transition metals) based single-phase perovskites are widely investigated due to high oxygen flux performance [1, 3, 6-8]. However, long-term thermal and chemical stability of these perovskites are still a challenge for stable operation of OTM [1, 9]. On the other hand, perovskite-fluorite based dual phase composites are currently being investigating for dual benefit i.e. high performance and stability under OTM operating conditions [1-7, 10]. It is found that the performance and stability of the composites are higher when compared to single-phase perovskite oxides [1, 9].

Due to high stability at high temperature (≥1000°C) in a wide range of oxygen partial pressure ($1\text{-}10^{-24}$ atm), lanthanum chromite based materials are considered to be a promising material for OTM [1-4, 8, 10]. When mixed with fluorite phase, high oxygen

flux performance can be obtained as required for OTM [1, 9]. A review article on lanthanum chromite based materials for oxygen transport membrane is published recently by the authors [1].

In this study, the authors have chosen strontium and manganese co-doped $(La_{0.75}Sr_{0.25})_{0.95}Cr_{0.7}Mn_{0.3}O_3$ (LSCM) as OTM for investigation as it can provide high performance and stability when mixed with fluorite phase based on the literature review [1, 11-13]. 8YSZ and 10ScSZ are two commonly reported stable fluorite materials [1, 14-16]. Most of the literature reports result on LSCM and 8YSZ [1, 17-18]. 10ScSZ provides higher ionic conductivity than 8YSZ which could be beneficial for OTM performance [19]. It is important to find the right combination of perovskite and fluorite phases to get the maximum performance and stability under OTM operating conditions. Therefore, in this study, the authors investigate a comparative study on LSCM processing (under OTM fabricating conditions), performance (under OTM operating conditions) and stability when combined with 8YSZ and 10ScSZ and exposed to oxidizing and reducing gas atmosphere.

8.3. Experimental Procedure

8.3.1. *$(La_{0.75}Sr_{0.25})_{0.95}Cr_{0.7}Mn_{0.3}O_{3-\delta}$ and 8YSZ/10ScSZ synthesis*

LSCM powder was received from Praxair Inc. The powder was mixed with 8YSZ/10ScSZ in the weight ratio of 50: 50. Mixed powders were then uniaxially pressed into cylindrical pellets and subsequently sintered in oxidizing (air) and reducing (Ar-3%H_2-3%H_2O) atmosphere at 1400°C with 10h dwell time. To ensure the maintenance of the oxygen pressure during cooling, samples were cooled in the flowing gas environment.

8.3.2. *Characterization*

Using Archimedes principle, density of LSCM/8YSZ and LSCM/10ScSZ samples was measured. Scanning electron (FEI - ESEM Quanta 250) and transmission electron (FEI Tecnai T12 S/TEM) microscopes were utilized for microstructural analysis of the sintered and tested samples. Elemental profile analysis of the samples was conducted using Energy dispersive spectroscopy (EDS) attached to the SEM as well as TEM. Focused ion beam (FEI Strata 400S DUALBEAM FIB) technique was used to prepare samples for TEM microstructural analysis.

X-ray diffraction (BRUKER-D8 ADVANCE, Bruker AXS Inc.) technique was utilized to determine the crystal structure of LSCM composite with 8YSZ/10ScSZ and secondary compounds, if any when exposed to oxidizing and reducing gas atmosphere. The scan step used for X-ray diffraction was 0.02° using CuK_{α} radiation (λ = 1.5406 Å). High temperature X-ray diffraction of LSCM/8YSZ and LSCM/10ScSZ was conducted in the temperature range of 30-1200°C in oxidizing (air) and reducing atmosphere (Ar-3%H_2-3%H_2O) in order to further understand the structural changes, compound formation, stability and interaction between LSCM and 8YSZ/10ScSZ. Minimum of 1 hour dwell time was provided at each temperature for equilibration.

8.3.3. *Symmetric cell fabrication*

LSCM/8YSZ and LSCM/10ScSZ paste was prepared using ink vehicle (Fuel Cell Materials). As working and counter electrodes (thickness: ~20 µm, diameter: 10 mm), LSCM and 8YSZ/10ScSZ were screen-printed on both sides of $(ZrO_2)_{0.92}(Y_2O_3)_{0.08}$(YSZ) electrolyte (200 µm thick, Fuel Cell Materials). The electrodes were then dried at room temperature and subsequently sintered at 1200°C (heating rate of 3°C/min) for 2 h in air. The electrochemical

active area of the cell electrode was 0.8 cm^2. Platinum screen current collector (Alfa Aesar, 50 mesh) and platinum wires (Alfa Aesar, 0.25 mm) were attached to both electrodes using platinum paste (Electro-Science Laboratories Inc.). Curing of platinum paste was obtained in air at 900°C with 1 h (3°C/min) dwell time. As-assembled LSCM/8YSZ//8YSZ//LSCM/ 8YSZ and LSCM/10ScSZ//8YSZ//LSCM/10ScSZ symmetric cells were then installed in a tubular alumina chamber and placed in the constant temperature zone of a furnace. Multi-channel potentiostat (VMP2, Bio-Logic) leads were attached to the assembled symmetric cell for electrochemical impedance measurement.

8.3.4. *Electrochemical testing*

LSCM/8YSZ and LSCM/10ScSZ based symmetrical cells were heated up to 950°C (3°C/min) in air and Ar-3%H_2 (humidified at room temperature) with flow rate of 300sccm. The cells were tested for 80 h under the constant bias of 0.5V. The impedance measurement was performed (at two hour intervals) in the frequency range starting from 100 mHz to 200 kHz using a 10 mV alternating current. Experiments were repeated a couple of times under same condition to ensure reproducibility. Post-test characterizations of the samples were performed using SEM-EDS (FEI - ESEM Quanta 250).

8.4. Results and Discussion:

8.4.1. *Crystal Structure*

Fig. 8.1 and Fig. 8.2 shows the XRD pattern of LSCM composite with 8YSZ and 10ScSZ sintered in oxidizing (air ~ 0.21atm) and reducing atmosphere (Ar-3%H_2-3%H_2O ~10^{-10} atm) at 1400°C. Crystal structure of LSCM is rhombohedral (JCPDS 75-9872) in air. However, in both cases (LSCM/8YSZ and LSCM/10ScSZ), it is noted that the peaks splitting corresponding to rhombohedral phase disappears for the samples sintered in Ar-

3%H_2-3%H_2O as shown in Fig. 8.1 (inserted plot). This corresponds to phase transformation to higher symmetry cubic phase (JCPDS 074-1961) [10, 20]. Furthermore, it indicates that cubic phase becomes dominant in Ar-3%H_2-3%H_2O atmosphere as the peak splitting corresponding to rhombohedral phase almost disappears. Extra peaks corresponding to the strontium zirconate ($SrZrO_3$) (JCPDS-01-074-1297) are identified in Ar-3%H_2-3%H_2O sintered samples unlike air. Fig. 8.2 shows XRD pattern comparison of LSCM composite with 8YSZ and 10ScSZ when processed in Ar-3%H_2-3%H_2O atmosphere at 1400°C. Peak intensity of $SrZrO_3$ is higher in case of LSCM/8YSZ composite when compared to LSCM/10ScSZ under same conditions. This corresponds to higher amount of $SrZrO_3$ formation when LSCM is mixed with 8YSZ when compared to 10ScSZ.

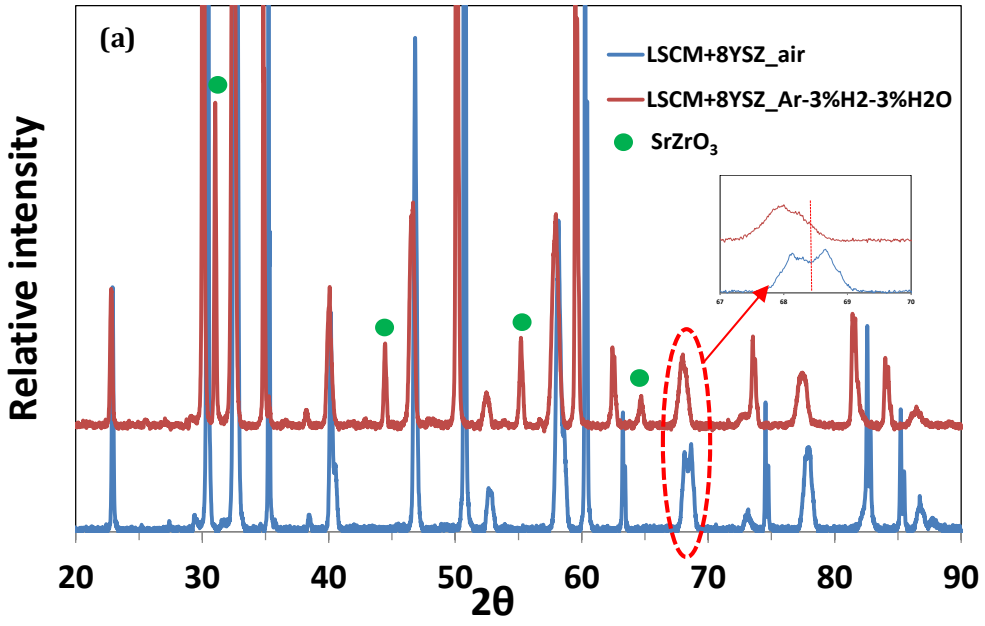

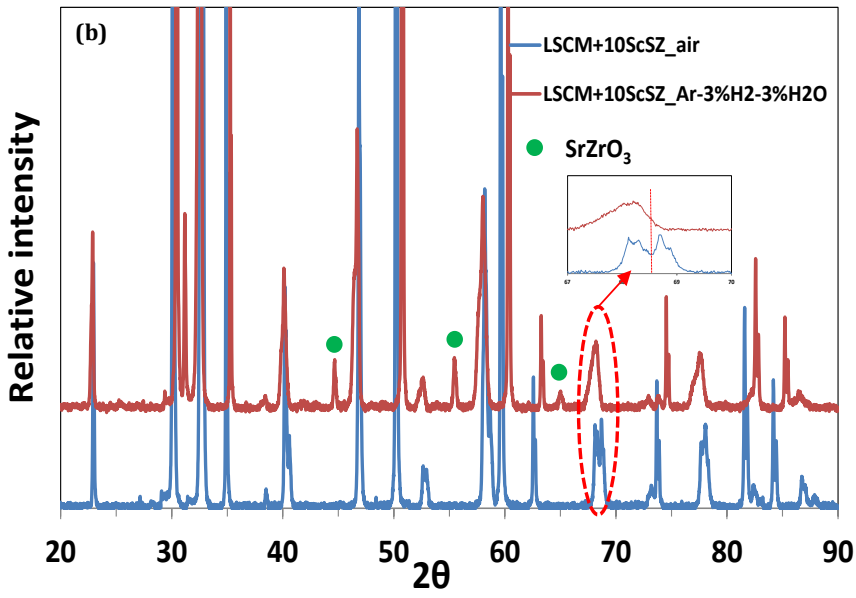

Fig. 8.1. XRD pattern of LSCM and 8YSZ/10ScSZ composites when exposed to air and Ar-3%H_2-3%H_2O at 1400°C for 10h: a) LSCM + 8YSZ and b) LSCM + 10ScSZ

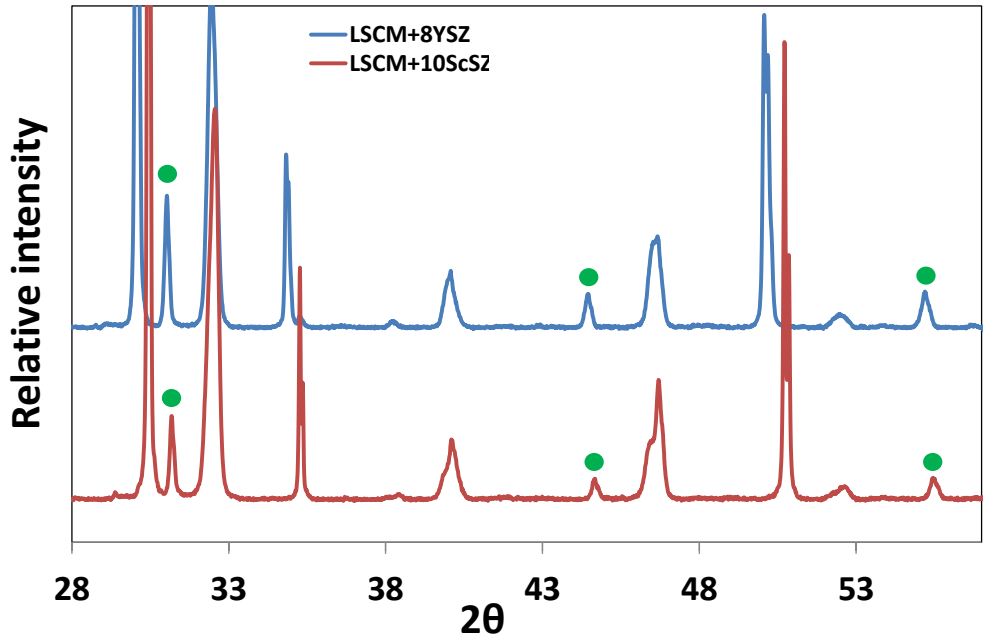

Fig. 8.2. XRD comparison plot of LSCM when mixed with 8YSZ and 10ScSZ in Ar-3%H_2-3%H_2O at 1400°C for 10h.

8.4.2. *Sintering behavior and Microstructural Analysis*

Table 8.1 shows relative density of LSCM/8YSZ and LSCM/10ScSZ sintered in oxidizing (air) and reducing atmosphere (Ar-3%H_2-3%H_2O) at 1400°C for 10h. Higher density of LSCM/8YSZ composite is obtained in Ar-3%H_2-3%H_2O (74.8±1.3%) atmosphere when compared to air (59±2.2%). On the other hand, LSCM/10ScSZ composite density increases from 78.1±1.5% to 88.2±0.9% when gas atmosphere is switched from oxidizing (air) to reducing (Ar-3%H_2-3%H_2O) respectively. In both cases, it is noted that higher density is obtained when the composites are processed in Ar-3%H_2-3%H_2O atmosphere. On comparison with LSCM/8YSZ composite, LSCM/10ScSZ achieves higher density in oxidizing as well as reducing atmosphere. Fig. 8.3 shows the SEM microstructures of LSCM composite with 8YSZ and 10ScSZ, sintered in air and Ar-3%H_2-3%H_2O gas atmosphere. No secondary phases have been identified in oxidizing as well as reducing atmosphere using SEM. However, $SrZrO_3$ secondary phase formation is detected using XRD technique for the samples sintered in Ar-3%H_2-3%H_2O.

To confirm on the secondary phase formation, TEM microstructural analysis is conducted on LSCM/8YSZ and LSCM/10ScSZ samples sintered in air as well as Ar-3%H_2-3%H_2O atmosphere as shown in Fig. 8.4. The sample preparation for TEM analysis is performed using FIB as shown in the insert of Fig. 8.4a. It is clear that the dense microstructure is obtained for LSCM when mixed with 10ScSZ than 8YSZ. No secondary phase is identified in the samples sintered in air atmosphere. On the other hand, as expected from XRD analysis, secondary phases are identified in both the composites in reducing gas atmosphere (Fig. 8.4c and d). TEM elemental analysis reveals that the secondary phase predominantly consists of Sr and Zr corresponding to $SrZrO_3$ formation as shown in Table

8.1 (LSCM/8YSZ) and Table 8.2 (LSCM/10ScSZ). However, a second new phase is identified only in Ar-3%H_2-3%H_2O sintered LSCM/8YSZ composite as shown in the TEM micrograph (Fig. 8.4c). The secondary phase is enriched in Mn and Cr as shown in the Table 8.1. This corresponds to $MnCr_2O_4$ spinel formation attributing to Mn: Cr :: 1: 2. The phase is not identified in the XRD. This is probably because; the phase is present in small amount and outside the XRD detection limit.

Fig. 8.5 shows the TEM elemental mapping of FIB-cross-section of sintered LSCM/8YSZ in Ar-3%H_2-3%H_2O. It is clearly identified that one of the secondary phase is enriched in Sr and Zr and other in Mn and Cr. However, TEM elemental mapping of LSCM/10ScSZ indicates only one secondary phase formation enriched in Sr and Zr as shown in Fig. 8.6.

Table 8.1. Relative density of LSCM/8YSZ and LSCM/10ScSZ sintered at 1400°C for 10h.

Relative density (%)		
Material	**Air**	**Ar-3%H_2-3%H_2O**
LSCM+8YSZ	59±2.2	74.8±1.3
LSCM+10ScSZ	78.1±1.5	88.2±0.9

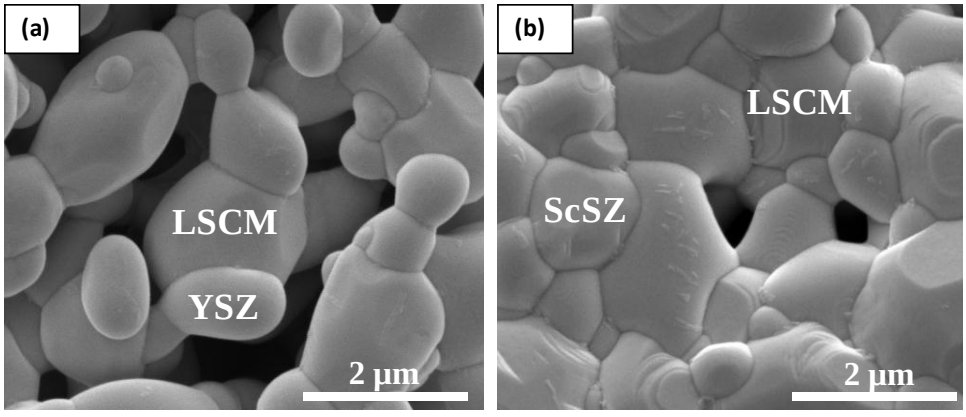

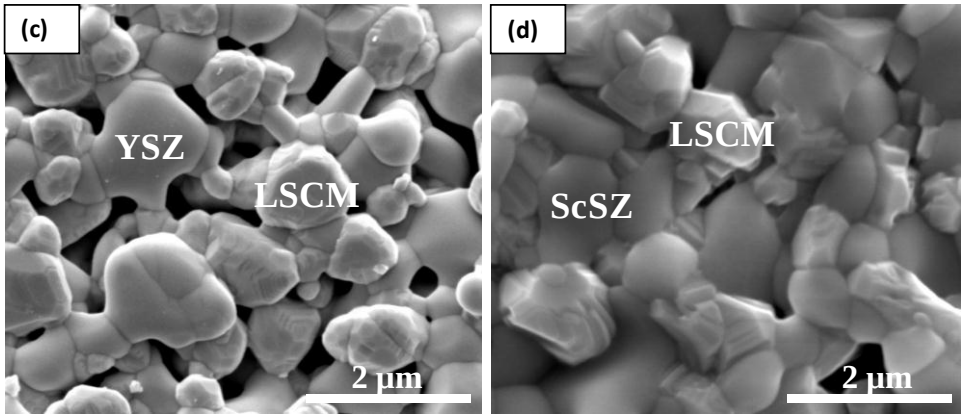

Fig. 8.3. SEM micrographs of LSCM and 8YSZ/10ScSZ composite sintered at 1400°C for 10h in air a) LSCM/8YSZ, b) LSCM/10ScSZ; in Ar-3%H_2-3%H_2O c) LSCM/8YSZ and d) LSCM/10ScSZ.

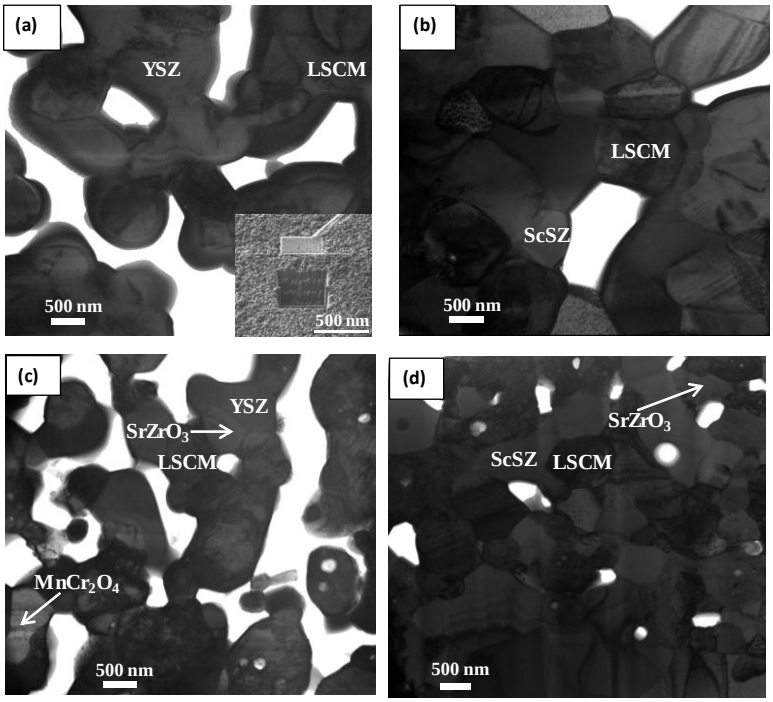

Fig. 8.4. TEM micrographs of LSCM and 8YSZ/10ScSZ composite sintered at 1400°C for 10h in air a) LSCM/8YSZ, b) LSCM/10ScSZ ; in Ar-3%H_2-3%H_2O c) LSCM/8YSZ and d) LSCM/10ScSZ.

Table 8.1. STEM-EDS elemental analysis of LSCM/8YSZ sintered in Ar-3%H_2-3%H_2O.

Element	La	Sr	Cr	Mn	Y	Zr
LSCM (at. %)	42.1	9.8	35.6	10.6	0	1.1
YSZ (at. %)	0	1.6	0.3	3.5	14.1	80.5
Sr-Zr rich phase (at. %)	3.5	38	4.8	0	0.4	53.3
Mn-Zr rich phase (at. %)	0	0	65.4	32.6	0.2	1.8

Table 8.2. STEM-EDS elemental analysis of LSCM/10ScSZ sintered in Ar-3%H_2-3%H_2O.

Element	La	Sr	Cr	Mn	Sc	Zr
LSCM (at. %)	41.5	9.7	36.7	10.7	0	1.3
ScSZ (at. %)	0.1	0	0.1	1.1	12.9	85.7
Sr-Zr rich phase (at. %)	12.7	40.8	6.9	0.4	1.4	37.7

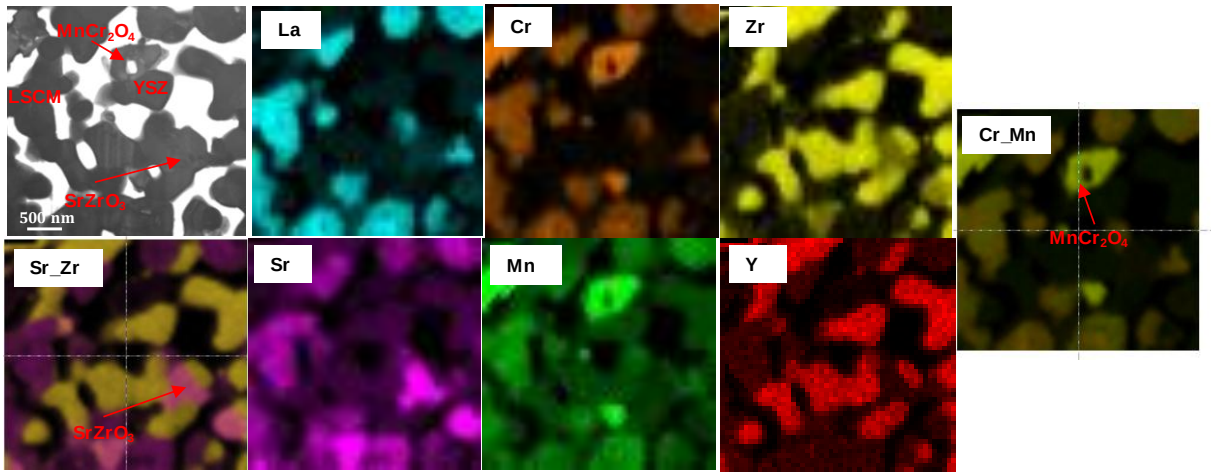

Fig. 8.5. Elemental mapping of FIB cross-section of sintered LSCM/8YSZ in Ar-3%H2-3%H2O.

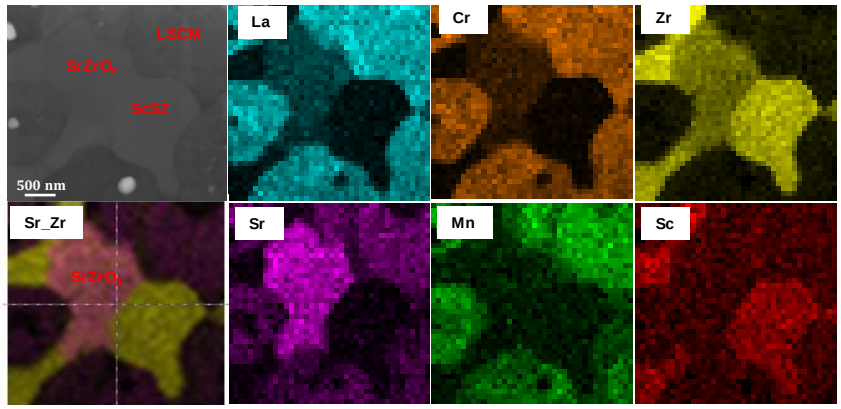

Fig. 8.6. Elemental mapping of FIB cross-section of sintered LSCM/10ScSZ in Ar-3%H_2-3%H_2O atmosphere.

8.4.3. *Electrochemical measurements and post-test characterization*

Fig. 8.7a and b shows comparison plot of non-ohmic resistances of symmetrical cells of configuration LSCM/8YSZ//8YSZ//LSCM/8YSZ and LSCM/10ScSZ//8YSZ//LSCM/ 10ScSZ as a function of time (80h) at 950°C in air and Ar-3%H_2-3%H_2O respectively. For both cases, higher resistance is obtained in reducing gas atmosphere. However, LSCM/10ScSZ//8YSZ//LSCM/10ScSZ symmetrical cell obtain lower resistance when compared to LSCM/8YSZ//8YSZ//LSCM/8YSZ in air as well as Ar-3%H_2-3%H_2O. This corresponds to higher stability of LSCM/10ScSZ based symmetrical cells on comparison with LSCM/8YSZ. In oxidizing atmosphere (air), the non-ohmic resistances increases with time but there is no significant variation observed specially after 30h as shown in Fig. 8.7. On the other hand, in reducing atmosphere, the non-ohmic resistance of LSCM/10ScSZ based symmetrical cells also does not vary significantly with increase in time as shown in Fig. 8.7b. However, non-ohmic resistance for LSCM/8YSZ based cell increases continuously with time (Fig. 8.7b). This corresponds to lower stability and degradation in the LSCM/8YSZ cell when compared to LSCM/10ScSZ in Ar-3%H_2-3%H_2O atmosphere. The non-ohmic

resistance for the LSCM/8YSZ based tested cell is ~12.0 $\Omega.cm^2$ (0 h), and increased to ~24.9 $\Omega.cm^2$ (80 h) in Ar-3%H_2-3%H_2O at 950°C under the constant bias of 0.5V. On the other hand, the resistance varied from ~3.4 (0 h) to 5.9 (80 h) for LSCM/10ScSZ based cell under same testing conditions. This indicates LSCM/10ScSZ based composition provides higher performance corresponding to its higher stability.

Microstructure analysis of the tested symmetrical cells was performed after completion of the electrochemical tests to understand the degradation of the tested symmetrical cells. Fig. 8.8a and d shows the interface of LSCM/8YSZ, and LSCM/10ScSZ composite with 8YSZ (electrolyte) respectively. There is no interface layer or compound formation observed at the interface in air and Ar-3%H_2-3%H_2O. Furthermore, no microstructural changes are identified in the cells tested in air as shown in Fig. 8.8b and e respectively. For LSCM/10ScSZ, no significant changes are observed in the microstructure (Fig. 8.8f) of the tested cell in reducing atmosphere (Ar-3%H_2-3%H_2O). However, surface morphology of LSCM phase is significantly modified for LSCM/8YSZ tested cell in Ar-3%H_2-3%H_2O as shown in Fig. 8.8c. Nano-size particles segregation is observed on the anode surface of the tested cell as shown in Fig. 8.8c. Boxun et al. [20] have observed similar surface morphological changes attributing to Sr-segregation in $(La_{0.8}Sr_{0.2})_{0.98}MnO_3$ (LSM) after electrochemical cell testing in air (with 50% water vapor) at 850°C for 100h. Similarly, it is suggested that the SrO segregation on LSCM surface results in the degradation of the LSCM/8YSZ tested cell corresponding to higher resistance unlike LSCM/10ScSZ.

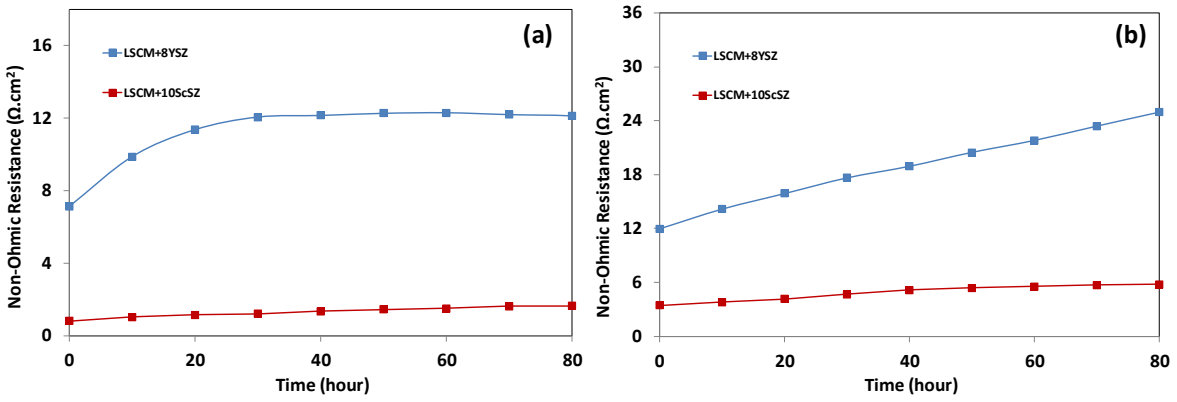

Fig. 8.7. Comparison plots of resistance (non-ohmic) changes with time for LSCM/8YSZ//8YSZ//LSCM/8YSZ and LSCM/10ScSZ//8YSZ//LSCM/10ScSZ cell tested at 0.5 V: a) in air, and b) Ar-3%H_2-3%H_2O.

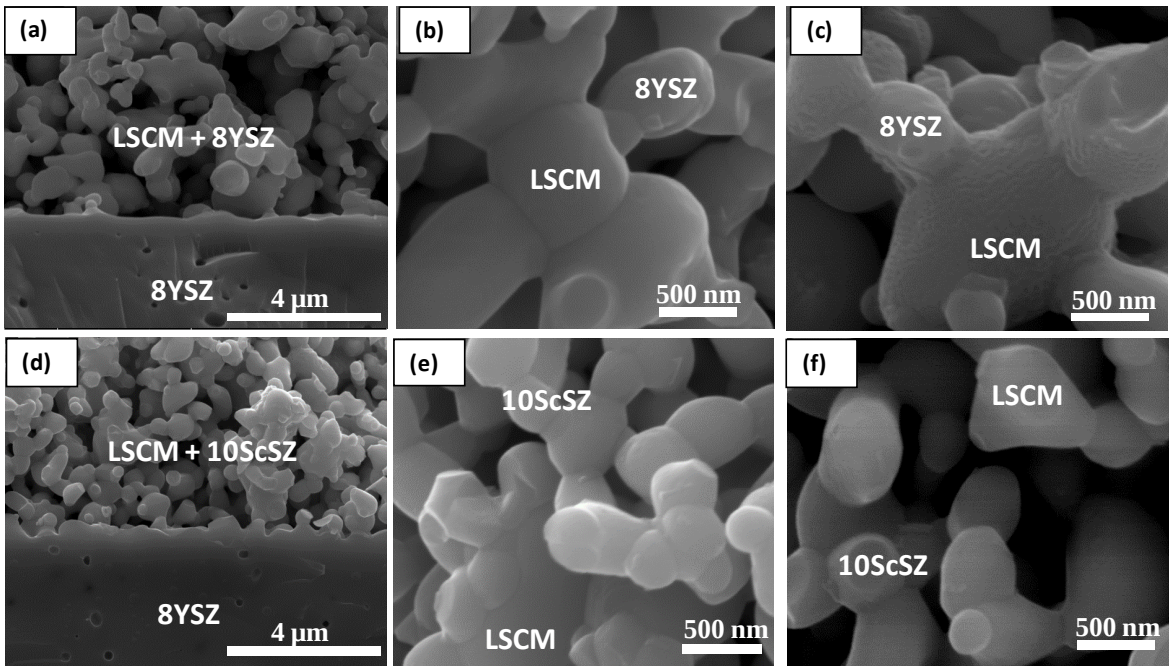

Fig. 8.8. SEM micrographs of the tested symmetrical cell of LSCM/8YSZ//8YSZ//LSCM/8YSZ (anode surface): a) LSCM+8YSZ and 8YSZ interface, b) in air, c) in Ar-3%H_2-3%H_2O; LSCM/10ScSZ//8YSZ//LSCM/10ScSZ: d) LSCM/10ScSZ and 8YSZ interface, e) in air, and e) Ar-3%H_2-3%H_2O.

8.4. Conclusion

LSCM/8YSZ and LSCM/10ScSZ has been synthezied in oxidizing and reducing atmosphere (Ar-3%H_2-3%H_2O) at 1400°C. Results of this study and comparison of LSCM/8YSZ and LSCM/10ScSZ composites are listed in Table 8.3.

Table 8.3. Summary and comparison of LSCM/8YSZ and LSCM/10ScSZ composites.

LSCM/8YSZ		**LSCM/10ScSZ**	
Lower relative density (%)		*Higher relative density (%)*	
Air	59±2.2	Air	78.1±1.5
Ar-3%H_2-3%H_2O	74.8±1.3	Ar-3%H_2-3%H_2O	88.2±0.9
Secondary Phases (More)		*Secondary Phases (Less)*	
Air	No	Air	No
Ar-3%H_2-3%H_2O	$SrZrO_3$ and $MnCr_2O_4$	Ar-3%H_2-3%H_2O	$SrZrO_3$
Mn diffusion into YSZ (Higher)		*Mn diffusion into ScSZ (Lower)*	
Air	No	Air	No
Ar-3%H_2-3%H_2O	~ 3.5 at. %	Ar-3%H_2-3%H_2O	~ 1 at. %
Polarization resistance (Higher)		*Polarization resistance (Lower)*	
Air	~ 7.1 Ω.cm^2	Air	~ 0.8 Ω.cm^2
Ar-3%H_2-3%H_2O	~ 12.0 Ω.cm^2	Ar-3%H_2-3%H_2O	~ 3.4 Ω.cm^2

8.5. References

[1] S. Gupta, M.K. Mahapatra, P. Singh. MSE: R: Reports 90 (2015) 1-36.

[2] S. Gupta, M.K. Mahapatra, P. Singh. Mat. Res. Bull. 48 (2013) 3262-67

[3] S. Gupta, P. Singh. ECS Transactions 66 (2015) 117-123.

[4] K.T. Jacob, S. Gupta, P. Singh. J. Am. Ceram. Soc. 96 (2013) 3933-38.

[5] K.T. Jacob, S. Gupta, P. Singh. J. Am. Ceram. Soc. 96 (2013) 3272-3278.

[6] H.J.M. Bouwmeester, A.J. Burggraaf, in: A.J. Burggraaf, L. Cot (Eds.). Fundamentals of inorganic membrane science and technology. Membrane Science and Technology Series 4, Elsevier, Amsterdam, 1996, pp. 435–510.

[7] N. Nagabhushana, L.A. Lane, G.M. Christie, B.A.V. Hassel. Composite oxygen ion transport membrane. US Patent 7556676B2, 2009.

[8] J.J. Liu, T. Liu, W.D. Wang, J.F. Gao, C.S. Chen. J. Mem. Sci. 2012;389:435-440.

[9] J. Sunarso, S. Baumann, J.M. Serra, W.A. Meulenberg, S.Liu, Y.S. Lin, J.C. Diniz da Costa. Journal of Membrane Science 320 (2008) 13–41.

[10] W. Fang, Y. Zhang, J. Gao, C. Chen. Ceramics International 40 (2014) 799-803.

[11] S. Tao, J.T.S. Irvine. Chem. Mater. 18 (2006) 5453–5460.

[12] S. Tao, J.T.S. Irvine. J. Electrochem. Soc. 151 (2004) A252–A259.

[13] S. Tao, J.T.S. Irvine. Nat. Mater. 2 (2003) 320–323.

[14] M. Mori, Y. Hiei, T. Yamamoto. J. Am. Ceram. Soc. 84 (2001) 781–786.

[15] M. Mori, T. Yamamoto, H. Itoh, H. Inaba, H. Tagawa. J. Electrochem. Soc. 145 (1998) 1374–1381.

[16] A. Bieberle, L.J. Gauckler, in: H. Tuller, J. Schoonman, I. Riess (Eds.), Kluwer Academic Publishers, Dordrecht, 2000.

[17] S.P. Jiang, X.J. Chen, S.H. Chan, J.T. Kwok, K.A. Khor. Solid State Ionics 177 (2006) 149–157.

[18] I. Junga, D. Leea, S. O. Leea, D. Kima , J. Kimb , S. H. Hyuna , J. Moona. Ceramics International 39 (2013) 9753–9758.

[19] S. Kazlauskas, A. Kežionis, T. Šalkus, and A.F. Orliukas. Lithuanian J. Physics 52 (2012) 231–237.

[20] B. Hu, M. Keane, M.K. Mahapatra, P. Singh. J. Power Sources 248 (2014) 196-204.

CHAPTER 9: PROCESSING AND ELECTROCHEMICAL PERFORMANCE OF IRON DOPED LANTHANUM STRONTIUM CHROMITE IN OXIDIZING AND REDUCING ATMOSPHERE

9.1. Abstract

Processing of $(La_{0.8}Sr_{0.2})_{0.95}Cr_{0.7}Fe_{0.3}O_3$ (LSCF) is investigated under oxygen transport membrane device fabrication conditions at 1400°C and oxygen partial pressure (PO_2) varying from 0.21 – 10^{-10} atm. Formation of Fe enriched phase is identified in the samples exposed to reducing atmosphere and the amount of the phase increases with decrease in PO_2. LSCF dissociates and forms FeO_x when exposed to Ar-3%H_2-3%H_2O at 1400°C. The compound formations are identified using XRD and SEM-EDS elemental point analysis and mapping profile. Electrochemical impedance spectroscopy measurement on the symmetrical cell of configuration LSCF+8YSZ//8YSZ//LSCF+8YSZ shows high polarization resistance in oxidizing atmosphere when compared to reducing atmosphere under OTM operating conditions (T ~ 950°C and PO_2 ~ 0.21- 10^{-16} atm). No degradation and microstructural changes are identified in the samples exposed to air for 80h. Surface of LSCF phase is significantly modified after EIS measurement in Ar-3%H_2-3%H_2O atmosphere for 80h. Higher stability and electrochemical performance of LSCF is obtained in air than Ar-3%H_2-3%H_2O. Post characterization results show no electrode layer delamination and interface layer formation in the bulk and/or interface in both oxidizing and reducing atmosphere.

9.2. Introduction

Oxygen transport membrane (OTM) technology is being currently developed for utilization of fossil fuels/hydrocarbons with CO_2 capture and no gas emissions [1-6]. Efficient and clean oxy-combustion of fossil fuels/hydrocarbon allows minimization in greenhouse gas emissions resulting in global climate change [7-8]. The technology is also useful for syngas production which can be further processed via water shift gas reaction to generate hydrogen as a fuel [9]. Using Fisher-Tropsch process, the syngas can also be utilized to generate liquid fuel for transportation. Furthermore, oxygen transport membrane system is beneficial for the industries where high purity oxygen is utilized for better production such as petrochemical, medical, paper industries, and metallurgical (iron/steel plants) and welding/cutting [10].

Oxygen transport membrane consists of three layers i.e. air electrode layer, membrane and fuel electrode layer. Oxygen exchange between the membrane surface and gas phase consists of several steps that are involved in the process of the oxygen separation through the membrane: adsorption and dissociation of oxygen molecules at the air electrode, oxygen transport through oxygen vacancies across the membrane, and desorption and association of oxygen ions at the fuel electrode [11-12]. The driving force for the oxygen separation is oxygen partial pressure (PO_2) gradient. Therefore, it is important that the materials of the OTM system (membrane and fuel electrode) are stable in a wide range of PO_2 at the operating temperature (~950°C) [1].

Lanthanum chromite based perovskites are currently being investigated as materials for membrane and fuel electrode for oxygen transport membrane due to its high structural and chemical stability at high temperatures in both oxidizing and reducing

atmospheres [1,13-15]. Lanthanum chromites are commonly doped at A-site with alkaline earth metal and at B-site with transition metal to enhance its sintering capability, electrical conductivity and electrochemical performance [15-18]. However, the dopants tend to deteriorate the structural and thermo-chemical stability of lanthanum chromite based materials specifically in lower PO_2 ($\leq 10^{-10}$ atm) [19-21]. To overcome this barrier, the materials are further doped at B-site with transition metals to maintain the stability and further improve the electrochemical properties [22-26].

$(La,Sr)(Cr,Fe)_{3-\delta}$ (LSCF) is being investigated as mixed ionic electronic conductor (MIEC) membrane and fuel side electrode for oxygen transport membrane (OTM) system [1, 25-28]. Pena-Martinez [29] and Haag et al. [30] reported that acceptor-substituted $LaCrO_{3-\delta}$ with Fe-doping enhances electrode performance in SOFC and other electrochemical devices. For instance, Fe-containing $La_{0.75}Sr_{0.25}Cr_{0.5}Fe_{0.5}O_{3-\delta}$ (LSCF55) showed lower polarization resistance when compared to $La_{0.75}Sr_{0.25}Cr_{0.5}Mn_{0.5}O_{3-\delta}$ (LSCM) [29]. Lee et al. [31] reported the ionic conductivity of $(La_{0.75}Sr_{0.25})_{0.95}Cr_{1-x}Fe_xO_{3-\delta}$ to be higher than the acceptor-doped lanthanum chromites and $(La,Sr)(Cr,Mn)_{3-\delta}$ (LSCM) [32]. However, most of the literature exists on LSCF55 with 50 mol% Fe [27, 29, 33]. He et al. [27] have examined stability and oxygen transport property of LSCF55. Under air/CO gradient (air was fed at one side of the sample, while CO was led over the other side to react with the oxygen permeated from the air side), an oxygen permeation flux of 2.5×10^{-7} mol cm^{-2} s^{-1} was measured at 950°C and the oxygen ionic conductivity was estimated to be ~0.01 S/cm at 950°C. The authors also reported that LSCF55 partially decomposed into metallic iron and some unknown phases when exposed to pure H_2 gas atmosphere for 30h at 950°C. Based on thermodynamic calculations, Fang et al. [33] reported the decomposition oxygen partial pressure of LSCF55

to be 6.3×10^{-28} atm. According to the literature search, it is identified that LSCF55 is not very stable under reducing atmosphere. Furthermore, only limited literature exists on (LSCF) based perovskites and composites. The literature search also shows lack of information pertaining to the interaction of perovskite (LSCF) and fluorite (e.g. 8YSZ) phases under oxidizing as well as reducing gas atmosphere required for the operation of OTM device.

Due to the reported lower stability of higher Fe-containing LSCF perovskites, this study is focused on identifying the processing behavior, structural-chemical stability and electrochemical performance of LSCF perovskite/composites with lower concentration of Fe (30 mol%) in reducing gas atmosphere. The results are obtained under simulating OTM fabrication (1400°C, ~ 0.21-10^{-6} atm) and operating (~950°C, ~ 0.21 – 10^{-18} atm) conditions.

9.3. Experimental

9.3.1. *$(La_{0.8}Sr_{0.2})_{0.95}Cr_{0.7}Fe_{0.3}O_{3-\delta}$ synthesis*

LSCF73 powder was obtained from Praxair Inc. and then uniaxiallly pressed into pellets as well as bisque fired at 1100°C (2h) in air atmosphere. The pellets were sintered at 1400°C in three different gas atmosphere i.e. air (0.21 atm), N_2 (~10^{-5} atm) and Ar-3%H_2-3%H_2O (~10^{-10} atm).

9.3.2. *Characterization*

Archimedes principle was utilized for density measurement of all LSCF73 sintered samples. The microstructural and elemental analysis was performed using scanning electron microscope (FEI - ESEM Quanta 250, Hillsboro, OH) with energy dispersive spectroscopy (EDS). Crystal structure and compound formation of LSCF73 were identified using X-ray

diffraction (BRUKER-D8 ADVANCE, Bruker AXS Inc. Madison, WI) technique with scan step of 0.02° using CuK_{α} radiation (λ = 1.5406 Å).

9.3.3. *Symmetric cell fabrication*

To enhance the ionic conduction, a mixture of LSCF73 with commonly used ionic conductor (8YSZ) was prepared in the weight ratio of 50:50 for electrochemical testing. LSCF73/8YSZ ink was prepared using Fuel ink vehicle (Fuel Cell Materials). Symmetrical cells were then prepared by screen printing LSCF73/8YSZ on both sides of $(ZrO_2)_{0.92}(Y_2O_3)_{0.08}$ (YSZ) electrolytes (200 μm thick Fuel Cell Materials) as working and counter electrodes (thickness: ~20 μm, diameter: 10 mm). The electrode layers on both sides were dried and subsequently, the cell was sintered at 1200°C (heating rate of 3°C/min) for 2h in air. Lower sintering temperature (1200°C) was chosen for the cell fabrication to obtain porous electrode layer and also to avoid secondary phase's formation observed at 1400°C. As-sintered symmetrical cells do not show any indication of secondary phases. Platinum screen current collector (Alfa Aesar, 50 mesh) and wires (Alfa Aesar, 0.25 mm) were then attached to each electrode. The electrochemical active area of the cell electrode was 0.8 cm^2.

9.3.4. *Electrochemical testing*

Symmetrical cells were heated to 950°C (3°C/min) and tested in two different gas atmospheres i.e. air and Ar-3%H_2-3%H_2O. The electrochemical measurement was done using potentiostat under constant bias of 0.5V for 80 h. Every two hour of interval, the electrochemical impedance was measured in the frequency range of 100 mHz - 200 kHz using alternating current of 10 mV. The measurement was repeated on different cells to ensure repeatability under similar conditions. After testing, the symmetrical cells were then characterized using SEM-EDS (FEI - ESEM Quanta 250).

9.4. Results and Discussion:

9.4.1. *Crystal structure*

The crystal structure and phase evolution of LSCF73 is investigated in air, N_2 and Ar-3%H_2-3%H_2O atmosphere as shown in Fig. 9.1. LSCF73 samples sintered in air at 1400°C show rhombohedral structure. However, the peak splitting corresponding to rhombohedral structure disappears in lower PO_2 sintered samples (N_2 and Ar-3%H_2-3%H_2O). This attributes to a phase transformation from lower (rhombohedral; JCPDS 75-9872) in oxidizing atmosphere to higher symmetry phase (cubic; JCPDS 074-1961) in reducing atmosphere [14]. No secondary phases are identified for the samples sintered in air at 1400°C. However, the XRD patterns corresponding to N_2 and Ar-3%H_2-3%H_2O sintered samples shows new peaks (indicated by asterisk) when compared to air. The new peaks are identified and correspond to secondary phase (FeO_x) formation and/or FeO. $(Fe_x.Cr_{2-x})O_3$. This provides us with the important information that LSCF73 is not stable and decomposes to form FeO_x and FeO. $(Fe_x.Cr_{2-x})O_3$ if fabricated under reducing gas atmosphere (Ar-3%H_2-3%H_2O). Oxidizing atmosphere (air) is an appropriate condition to be utilized for fabrication of OTM when membrane or electrode layer is made of LSCF based materials.

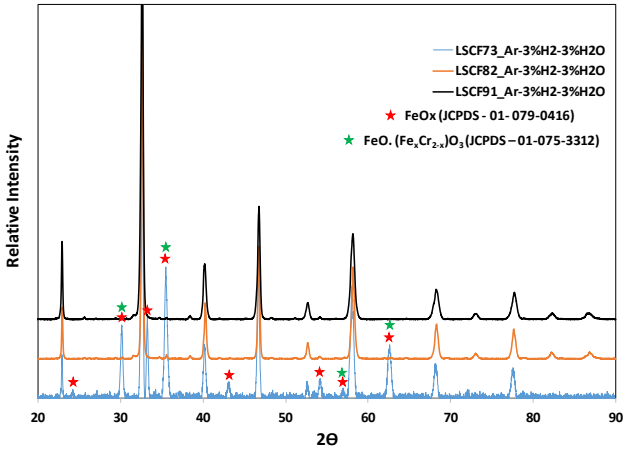

Fig. 9.1. XRD pattern of LSCF73 sintered at 1400°C in air, N_2 and Ar-3%H_2-3%H_2O.

9.4.2. *Sintering behavior and microstructural analysis*

Table 9.1 shows the relative density of LSCF73 sintered in air, N_2 and Ar-3%H_2-3%H_2O at 1400°C for 10h. The density increases with decrease in PO_2. Highest density is achieved in reducing gas atmosphere (Ar-3%H_2-3%H_2O).

Table 9.1. Relative density of LSCF73 sintered at 1400°C.

Relative density (%)	
Air	65.6±2.0
N_2	74.9±1.4
Ar-3%H_2-3%H_2O	96.3±1.2

Fig. 9.2 shows scanning electron micrographs (SEM) of LSCF73 samples sintered in air, N_2 and Ar-3%H_2-3%H_2O atmosphere at 1400°C. Microstructural and elemental analysis of air sintered samples does not show any compound formation as shown in Fig 9.2a. However, in N_2 and Ar-3%H_2-3%H_2O atmosphere, significant changes in the microstructure are identified when compared to air. Reduced gas atmosphere resulted in significant smaller grains size corresponding to the lower stability of LSCF73 microstructure in lower oxygen partial pressure atmosphere ($\leq 10^{-6}$ atm) at 1400°C.

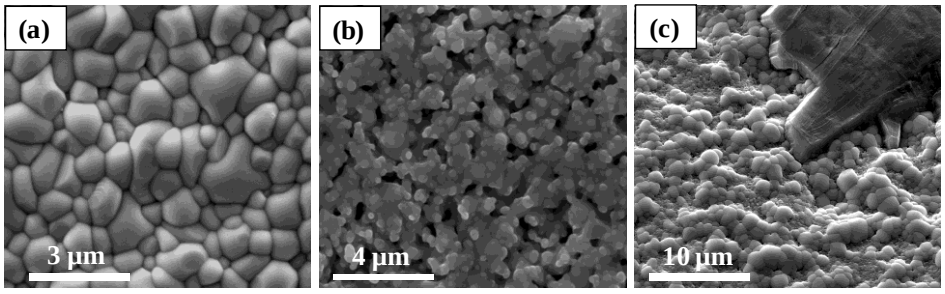

Fig. 9.2. SEM micrographs of sintered LSCF73: (a) air, (b) N_2 and (c) Ar-3%H_2-3%H_2O at 1400°C (10h).

Furthermore, FeO_x secondary phase formation is identified in the LSCF samples sintered in Ar-3%H_2-3%H_2O atmosphere in agreement with our XRD results. This corresponds to the decomposition of LSCF perovskite into FeO_x in reducing gas atmosphere. The secondary phase is evolved in the form of layered structure. SEM-EDS analysis shows the phase is predominantly Fe and O-rich (Fig. 9.3a and c). Small and large size grains are observed indicating inhomogeneity in the microstructure as shown in Fig 9.3b. In addition, EDS semi-quantitative results show composition variation with respect to different grain size (Fig 9.3b). SEM-EDS elemental mapping profile is also investigated to further analyze the elemental distribution. Fig 9.4 shows the distribution of each element in the LSCF73 composition. It is clearly identified that La (red), Sr (green), Cr (yellow) and oxygen (cyan) are all present in the region 1 (mentioned in Fig 9.4), and Fe (margenta) is not observed in the area 1. On the other side, only Fe and O are present in the region 2 as shown in Fig. 9.4. This supports our EDS semi-quantitative elemental analysis and XRD results. Furthermore, LSCF samples are polished for the bulk microstructural analysis using SEM-EDS. This is shown in Fig 9.5. Interestingly, a small amount of new Fe and Cr enriched phase is identified in the LSCF sample processed in N_2 atmosphere. In addition to Fe enriched phase (La – 1.4±0.1%, Sr – 0.5±0.1%, Cr – 3.1±0.1% and Fe – 95.5±0.3%), the Fe and Cr enriched phase (La – 1.4±0.2%, Sr – 1.1±0.1%, Cr – 50.8±2.1% and Fe – 47.9±1.8%) is also identified in the sample exposed to Ar-3%H_2-3%H_2O atmosphere. Our XRD results identify the phase as FeO. $(Fe_x.Cr_{2-x})O_3$ compound (Fig. 9.1).

It is also reported in the literature that Fe containing lanthanum chromite based materials tend to reduce into Fe metal and $LaCrO_3$ phase when exposed to reducing atmosphere [34]. For instance, at 850°C, the Fe substituted lanthanum chromite would

decompose to Fe metal and $LaCrO_3$ at PO_2~10^{-23} atm [34]. In addition, LSCF55 partially decomposed into metallic iron and some unknown phases when exposed to pure H_2 gas atmosphere for 30h at 950°C [35]. However, our results indicate formation of FeO_x/FeO. $(Fe_x.Cr_{2-x})O_3$ secondary phase. This is due to the exposure to less reducing gas atmosphere (PO_2~10^{-10} atm). We postulate that LSCF73 perovskite lattice structure destabilizes in lower oxygen partial pressure due to reduction in the valence state of $Fe^{4+}\rightarrow Fe^{3+}$ and $Fe^{3+}\rightarrow Fe^{2+}$ resulting in oxygen vacancies formation required for charge compensation. Furthermore, an ionic radius of Fe^{2+} (0.78Å) is greater than Fe^{3+} (0.645Å). Consequently, in reducing atmosphere, Fe^{2+} does not retain in the $A^{3+}B^{3+}O_3^{2-}$ lattice of LSCF73 and exolve as FeO_x. The reason for the formation of Fe and Cr enriched phase (FeO. $(Fe_x.Cr_{2-x})O_3$) is not clear. However, like LSCM73, it is possible due to Cr reaction with FeO_x.

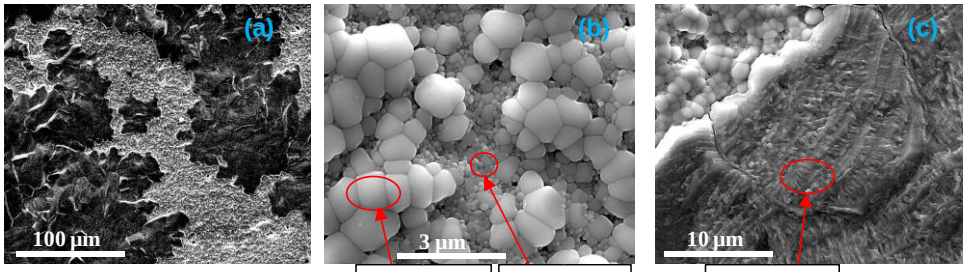

El	At%
O	59.7
Sr	5.8
La	16.4
Cr	14.1
Fe	4.1

El	At%
O	40.0
Sr	5.6
La	25.7
Cr	22.9
Fe	5.7

El	At%
O	50.5
Sr	0.2
La	0.7
Cr	1.1
Fe	47.5

Fig. 9.3. SEM micrographs and elemental analysis of LSCF73 sintered at 1400°C (10h) in reducing gas atmosphere (Ar-3%H_2-3%H_2O).

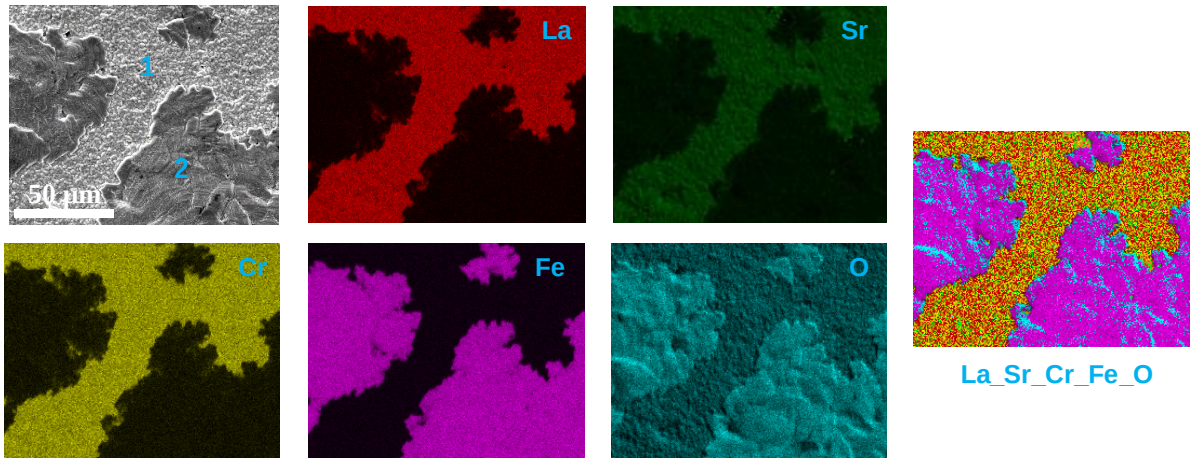

Fig. 9.4. SEM mapping micrograph of LSCF73 sintered at 1400°C (10h) in reducing gas atmosphere (Ar-3%H_2-3%H_2O).

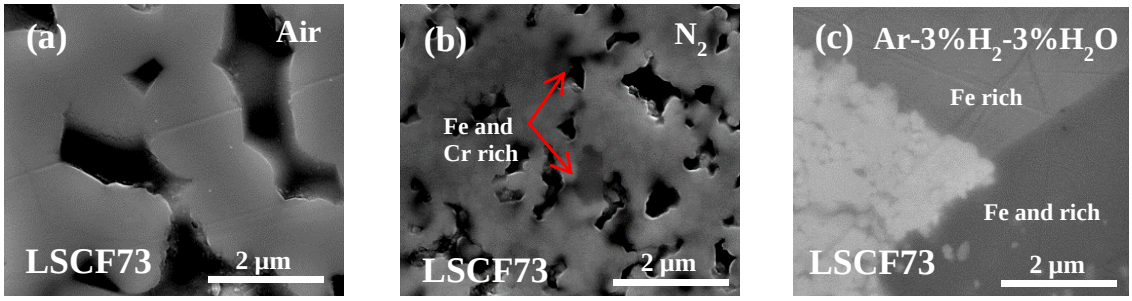

Fig. 9.5. SEM micrographs of polished LSCF73 sintered at 1400°C (10h): (a) air, (b) N_2 and (c) Ar-3%H_2-3%H_2O at 1400°C (10h).

9.4.3. *Electrochemical measurements and post-test observations*

Fig. 9.6a and b shows impedance spectra of the symmetrical cell of configuration LSCF73+8YSZ//8YSZ//LSCF73+8YSZ at 950°C in oxidizing (air) and reducing (Ar-3%H_2-3%H_2O) atmosphere under constant voltage of 0.5 V. High frequency intercept corresponds to ohmic resistance and the semicircle diameter attributes to non-ohmic contributions [36]. Two semicircles are observed in reducing atmosphere and correspond to the ion transfer through the microstructure at high frequency and charge transfer at the interface at low

frequency [37]. Unlike reducing atmosphere, the two semicircles are merged in oxidizing atmosphere [38]. Comparisons of non-ohmic resistances are shown in Fig. 9.7. Under oxidizing atmosphere, the symmetrical cells show a small increment in the non-ohmic resistance as the time changes from 0 (1.6 $\Omega.cm^2$) to 80h (2.8 $\Omega.cm^2$) with a time interval of 2h (only five spectra are shown for clarity) as shown in Fig. 9.6. On the other hand, in reducing atmosphere, non-ohmic resistance increases rather significantly with increase in time as indicated in Fig. 9.7. The non-ohmic resistance for the tested cell increases from ~3.8 $\Omega.cm^2$ (0h) to ~6.9 $\Omega.cm^2$ (80h) when exposed to Ar-3%H_2-3%H_2O at 950°C under the applied bias of 0.5V.

Fig. 9.8 shows an image of LSCF73+8YSZ//8YSZ//LSCF73+8YSZ symmetrical cells before and after electrochemical measurement. Electrode layer adheres well to the 8YSZ substrate even after testing for 80h in oxidizing and reducing gas atmosphere. Post-test characterization is conducted on the symmetrical cells after testing. No interface layer formation is identified at the interface of LSCF73/8YSZ and 8YSZ (Fig. 9.9a). Microstructural analysis of the air tested cells (Fig. 9.9c) shows no modification in the bulk/surface of LSCF73/8YSZ when compared to as-sintered cell (Fig. 9.9b). On the other hand, in reducing atmosphere, the cell shows a significant modification in the microstructure of LSCF73/8YSZ (Fig. 9.9d). LSCF surface is modified when compared to the as-sintered sample. This corresponds to the lower performance of the cell in Ar-3%H_2-3%H_2O atmosphere than air.

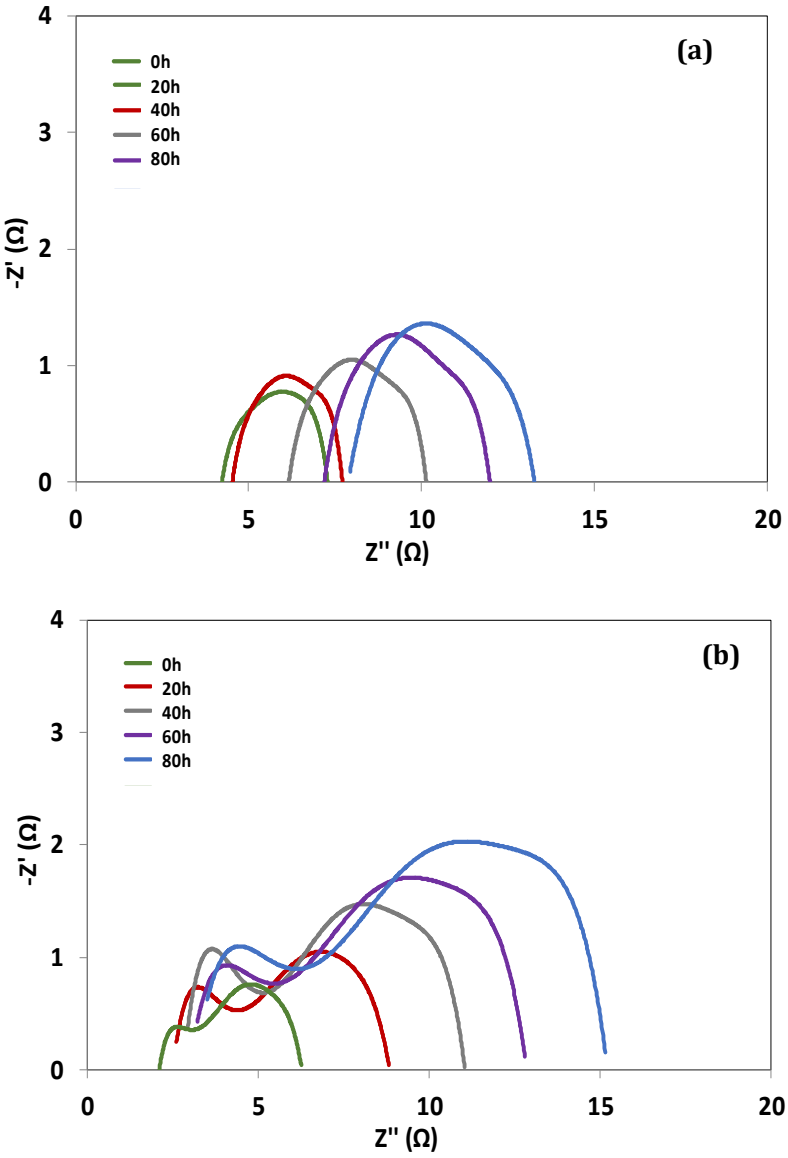

Fig. 9.6. Nyquist plots of impedance spectra obtained from symmetrical cell (LSCF73+8YSZ//8YSZ//LSCF73+8YSZ) tested at 950°C with 0.5 V from 0 to 80 h: a) in air, and b) in Ar-3%H_2-3%H_2O.

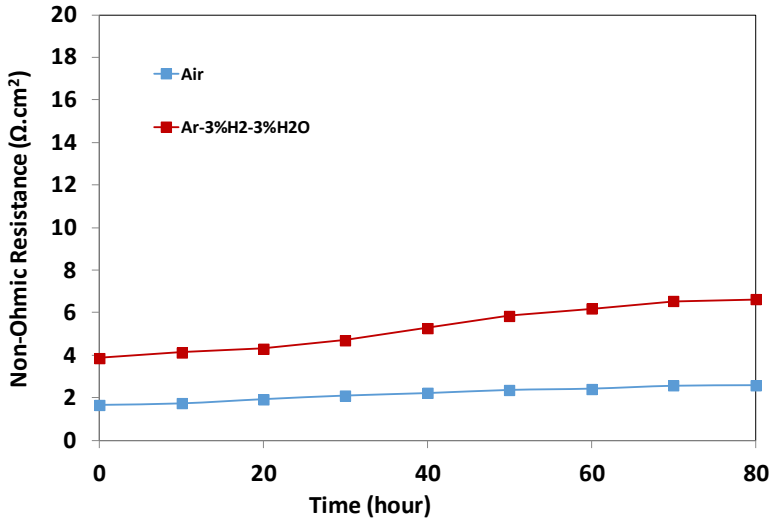

Fig. 9.7. Comparison plots of non ohmic resistance changes with time for the cell (LSCF73+8YSZ//8YSZ//LSCF73+8YSZ) tested at 0.5 V in air and Ar-3%H_2-3%H_2O.

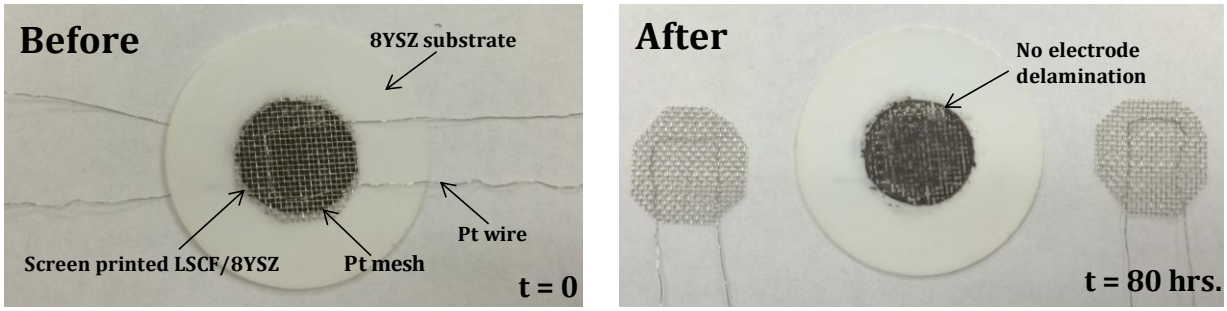

Fig. 9.8. Symmetrical cell (LSCF73+8YSZ//8YSZ//LSCF73+8YSZ): Left - before testing and Right - after testing (Pt mesh along with Pt wires are manually removed) at 950°C with applied bias of 0.5 V for 80h.

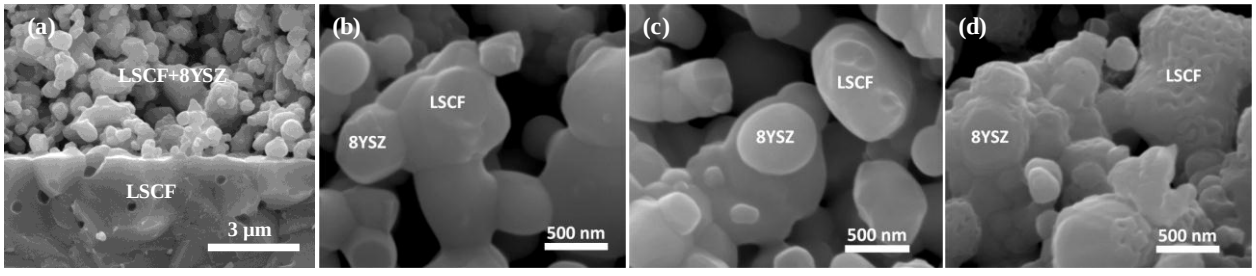

Fig. 9.9. SEM micrographs of the symmetrical cell of LSCF73+8YSZ//8YSZ//LSCF73+8YSZ (anode surface): a) LSCF+8YSZ and 8YSZ interface b) as-sintered in air, c) tested in air, and d) tested in Ar-3%H_2-3%H_2O.

9.5. Conclusion

$(La_{0.8}Sr_{0.2})_{0.95}Cr_{0.7}Fe_{0.3}O_3$ (LSCF73) synthesis is conducted in three different gas atmospheres (air, N_2, Ar-3%H_2-3%H_2O) with varying PO_2 at 1400°C. It is found that the stability of LSCF73 perovskite structure decreases with decrease in PO_2. LSCF phase separation and FeO_x/FeO. $(Fe_x.Cr_{2-x})O_3$ formation is identified in the samples sintered in Ar-3%H_2-3%H_2O corresponding to the lower stability in reducing gas atmosphere. High electrochemical performance of symmetrical cells of configuration LSCF73+8YSZ//8YSZ//LSCF73+8YSZ is obtained in oxidizing when compared to reducing atmosphere at 950°C for 80h. Microstructural analysis of the post-tested cells shows no changes in the air tested cells. Surface modification of LSCF phase is identified in the Ar-3%H_2-3%H_2O tested cells resulting in the lower performance. Electrode layer adheres well to the substrate even after testing for 80h. After electrochemical testing, no compound formation including $SrZrO_3$ is found in the bulk and/or at the interface LSCF/8YSZ in both oxidizing and reducing atmosphere.

9.6. References

[1] S. Gupta, M.K. Mahapatra and P. Singh, MSE: R: Reports., Materials Science and Engineering R 90 (2015) 1–36.

[2] D. Kang, R.S. Srinivasan, R.T. Thorogood, E.P. Foster. Integrated high temperature method for O_2 production. US Patent 5516359:1996.

[3] M. F. Carolan, P.N. Dyer. Compositions capable of operating under high CO partial pressures for use in solid-state producing devices. US Patent 5712220:1998.

[4] M.F. Carolan, P.N. Dyer. Tubular solid state membrane module. US Patent 5599383: 1997.

[5] A.G. Dixon, W.R. Moser, Y.H. Ma. Ind Eng Chem Res 33 (1994) 3015-24.

[6] H. Stadler, F. Beggel, M. Habermehl, B. Persigehl, R. Kneer, M. Modigell, P. Jeschke. Int J Greenhouse Gas Control 5 (2011) 7-15.

[7] A. Frassoldati, A. Cuoci, T. Faravelli, E. Ranzi, C. Candusso, D. Tolazzi, 1st International Conference on Sustainable Fossil Fuels for Future Energy – S4FE, 2009.

[8] H. Stadler, F. Beggel, M. Habermehl, B. Persigehl, R. Kneer, M. Modigell, P. Jeschke, Int. J. Greenhouse Gas Control 5 (2011) 7–15.

[9] S. Cooper, N. Frazier, P. Urane. Calvin College Department of Engineering 339/340 (2011) 1–6.

[10] S.P.S Badwal, F.T Ciacchi. Adv Mater 13 (2001) 993-96.

[11] J. Sunarso, S. Baumann, J.M. Serra, W.A. Meulenberg, S. Liu, Y.S. Lind, J.C.D. Costa. J. Membr. Sci. 320 (2008) 13–41.

[12] Y.S. Lin, W. Wand, J. Han. AlChE J. 40 (1994) 786–798.

[13] J. Mizusaki. Solid State Ionics 52 (1992) 79–91.

[14] S. Gupta, M.K. Mahapatra, P. Singh, Mater. Res. Bull. 48 (2013) 3262– 3267.

[15] M. Mori, Y. Hiei, N.M. Sammes. Solid State Ionics 135 (2000) 743–748.

[16] M. Mori, Y. Hieia, N.M. Sammes. Solid State Ionics 123 (1999) 103–111.

[17] S.P. Jiang, L. Liua, K.P. Ong, P. Wu, J. Li, J. Puc. J. Power Sources 176 (2008) 82–89.

[18] P.S. Devi, S.M. Rao. J. Solid State Chem. 98 (1992) 237–244.

[19] M. Oishi, K. Yashiro, J.O. Hong, Y. Nigara, T. Kawada. J. Mizusaki, Solid State Ionics 178 (2007) 307–312.

[20] J. Mizusaki, S. Yamauchi, K. Fueki, A. Ishikawa. Solid State Ionics 12 (1984) 119–124.

[21] S. Onumaa, K. Yashiroa, S. Miyoshia, A. Kaimaia, H. Matsumotoa, Y. Nigaraa, T. Kawadaa, J. Mizusakia, K. Kawamurab, N. Sakaic, H. Yokokawa. Solid State Ionics 174 (2004) 287–293.

[22] L.A. Chick, J. Liu, J.W. Stevenson, T.R. Armstrong, D.E. McCready. J. Am. Ceram. Soc. 80 (1997) 2109–2120.

[23] X. Ding, Y. Liu, L. Gao, L. Guo. J. Alloys Compd. 425 (2006) 318–322.

[24] V.V. Kharton, E.V. Tsipis, I.P. Marozau, A.P. Viskup, J.R. Frade, J.T.S. Irvine. Solid State Ionics 178 (2007) 101–113.

[25] M.F. Lu¨ , E.V. Tsipis, J.C. Waerenborgh, A.A. Yaremchenko, V.A. Kolotygin, S. Bredikhin, V.V. Kharton. J. Power Sources 206 (2012) 59–69.

[26] K.J. Yoon, C.N. Cramer, J.W. Stevenson, O.A. Marina, Electrochem. Solid State Lett. 13 (2010) B101–B105.

[27] W. He, H. Huang, M. Chen, J.F. Gao, C.S. Chen. Solid State Ionics 260 (2014) 86–89.

[28] A.A. Yaremchenko, V.V. Kharton, V.A. Kolotygin, M.V. Patrakeev, E.V. Tsipis, J.C. Waerenborgh. J. Power Sources 249 (2014) 483–496.

[29] J. Pe˜na-Martinez, D. Marrero-Lopez, D. Perez-Coll, J.C. Ruiz-Morales, P. Nu˜nez. Electrochim. Acta 52 (2007) 2950.

[30] J.M. Haag, B.D. Madsen, S.A. Barnett, K.R. Poeppelmeier. Electrochem. Solid State Lett. 11 (2008) B51.

[31] D.K. Lee, H.I. Yoo. J. Electrochem. Soc. 147 (2000) 2835.

[32] V.V. Kharton, E.V. Tsipis, I.P. Marozau, A.P. Viskup, J.R. Frade, J.T.S. Irvine. Solid State Ionics 178 (2007) 101.

[33] W. Fang, Y. Zhang, J. Gao, C. Chen. Ceramics International 40 (2014) 799– 803.

[34] J. Sfeir. J. Power Sources 118 (2003) 276-285.

[35] V.V. Kharton, E.V. Tsipis, I.P. Marozau, A.P. Viskup, J.R. Frade and J.T.S. Irvine, Solid State Ionics 178 (2007) 101–113.

[36] P. N. Suriyayothin. Structure and electrical properties of strontium Zirconate, PhD thesis, July, 1984.

[37] Y. Arachi, H. Sakai, O. Yamamoto, Y. Takeda, N. Imanishai. Solid State Ionics 121 (1999) 133–139.

[38] D. Ligny and P. Richet. Phys. Rev. B 53 (3013-3022).

[39] Y. Chen, L. Yang, F. Ren and A. Ke. Scientific Reports 4 (2014) 1-9.

[40] L. Caroline, Y. Zhong, M. Constance and S. Samuel. J. Electrochemical Society 157 (2010) B1597-B1601.

[41] M. de Ridder, P. C. van de Ven, R. G. van Welzenis, H. H. Brongersma, S. Helfensteyn, C. Creemers, P. Van Der Voort, M. Baltes, M. Mathieu and E. F. Vansant. J. Phys. Chem. B 106 (2002) 13146-13153.

[42] M. Keane, M.K. Mahapatra, A. Verma, P. Singh. Int. J. Hydrogen Energy 37 (2012) 16776-16785.

[43] D.M. Bastidas, S. Tao, J.T.S. Irvine, J. Mat. Chem. 16 (2006) 1603-1605.

[44] M. Mori, Y. Hiei, N.M. Sammes, Solid State Ionics 123 (1999) 103-111.

CHAPTER 10: EFFECT OF CHROMIUM: IRON RATIO AND OXYGEN PARTIAL PRESSURE ON PROCESSING AND STABILITY OF IRON DOPED LANTHANUM STRONTIUM CHROMITE

10.1. Abstract:

This study reports the co-effect of Cr: Fe (7:3, 8:2 and 9:1) ratio and oxygen partial pressure (PO_2) on processing, structural and chemical stability of doped $(La_{0.8}Sr_{0.2})_{0.95}Cr_{1-x}Fe_xO_3$ (LSCF, x ~ 0.1-0.3) for the application of oxygen transport membrane (OTM) system. Relative density decreases with increase in Cr: Fe ratio and PO_2. Highest density of 96.3 (±0.5) % is achieved for LSCF with Cr: Fe ratio equals to 7:3 at 1400°C and PO_2~10^{-10} atm. LSCF (7:3) dissociates into FeO_x and FeO. $(Fe_x.Cr_{2-x})O_3$ in reducing gas atmosphere (Ar-3%H_2-3%H_2O). LSCF perovskite stability increases with increase in Cr: Fe ratio in reducing gas atmosphere. LSCF (9:1) perovskite does not show any secondary phase formation with decrease in PO_2 unlike LSCF (7:3 and 8:2).

10.2. Introduction

Transition metals doped lanthanum strontium chromites have been investigated for applications varying from oxygen transport membrane (OTM) system, electrodes/interconnect in solid oxide fuel and electrolysis cell (SOFC and SOEC) and oxidation catalysts [1-5]. Fe-doped (La,Sr)(Cr,Fe)$O_{3-\delta}$ (LSCF) are found to be promising candidate for the above mentioned application due to good electrochemical and catalytic properties for hydrocarbon oxidation as well as thermal expansion match with adjacent materials (e.g. 8YSZ) [1-4, 6].

Most of the literature focuses on the electrochemical performance and properties measurement of LSCF based materials. He et al. [7] reported oxygen permeation flux of $La_{0.8}Sr_{0.2}Cr_{0.5}Fe_{0.5}O_{3-\delta}$ (LSCF55) as 2.5×10^{-7} mol cm^{-2} s^{-1} at 950 °C under air/CO gradient. Oxygen ion conductivity of ~0.01 S/cm was extracted using the oxygen flux data at 950 °C. The electrical conductivity of LSCF is measured ~21.9 S/cm in oxidizing (air) and 6.4 S/cm in reducing (5%H_2-Ar) gas atmosphere at 800°C [8]. Furthermore, conductivity of $(La_{0.75}Sr_{0.25})_{0.95}Cr_{0.7}Fe_{0.3}O_{3-\delta}$ changes from ~31.6 to ~2 S/cm when oxygen partial pressure varies from 0.21 to ~10^{-18} atm at 900°C [9]. The effect of iron doping level on thermo-mechanical, transport and anodic properties of $(La_{0.75}Sr_{0.25})_{0.95}Cr_{1-x}Fe_xO_{3-\delta}$ (x = 0.3–0.4) have been investigated by Lu et al. [9]. The ionic conductivity of the perovskite varies in the range of 0.05-0.08 S cm^{-1} at 950°C under air/H_2-H_2O-N_2 gradient (PO_2~10^{-17} atm). Oxygen ion conductivity increases with increase in the value of x due to increase in oxygen deficiency. On the other hand, it is found that the electronic transport decreases with increase in iron concentration. This is due to a decrease in the hole concentration and mobility with iron additions. The total conductivity of LSCF decreases from 1.41 to 0.54 S/cm when x increases from 0.3 to 0.4 at 950°C and PO_2~10^{-17} atm. However, ionic conductivity increases from 0.056 to 0.079 S/cm respectively under same conditions [9].

It is found that LSCF with higher doping level (Cr: Fe ~ 5:5) is not stable and tend to decompose into metallic iron/iron oxide in reducing atmosphere [6, 10]. For instance, decomposition of LSCF55 is identified at 950°C when exposed to pure H_2 atmosphere for 30h [10]. The chemical-structural stability of LSCF perovskites is important for the above mentioned applications under operating conditions. At the same time, it is critical to understand the behavior of LSCF under processing conditions as it

influences the chemical-structural stability and electrochemical properties/performance of the perovskite oxide.

In this study, the effect of Cr: Fe ratio (7:3, 8:2 and 9:1) on the processing/sintering behavior of $(La_{0.75}Sr_{0.25})_{0.95}Cr_{1-x}Fe_xO_{3-\delta}$ (LSCF) is investigated in the PO_2 ranging from 0.21-10^{-10} atm at 1400°C. Higher Cr: Fe ratios are chosen in this study due to the reported lower stability of LSCF with higher Fe-doping level such as LSCF55. Processing behavior of LSCF perovskites with lower concentration of iron (30-10 mol %) is also not reported in the literature. Furthermore, in this study, LSCF based materials with varying Cr: Fe ratios are exposed to the operating conditions of high temperature electrochemical devices (e.g. OTM) to understand the stability and degradation behavior of the LSCF perovskites.

10.3. Experimental

10.3.1. *$(La_{0.8}Sr_{0.2})_{0.95}Cr_{1-x}Fe_xO_{3-\delta}$ (x ~ 0.3-0.1) synthesis*

$(La_{0.8}Sr_{0.2})_{0.95}Cr_{0.7}Fe_{0.3}O_{3-\delta}$ (LSCF73), $(La_{0.8}Sr_{0.2})_{0.95}Cr_{0.8}Fe_{0.2}O_{3-\delta}$ (LSCF82) and $(La_{0.8}Sr_{0.2})_{0.95}Cr_{0.9}Fe_{0.1}O_{3-\delta}$ (LSCF91) bisque fired (1100°C and 2h) pellets were received from Praxair Inc. The bisque fired samples were then sintered in air (0.21 atm), N_2 (~10^{-6} atm) and Ar-3%H_2-3%H_2O (~10^{-10} atm) at 1400°C with holding time of 10h. The pellets that were sintered in air atmosphere were also exposed to the operating temperature (1000°C) in reducing gas atmosphere i.e. 5%H_2-CO_2 (PO_2~10^{-12} atm) for 500h.

10.3.2. *Characterization*

Density of the LSCF perovskites with varying Cr: Fe ratio was measured according to the Archimedes principle. Microstructural changes and compound formations are identified

using scanning electron microscope (FEI - ESEM Quanta 250, Hillsboro, OH). Compositional analysis was conducted using energy dispersive spectroscopy (EDS) attached to the SEM. X-ray (BRUKER-D8 ADVANCE, Bruker AXS Inc. Madison, WI) diffraction was utilized for analyzing the changes related to crystal structure of LSCF and identifying secondary phase compounds. The scan step of 0.02° and CuK_{α} radiation (λ = 1.5406 Å) were used during the experiment.

10.4. Results and Discussion

10.4.1. *After exposure to the processing conditions*

10.4.1.1. *Crystal structure*

Fig. 10.1 shows XRD comparison of $(La_{0.8}Sr_{0.2})_{0.95}Cr_{0.7}Fe_{0.3}O_3$ (LSCF73) after exposure to three different processing conditions (PO_2 ~ 0.21, 10^{-6} and 10^{-10} atm) at 1400°C. Rhombohedral crystal structure (JCPDS 75-9872) is identified for the air sintered samples at 1400°C. No secondary phase peaks are observed corresponding to the formation of LSCF single phase. However, extra peaks corresponding to FeO_x (JCPDS 079-0416) and/or FeO. $(Fe_xCr_{2-x})O_3$ (JCPDS 075-3312) starts to appear with decrease in PO_2 (~10^{-6} atm). A significant increase in the secondary phase peaks intensity is identified for the samples sintered in further lower PO_2 (~10^{-10} atm). This corresponds to the fact that stability of LSCF73 perovskite decreases with decrease in PO_2. Disappearance of peaks splitting corresponding to rhombohedral phase is also observed for the samples sintered in reducing atmosphere. This attributes to change in crystal structure with decrease in PO_2. As per the literature review, phase transformation from lower symmetry rhombohedral structure to

higher symmetry cubic structure (JCPDS 074-196) is postulated with decrease in oxygen partial pressure [6, 11-12].

XRD comparison of $(La_{0.8}Sr_{0.2})_{0.95}Cr_{0.8}Fe_{0.2}O_3$ (LSCF82) with varying PO_2 (~0.21-10^{-10} atm) is shown in Fig. 10.2. Similar to LSCF73, single phase LSCF82 is obtained in air atmosphere. Unlike LSCF73, no secondary phase peaks are identified when exposed to PO_2~10^{-6} atm. However, peak corresponding to FeO. $(Fe_xCr_{2-x})O_3$ are identified in further reducing atmosphere (PO_2~10^{-10} atm). Likewise LSCF73, changes in the LSCF82 crystal structure are identified that corresponds to phase transformation from rhombohedral to cubic with decrease in PO_2.

Fig. 10.3 shows crystal structure and compound formation of LSCF with Cr: Fe ~ 9:1. In contrast with LSCF82 and LSCF91, no secondary phase peaks are identified for $(La_{0.8}Sr_{0.2})_{0.95}Cr_{0.9}Fe_{0.1}O_3$ (LSCF91). Furthermore, peak splitting corresponding to the rhombohedral structure is not observed in any of the cases for LSCF91. Cubic structure (JCPDS 074-196) is obtained for all three cases (PO_2 ~ 0.21, 10^{-6} and 10^{-10} atm). There is no phase transformation from rhombohedral to cubic structure with change in PO_2, which could otherwise result into stress generation in the material during processing and operation. This corresponds to the highest stability of LSCF91 when compared to LSCF73 and LSCF82 in reducing gas atmosphere as required for high temperature electrochemical devices.

XRD comparison of reducing gas atmosphere (PO2~10^{-10} atm) sintered LSCF73, LSCF82 and LSCF91 is shown in Fig. 10.4. It is clear that FeO_x peaks are only observed for LSCF73. FeO. $(Fe_xCr_{2-x})O_3$ peaks are observed for both LSCF73 and LSCF82. However, a significant increase in the intensity of the phase peaks is identified for LSCF73 when compared to LSCF82. No extra peaks corresponding to the secondary phase formation are

observed for LSCF91. This provides us with the important information on the stability of LSCF based materials at lower PO_2. The stability of LSCF increases with increase in Cr: Fe ratio in reducing atmosphere and LSCF91 is most stable among the studied compositions.

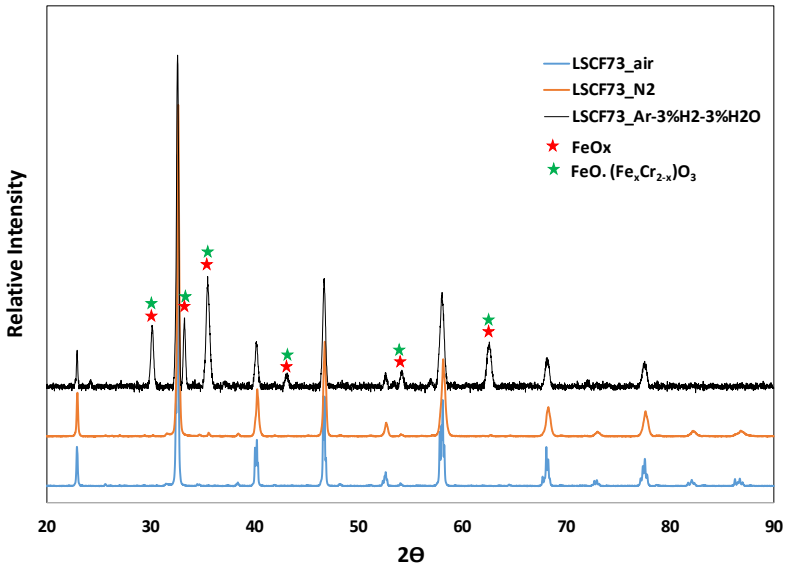

Fig. 10.1. XRD pattern of LSCF73 sintered at 1400°C in air, N_2 and Ar-3%H_2-3%H_2O.

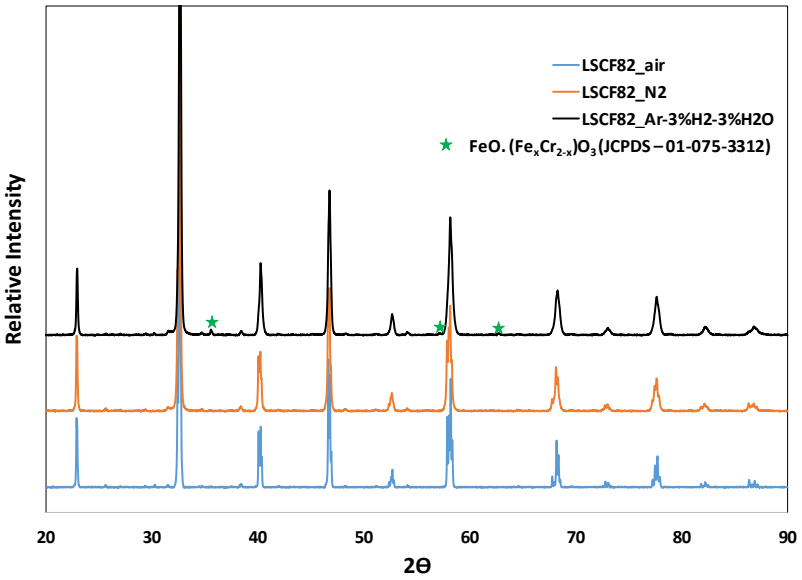

Fig. 10.2. XRD pattern of LSCF82 sintered at 1400°C in air, N_2 and Ar-3%H_2-3%H_2O.

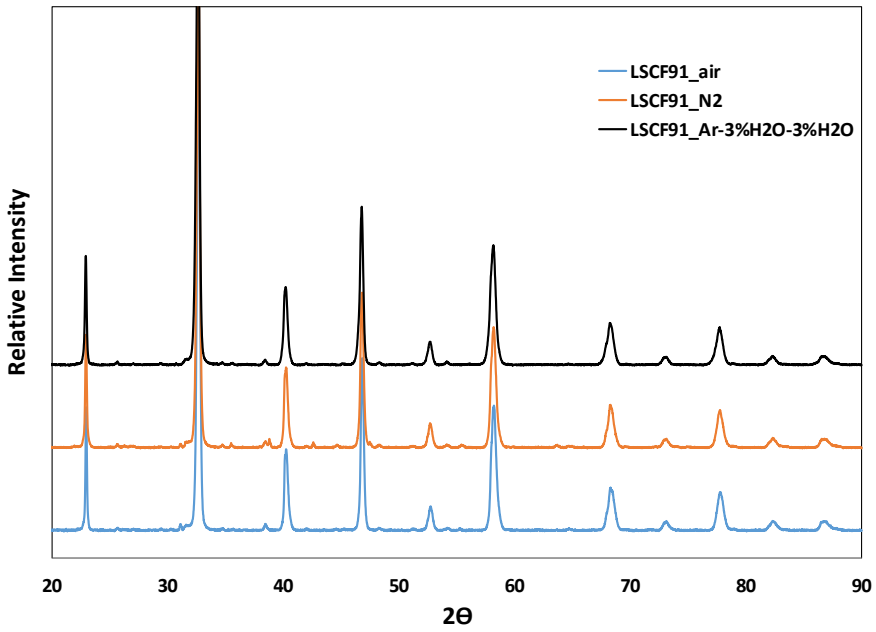

Fig. 10.3. XRD pattern of LSCF91 sintered at 1400°C in air, N_2 and Ar-3%H_2-3%H_2O.

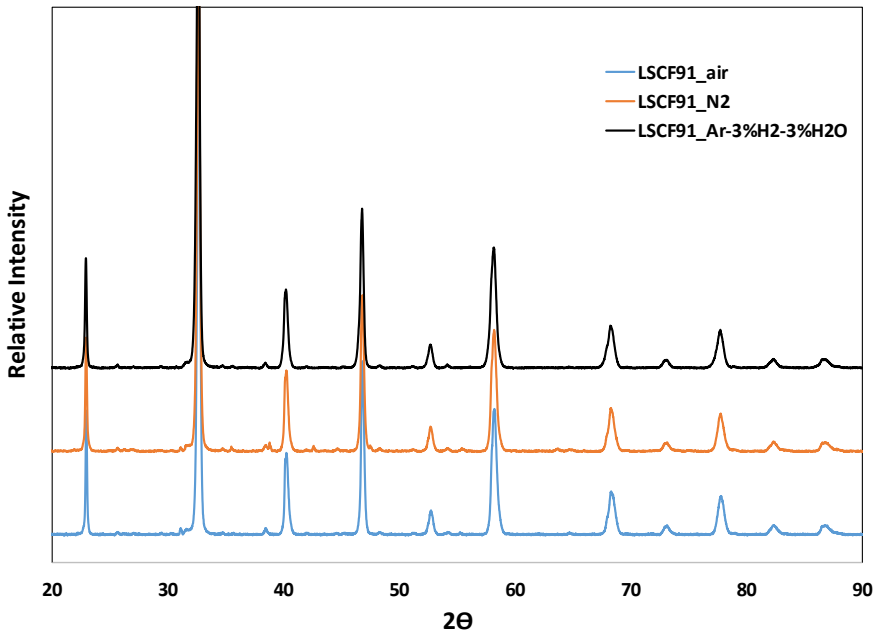

Fig. 10.4. Comparison of XRD pattern of LSCF73/82/91 and 10Sc1CeSZ sintered at 1400°C in Ar-3%H_2-3%H_2O.

10.4.1.2. *Sintering behavior and microstructural analysis*

Table 10.1 shows a trend in between relative densities of LSCF with varying Cr: Fe ratio (7:3, 8:2 and 9:1) and PO_2 (0.21, 10^{-6} and 10^{-10} atm). The density of LSCF increases with increase in Fe doping level and decrease in Cr: Fe ratio. For example, LSCF91 relative density is 51.7% (±2.4) which increases up to 74.9% (±1.5) for LSCF73 in N_2 atmosphere at 1400°C. Similarly, the density also increases with decrease in PO_2. For instance, the relative density of LSCF82 increases from 53.1% (±2.9) to 95.6% (±0.8) when PO_2 decreases from 0.21 to 10^{-10} atm. Similar trend is obtained for LSCF73 and LSCF91.

SEM micrographs of LSCF with varying Cr: Fe ratio and PO_2 are shown in Fig. 10.5. In agreement with the relative density measurement, denser microstructure is obtained for LSCF73 when compared to LSCF82 and LSCF91 under the same conditions. This again indicates that Fe-doping level increases the density of LSCF perovskites. Moreover, the microstructural density also increases with decrease in PO_2. In case of LSCF73, no secondary phase is identified when sintered in air. However, secondary phases enriched in Cr and Fe (indicated by red arrow) is identified in the samples sintered in N_2 (~10^{-6} atm) as well as Ar-3%H_2-3%H_2O (~10^{-10} atm) using SEM-EDS (Table 10.2). The amount of secondary phase increases with decrease in PO_2 as shown in the Fig. 10.5b and c. Furthermore, another phase predominantly enriched in Fe (Fig. 10.5c) is found in the LSCF73 sample when processed in Ar-3%H_2-3%H_2O at lower PO_2. This attributes to dissociation of LSCF73 into FeO_x and FeO. $(Fe_xCr_{2-x})O_3$ in reducing atmosphere. Elemental analysis of LSCF73 bulk and Fe and/or Cr enriched secondary phases is shown in Table 10.2. Fig. 10.6 shows the elemental mapping (La - Blue, Sr – Green, Cr - Yellow and Fe - Purple) of reducing atmosphere sintered

LSCF73. SEM elemental mapping of LSCF73 clearly exhibits the phases that are enriched in Fe and/or Cr indicated by white arrow. The phases are identified using XRD.

In case of LSCF82, likewise LSCF73, no secondary phases are found in air atmosphere. However, unlike LSCF73, LSCF82 does not show any compound formation in N_2 atmosphere. When processed in Ar-3%H_2-3%H_2O reducing atmosphere, LSCF82 also starts to show secondary phases enriched in Fe and Cr corresponding to FeO. $(Fe_xCr_{2-x})O_3$. The phases are indicated by red arrow in Fig. 10.5f. Fe and Cr enriched phases are observed using SEM-EDS in LSCF82 sample and shown in Table 10.3. Fig. 10.7 shows the elemental mapping of LSCF82 processed in Ar-3%H_2-3%H_2O. Phases enriched in Fe and Cr are also spotted (indicated by white arrow) in the elemental mapping image of LSCF82. However, the phases enriched only in Fe are not found in case of LSCF82 unlike LSCF73. This indicates that LSCF82 is more stable than LSCF73 in reducing atmosphere.

Fig. 10.5g, h and i shows SEM micrographs of LSCF91after possessing in air, N_2 and Ar-3%H_2-3%H_2O gas atmosphere respectively. In contrast with LSCF73 and LSCF82, no secondary phases associated with FeO_x and/or FeO. $(Fe_xCr_{2-x})O_3$ are identified in reducing atmosphere. No Fe and/or Cr enriched phases are observed in the LSCF91 elemental analysis using SEM-EDS as shown in Table 10.4. Moreover, elemental mapping of LSCF91 does not show any indication of Fe and/or Cr rich phases in contrast with LSCF73 and LSCF82 as shown in Fig. 10.8. This confirms on the highest stability of LSCF91 among all the studied compositions. In reducing atmosphere, therefore, the observed stability trend is LSCF91>LSCF82>LSCF73. The stability increases with increase in Cr: Fe ratio and decrease in Fe-doping level.

Table 10.1. Relative density of LSCF73/82/91 and 10Sc1CeSZ sintered at 1400°C.

Material	Air	N_2	Ar-3%H_2-3%H_2O
LSCF73	65.6±2.1	74.9±1.5	96.3±0.5
LSCF82	53.1±2.9	57.2±2.8	95.6±0.8
LSCF91	49.0±2.6	51.7±2.4	58.2±1.7

Table 10.2. SEM-EDS elemental analysis of LSCF73 sintered in Ar-3%H_2-3%H_2O at 1400°C.

Element	La (at. %)	Sr (at. %)	Cr (at. %)	Fe (at. %)
Bulk (White)	42.1±1.0	12.5±4.3	34.4±1.1	11.0±4.6
Fe-rich (Gray)	1.4±0.1	0.5±0.1	3.1±0.1	95.5±0.3
Fe and Cr rich (Black)	1.4±0.2	1.1±0.1	50.8±2.1	47.9±1.8

Table 10.3. SEM-EDS elemental analysis of LSCF82 sintered in Ar-3%H_2-3%H_2O at 1400°C.

Element	La (at. %)	Sr (at. %)	Cr (at. %)	Fe (at. %)
Bulk (Gray)	39.6±2.0	14.3±1.3	37.2±1.5	8.8±1.1
Fe and Cr rich (Black)	15.9±1.0	5.2±0.5	50.7±2.1	28.2±1.3

Table 10.4. SEM-EDS elemental analysis of LSCF91 sintered in Ar-3%H_2-3%H_2O at 1400°C.

Element	La (at. %)	Sr (at. %)	Cr (at. %)	Fe (at. %)
Bulk (Gray)	39.1±3.1	17.1±2.7	38.7±2.5	5.1±1.4

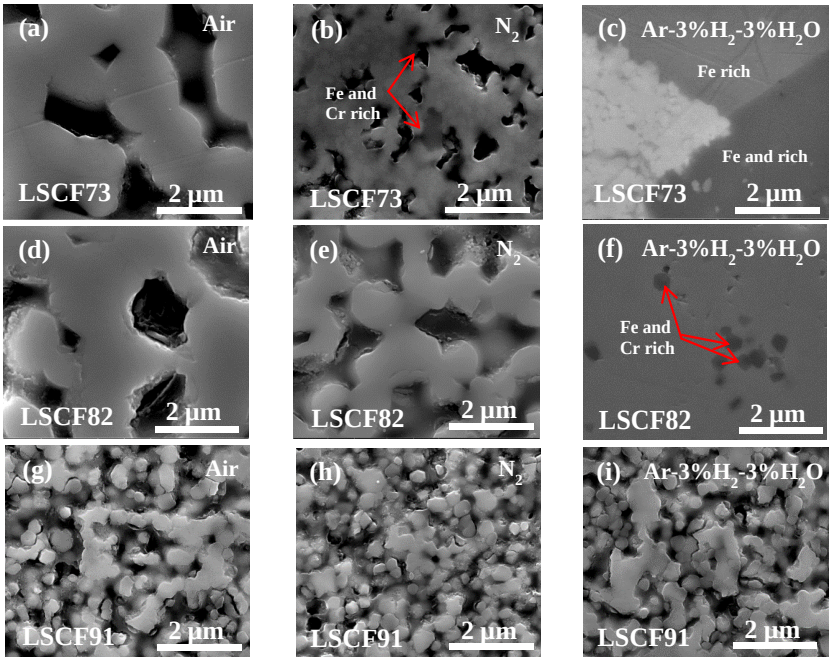

Fig. 10.5. SEM micrographs of sintered LSCF and 10Sc1CeSZ composite with varying Cr: Fe ratio and PO_2: (a) 7:3, air (b) 7:3, N_2, (c) 7:3, Ar-3%H_2-3%H_2O, (d) 8:2, air, (e) 8:2, N_2, (f) 8:2, Ar-3%H_2-3%H_2O, (f) 9:1, air, (g) 9:1, N_2 and (i) 9:1, Ar-3%H_2-3%H_2O.

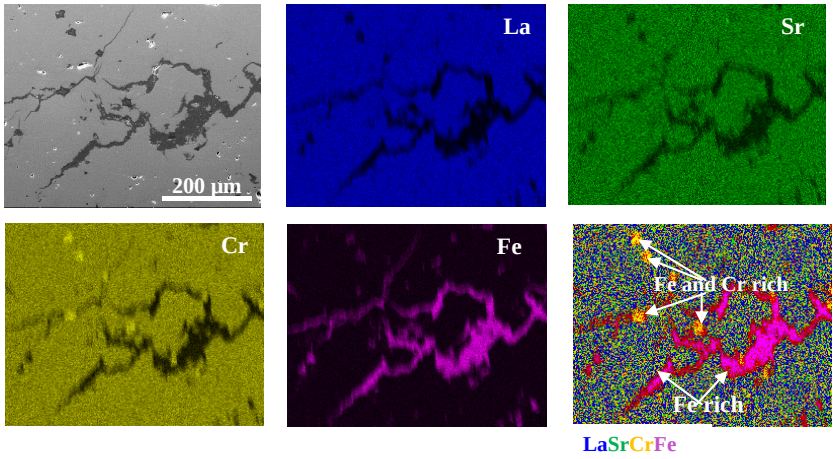

Fig. 10.6. SEM elemental mapping of LSCF73 after processing in PO_2~10^{-10} atm at 1400°C for 10h.

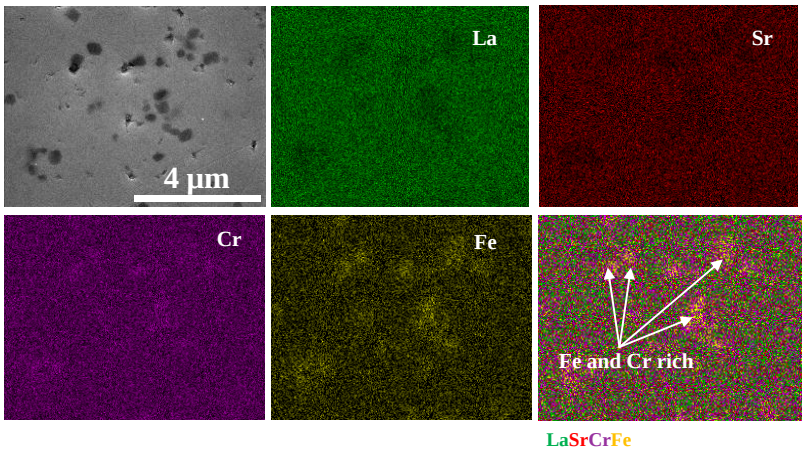

Fig. 10.7. SEM elemental mapping of LSCF82 after processing in oxygen partial pressure of PO_2~10^{-10} atm at 1400°C for 10h.

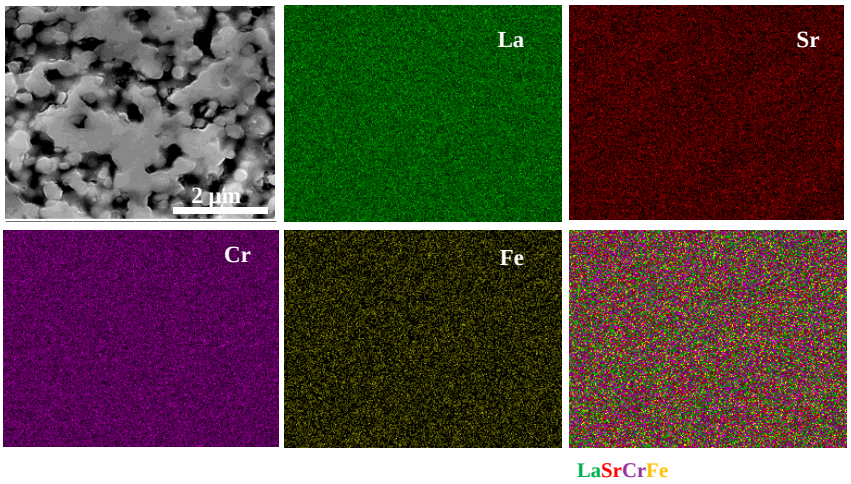

Fig. 10.8. SEM elemental mapping of LSCF91 after processing in PO_2~10^{-10} atm at 1400°C for 10h.

10.4.2. *After exposure to the OTM operating conditions:*

10.4.2.1. *Crystal Structure*

LSCF73, LSCF82 and LSCF91 perovskites with varying Cr: Fe ratio are exposed to OTM operating conditions (1000°C, PO_2 ~ 10^{-12} atm) after processing in air atmosphere.

XRD comparison results of the exposed LSCF with varying Cr: Fe ratio (7:3, 8:2 and 9:1) are shown in Fig. 10.9. Peaks corresponding to the formation of FeO. $(Fe_xCr_{2-x})O_3$ (indicated by green asterisk) are identified in case of LSCF73 perovskite with highest Fe-doping level. Unlike LSCF73, no peaks attributing to secondary compounds are observed for LSCF82 and LSCF91 as shown in Fig. 10.9. In consistent with the above mentioned processing results, the OTM operating condition exposure results also exhibit the less stability and phase separation of LSCF73 when compared to LSCF82 and LSCF91. The results also indicate that the stability of LSCF based materials are dependent on Cr: Fe ratio and increases with increase in Cr: Fe ratio.

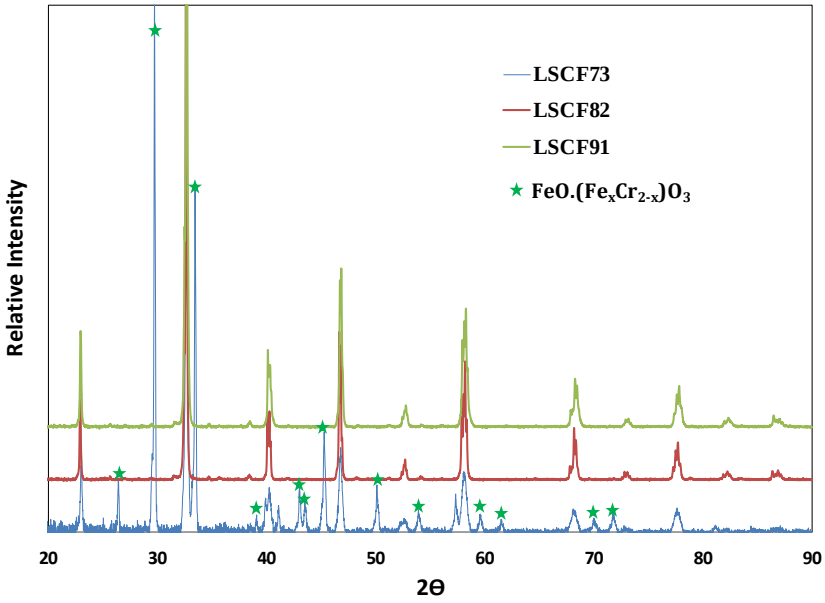

Fig. 10.9. Comparison of XRD pattern of LSCF73/82/91 perovskites after sintering in air and exposed to PO_2 ~10^{-12} atm for 500h at 1000°C.

10.4.2.2. *Microstructure analysis*

SEM micrographs of LSCF73, LSCF82 and LSCF91 are shown in Fig. 10.10a, b and c respectively, after exposure to lower PO_2 at ~1000°C. In agreement with the XRD results

of LSCF73 perovskite, phases enriched in Fe and Cr are identified during microstructural analysis. This is shown in Fig. 10.10a. However, unlike processing condition results, no Fe enriched phases are observed in case of LSCF73 after exposure to the same atmosphere. Similarly, on the other hand, LSCF82 does not show the phases enriched in Fe and Cr. This is in contrast with the processing results. It is to be noted that the processing temperature (~1400°C) is much higher than operating temperature (~1000°C). It is hypothesized that the large difference in temperature is resulting into the variance under the same reducing atmosphere. This is due to faster kinetics occurrence at higher temperature. In case of LSCF91 composition with highest Cr: Fe:: 9:1 ratio, the results obtained after exposure to the reducing atmosphere are similar to the one achieved under processing conditions. No secondary phases are observed in both OTM processing and operating conditions. This indicates towards the higher stability of LSCF91 when compared to higher Fe-doping level containing LSCF82 and LSCF73.

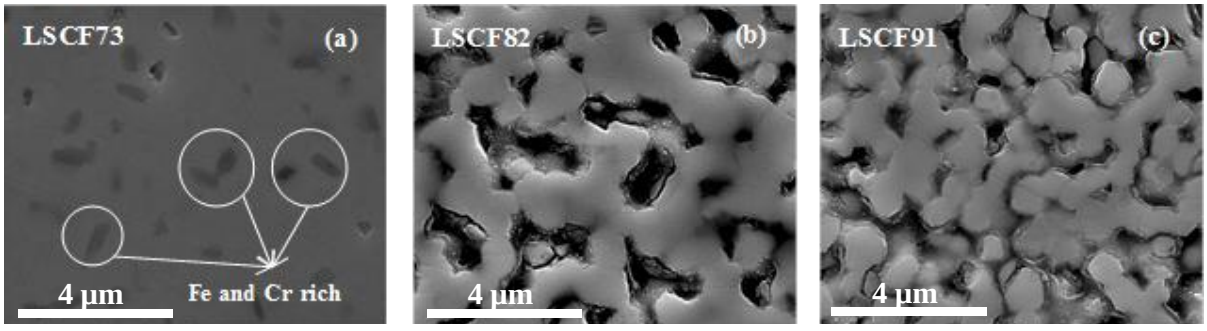

Fig. 10.10. SEM micrographs of sintered LSCF73/82/91 after exposure to PO_2~10^{-12} atm at 1000°C: (a) LSCF73, (b) LSCF82 and (c) LSCF91.

10.4.5. *Defect chemistry and mechanism hypothesis for FeO_x and FeO. $(Fe_xCr_{2-x})O_3$ formation in reducing atmosphere:*

In case of LSCF, Cr can exist in either Cr^{3+} and/or Cr^{4+} valence state. Similarly, Fe can exist in $Fe^{4+}/Fe^{3+/}Fe^{2+}$ valence state depending on the exposure conditions. As a result, LSCF defects equilibrium includes $V_O^{\cdot\cdot}$, $Fe_{Fe}^{\cdot}$, $O_O^{\times}$, $Fe_{Fe}^{\times}$, Fe_{Fe}', $Cr_{Cr}^{\times}$, $Cr_{Cr}^{'}$, Sr_{La}' where $V_O^{\cdot\cdot}$ represents oxygen vacancies with two positive charges, $Fe_{Fe}^{\cdot}$ indicates Fe^{4+} ions on Fe^{3+} sites with one positive charge, $Fe_{Fe}^{\times}$ represents Fe^{3+} on Fe^{3+} sites with neutral charge, Fe_{Fe}' indicates Fe^{2+} on Fe^{3+} sites with one negative charge, $Cr_{Cr}^{\times}$ represents Cr^{3+} on Cr^{3+} sites with neutral charge, $Cr_{Cr}^{'}$ indicates Cr^{4+} on Cr^{3+} sites and Sr_{La}' represents Sr^{2+} on La^{3+} sites with one negative charge.

In <u>oxidizing atmosphere</u> with higher PO_2, LSCF with Cr: Fe ratio equals 7:3 i.e. $(La_{0.8}Sr_{0.2})_{0.95}Cr_{0.7}Fe_{0.3}O_{3-\delta}$ can be written in the Kröger notation form as:

$$[(La_{La}^{\times})_{0.8}(Sr_{La}')_{0.2}]_{0.95}[(Cr_{Cr}^{\times})_{0.7-x}(Cr_{Cr}^{\cdot})_{x}]\left[(Fe_{Fe}^{\times})_{0.3-y}(Fe_{Fe}^{\cdot})_{y}\right][V_O^{\cdot\cdot}]_{\delta}[O_O^{\times}]_{3-\delta}$$

When Sr^{2+} is substituted on the La^{3+} site, the charge on Sr_{La}' would either be balanced by $Cr^{3+}\rightarrow Cr^{4+}$ and/or $Fe^{3+}\rightarrow Fe^{4+}$. There are two possibilities for charge balance as mentioned below:

$$La_{La}^{\times} + Cr_{Cr}^{\times} \xrightarrow{Sr} Sr_{La}^{\times} + Cr_{Cr}^{\cdot} \qquad (1)$$

$$La_{La}^{\times} + Cr_{Cr}^{\times} \xrightarrow{Sr} Sr_{La}^{\times} + Fe_{Fe}^{\cdot} \qquad (2)$$

The reaction between defects and oxygen gas in LSCF can be expressed as:

$$\frac{1}{2}O_2 + V_O^{\cdot\cdot} + 2Fe_{Fe}^{\times} = O_O^{\times} + 2Fe_{Fe}^{\cdot} \qquad (3)$$

$$K = \frac{a_{O_O^{\times}}a_{Fe_{Fe}^{\cdot}}^2}{a_{V_O^{\cdot\cdot}}a_{Fe_{Fe}^{\times}}^2}P_{O_2}^{-1/2} \qquad \rightarrow P_{O_2} = \sqrt{\frac{a_{O_O^{\times}}a_{Fe_{Fe}^{\cdot}}^2}{a_{V_O^{\cdot\cdot}}a_{Fe_{Fe}^{\times}}^2}K} \qquad (4)$$

where K is the equilibrium constant, $a_{O_O^{\times}}$, $a_{Fe_{Fe}^{\times}}$, $a_{V_O^{\cdot\cdot}}$ and $a_{Fe_{Fe}^{\cdot}}$ are activity of $O_O^{\times}$, $Fe_{Fe}^{\times}$, $V_O^{\cdot\cdot}$ and $Fe_{Fe}^{\cdot}$ respectively.

The condition of charge neutrality in oxidizing atmosphere can be written as:

$$[Sr'_{La}] = [Cr^{\cdot}_{Cr}] + [Fe^{\cdot}_{Fe}] + 2[V_O^{\cdot\cdot}] \quad (5)$$

If $[Cr^{\cdot}_{Cr}] = x$, $[Fe^{\cdot}_{Fe}] = y$ and $[V_O^{\cdot\cdot}] = \delta$, then we obtain a relation;

$$x+y+2\delta = 0.19 \quad (6)$$

In case of <u>reducing atmosphere</u>, $Cr^{4+} \rightarrow Cr^{3+}$ and $Fe^{4+}/Fe^{3+} \rightarrow Fe^{2+}$ and Kröger notation of $(La_{0.8}Sr_{0.2})_{0.95}Cr_{0.7}Fe_{0.3}O_{3-\delta}$ can be written as:

$$[(La_{La}^{\times})_{0.8}(Sr'_{La})_{0.2}]_{0.95}[Cr_{Cr}^{\times}]_{0.7}[(Fe_{Fe}^{\times})_{0.3-y}(Fe'_{Fe})_y][V_O^{\cdot\cdot}]_{\delta}[O_O^{\times}]_{3-\delta}$$

Defect reactions for charge compensation in LSCF at lower PO_2would include:

$$La_{La}^{\times} + O_O^{\times} \xrightarrow{Sr} 2Sr'_{La} + V_O^{\cdot\cdot} + \frac{1}{2}O_2 \rightarrow K_1 = \frac{a_{V_O^{\cdot\cdot}} a_{Sr'_{La}}^2}{a_{O_O^{\times}} a_{La_{La}^{\times}}^2} P_{O_2}^{1/2} \rightarrow P_{O_2} = \sqrt{\frac{a_{O_O^{\times}} a_{La_{La}^{\times}}^2}{a_{V_O^{\cdot\cdot}} a_{Sr'_{La}}^2} K_1} \quad (7)$$

$$\frac{1}{2}O_2 + V_O^{\cdot\cdot} + 2Cr_{Cr}^{\times} = O_O^{\times} + 2Cr^{\cdot}_{Cr} \rightarrow K_2 = \frac{a_{O_O^{\times}} a_{Cr^{\cdot}_{Cr}}^2}{a_{V_O^{\cdot\cdot}} a_{Cr_{Cr}^{\times}}^2} P_{O_2}^{-1/2} \rightarrow P_{O_2} = \sqrt{\frac{a_{O_O^{\times}} a_{Cr^{\cdot}_{Cr}}^2}{a_{V_O^{\cdot\cdot}} a_{Cr_{Cr}^{\times}}^2} K_2} \quad (8)$$

$$\frac{1}{2}O_2 + V_O^{\cdot\cdot} + 2Fe_{Fe}^{\times} = O_O^{\times} + 2Fe^{\cdot}_{Fe} \rightarrow K_3 = \frac{a_{O_O^{\times}} a_{Fe^{\cdot}_{Fe}}^2}{a_{V_O^{\cdot\cdot}} a_{Fe_{Fe}^{\times}}^2} P_{O_2}^{-1/2} \rightarrow P_{O_2} = \sqrt{\frac{a_{O_O^{\times}} a_{Fe^{\cdot}_{Fe}}^2}{a_{V_O^{\cdot\cdot}} a_{Fe_{Fe}^{\times}}^2} K_3} \quad (9)$$

$$\frac{1}{2}O_2 + V_O^{\cdot\cdot} + 2Fe'_{Fe} = O_O^{\times} + 2Fe_{Fe}^{\times} \rightarrow K_4 = \frac{a_{O_O^{\times}} a_{Fe_{Fe}^{\times}}^2}{a_{V_O^{\cdot\cdot}} a_{Fe'_{Fe}}^2} P_{O_2}^{-1/2} \rightarrow P_{O_2} = \sqrt{\frac{a_{O_O^{\times}} a_{Fe_{Fe}^{\times}}^2}{a_{V_O^{\cdot\cdot}} a_{Fe'_{Fe}}^2} K_4} \quad (10)$$

where *K* is equilibrium constant and *a* corresponds to activity of respective defect mentioned in the subscript.

The above mentioned relation tells that defect concentrations of $[Fe'_{Fe}]$ and $[V_O^{\cdot\cdot}]$ will increase with decrease in P_{O_2}.

In general, the reaction between LSCF defects and oxygen gas can be expressed as [13]:

$$\frac{1}{2}O_2 + V_O^{\cdot\cdot} + 2Fe_{Fe}^{\times} = O_O^{\times} + 2Fe^{\cdot}_{Fe} \quad (11)$$

$$K = \frac{[O_O^{\times}][Fe_{Fe}^{\cdot}]^2}{P_{O_2}^{1/2}[V_O^{\cdot\cdot}][Fe_{Fe}^{\times}]^2} \quad (12)$$

$$2[Fe_{Fe}^{\times}] = [Fe_{Fe}'] + [Fe_{Fe}^{\cdot}] \quad (13)$$

The condition of charge neutrality can be written as:

$$[Sr_{La}'] + [Fe_{Fe}'] = 2[V_O^{\cdot\cdot}] + [Fe_{Fe}^{\cdot}] \quad (14)$$

$$[Fe_{Fe}^{\times}] + [Fe_{Fe}'] + [Fe_{Fe}^{\cdot}] = 0.3 \quad (15)$$

$$K_{eq} = \frac{[Fe_{Fe}^{\cdot}][Fe_{Fe}']}{[Fe_{Fe}^{\times}]^2} \quad (16)$$

Consider, $[Sr_{La}'] = x$, $[V_O^{\cdot\cdot}] = \delta$ and $[O_O^{\times}] = 3 - \delta$

Using above equations, the general relation between δ and P_{O_2} is shown below:

$$\frac{(2\delta - x + 0.3)\delta^{1/2}}{(2\delta - x)(3-\delta)^{1/2}} P_{O_2}^{1/4} = \frac{K_i}{K_{OX}} \frac{(3-\delta)^{1/2}(x + 0.3 - 2\delta)}{(2\delta - x)\delta^{1/2}\, P_{O_2}^{1/4}} - K_{OX}^{-1/2} \quad (17)$$

As mentioned above, in reducing atmosphere, $Fe^{4+} \rightarrow Fe^{3+}$ and $Fe^{3+} \rightarrow Fe^{2+}$. The charge is compensated by oxygen vacancies formation. However, Fe^{3+} transforms partially to Fe^{2+} at 1400°C and $PO_2 \sim 10^{-10}$ atm. Fe^{2+} doesn't retain in the $A^{3+}B^{3+}O_3$ perovskite lattice and therefore, it comes out of the lattice and form oxide layer (FeO_x) in case of LSCF73. The ionic radius of Fe^{2+} (Fe^{2+} = 0.78 Å) is also greater than Cr^{3+} (Cr^{3+} = 0.615Å) and Fe^{3+} (Fe^{3+} = 0.645Å). After, Fe (B-site) exolution as FeO_x, there should be a presence of A-site enriched phase for mass balance. Since, we have not observed any separate lanthanum (A-site) rich phase, it is understood that the lattice is now lanthanum enriched. Locally, presence of FeO. $(Fe_xCr_{2-x})O_3$ phase is also identified. However, the reason for its formation is not very clear. It could be due to Cr reaction with FeO_x.

In case of LSCF82, no FeO_x phase is identified. However, uniform distribution of FeO. $(Fe_xCr_{2-x})O_3$ phase is observed. In this case, it is postulated that limited FeO_x exolved and all of it reacted with Cr to form FeO. $(Fe_xCr_{2-x})O_3$ to keep the mass balance. Unlike, LSCF73 and LSCF82, no secondary phase formation are identified corresponding to higher stability of LSCF91 perovskite. Reaction process for LSCF with varying Cr: Fe ratio can be represented as:

LSCF73 + FeOx + FeO. $(Fe_xCr_{2-x})O_3$ -----> LSCF82 + FeO. $(Fe_xCr_{2-x})O_3$ ----> LSCF91

A schematic of LSCF73 perovskite lattice structure with change in PO_2 can be shown as below in Fig. 10.10:

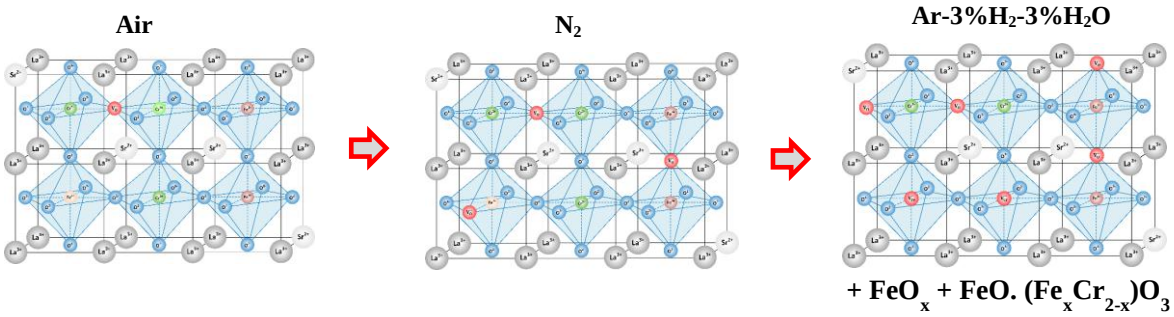

Fig. 10.10. A schematic of LSCF perovskite lattice structure in three different gas atmosphere (Air, N_2, Ar-3%H_2-3%H_2O) condition.

The above schematic shows that the defects/oxygen vacancies increase with decrease PO_2. Subsequently, stability decreases with decrease in PO_2. Similarly, Fig. 10.11 shows a schematic of LSCF perovskite lattice structure with varying Cr: Fe ratio in reducing atmosphere. Defects/oxygen vacancies decrease with increase in Cr: Fe ratio. And, stability increases with increase in Cr: Fe ratio.

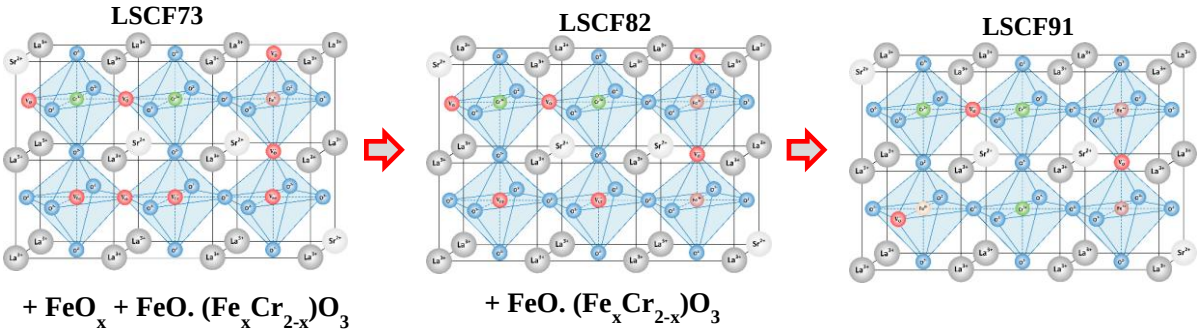

Fig. 10.11. A schematic of change in LSCF perovskite lattice structure with varying Cr: Fe ratio (7:3, 8:2 and 9:1).

Overall, it is to be noted that chromium: iron ratio is the only known difference in LSCF73, LSCF82 and LSCF91 composition. This indicates that variation in Cr: Fe ratio results in stability variation in theses perovskites. Stability tends to decrease with increase in Fe doping level. Furthermore, LSCF with higher doping level dissociates into FeO_x and/or FeO. $(Fe_xCr_{2-x})O_3$ in reducing atmosphere. A co-relation exists between Cr: Fe ratio, FeO_x and FeO. $(Fe_xCr_{2-x})O_3$ secondary phases formation. With decrease in Fe content, formation of Fe and/or Cr rich phases decreases. This shows that the doping amount of Fe has significant role on the stability of LSCF based membrane/fuel electrode of the OTM system. To minimize the secondary phase's formation, therefore, it is suggested to decrease the Fe-content in the LSCF perovskite and utilize LSCF91 based composition.

10.5. Conclusion

Stability of LSCF perovskite decreases with decrease in PO_2 and Cr: Fe ratio. Compound formations as well as localized enrichment of cations within the perovskite phase are observed during exposure to reducing atmospheres. FeO_x secondary phases have been observed during sintering of LSCF73 in Ar-3%H_2-3%H_2O at 1400°C. However, FeO.

$(Fe_xCr_{2-x})O_3$ secondary phase is observed at lower PO_2 in both LSCF73 and LSCF82. Under OTM operational conditions, LSCF73 tends to destabilize. LSCF91 perovskite does not show any of the second phase formation (FeO_x and FeO. $(Fe_xCr_{2-x})O_3$) with decrease in PO_2 unlike LSCF73 and LSCF82. Hypothesis for the formation of FeO_x and FeO. $(Fe_xCr_{2-x})O_3$ in LSCF is proposed based on experimental observations, thermodynamic stability and defect chemistry.

10.6. References

[1] S.W. Tao, J.T.S. Irvine, Nat. Mater. 2 (2003) 320.

[2] S.M. Plint, P.A. Connor, S. Tao, J.T.S. Irvine, Solid State Ionics 177 (2006) 2005.

[3] S.W. Tao, J.T.S. Irvine, Chem. Mater. 16 (2004) 4116.

[4] J.J. Liu, T. Liu, W.D. Wang, J.F. Gao, C.S. Chen, J. Membr. Sci. 389 (2012) 435.

[5] J.J. Liu, S.Q. Zhang, W.D. Wang, J.F. Gao, W. Liu, C.S. Chen, J. Power Sources 217 (2012) 287.

[6] S. Gupta, M.K. Mahapatra and P. Singh, Materials Science and Engineering R 90 (2015) 1–36.

[7] W. He, H. Huang, M. Chen, J.F. Gao, C.S. Chen, Solid State Ionics 260 (2014) 86–89.

[8] T. Wei, X. Liu, C. Yuan, Q. Gao, X. Xin, S. Wang, J. Power Sources 250 (2014) 152–159.

[9] M.F. Lu¨ , E.V. Tsipis, J.C. Waerenborgh, A.A. Yaremchenko, V.A. Kolotygin, S. Bredikhin, V.V. Kharton, J. Power Sources 206 (2012) 59–69.

[10] Wei Fang, Yu Zhang, Jianfeng Gao, Chusheng Chen, Ceramics International 40 (2014) 799–803.

[11] S. Gupta, M.K. Mahapatra, P. Singh, Mater. Res. Bull. 48 (2013) 3262– 3267.

[12] Tao S, Irvine JTS. Chem. Mater. 2006;18:5453-5460.

[13] M. Oishia, K. Yashiroa, K. Satoa, J. Mizusakia, T. Kawadab. J. Solid State Chemistry 181 (2008) 3177–3184.

CHAPTER 11: EFFECT OF CHROMIUM: IRON RATIO AND OXYGEN PARTIAL PRESSURE ON THE SINTERING BEHAVIOR AND STABILITY OF IRON DOPED LANTHANUM STRONTIUM CHROMITE AND SCANDIA STABILIZED ZIRCONIA

11.1. Abstract:

This study reports the effect of chromium- iron ratio on processing, structural and interfacial stability of doped $(La_{0.8}Sr_{0.2})_{0.95}Cr_{1-x}Fe_xO_3$ (LSCF, x ~ 0.1-0.3) and 10Sc1CeSZ composite in oxidizing and reducing atmosphere for the application of oxygen transport membrane (OTM) system. Role of oxygen partial pressure (PO_2) on the microstructural changes and bulk/interfacial stability of LSCF with 10Sc1CeSZ is also reported under OTM fabrication conditions (1400°C, $PO_2 \sim 0.21 - 10^{-10}$ atm.) and operating conditions (1000°C, $PO_2 \sim 10^{-12}$ atm). We observe an increase in density with decrease in Cr: Fe ratio and PO_2. On the contrary, bulk and interfacial stability corresponding to the interaction between LSCF and 10Sc1CeSZ increases with increase in Cr: Fe ratio and PO_2. Under processing conditions, formation of $SrZrO_3$ and FeO. $(Fe_xCr_{2-x})O_3$ are identified only for the samples sintered in reducing atmosphere ($PO_2 \sim 10^{-10}$ atm). The amount of the two secondary phases decreases with increase in Cr: Fe ratio. $SrZrO_3$ formation is also observed in LSCF composite with x=0.3 and x=0.2 after long term exposure (500h) under simulating operating conditions ($PO_2 \sim 10^{-12}$ atm). No $SrZrO_3$ phase are identified in LSCF with x=0.1. Increase in Fe-doping level enhances the interaction between LSCF and 10Sc1CeSZ and suppresses the stability of the composite.

11.2. Introduction

Dense ceramic materials with high mixed ionic-electronic conductivity (MIEC) have shown promising potential for economic, clean and efficient oxygen separation from air [1-2]. Applications range from small-scale oxygen pumps which can be utilized in medical industries to large scale oxygen production system for coal gasification/combustion in power plants [3-7]. MIEC materials also find application in chemical processing which includes the partial oxidation of hydrocarbons [1-2, 8]. For example, oxygen transport membrane prepared with MIEC materials can be used to convert natural gas to value-added chemicals such as syngas which can be further processed for hydrogen production and liquid fuels [2, 9-10].

An overview of MIEC materials for use in oxygen separation devices like OTMs and technology development was recently published [2]. Lanthanum chromite doped at A-site with strontium and B-site with iron (La Sr)(Cr, Fe)$_{3-\delta}$ (LSCF) is currently being investigated for use in membranes and fuel side electrodes for use in oxygen transport membrane (OTM) systems [2, 11-12]. It is reported that Fe-doping improves electrode performance in solid state electrochemical devices (e.g. SOFC) [13-14]. Lower polarization resistance is obtained for iron doped $La_{0.75}Sr_{0.25}Cr_{0.5}Fe_{0.5}O_{3-\delta}$ (LSCF55) than Mn-doped $La_{0.75}Sr_{0.25}Cr_{0.5}Mn_{0.5}O_{3-\delta}$ (LSCM55) [13]. Furthermore, ionic conductivity of (La Sr)(Cr, Fe)$_{3-\delta}$ (LSCF) is found to be higher than acceptor-doped lanthanum chromites and (La Sr)(Cr, Mn)$_{3-\delta}$ (LSCM) [15-16]. However, the authors have noted that most of the literature exists on LSCF55 [11, 13, 17]. An oxygen permeation flux and oxygen ionic conductivity of 2.5 × 10^{-7} mol cm^{-2} s^{-1} and ~0.01 S/cm were found at 950 °C under air/CO gradient [11]. On the other hand, it is reported that LSCF55 is not stable and partially decomposes into metallic

iron along with some unknown phases when exposed to pure H_2 atmosphere at 950°C (30h). Fang et al. [17] have calculated the decomposition oxygen partial pressure of LSCF55 as 6.3 × 10^{-28} atm. Addition of a fluorite phase is required to achieve the higher ionic conduction and oxygen flux performance required for oxygen separation devices such as OTMs [2]. For instance, single phase $La_{0.8}Sr_{0.2}Cr_{0.5}Fe_{0.5}O_{3-d}$ perovskite exhibited an oxygen flux of ~2.5×10^{-7} mol $cm^{-2}s^{-1}$ and $La_{0.8}Sr_{0.2}Cr_{0.5}Fe_{0.5}O_{3-d}/Zr_{0.84}Y_{0.16}O_{1.92}$ composite exhibited a higher oxygen flux of JO_2~2.6×10^{-6} mol cm^{-2} s^{-1} under an air/CO gradient at 950°C [18-19].

It is observed that LSCF55 perovskite cannot withstand a reducing atmosphere for an extended time under high temperatures and low oxygen partial pressure operating conditions. Limited data exists on LSCF based perovskites and composites. Furthermore, degradation and stability (structural, thermal and microstructural) of LSCF based materials with higher Cr: Fe ratio are not reported in literature under fabrication conditions (1400°C, ~ 0.21-10^{-6} atm) required for oxygen separation devices like OTMs and operating conditions (1000°C, ~ 10^{-12} atm). Due to the reported lower stability of higher Fe-containing LSCF perovskites, this study examines the effect of lower Fe doping level on processing and stability of LSCF based materials in reducing gas atmosphere for the application to the OTM system. It is important to understand the interaction between LSCF perovskite and 10Sc1CeSZ fluorite under OTM processing and operating conditions which have not been reported upon in the literature [2]. This study, therefore, also focuses on the role of Cr: Fe ratio and oxygen partial pressure on the stability (thermal, structural and microstructural) and processing of LSCF composites with 10Sc1CeSZ under OTM fabrication and operating conditions.

11.3. Experimental

11.3.1. *$(La_{0.8}Sr_{0.2})_{0.95}Cr_{1-x}Fe_xO_{3-\delta}$ (x ~ 0.3-0.1) and 10Sc1CeSZ synthesis*

$(La_{0.8}Sr_{0.2})_{0.95}Cr_{0.7}Fe_{0.3}O_{3-\delta}$ (LSCF73), $(La_{0.8}Sr_{0.2})_{0.95}Cr_{0.8}Fe_{0.2}O_{3-\delta}$ (LSCF82) and $(La_{0.8}Sr_{0.2})_{0.95}Cr_{0.9}Fe_{0.1}O_{3-\delta}$ (LSCF91) mixed with 10Sc1CeSZ in the volume percent ratio of 60: 40 were bisque fired (1100°C, 2h) and pressed into pellets. The pellets were then sintered in air (0.21 atm), N_2 (~10^{-5} atm) and Ar-3%H_2-3%H_2O (~10^{-10} atm) at 1400°C for 10h. The air sintered pellets were subsequently exposed to OTM operating conditions i.e. 5%H_2-CO_2 (~10^{-12} atm) atmosphere for 500h. For interfacial study, pellets of 10Sc1CeSZ fluorite were made and then calcined at 1100°C for 2h. LSCF73 composition ink was prepared using Fuel Cell Materials ink vehicle. The ink was then screen printed onto the 10Sc1CeSZ disk shape pellet and dried at 125°C for 2h. The LSCF73/10Sc1CeSZ system was also sintered at 1400°C for 10h in oxidizing (air) and reducing (Ar-3%H_2-3%H_2O) atmosphere.

11.3.2. *Characterization*

Density of sintered LSCF73, LSCF82 and LSCF91 composites with 10Sc1CeSZ were measured using Archimedes principle. Microstructural changes, elemental analysis and second phase formation of the sintered and exposed samples were analyzed using scanning electron microscope (SEM) (FEI - ESEM Quanta 250, Hillsboro, OH) with energy dispersive spectroscopy (EDS). Focused Ion Beam (FEI Strata 400S DUALBEAM FIB) was used for the sample preparation of LSCF73+10Sc1CeSZ for transmission electron microscopy (TEM) analysis. Elemental compositional analysis was further conducted using energy dispersive spectroscopy (EDS) attached to the TEM. Crystal structure and bulk/interfacial compound formation of the sintered and exposed samples were analyzed using X-ray (BRUKER-D8

ADVANCE, Bruker AXS Inc. Madison, WI) diffraction technique with scan step of 0.02° and CuK_{α} radiation (λ = 1.5406 Å).

11.4. Results and Discussion

11.4.1. *After exposure to the OTM processing conditions*

11.4.1.1. *Crystal structure*

Crystal structure and compound formation of sintered $(La_{0.8}Sr_{0.2})_{0.95}Cr_{0.7}Fe_{0.3}O_3$ (LSCF73), $(La_{0.8}Sr_{0.2})_{0.95}Cr_{0.8}Fe_{0.2}O_3$ (LSCF82) and $(La_{0.8}Sr_{0.2})_{0.95}Cr_{0.9}Fe_{0.1}O_3$ (LSCF91) composites with 10Sc1CeSZ are analyzed and compared. Fig. 11.1 shows XRD comparison of LSCF73/10Sc1CeSZ sintered in air, N_2 and Ar-3%H_2-3%H_2O. LSCF exhibits a rhombohedral crystal structure. Unlike air and N_2 atmosphere, formation of $SrZrO_3$ corresponding to the interaction between LSCF73 and 10Sc1CeSZ is identified in Ar-3%H_2-3%H_2O atmosphere. In addition, peaks attributed to the FeO. $(Fe_xCr_{2-x})O_3$ phase is observed in the LSCF73/10Sc1CeSZ composite as shown in Fig. 11.1. Similar results are obtained for the LSCF82/10Sc1CeSZ and LSCF91/10Sc1CeSZ composite as shown in Fig. 11.2 and 11.3 respectively. In air and N_2 atmospheres, no secondary phase peaks are observed. However, in Ar-3%H_2-3%H_2O, $SrZrO_3$ peaks are observed in both cases. FeO. $(Fe_xCr_{2-x})O_3$ phase peaks are also identified in the LSCF82/10Sc1CeSZ composite in addition to $SrZrO_3$.

Comparison of LSCF based composites with varying Cr: Fe ratio or Fe doping level is shown in Fig. 11.4. Strontium zirconate ($SrZrO_3$, JCPDS-01-074-1297) formation is identified in all three LSCF73, LSCF82 and LSCF91 composites. However, the peak intensity decreases with decrease in Fe doping level corresponding to the zirconate formation decrease with a decrease in Fe concentration. However, extra peaks corresponding to FeO.

$(Fe_xCr_{2-x})O_3$ are identified in LSCF73 and LSCF82 composites when processed in Ar-3%H_2-3%H_2O atmosphere as shown in Fig. 11.4.

The above mentioned results show that the stability of LSCF composite increases with increase in Cr: Fe ratio and LSCF91/10Sc1CeSZ composite is most stable among all the studied compositions under OTM processing conditions. Our results also demonstrate that oxidizing atmospheres (air and N_2) are suitable for OTM materials processing.

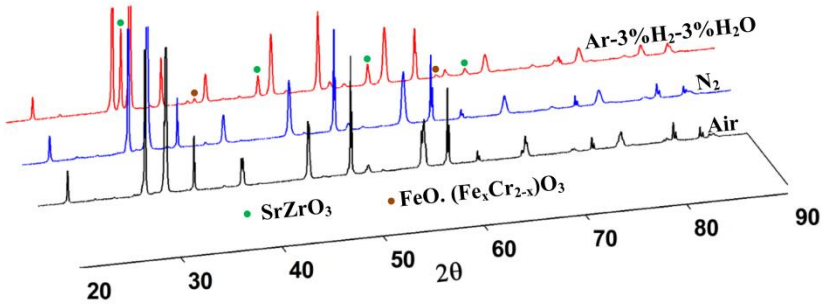

Fig. 11.1. XRD pattern of LSCF73/10Sc1CeSZ sintered at 1400°C in air, N_2 and Ar-3%H_2-3%H_2O.

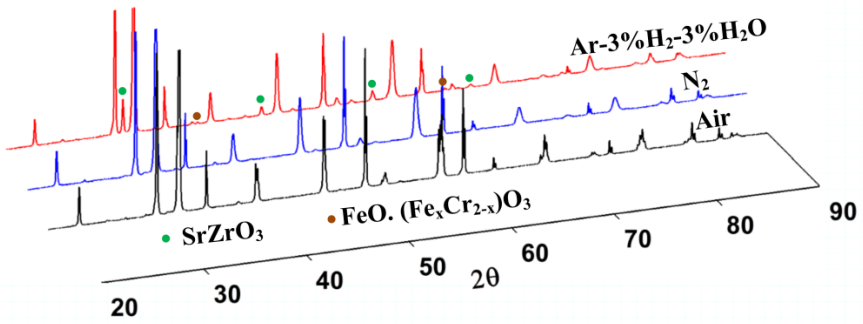

Fig. 11.2. XRD pattern of LSCF82/10Sc1CeSZ sintered at 1400°C in air, N_2 and Ar-3%H_2-3%H_2O.

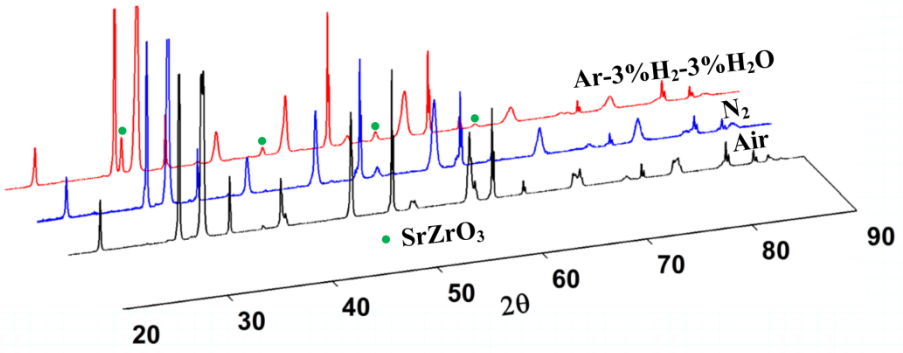

Fig. 11.3. XRD pattern of LSCF91/10Sc1CeSZ sintered at 1400°C in air, N_2 and Ar-3%H_2-3%H_2O.

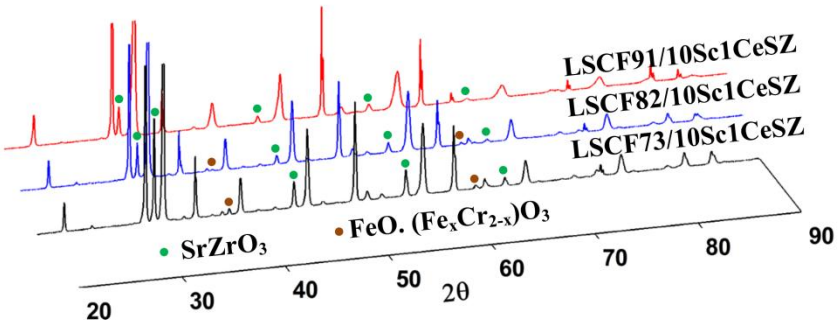

Fig. 11.4. Comparison of XRD pattern of LSCF73/82/91 and 10Sc1CeSZ sintered at 1400°C in Ar-3%H_2-3%H_2O.

11.4.1.2. *Sintering behavior and microstructural analysis*

Relative density of LSCF/10Sc1CeSZ composite increases with decrease in Cr: Fe ratio (7:3, 8:2 and 9:1) and oxygen partial pressure as shown in Table 11.1. For instance, density of LSCF composite is 53.9% (±2.1) for Cr: Fe :: 9: 1 and increases up to 72.5 % (±2.0) with decrease in Cr: Fe ratio to 7: 3. The highest density is achieved for LSCF73/10Sc1CeSZ composite. This is probably because Fe acts as a sintering aid in LSCF

and therefore, the density decreases with a decrease in the Fe-doping level. Similar to Cr: Fe ratio, density of these composites increases with decrease in oxygen partial pressure. For example, LSCF82 composite exhibits 62.2 % (±1.5) density in air (0.21 atm) atmosphere which increases up to 84.8% (±1.3) with decrease in PO_2 (10^{-10} atm). In oxidizing atmosphere, densification of lanthanum chromite based materials is inhibited due to CrO_3 evaporation and condensation as Cr_2O_3 [2-3]. However, the CrO_3 (evaporation)/Cr_2O_3 (condensation) decreases with a decrease in PO_2 and therefore, the density increases with a decrease in oxygen partial pressure.

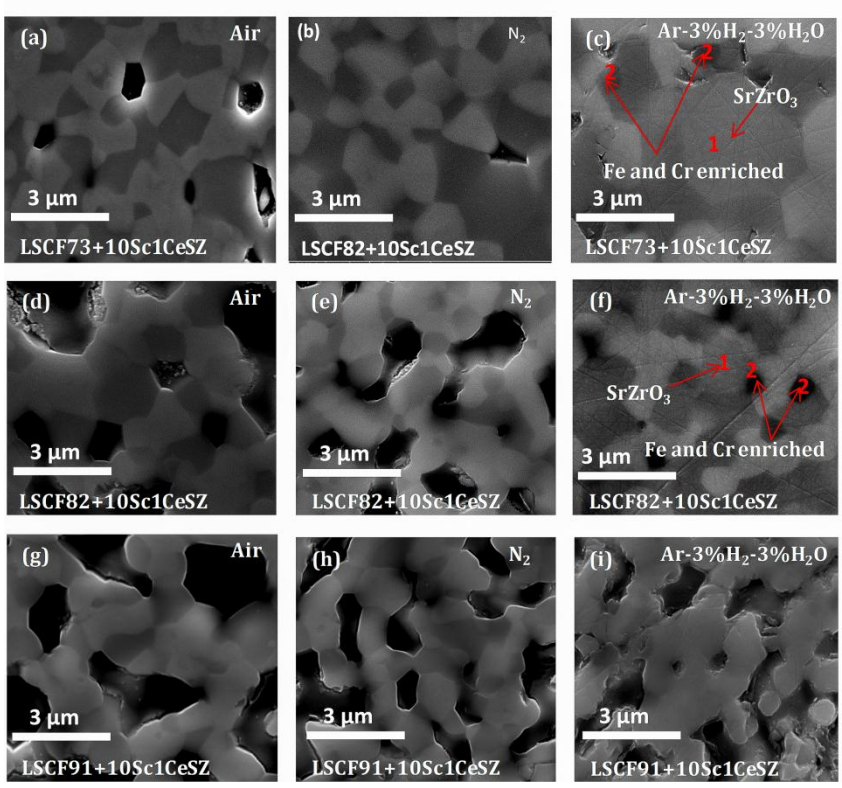

Fig. 11.5. SEM micrographs of sintered LSCF and 10Sc1CeSZ composite with varying Cr: Fe ratio and PO_2: (a) 7:3, air (b) 7:3, N_2, (c) 7:3, Ar-3%H_2-3%H_2O, (d) 8:2, air, (e) 8:2, N_2, (f) 8:2, Ar-3%H_2-3%H_2O, (g) 9:1, air, (h) 9:1, N_2 and (i) 9:1, Ar-3%H_2-3%H_2O.

Fig. 11.5 shows a comparison of scanning electron micrographs of sintered LSCF73/82/91 and 10Sc1CeSZ composites with varying Cr: Fe ratio in air, N_2 and Ar-3%H_2-3%H_2O atmosphere. The highest density microstructure is obtained for LSCF with the highest Fe doping level (30 mol. %). Table 11.2 shows the SEM-EDS analysis of LSCF73/10Sc1CeSZ processed in Ar-3%H_2-3%H_2O. Area 1 and 2 are marked in Fig. 11.5c and f. Sr and Zr enriched phases corresponding to $SrZrO_3$ secondary phase formation are observed in LSCF73/82 and 10Sc1CeSZ composites (Fig. 11.5c and f, Table 11.2) in reducing atmosphere in agreement with the XRD results. Furthermore, Fe-Cr enriched phases corresponding to FeO. $(Fe_xCr_{2-x})O_3$ formation is also observed in case of LSCF73 and LSCF82 composites in Ar-3%H_2-3%H_2O as shown in Fig. 11.5c/f and Table 11.2. Similar to $SrZrO_3$ formation, Fe and Cr enriched phase formation also decreases with decrease in Fe doping level.

Table 11.2. Relative density of LSCF73/82/91 and 10Sc1CeSZ sintered at 1400°C.

Material	**Air**	**N_2**	**Ar-3%H_2-3%H_2O**
LSCF73+10Sc1CeSZ	72.5±2.0	73.7±1.7	91.9±0.8
LSCF82+10Sc1CeSZ	62.2±1.5	64.8±1.4	84.8±1.3
LSCF91+10Sc1CeSZ	53.9±2.1	56.1±2.2	62.5±1.8

SEM micrographs of LSCF/10Sc1CeSZ also show higher densification with decrease in PO_2. Fig. 11.5a, d and g show SEM micrographs of LSCF73/82/91 and 10Sc1CeSZ composites sintered in air respectively. Higher density is obtained for Ar-3%H_2-3%H_2O sintered samples (Fig. 11.5c, f and i) when compared to air. No $SrZrO_3$ and/or FeO. $(Fe_xCr_{2-x})O_3$ secondary phases are identified in all three cases (Cr: Fe – 7:3, 8:2, and 9:1) in air

atmosphere unlike Ar-3%H_2-3%H_2O reducing gas sintered samples. This indicates that the Cr: Fe does not significantly affect the materials stability in air under processing conditions.

Table 11.2. SEM-EDS analysis of LSCF73/10Sc1CeSZ processed in Ar-3%H_2-3%H_2O.

Element (at. %)	La	Sr	Cr	Fe	Zr	Sc	Ce
Area 1 (Sr/Zr rich)	7±2.9	35±3.1	9.5±2.8	3.3±1.5	40.1±3.8	3±2.1	2.2±1.1
Area 2 (Fe/Cr rich)	1.3±0.5	1.2±0.3	43.8±2.5	41.3±1.9	8.5±2.3	3.5±1.8	0.5±0.1

11.4.2. *After exposure to the OTM operating conditions*

11.4.2.1. *Crystal Structure*

Considering the above mentioned optimized processing conditions, air atmosphere is chosen for LSCF composite sintering. To further understand the stability as well as degradation of LSCF/10Sc1CeSZ composite under OTM operating conditions, all three compostions with varying Cr: Fe ratio (7:3, 8:2 and 9:1) are sintered in air atmosphere and then exposed to reducing atmosphere at lower temperature. Air sintered LSCF73/82/91 and 10Sc1CeSZ composites are exposed to simulating OTM operating conditions (1000°C, PO_2 ~ 10^{-12} atm). Fig. 11.6 shows comparison of all three composites with varying Cr: Fe ratio (7:3, 8:2 and 9:1) after exposure to PO_2 ~ 10^{-12} atm at 1000°C for 500h. Three major peaks corresponding to strontium zirconate formation (JCPDS-01-074-1297) are identified in case of LSCF73 and LSCF82 composites. However, the peaks intensity decreases with an increase in Cr: Fe ratio. No $SrZrO_3$ secondary phase peaks corresponding to the interaction between LSCF perovskite and 10Sc1CeSZ fluorite phase are identified in the case of the LSCF91/10Sc1CeSZ composite. The LSCF91 composite exhibited the highest stability under OTM operating conditions.

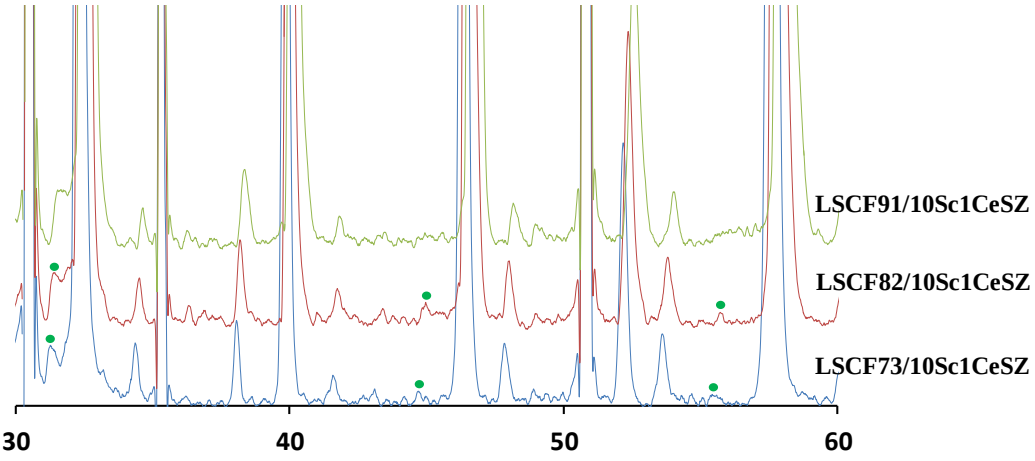

Fig. 11.6. XRD pattern comparison of LSCF73/82/91 and 10Sc1CeSZ composites after processing in air and exposure to PO_2 ~10^{-12} atm for 500h at 1000°C.

11.4.2.2. *Microstructure analysis*

Fig. 11.7 shows scanning electron micrographs of LSCF73/82/91 and 10Sc1CeSZ composites after exposure to PO_2~10^{-12} atm for 500h. The LSCF73/10Sc1CeSZ sample showed changes in surface morphology (Fig. 11.7a and d) and localized compound ($SrZrO_3$) formation as shown in Fig. 11.7a. It is identified that the surface morphology of 10Sc1CeSZ changes only in the case of LSCF73 and LSCF82 composites when compared to LSCF91 composite. Similar surface modification of fluorite phase (8YSZ) is reported due to Mn diffusion from LSM into 8YSZ [20]. The authors also hypothesize that changes in the surface morphology of 10Sc1CeSZ is due to Fe diffusion into 10Sc1CeSZ. To confirm the Fe diffusion into the 10Sc1CeSZ phase, TEM-EDS spot analysis was conducted on the focused ion beam cross-sectioned LSCF73/10Sc1CeSZ sample. 5-7 at. % of Fe is identified in 10Sc1CeSZ corresponding to Fe diffusion from the perovskite phase to fluorite phase. Furthermore, the $SrZrO_3$ phase is observed only in the LSCF73 and LSCF82 composites. The amount of $SrZrO_3$ decreases with an increase in Cr: Fe level. Porosity formation is also

identified on the surface of 10Sc1CeSZ for the LSCF73 composite as shown in Fig. 11.7d. No significant changes are identified in the LSCF91 composite even after 500h exposure to reducing atmosphere (PO_2~10^{-12} atm) as shown in Fig. 11.7c and f. This corresponds to the higher stability of LSCF91 composite under OTM operating conditions. Overall, the stability of LSCF composites increases with increase in Cr: Fe ratio in reducing atmosphere.

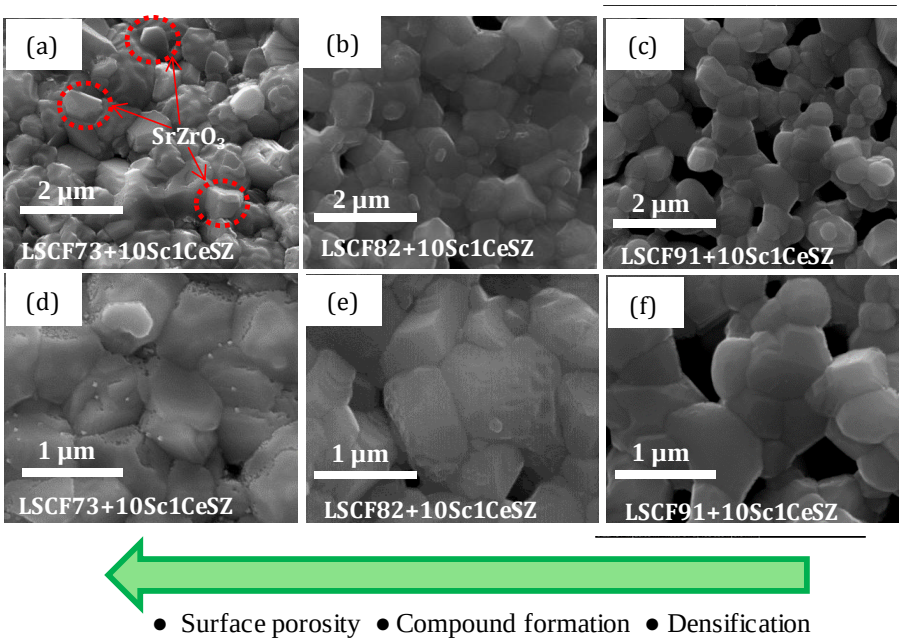

Fig. 11.7. SEM micrographs of sintered LSCF73/82/91 and 10Sc1CeSZ composites after exposure to PO_2~10^{-12} atm at 1000°C: (a, d) LSCF73/10Sc1CeSZ, (b, e) LSCF82/10Sc1CeSZ and (c, f) LSCF91/10Sc1CeSZ.

Fig. 11.8a and b shows elemental mapping of the exposed LSCF73/10Sc1CeSZ composite. The overlay elemental map show Sr and Zr enriched phases corresponding to $SrZrO_3$ formation. Unlike LSCF73/10Sc1CeSZ, LSCF91 composite elemental mapping (Fig. 11.8c and d) does not show any indication of the enriched phase after 500h exposure to PO_2~10^{-12} atm. The elemental mapping results again confirm on the stability of LSCF91/10Sc1CeSZ under OTM operating conditions.

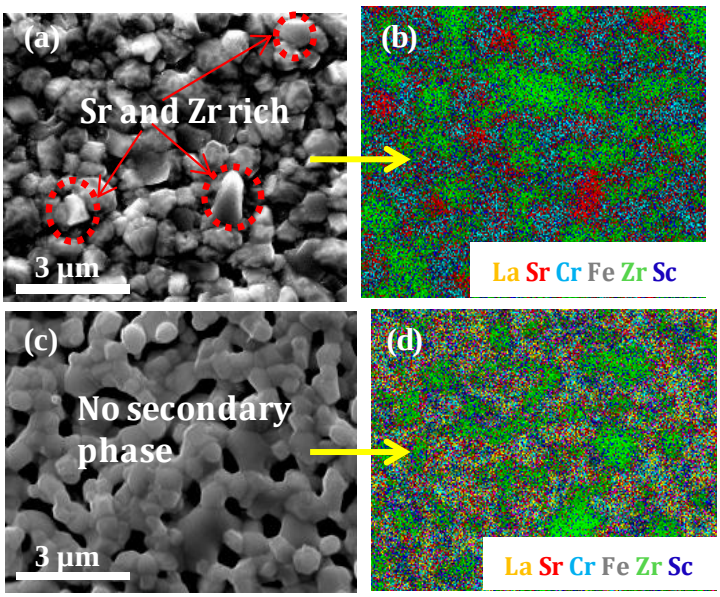

Fig. 11.8. SEM-EDS elemental mapping of LSCF73/10Sc1CeSZ (a, b) and LSCF91/10Sc1CeSZ (c, d) after exposure to PO_2~10^{-12} atm for 500h.

11.4.3. *Interfacial stability*

The above mentioned results show that the LSCF73 composite is the most unstable and prone to form interfacial compounds. Therefore, the LSCF73 composite is chosen to further understand the interfacial stability and compound formation at the interface of LSCF/10Sc1CeSZ. Single phase LSCF73 was screen-printed on a 10Sc1CeSZ disk and processed under accelerated conditions (1400°C and PO_2~10^{-10} atm) and air. Fig. 11.9 shows the SEM micrographs of LSCF73 screen printed on 10Sc1CeSZ disk and sintered in air (Fig. 11.9a) and Ar-3%H_2-3%H_2O (Fig. 11.9b). No compound formation is identified in the bulk or LSCF73/10Sc1CeSZ interface when processed in oxidizing atmosphere. However, a uniform and dense layer with a thickness of ~1.7µm is found at the interface of LSCF73 and 10Sc1CeSZ attributed to an interaction between LSCF73 and 10Sc1CeSZ in a reducing atmosphere. Using SEM-EDS, it is identified that the layer is enriched in Sr and Zr as shown

in Fig. 11.10. Elemental mapping showed Sr and Zr enrichment at the interface of LSCF73 and 10Sc1CeSZ corresponding to $SrZrO_3$ layer formation in Ar-3%H_2-3%H_2O (Fig. 11.9e) atmosphere, but not in air (Fig. 11.9b). A line profile of LSCF73/10Sc1CeSZ system shows two zones (LSCF73 and 10Sc1CeSZ) when exposed to air. However, three zones (LSCF73, $SrZrO_3$ and 10Sc1CeSZ) are identified in a reducing gas atmosphere. Interaction of LSCF73 and 10Sc1CeSZ results in to the intermediate zone of $SrZrO_3$ phase as shown in Fig. 11.10f.

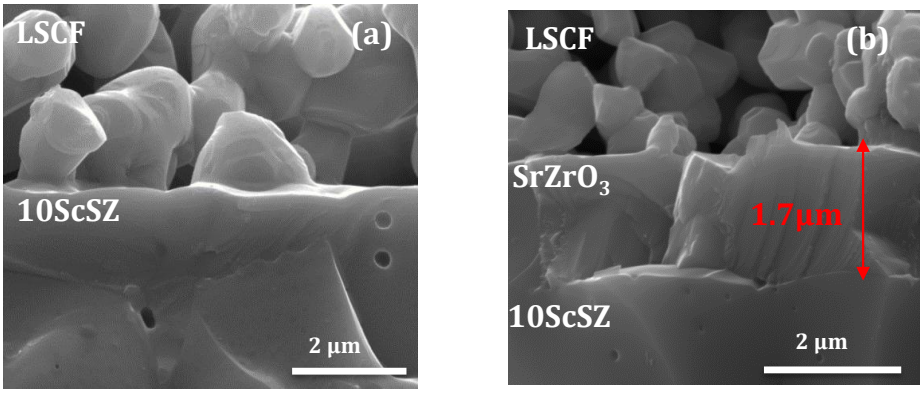

Fig. 11.9. SEM micrograph of LSCF73 screen printed on 10Sc1CeSZ and sintered in: (a) air and (b) Ar-3%H_2-3%H_2O.

The electrical conductivity of $SrZrO_3$ phase is ~10^{-3} and 10^{-6} S cm^{-1} at 1000°C in oxidizing (1 atm.) and reducing atmosphere (10^{-16} atm.) respectively [21]. This is significantly lower than the conductivity of 10ScSZ which is 0.3 S cm^{-1} at 1000°C [22]. Due to the formation of the insulating phase at the LSCF73 and 10Sc1CeSZ interface, fast degradation and lower performance is expected for oxygen separation devices incorporating this composite. The phase would act as a barrier to the ion conduction and greatly increase the overall cell resistance, causing low performance and durability. The thermal expansion coefficient of $SrZrO_3$ (2.6×10^{-5} K^{-1}) is lower than 10ScSZ (10.3×10^{-6} K^{-1}) [23]. This can generate stress and small cracks over time leading to failure.

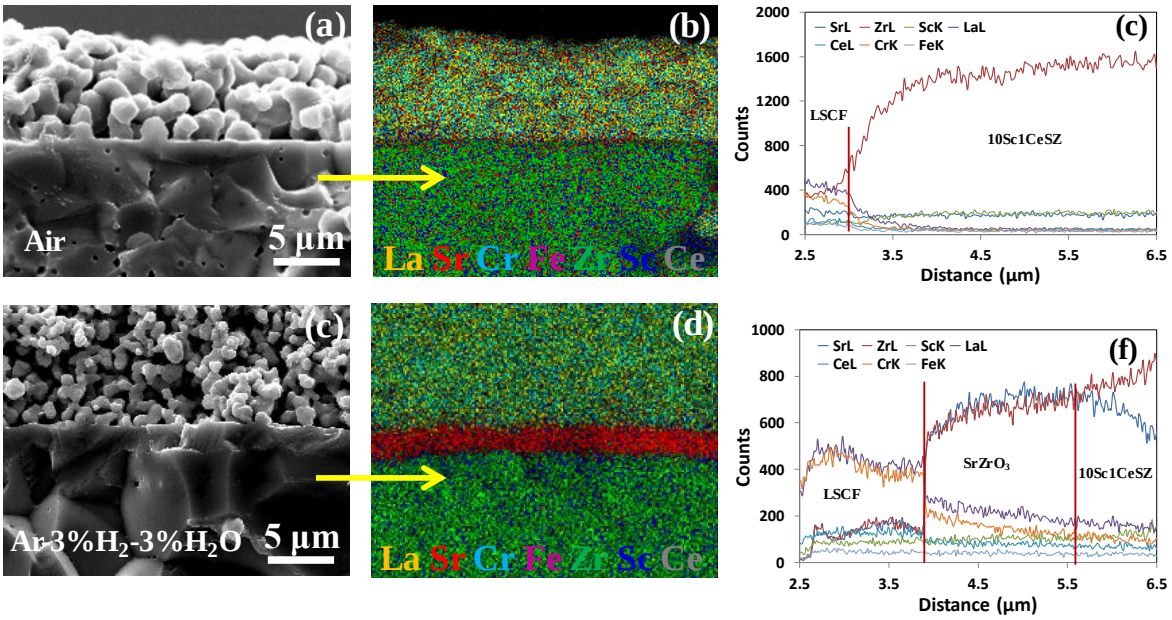

Fig. 11.10. SEM-EDS elemental mapping and line profiles of LSCF73 screen printed on 10Sc1CeSZ and sintered in air and Ar-3%H_2-3%H_2O: (a, d) secondary electron image, (b, e) elemental mapping, (c, f) elemental line profiles.

11.4.4. *Mechanism hypothesis for $SrZrO_3$ and FeO. $(Fe_xCr_{2-x})O_3$ formation in reducing atmosphere*

Cr: Fe ratio is playing a significant role in the formation of $SrZrO_3$ formation and its amount variation in LSCF73/82/91 composite. The higher the Fe doping levels in the LSCF perovskite, the higher the $SrZrO_3$ formation. Iron tends to reduce its valence state from $Fe^{4+} \rightarrow Fe^{3+}$ (Eq. (1)) and $Fe^{3+} \rightarrow Fe^{2+}$ (Eq. (2)) in reducing atmospheres and the charge is compensated by oxygen vacancies as shown below:

$$\frac{1}{2}O_2 + V_O^{\cdot\cdot} + 2Fe_{Fe}^{\times} = O_O^{\times} + 2Fe_{Fe}^{\cdot} \quad (1)$$

$$\frac{1}{2}O_2 + V_O^{\cdot\cdot} + 2Fe_{Fe}^{\prime} = O_O^{\times} + 2Fe_{Fe}^{\times} \quad (2)$$

where $Fe_{Fe}^{\times}$ refers to Fe^{3+} on Fe^{3+} sites, $Fe_{Fe}^{\cdot}$ refers to Fe^{4+} on Fe^{3+} sites, $Fe_{Fe}^{\prime}$ refers to Fe^{2+} on Fe^{3+} sites, and $V_O^{\cdot\cdot}$ refers to oxygen vacancy with two positive charges.

The higher the Fe concentration, the higher the oxygen non-stoichiometry or oxygen vacancies formation in the LSCF lattice corresponding to less stability of the material. The interaction between the perovskite and fluorite resulting in the formation of $La_2Zr_2O_7$ and/or $SrZrO_3$ is documented in the literature for lanthanum strontium manganite (LSM)/8YSZ composite. The reported mechanism suggests that interaction between perovskite/fluorite phases proceeds by the unidirectional diffusion of manganese into YSZ. After Mn diffuses from the B-site into YSZ, LSM perovskite gets enriched on the A-site resulting into La/Sr interaction with Zr at the interface of LSM/8YSZ and the formation of $La_2Zr_2O_7$ and/or $SrZrO_3$ [24-25].

A similar mechanism for $SrZrO_3$ formation is proposed in LSCF/10Sc1CeSZ composites. The diffusion coefficient of Fe in YSZ is 10^{-23} m^2/s at 800°C [15]. Likewise for the LSM/8YSZ system, Fe diffuses into 10Sc1CeSZ and the perovskite lattice is then enriched on the A-site and therefore, Sr from the A-site reacts with Zr resulting in the formation of $SrZrO_3$ (SZO). Concurrently, the Cr and Fe components at the B-site, now in excess within the LSCF perovskite lattice, react to form FeO. $(Fe_xCr_{2-x})O_3$ to keep the mass balance. Similar $SrZrO_3$ and Co/Fe containing compound formations are reported for the LSCoF/10GDC/8YSZ system [26]. With an increase in the Cr: Fe ratio, the Fe diffusion into the 10Sc1CeSZ lattice decreases and therefore, the perovskite A-site enrichment due to B-site cation or Fe diffusion into the Zr phase also decreases. Consequently, the formation of $SrZrO_3$ and FeO. $(Fe_xCr_{2-x})O_3$ also decreases with a decrease in Fe content.

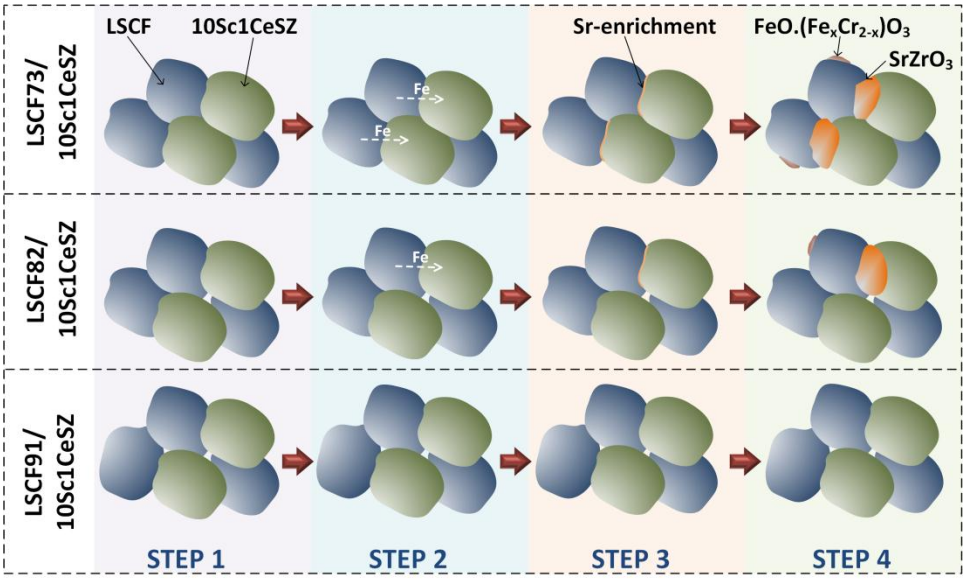

Fig. 11.11. Schematic of reaction steps for the formation of $SrZrO_3$ and FeO. $(Fe_xCr_{2-x})O_3$ in reducing atmosphere.

Fig. 11.11 shows a schematic of mechanistic steps for $SrZrO_3$ and FeO. $(Fe_xCr_{2-x})O_3$ formation in reducing atmosphere. Step 1 shows an initial stage of all three LSCF/10Sc1CeSZ composites with varying Cr: Fe ratio heating to reaction temperature. Diffusion assisted changes occur in step 2. In the case of LSCF73/10Sc1CeSZ and LSCF82/10Sc1CeSZ, Fe diffuses from the LSCF lattice to 10Sc1CeSZ. Fe diffusion decreases with a decrease in Fe-doping level. Due to low Fe concentration, no Fe-diffusion occurs in LSCF91/10Sc1CeSZ under OTM operating conditions. In step 3, LSCF perovskite lattice is A-site enriched after the Fe-diffusion. Subsequently, in step 4, Sr from the A-site reacts with Zr to form $SrZrO_3$ at the interface of LSCF/10Sc1CeSZ and Cr/Fe react to form FeO. $(Fe_xCr_{2-x})O_3$ to maintain a mass balance. No reactions compounds are formed in the case of the LSCF91 composite. It is to be noted that LSCF91/10Sc1CeSZ remains the same during the process attributed to its higher stability in reducing atmosphere.

A co-relation exists between Cr: Fe ratio, $SrZrO_3$ and FeO. $(Fe_xCr_{2-x})O_3$ secondary phase formation. With a decrease in Fe content, $SrZrO_3$ formation decreases suggesting that the doping amount of Fe will play a significant role on the stability of LSCF based membrane/fuel electrodes. To minimize the secondary phase formation, a decrease in the Fe-content in the LSCF perovskite and utilization of LSCF91 based composites are suggested for ceramic oxygen separation devices such as OTMs.

11.5. Conclusion

The effect of Cr: Fe ratio on processing and bulk/interface stability has been studied under OTM processing (1400°C and PO_2~0.21-10^{-10} atm) and operating conditions (1000°C and PO_2~10^{-12} atm). The highest stability is obtained for LSCF91 composite in both OTM processing and operating conditions. The density of LSCF/10Sc1CeSZ composite increases with decreasing Cr: Fe ratio and PO_2. The highest measured densification was achieved with the LSCF73/10Sc1CeSZ composite in reducing atmosphere (Ar-3%H_2-3%H_2O). $SrZrO_3$ and FeO. $(Fe_xCr_{2-x})O_3$ formation is identified in the samples sintered in reducing atmosphere and increases with decreasing Cr: Fe ratio and PO_2. After exposure to OTM operating conditions (1000°C and PO_2~10^{-12} atm) for 500h, LSCF73 and LSCF82 composites show $SrZrO_3$ formation. No secondary phase formation including $SrZrO_3$ and FeO. $(Fe_xCr_{2-x})O_3$ are identified in LSCF91 composite with Cr: Fe:: 9: 1.

11.6. References

[1] H.J.M. Bouwmeester, A.J. Burggraaf, in: A.J. Burggraaf, L. Cot (Eds.), Membrane Science and Technology Series, Elsevier, Amsterdam, 1996, pp. 435–510.

[2] S. Gupta, M.K. Mahapatra, P. Singh. Materials Science and Engineering R 90 (2015) 1–36.

[3] M. Liu, A.V. Joshi, Y. Shen, K. Krist, US Patent 5,273,628, 1993.

[4] R.M. Thorogood, Developments in air separation. Gas Sep. Purif. 5 (1991) 83-94.

[5] E.A. Hazbun, US Patent 4,791,079, 1988.

[6] W. Wang, Y.S. Lin, J. Membr. Sci. 103 (1995) 219-233.

[7] J.E. ten Elshof, H.J.M. Bouwmeester and H. Verweji. Appl. Catal. A: General 130 (1995) 195-212.

[8] S.P.S. Badwal, F.T. Ciacchi. Adv Mater. 13 (2001) 993-96.

[9] S. Pei, M.S. Kleefisch, T.P. Kobylinski, K. Faber, C.A. Udovich, V. Zhang-McCoy, B.Dabrowski, U. Balachandran, R.L. Mieville, R.B. Poeppel. Catal. Lett. 30 (1995) 201-212.

[10] U. Balachandran, J.T. Dusek, S.M. Sweeney, R.B. Poeppel, R.L. Mieville, P.S. Maiya, M.S. Kleefisch, S. Pei, T.P. Kobylinski, C.A. Udovich, A.C. Bose. Am. Ceram. Soc. Bull. 74 (1995) 71-75.

[11] A.G. Dixon, W.R. Moser, Y.H. Ma. Ind. Eng. Chem. Res. 33 (1994) 3015-3024.

[12] W. He, H. Huang, M. Chen, J.F. Gao, C.S. Chen. Solid State Ionics 260 (2014) 86–89.

[13] A.A. Yaremchenko, V.V. Kharton, V.A. Kolotygin, M.V. Patrakeev, E.V. Tsipis, J.C. Waerenborgh. J. Power Sources 249 (2014) 483–496.

[14] J. Pe˜na-Martinez, D. Marrero-Lopez, D. Perez-Coll, J.C. Ruiz-Morales, P. Nu˜nez, Electrochim. Acta 52 (2007) 2950.

[15] J.M. Haag, B.D. Madsen, S.A. Barnett, K.R. Poeppelmeier, Electrochem. Solid State Lett. 11 (2008) B51.

[16] D.K. Lee, H.I. Yoo. J. Electrochem. Soc. 147 (2000) 2835.

[17] V.V. Kharton, E.V. Tsipis, I.P. Marozau, A.P. Viskup, J.R. Frade. J.T.S. Irvine, Solid State Ionics 178 (2007) 101.

[18] W. Fang, Y. Zhang, J. Gao, C. Chen. Ceramics International 40 (2014) 799–803.

[19] J.J. Liu, T. Liu, W.D. Wang, J.F. Gao, C.S. Chen. J. Membr. Sci. 389 (2012) 435–440.

[20] W. He, H. Huang, M. Chen, J.F. Gao, C.S. Chen. Solid State Ionics 260 (2014) 86–89.

[21] M.K. Mahapatra, P. Singh, S.T. Misture. Applied Physics Letters 101 (2012) 131606.

[22] Nongluck P. Suriyayothin, PhD thesis, 1984.

[23] Y. Arachi, H. Sakai, O. Yamamoto, Y. Takeda, N. Imanishai. Solid State Ionics 121 (1999) 133–139

[24] D. Ligny, P. Richet. Physical Review B 53 (1996) 3013-3022.

[25] M. Chen, PhD thesis, Zurich, 2005

[26] C. Levy, Y. Zhong, C. Morel. J. Electrochemical Society 157 (2009) B1597-B1601.

[27] F. Wang, M. Nishi, M. E. Brito, H. Kishimoto, K. Yamaji, H. Yokokawa, T. Horita. J. Power Sources 258 (2014) 281-289.

CHAPTER 12: PERFORMANCE AND POST-TEST CHARACTERIZATION OF OTM SYSTEM IN EXPERIMENTAL COAL GASIFIER

12.1. Abstract

An early design of oxygen transport membranes (OTM) developed and fabricated by Praxair have been tested at 850-900°C in an experimental coal gasifier using a blend of Illinois and Powder River Basin (PRB) coals. Oxygen flux was measured and found to be stable over approximately 80 hours of gasifier operation. Study of interactions between the OTM and coal ash and gas phase impurities indicated that the OTM components remain chemically and structurally stable against coal ash and do not show any indication of solid or liquid (slagging) compound formation. The structure of the active fuel oxidation layer in the OTM exposed to the coal gas also remained stable and no interactions between the consecutive layers (porous support/fuel oxidation layer/gas separation layer/oxygen incorporation layer) were identified in the tested OTM system.

12.2. Introduction

High temperature ceramic oxide based oxygen transport membranes (OTM) offer flexibility of operation ranging from clean coal combustion and efficient power generation to syngas production for a variety of industrial applications [1-10]. Selective separation of oxygen from an oxidizing gas stream is achieved through the transport of oxygen ions through dense ceramic membranes under an imposed oxygen chemical potential gradient or an applied electrical potential. An overview of the oxygen transport membrane technology and its applications in the above-mentioned industrial processes, including power generation

with near-zero greenhouse gas emissions, has been recently published in a review article by Gupta et al. [11].

Challenges in terms of efficiency and gas phase pollutants such as SO_x, NO_x, and PM's in conventional coal-based power generation have been well documented in the literature [9-11]. Approaches for improving power plant efficiency along with reduction in greenhouse gas emissions have also been studied and reported [12-15]. In a retrofit situation using oxy-fuel combustion [16], pure oxygen would replace air required for combustion, and the oxygen would be supplied nominally via a cryogenic air separation unit (ASU). The above power plant configuration, however, imposes a significant energy penalty due to parasitic power requirements of the cryogenic ASU [11]. An oxygen transport membrane system, on the other hand, provides high purity gaseous oxygen for efficient and clean combustion of fossil fuels in integrated gasification combined cycle (IGCC) systems or coal fired oxy-fuel combustion boilers and allows for the development of cost-effective system configurations amenable for the capture and sequestration of CO_2 [16-18]. In comparison to the cryogenic and pressure swing processes, the distinct advantages of the oxygen production by dense ceramic membranes are that they can be integrated into a process cycle or unit operation leading to capital cost savings and reduced operating costs for power cycles with CO_2 capture and compression [14].

The Advanced Power Cycle (APC) has been developed by Praxair to incorporate ceramic oxygen transport membranes (OTM) into coal-fired power plants in order to facilitate carbon dioxide capture, depicted in Fig. 12.1. The process includes coal being reacted in an oxygen-blown gasifier to generate synthesis gas. A cyclone or a candle filter removes fines from the synthesis gas, before the synthesis gas is fed to an OTM partial

oxidation reactor (OTM POx). In the POx unit, the reaction between oxygen generated by the OTM tubes and synthesis gas provides heat, increasing the temperature of the synthesis gas. Power is then recovered by expanding the hot synthesis gas. After expansion, the synthesis gas is fed to the OTM boiler.

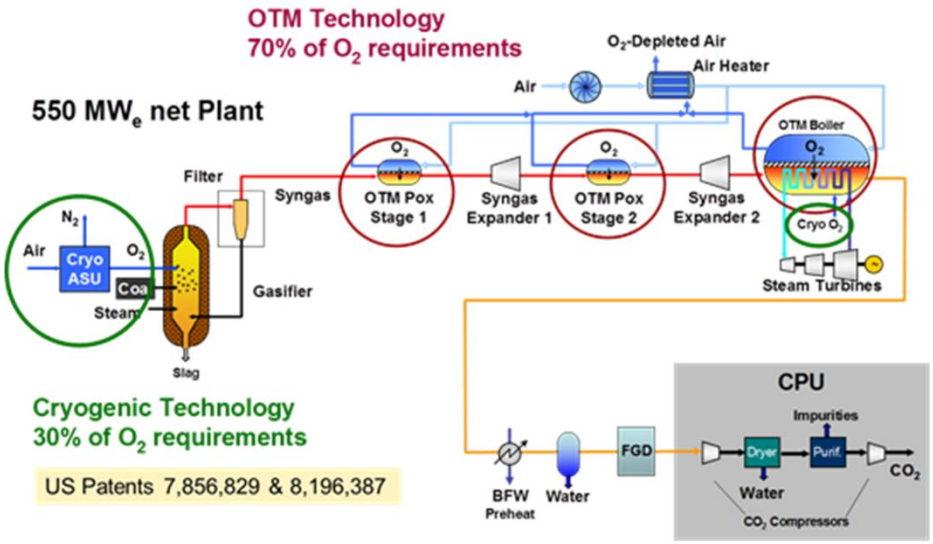

Fig. 12.1. Process for integration of OTM into power generation cycle with CO_2 Capture.

In the OTM boiler, synthesis gas reacts with oxygen produced from the OTM tubes. The exiting flue gas consists of ~ 45% H_2O, 52% CO_2, with a balance of N_2, SO_2, and O_2 is fed to a convective section of the boiler for further steam generation and boiler feed water preheating. The flue gas exiting the FGD scrubber consists mainly of CO_2 (>95%) and is compressed in a multistage compressor to >2000 psia for transport to the sequestration site.

OTM technology within the OTM Boiler and the OTM POx units in the Advanced Power Cycle utilizes the large gradient in oxygen partial pressure between the fuel and air side to drive and transport oxygen through the membrane. In its simplest form, a mixed conducting ceramic perovskite–fluorite dense composite film serves as the oxygen transport membrane when exposed to an oxygen gradient established between anodic (fuel) and the

cathodic (oxidant) atmospheres. A schematic of a mixed ionic-electronic (MIEC) based oxygen ceramic membrane is shown in Fig. 12.2. Significant research over the last decade has resulted in the identification, selection, testing and optimization of several A and B site doped perovskites (electronic/ionic conductors) and doped zirconia (ionic conductor) for devices operating at ~1000°C [11-27]. Mechanistic understanding of the OTM system and the behavior of various perovskite–fluorite materials under OTM operating conditions can be found in the recently published article by the authors [11]. Although some results have been reported for select membrane and electrode configurations [28-32], the performance data is only captured by maintaining an oxygen partial pressure gradient using air at the feed side and reducing gas (e.g. H_2 and CO) at the permeate side. OTM system performance in a real coal gas atmosphere with post-test characterization has not previously been reported in the literature.

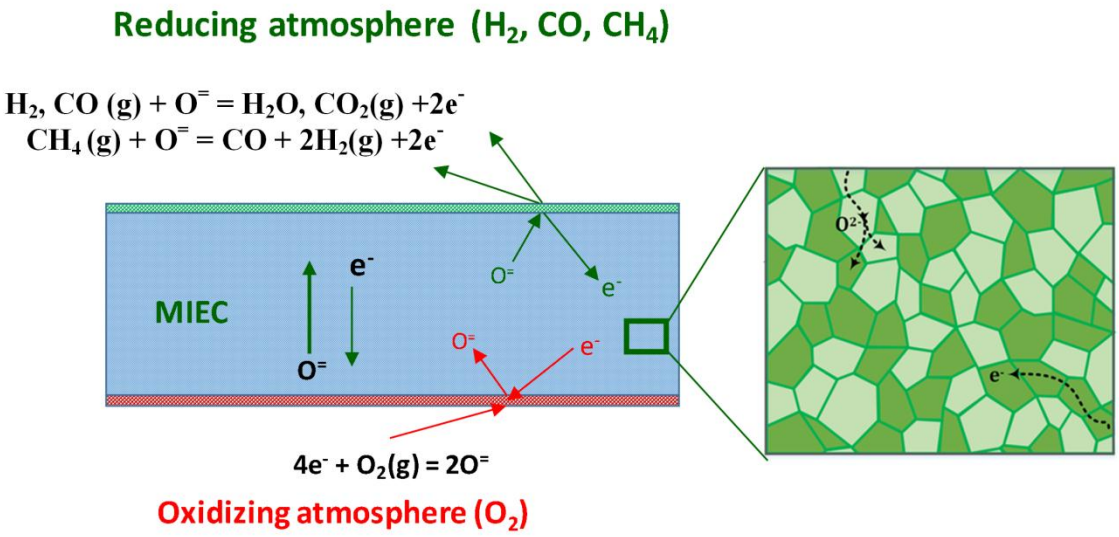

Fig. 12.2. Schematic of the operation of a mixed ionic-electronic conducting (MIEC) oxide based oxygen transport membrane.

This study provides the performance of fluorite – perovskite dual phase composite based OTM tubes tested in a gasified coal blend, which consisted of a high-sulfur bituminous Illinois coal and a sub-bituminous low-sulfur North Antelope Powder River Basin (PRB) coal. Post-test characterization of the tubes is performed to understand the materials degradation resulting from solid–solid interactions and solid–gas interactions during the exposure to the gasifier environment and electrochemical operation. The approach for the evaluation of the component structure (bulk, interface and surface) along with identification of the chemical composition and development of mechanistic understanding utilizes analytical tools and techniques such as FESEM, EDS, XRD, and DSC.

12.3. Experimental

12.3.1. *OTM device materials*

A tubular OTM device consisting of three layers (oxygen incorporation layer, gas separation layer and fuel oxidation layer) is fabricated and supported on porous $Zr_{0.942}Y_{0.058}O_{1.971}$ for mechanical strength. The air-side porous oxygen incorporation layer is made of 50 vol% $(La_{0.8}Sr_{0.2})_{0.98}MnO_{3-\delta}$ perovskite and 50 vol% $Zr_{0.802}Sc_{0.18}Y_{0.018}O_{1.901}$ (10Sc1YSZ) fluorite. The dense separation layer consisted of nominally 40 vol% $(La_{0.825}Sr_{0.175})_{0.94}Cr_{0.72}Mn_{0.26}V_{0.02}O_{3-\delta}$ and 60 vol% 10Sc1YSZ. The fuel-side porous fuel oxidation layer is comprised of nominally 60 vol% $(La_{0.825}Sr_{0.175})_{0.96}Cr_{0.76}Fe_{0.225}V_{0.015}O_{3-\delta}$ and 40 vol% 10Sc1YSZ. The thickness of the three layers is in the range of 20 to 30μm. The details on the materials chosen and fabrication of the OTM device is mentioned elsewhere [33-34].

12.3.2. *Coal-based OTM Gasifier*

An OTM reactor, shown in Fig. 12.3, was constructed at the University of Utah to test the performance of OTM tubes in a coal-derived syngas fuel [35-36]. A Hot Oxygen Burner (HOB), developed by Praxair, was used to generate the syngas. The HOB is a compact, high-intensity gasifier designed to generate activated carbon from coal. A scaled-down version was designed and fabricated by Praxair and sent to the University of Utah to attach to the OTM reactor. The HOB uses a very lean, hot oxygen/natural gas flame to gasify the coal at high temperatures and high heating rates. The products are a highly reactive coal char and a syngas fuel. The char particles were rejected at the outlet of the gasifier using a particle impact plate, and the syngas was then directed up into the OTM reactor, as shown in Fig. 12.3. In this configuration, the OTM tube avoided direct contact with the largest of the char and residual ash mineral particles in the coal. Only the very fine particulates remained entrained and entered the main OTM reactor chamber. Additionally, the fuel gas that interacted with the OTM tubes possessed a high concentration of active fuel species.

The OTM reactor consisted of three sections, as shown in Fig. 12.3. Section 1 (Fig. 12.3a) contained the hot oxygen burner (HOB) for production of syngas, as well as the particle impact plate to reject the largest of the coal and ash particles. Section 2 (Fig. 12.3b) housed the OTM tubes and was designed to provide sufficient contact with coal volatiles and gasification products. Section 3 (Fig. 12.3c) was the exhaust section, which also contained a natural gas torch that served as an afterburner for any unreacted fuel. The reactor and the OTM tubes were first preheated to the target operating temperature for the OTM tubes, using electrical heating panels that were located between the refractory and insboard insulation, and supplemented by some heat input from the torch afterburner. Included on the right side

of the reactor were sampling ports (Fig. 12.3b). These ports were used to sample synthesis gas before and after interaction with an OTM tube, when the OTM was positioned in the middle port. The ports were also used for extractive sampling of entrained solids.

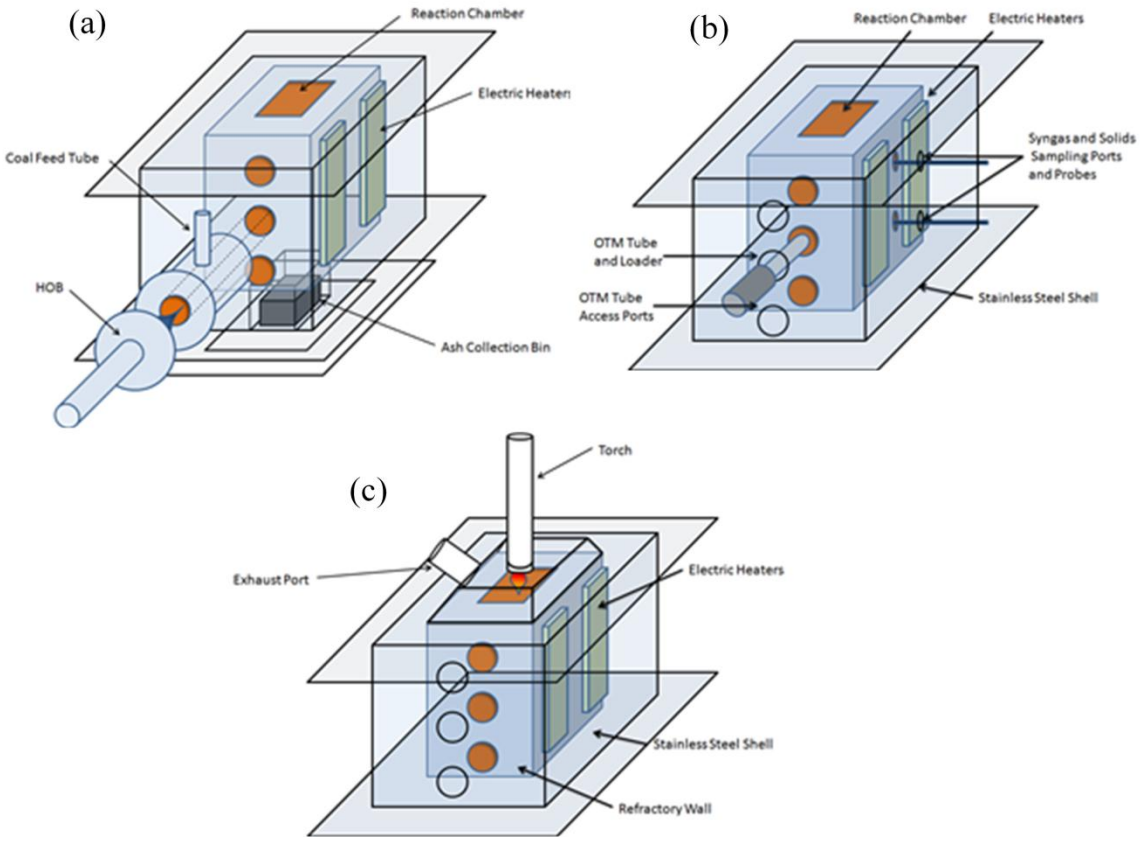

Fig. 12.3. Schematic showing: a) Section 1, b) Section 2 and c) Section 3 of the OTM Coal Gas Reactor at the University of Utah [36].

12.3.3. *Oxygen Flux Measurement*

OTM tubes (Fig. 12.4), were tested in the synthesis gas derived from a coal blend comprised of a high-sulfur bituminous Illinois coal and a sub-bituminous low sulfur North Antelope Powder River Basin (PRB) coal. The Illinois coal was blended at 50 wt % to 50 wt % with the PRB. The analysis of each coal is given in Table 12.1. The OTM reactor was

operated in the temperature range of 850-950°C for 80 h. Gas chromatography (Varian Micro GC) was used for the identification of major species in the synthesis gas. Fuel produced from combustion of the coal blends in the HOB was analyzed by ALS Environmental.

The oxygen transport rate, or oxygen flux, across the OTM membrane was calculated using the following equation:

$$J_{O2} = \frac{F_{\text{in}} x_{\text{O2in}} - F_{\text{out}} x_{\text{O2out}}}{A} \quad (1)$$

Where J_{O2} is the oxygen flux, F_{in} is the inlet air flow rate, F_{out} is the outlet air flow rate, x_{O2in} is the mole fraction of oxygen in the inlet air, x_{O2out} is the mole fraction of oxygen in the outlet air and A is the active area.

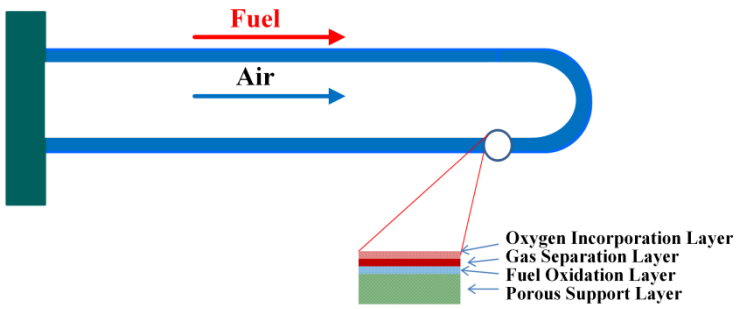

Fig. 12.4. Schematic of oxygen transport membrane tube.

Table 12.1. Analysis of Coals used in testing campaigns with Praxair OTM tubes (wt. %).

Coal Type	LOD (105°C)	Ash (705°C)	C	H	N	S	O (By diff.)	Volatile Matter	Fixed Carbon	HHV (BTU/lb)
Illinois	9.65	7.99	64.67	5.59	1.12	3.98	16.65	36.78	45.58	11598
PRB	23.69	4.94	53.72	6.22	0.78	0.23	34.11	33.36	38.01	9078

12.3.4. *Post-test Characterization*

OTM tubes tested while using the Illinois/PRB coal blend in the experimental coal gasifier were analyzed for surface, interface and bulk structure, as well as chemistry interactions between the OTM and surface ash deposits and electrochemically active cell components. Ash deposits were removed from the OTM using scotch tape, and samples were examined using a scanning electron microscope (FEI - ESEM Quanta 250, Hillsboro, OH). Energy dispersive spectroscopy (EDS) attached to the SEM was used for elemental compositional analysis. The porous support tube surface and selected fractured samples obtained from the OTM units were also analyzed for microstructure, chemistry, and elemental distribution using SEM-EDS.

X-ray diffraction (BRUKER-D8 ADVANCE, Bruker AXS Inc. Madison, WI) was used to identify the ash deposit and secondary compounds. The scan step was 0.02° using CuK_{α} radiation ($\lambda = 1.5406$ Å).

Differential scanning calorimeter (DSC; DSCQ100-TA) analysis was conducted on the ash deposit to understand its melting characteristics. The DSC experiment was conducted in air with ~ 10 mg of powder in the temperature range of 600-1200°C at a 20°C/min heating rate.

12.4. Results and discussion

12.4.1. *Oxygen Flux and Gas Chromatography Analysis*

During operation, a single OTM tube was typically positioned in the middle port or top port of the OTM section (Section 2). The gradient in oxygen partial pressure facilitated oxygen transport from the air side to the fuel side of the OTM tube. The exterior of the OTM tube was exposed to the coal-derived syngas produced in the HOB section (Section 1), and

the syngas had a very low oxygen partial pressure. Air was fed continuously through a lance tube into the OTM tube annulus, and oxygen-depleted air was continuously removed from OTM tube. An oxygen analyzer was used to measure the fraction of oxygen in the oxygen-depleted air. Mass flow meters were used to measure the flow rate of fresh air into the OTM tube, and the flow rate of oxygen depleted air out of the OTM tube. The oxygen transport rate, or oxygen flux, across the OTM membrane was calculated using Eq. (1).

During a short test campaign performed on OTM tubes in syngas derived from the blended Illinois/PRB coal, no discernible performance degradation was observed. Performance consistency over time is illustrated in Fig. 12.5 for various operating temperatures. After performance testing of OTM tubes in coal-derived syngas environments, buildup of loose and fixed ash on the outside of the OTM tube i.e. the porous substrate surface, was observed. Repeated tests were performed to determine if the loose ash negatively affected the tube performance through the introduction of additional mass transport resistance. The loose ash was removed from the surface of the OTM tube through an air blower after the OTM had been cooled down. It can be seen in Fig. 12.6 that the O_2 flux measurements with and without the loose ash are consistent over a range of operating temperatures. This result suggests that the collection of loose ash on the outside surface did not add a significant resistance to the transport of H_2 and CO to the OTM active layers.

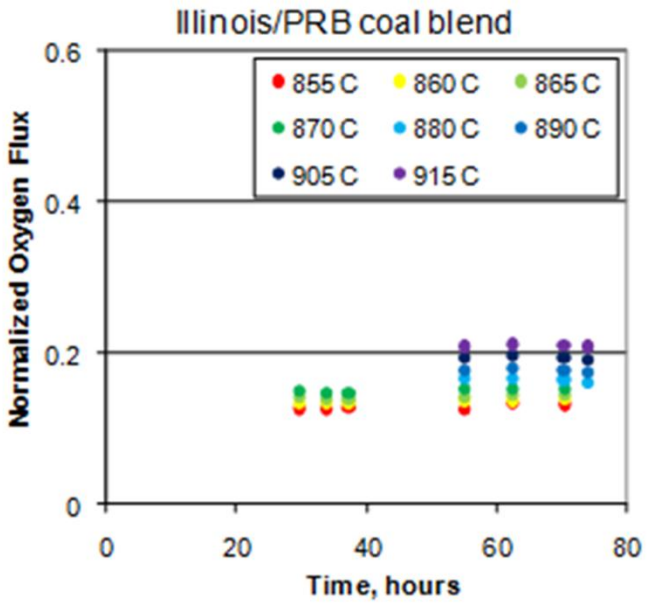

Fig. 12.5. OTM performance as a function of operating time in syngas derived from an Illinois/PRB coal blend.

In actual operation, both ash and char may be present in contact with the OTM tubes depending on the system configuration and extent of coal gas clean-up employed. The flow of char and ash into the OTM zone of the reactor was measured using an isokinetic sampling probe at two different points in the reactor during one of the tests. The sampled solids flow was between 2.15 and 2.56 g/s. Gas chromatography results collected with a Varian Micro GC provided compositional information for major species in the synthesis gas produced, and these results are shown in Table 12.2. The fuels produced from combustion of the coal blends in the HOB were also sampled and collected in Tedlar bags, and those samples were analyzed by ALS Environmental for concentrations of CH_4, C_2H_4, C_2H_6, H_2S, COS, CS_2, NH_3, HCN, and Cl. The results of these analyses are presented in Table 12.3.

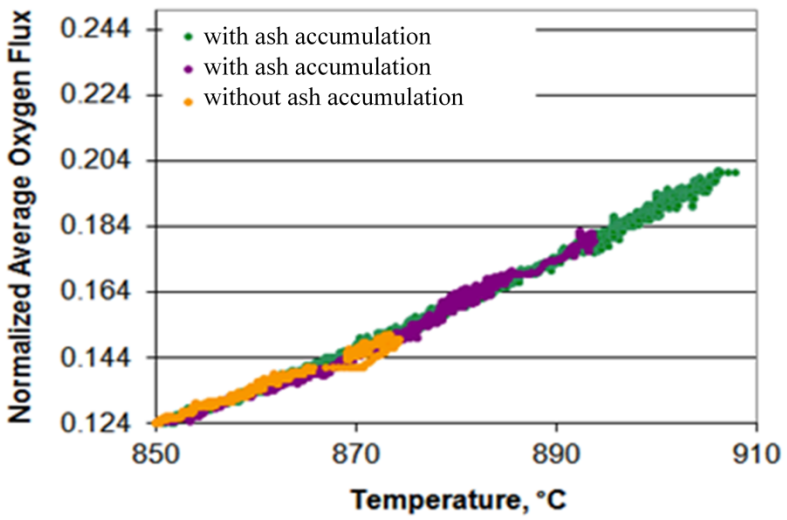

Fig. 12.6. OTM performance in Illinois/PRB coal derived synthesis gas with and without accumulated ash.

Table 12.2. Fuel compositional analysis (dry vol. %)

	H_2	N_2	CO	CH_4	CO_2
Illinois/PRB Blend	20 ± 1.6	0.93 ± 0.62	34.84 ± 3.41	0.86 ±0.08	42.42 ± 5.54

Table 12.3. Trace species analysis of synthesis gas (ppm).

Coal Blend	CH_4	C_2H_4	C_2H_6	H_2S	COS	CS_2	NH_3	HCN	Cl
Illinois/PRB	5600	1400	88	0.052	340	29	2.3	<0.063	<0.11

12.4.2. *OTM device after testing: Macroscopic observations*

Significant buildup of loose ash on the porous substrate, which is the outside of the OTM tube used in this configuration, was observed after the completion of the testing campaigns. The post-test OTM tubes were disassembled and the tubular section was removed from the fixture. The surface exposed to coal gas showed ash deposit formation as shown in

Fig. 12.7a. The ash deposit was loose and separated easily from the porous support tube as shown in Fig. 12.7b.

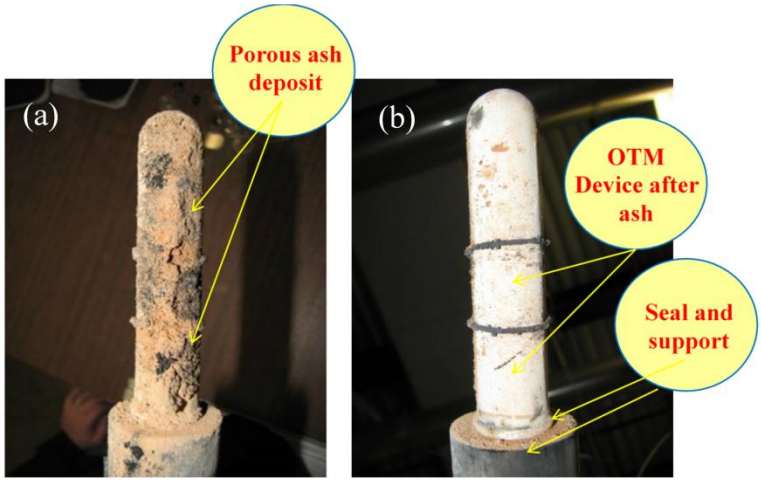

Fig. 12.7. OTM device after test: a) with ash accumulation and b) after ash removal.

12.4.3. *Post-test Characterization*

10.4.3.1. Ash Deposit – Morphology and elemental analysis

The porous support tube surface was analyzed by SEM and EDS techniques to examine the possibility of interaction, molten compound formation and surface pore closure. Surface analysis and the morphology of the ash deposit are shown in Fig. 12.8a, b and c. Powder agglomerates consisting of smooth and powdery ash are observed. The ash particles deposit at the pore surfaces, however, remain loose as shown in Fig. 12.8d, e and f. There is no indication of surface compounds or molten phase formations at the support tube surface. It is postulated that the molten phase present in the ash deposit formed via vaporization in the gasifier at elevated temperatures, and was then carried in the gas stream where it condensed in cooler regions and deposited on the OTM surface. SEM-EDS elemental analysis identifies the ash chemistry as shown in Fig. 12.8c and f.

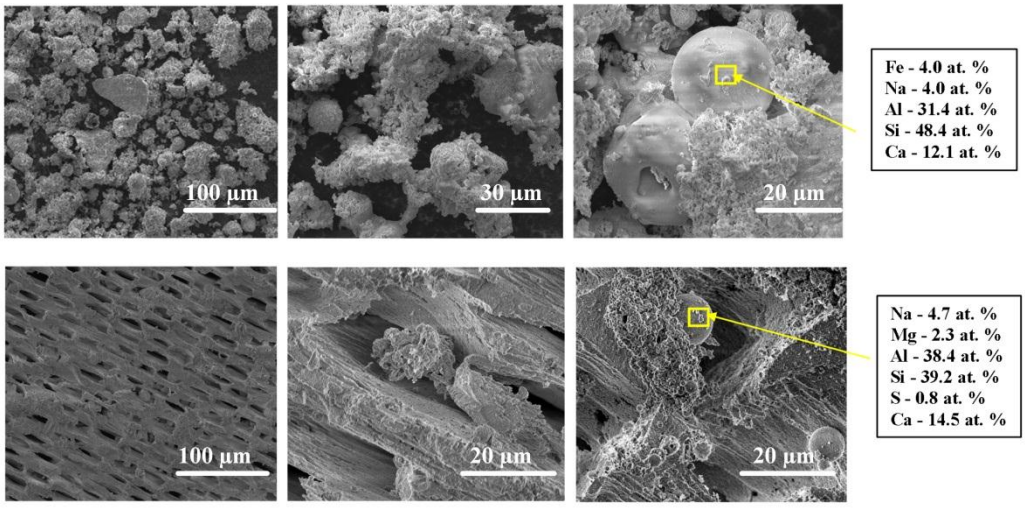

Fig. 12.8. Ash deposited on the OTM: (a) and (b) powdery deposit, (c) smooth deposit, (d), (e) and (f) localized ash deposit formed on the porous channel. Smooth deposits indicate formation of molten phase.

XRD patterns of the ash deposit are compared with standard JCPDS files for the identification of compounds. Complex silicates containing alkali, alkaline earth and transition metals are identified as possible compounds, as shown in Fig. 12.9. A literature search was subsequently carried out to understand the melting behavior of the silicates. It was postulated, based on the melting point, that the ash deposit on the OTM surface will not form liquid compounds under the experimental conditions (surface temperature ~ 1000°C). A complementary DSC analysis on the ash deposit was also performed in air to understand the melting characteristics. Our observations indicated endotherms (indicative of melting) above 1000°C, as shown in Fig. 12.10. This result confirms that the ash deposit will not adhere to the OTM surface in liquid form, as the melting point of the ash constituents are above the OTM operating temperature.

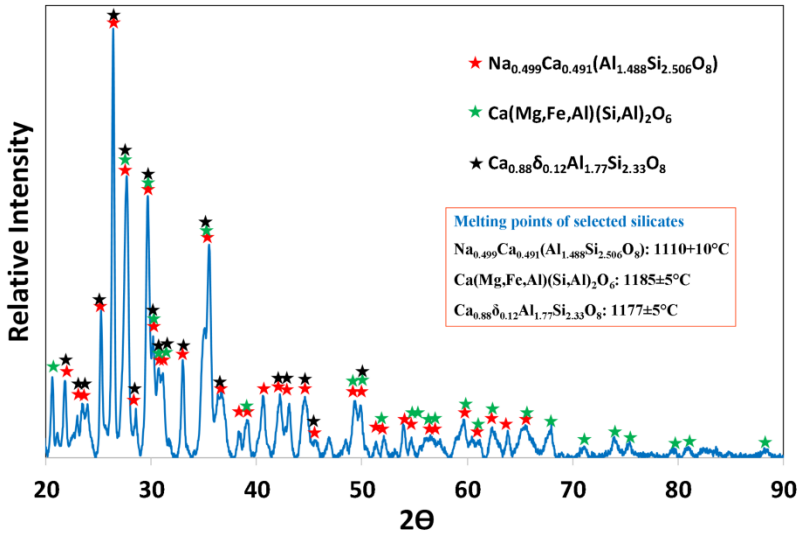

Fig. 12.9. XRD pattern obtained from the ash deposit. Chemistry and melting points are also shown.

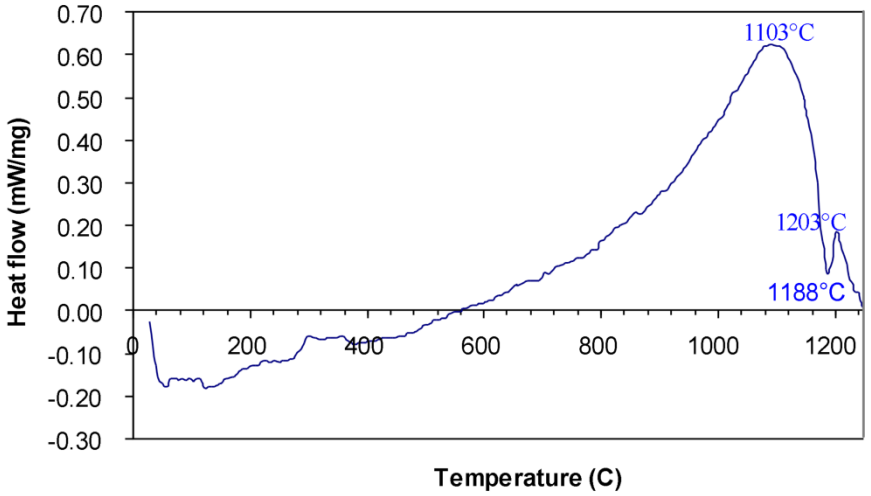

Fig. 12.10. DSC analysis on the ash deposit.

12.4.3.2. OTM tube cross-section: Microstructural analysis

Fig. 12.11 shows micrographs of the tested OTM tube cross-section. The oxygen incorporation layer, dense gas separation layer, fuel oxidation layer and porous support layer interfaces remain stable, as shown in Fig. 12.11. An interface reaction layer is not identified.

Smooth interfaces and lack of inter-diffusion is observed at the oxygen incorporation and fuel oxidation layer interfaces. No interaction between OTM active layers and coal ash is identified, as shown in Fig. 12.11. SEM-EDS analysis of each active layer and the interface between them does not indicate any secondary phase formation in the bulk as well as at the interface, as shown in Fig. 12.11b and d. Such microstructural features can be attributed to (a) thermochemical stability of the compounds under the exposure conditions and (b) short reaction times. No evidence of sulfur is detected in the fuel oxidation layer as shown in the active layer elemental analysis (Fig. 12.11d).

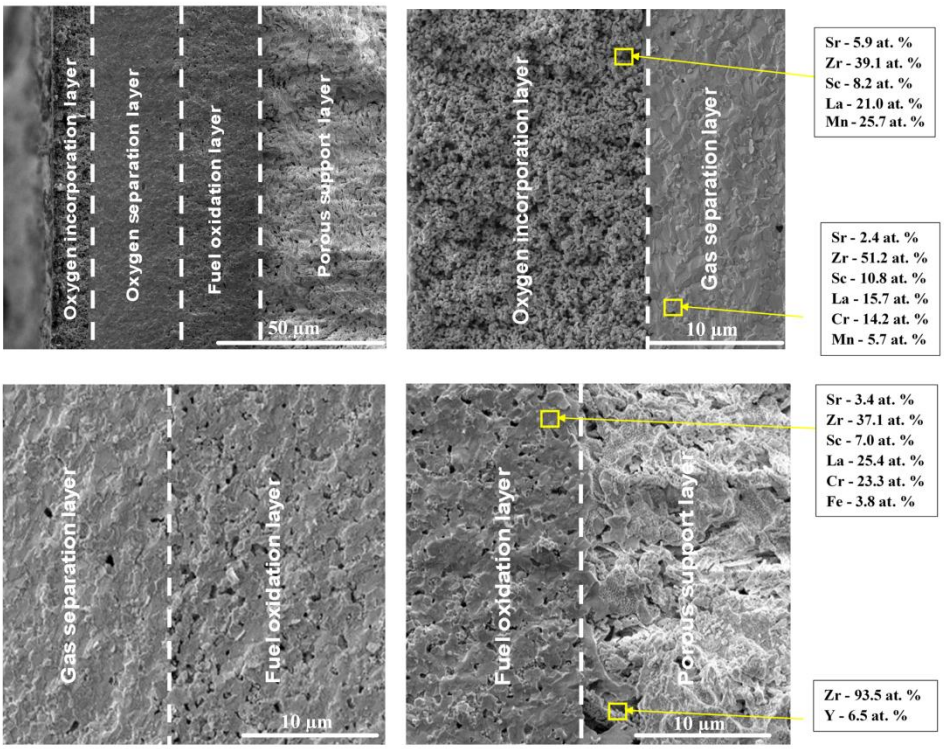

Fig. 12.11. Micrographs of OTM tube cross-section: (a) with all layers (oxygen incorporation layer, gas separation layer, fuel oxidation layer and porous support layer), (b) interface of oxygen incorporation layer and gas separation layer, (c) interface of gas separation layer and fuel oxidation layer, and (d) interface of fuel oxidation layer and porous support layer.

12.5. Conclusions

OTM tubes were tested in a reaction chamber coupled to a coal gasifier, and oxygen flux was measured over the temperature range of 850-900°C. Short-term stability of OTM operation in a high-sulfur atmosphere, and robustness of the material when exposed to direct coal ash contamination was demonstrated. Ash deposits did not form detectable reaction products when in contact with OTM tubes. Molten ash constituents, observed on the OTM surface, were most likely formed by mineral vaporization at the elevated temperatures in the gasifier zone, followed by condensation in cooler regions of the reactor. Porosity was maintained in the oxygen incorporation layer. No interfacial compound formation was observed between the separation and activation layers.

12.6. References

[1] D. Kang, R.S. Srinivasan, R.T. Thorogood, E.P. Foster. Integrated high temperature method for oxygen production. US Patent 5516359. 1996.

[2] A.G. Dixon, W.R. Moser, Y.H. Ma. Ind. Eng. Chem. Res. 33 (1994) 3015– 3024.

[3] S.S. Hashim, A.R. Mohamed, S. Bhatia. Renew. Sustain. Energy Rev. 15 (2011) 1284–1293.

[4] E.H. Shreiber EH, B.A.V. Hassel, R. Prasad. Oxygen separation method utilizing an oxygen transport membrane reactor. US Patent 7118612B2. 2006.

[5] Y. Zeng, Y.S. Lin, S.L. Swartz. J. Membr. Sci. 150 (1998) 87–98.

[6] B.C.H. Steele. Solid State Mater. Sci. 1 (1996) 684–691.

[7] I. Barnes. Next generation coal gasification technology. 2011;CCC/187 ISBN 978-92-9029-507-5:1-49.

[8] H.M. Associates, Princeton Energy Resources International, TFB Consulting. Assessment of the commercial potential for small gasification combined cycle and fuel cell systems phase II final draft report. US Department of Energy. 2003;1–44.

[9] A. Frassoldati, A. Cuoci, T. Faravelli, E. Ranzi, C. Candusso, D. Tolazzi. Simplified kinetics schemes for oxy-fuel combustion. 1st International Conference on Sustainable Fossil Fuels for Future Energy – S4FE 2009;1–2.

[10] H. Stadler, F. Beggel, M. Habermehl, B. Persigehl, R. Kneer, M. Modigell, P. Jeschke. Int. J. Greenhouse Gas Control 5 (2011) 7-15.

[11] S. Gupta, M.K. Mahapatra and P. Singh. MSE:R:Reports 90 (2015) 1-36.

[12] R.E. Williford, P. Singh. J. Power Sources 29 (2004) 45-53.

[13] H. Boxun, M. Keane, K. Patil, M.K. Mahapatra, U. Pasaogullari, P. Singh. Applied Energy 134 (2014) 342–348.

[14] H. Li, J. Yan. Applied Energy 86 (2009) 826–836.

[15] E.J.O. Promes, T. Woudstra, L. Schoenmakers, V. Oldenbroek, A.T. Thattai, Applied Energy 155 (2015) 181-194.

[16] H. Li, J. Yan, J. Yan. Applied Energy 86 (2009) 202–213.

[17] Y. Hu, X. Li, H. Li, J. Yan. Applied Energy 112 (2013) 747–754.

[18] Y. Hu, J. Yan. Applied Energy 90 (2012) 113–121.

[19] S. Gupta, M.K. Mahapatra, P. Singh. Mat. Res. Bull. 48 (2015) 3262-67.

[20] K.T. Jacob, S. Gupta, P. Singh. J. Am. Ceram. Soc. 96 (2013) 3933-38.

[21] K.T. Jacob, S. Gupta and P. Singh. J. Am. Ceram. Soc. 96 (2013) 3272-3278.

[22] V.V. Kharton, E.V. Tsipis, I.P. Marozau, A.P. Viskup, J.R. Frade, J.T.S. Irvine. Solid State Ionics 178 (2007) 101–113.

[23] T. Norby, R. Hildrum, M. Seiersten, R. Glenne, P.A. Osborg and O. Dyrlie. Proceedings of the European Solid Oxide Fuel Cell Forum, Switzerland 1994:217-226.

[24] V.A. Kolotygin, E.V. Tsipis, A.L. Shaula, E.N. Naumovich, J.R. Frade, S.I. Bredikhin, V.V. Kharton. J. Solid State Electrochem. 15 (2011) 313–327.

[25] J.G.M.I. Furtado, R.N. Oliveira. Revista Matéria 13 (2008) 147–153.

[26] T. Nakamura, G. Petzow and L. Gauckler. Mater. Res. Bull. 14 (1979) 649–659.

[27] S. Tao and J.TS. Irvine. J. Electrochem. Soc. 151 (2004) A252–259.

[28] J. Yi, Y. Zuo, W. Liu, L. Winnubst, C. Chen. J. Mem. Sci. 280 (2006) 849-855.

[29] T.F. Tian, W. Li, T. Liu, C.S. Chen. Solid State Ionics 225 (2012) 690-694.

[30] W. Li, J.J. Liu, C.S. Chen. J. Mem. Sci. 340 (2009) 266-271.

[31] W. Fang, Y. Zhang, J. Gao, C. Chen. Ceramics International 40 (2014) 799-803.

[32] J.H. Joo, G.S. Park, C.Y. Yoo, J.H. Yu. Solid State Ionics 253 (2013) 64-69.

[33] N. Nagabhushana, A.J. Lane, G.M. Christie, H.B.A. Van. Composite oxygen ion transport membrane. European Patent Specification EP 2054355 B1. 2009.

[34] G.M. Christie, J.R. Wilson, H.B.A. Van. Catalyst containing oxygen transport membrane. Patent– WO 2011090645A2. 2011.

[35] J. R. Wilson, G.M. Christie, N. Degenstein, M. Shah, J. Li, V. Venkateswaran, E. Eddings E and J. Adams. OTM Based Oxy-fuel Combustion for CO_2 Capture. 34th International Technical Conference on Clean Coal & Fuel Systems, FL 2009.

[36] J.J. Adams. Oxy-coal Combustion using Oxygen Transport Membranes. Dept. of Chemical Engineering, University of Utah. Ph.D. Dissertation 2012.

CHAPTER 13: CONCLUSIONS AND FUTURE WORK

Mixed ionic electronic conducting (MIEC) perovskite oxides have the potential to enhance electrochemical/catalytic activity for a variety of applications: clean energy conversion, chemical processes, gas separation, and high purity oxygen production for healthcare and coal combustion along with syngas production with near-zero greenhouse emission. Superior thermo-chemical stability in aggressive environments (800-1000°C, 0.21-10^{-20} atm), along with mixed ionic electronic transport properties, drives the intense research and development efforts for doped lanthanum chromite perovskite as an oxygen transport membrane (OTM) for oxy-combustion of fuels. New materials for oxygen transport membrane have been developed and evaluated under OTM fabricating and operating conditions. This study: a) critically analyzed and examined the pertinent information on lanthanum chromite based perovskites in terms of chemistry, structure, and properties required for OTM systems, b) correlated the 'chemistry-structure-property-stability' relationships, and c) suggested approaches for tuning the desired properties and reliability.

Thermo-physical properties required for oxygen transport can be tuned by modifying the crystal structure, chemical bonding, and transport phenomena through tailoring dopants' type and level. This doctoral research work has investigated various important relationships between the dopant type and level along with structural-chemical stability and performance. The driving force for oxygen transport membrane system is oxygen partial gradient. Therefore, the materials stability and degradation has also been studied under varying PO_2 and temperature. Furthermore, performance stability has been evaluated using electrochemical tests with a variety of materials with different dopants, operating temperatures, atmospheres, and voltages. In order to simulate long-term (thousands of hours)

testing in a shorter time period, voltages up to 0.5 V above OCV were applied for up to 100 h. Investigation of air and fuel electrode degradation was conducted using symmetric cells in order to simplify the test setup by eliminating seal requirements. When compared to Mn-doped LSCM73, higher performance is obtained for Fe-doped LSCF73 in oxidizing and reducing atmosphere at the OTM operating temperature.

LSCM/LSCF (with and without 8YSZ/10ScSZ/10Sc1CeSZ fluorite phase) based materials are also investigated under OTM processing and operating conditions. LSCF perovskites are also studied with varying Cr: Fe ratio. It is found that the stability of the perovskite increases with increase in Cr: Fe ratio. Secondary phase (FeO_x and FeO. $(Fe_x.Cr_{2-x})O_3$) formations are identified in LSCF73 samples corresponding to the lower stability of LSCF with higher Fe content. LSCF perovskite stability decreases with decrease in PO_2 and Cr: Fe ratio. Compound formation as well as localized enrichment of cations within the perovskite phase is observed during the exposure to varying PO_2 atmospheres. Highest stability is obtained for LSCF91 with Cr: Fe:: 9: 1. Mechanisms for the formation of FeO_x and FeO. $(Fe_xCr_{2-x})O_3$ are proposed based on experimental observations, thermodynamic stability and defect chemistry. In case of LSCM/LSCF composite with 8YSZ/10Sc1CeSZ, interaction between LSCF perovskite phase and fluorite phase is identified attributing to the formation of $SrZrO_3$ in reducing atmosphere. The electrical conductivity of $SrZrO_3$ is 10^{-4}–10^{-5} S cm^{-1} at 1000°C respectively. This is significantly lower than the conductivity of YSZ which is 0.185 S cm^{-1} at 1000°C. This would result into fast degradation due to the formation of insulating phases at LSCF/LSCM and YSZ/ScSZ interfaces. These phases act as a barrier to the ion conduction and greatly increase the overall cell resistance, causing low performance and durability. The thermal expansion coefficient of $SrZrO_3$ is 6.8×10^{-6} K^{-1}

(1123-1443K) also lower than 10.3×10^{-6} K^{-1} for 8YSZ. This can generate stress and small cracks in OTM with time leading to failure. However, the interaction decreases with increase in Cr: Fe ratio. No secondary compound formation is identified in case of LSCF91 based materials.

Long term exposure test on LSCF/10Sc1CeSZ based materials are also conducted in reducing atmosphere under this research work. Exposure of pre-sintered LSCF+10Sc1CeSZ samples (1400°C, 10h) to simulated fuel gas (5%H_2-balance CO_2) exposure conditions at 1000C for 500 h show morphological changes and reaction products formation. Key findings include: a) Formation of $SrZrO_3$ (SZ) is observed in LSCF73/10Sc1CeSZ and LSCF82/10Sc1CeSZ samples when exposed to 5%H_2-CO_2 gas atmosphere at 1000°C for 500h. Amount of $SrZrO_3$ increases with increase in Fe doping level in LSCF, b) Surface morphology of 10Sc1CeSZ changes in case of exposed LSCF73/10Sc1CeSZ and LSCF82/10Sc1CeSZ samples when compared to LSCF91/10Sc1CeSZ and c) $SrZrO_3$ phase and the surface morphology changes have not been observed for LSCF91/10Sc1CeSZ when exposed to 5%H_2-CO_2 gas atmosphere at 1000°C for 500h. Mechanism for the formation of $SrZrO_3$ along with the relationship between Fe doping level and PO_2 has been developed in this study.

To avoid the secondary compounds formation and simultaneously improve on density, stability and performance, a new class of B-site co-doped materials ($La_{0.85}Sr_{0.15}Cr_{1-2y}Ni_yTi_yO_3$; y ~ 0.05, 0.1, 0.2 and 0.3) is developed based on the materials optimization review. Smallest deviation in the oxygen stoichiometry is observed for $La_{0.85}Sr_{0.15}Cr_{0.8}Ni_{0.1}Ti_{0.1}O_{3-\delta}$ (δ ~ 0.011), even on comparison with LSCF and LSCM based materials. The density of this class of materials increases with increase in Ni concentration.

Thermal expansion of $La_{0.85}Sr_{0.15}Cr_{0.8}Ni_{0.1}Ti_{0.1}O_3$ and $La_{0.85}Sr_{0.15}Cr_{0.6}Ni_{0.2}Ti_{0.2}O_3$ matches closely with 8YSZ. Among all the studied compositions, highest electrical conductivity and electrochemical performance is obtained for $La_{0.85}Sr_{0.15}Cr_{0.8}Ni_{0.1}Ti_{0.1}O_3$ in oxidizing and reducing atmosphere.

In collaboration with Praxair, perovskite/fluorite based OTM tubes are also developed and tested in real-world conditions. OTM devices were tested with fuel generated from a coal gasifier. Ash deposits on the OTM device were observed. However, the flux performance is not affected by the ash deposition and consistent results are obtained for up to 80h. Post-test examination of the OTM devices showed no evidence of reaction with ash deposits and poisoning of the constituent with gas phase contaminants (e.g. Sulfur compounds). Oxygen incorporation layer and gas separation layer and other interfaces remained stable. Stability of OTM operation in a high sulfur atmosphere, and robustness of the material set to coal ash contamination is demonstrated.

Oxygen flux performance of OTM is also dependent on ionic conductivity of the materials used. LSCM/LSCF/LSCNT based materials obtain very low ionic conductivity. Therefore, the perovskites are mixed with fluorite phase which is predominantly ionic conductor. However, $SrZrO_3$ formation tends to occur at the perovskite (LSCF73)/fluorite (10Sc1CeSZ) interface when exposed to fuel atmosphere for longtime up to 500h. In future, therefore, a study focused on the effect of various dopants to enhance the ionic conductivity of the materials along with stability would be beneficial. Furthermore, this study has demonstrated the long-term stability of LSCF91 based materials under OTM processing and operating conditions. However, co-processing of LSCF91 based materials along with other constituents (when deposited) of OTM is a challenge. Different methodology/techniques or

change in current processing parameters (e.g. temperature and pressure) for the deposition of LSCF91 based materials are need to be investigated in future to minimize the above mentioned issue while maintaining stability.

A-site deficiency is found to be beneficial to avoid Sr-segregation and minimize $SrZrO_3$ formation. However, additional study could be performed focused on the effect of A-site deficiency to provide a better understanding of its behavior and effect on the structure-property-performance-stability of OTM materials. Furthermore, there are several steps involved in the oxygen transport through the membrane. These steps include oxygen dissociation and adsorption at the air (feed) side and oxygen desorption and association at the fuel (permeate) side. Surface exchange of oxygen at the air and fuel side seems to play an important role in the performance of OTM device. Therefore, materials development from the perspective of improvement in surface exchange properties of the materials would be beneficial for further enhancement in the membrane flux performance. But the materials structure and composition would still need optimization in order to provide acceptable performance and stability.

This Ph.D. dissertation work is focused on the development and characterization of advanced ionically, electronically and mixed conducting perovskite/fluorite ceramic oxides for oxygen transport membrane system. The research work is also applicable to other high temperature electro-chemical systems that can serve as platform for solid state power devices (solid-oxide fuel and electrolysis cells; SOFC and SOEC), efficient combustion and life support applications.

APPENDIX A: PEER-REVIEWED PUBLICATIONS AND PROCEEDINGS

Sapna Gupta, Manoj Mahapatra and Prabhakar Singh. Lanthanum chromite based perovskites for oxygen transport membrane. Materials Science and Engineering R 90 (2015) 1-36.

Sapna Gupta and Prabhakar Singh. Manganese doped lanthanum-strontium chromite fuel electrode for solid oxide fuel cell and oxygen transport membrane systems. ECS Transactions 66 (2015) 117-123.

Sapna Gupta, Manoj Mahapatra and Prabhakar Singh. Phase transformation, thermal expansion and electrical conductivity of lanthanum chromite. Materials Research Bulletin 48 (2013) 3262-3267.

Sapna Gupta and Prabhakar Singh. Structural and electrochemical performance stability of perovskite-fluorite composite for high temperature electrochemical devices. Proceedings of the 39th International Conference on Advanced Ceramics and Composites, 2015.

Kallarackel Thomas Jacob, **Sapna Gupta** and Prabhakar Singh. Electrochemical Determination of Gibbs Energy of Formation of $LaCrO_3$ Using a Composition-Graded Bielectrolyte. J. Am. Ceram. Soc. 96 (2013) 3272-3278.

Kallarackel Thomas Jacob, **Sapna Gupta** and Prabhakar Singh. Thermodynamic properties of $LaCrO_4$, La_2CrO_6 and $La_2Cr_3O_{12}$, and sub-solidus phase relations in the system lanthanum-chromium-oxygen. J. Am. Ceram. Soc. 96 (2013) 3933-3938.

Sapna Gupta, Yu Zhong, Manoj Mahapatra and Prabhakar Singh. Processing and electrochemical performance of manganese-doped lanthanum-strontium chromite in oxidizing and reducing atmospheres, under review.

Sapna Gupta and Prabhakar Singh. A new stable nickel and titanium co-doped lanthanum strontium chromite for high temperature electrochemical devices, under review.

Sapna Gupta, Jamie Wilson, Eric Eddings, Joseph Adams, Manoj Mahapatra and Prabhakar Singh. Performance and post-test characterization of an OTM system in an experimental coal gasifier, under review.

Sapna Gupta, Jonathan Lane, Jamie Wilson, Pawel Plonczak and Prabhakar Singh. Interfacial stability of iron doped lanthanum strontium chromite and scandia stabilized zirconia in oxidizing and reducing atmosphere, under review.

APPENDIX B: COPYRIGHT PERMISSIONS

Chapter 1 of this dissertation was modified from the following published article: S. Gupta, M.K. Mahapatra and P. Singh. Lanthanum chromite based perovskites for oxygen transport membrane. Materials Science and Engineering R 90 (2015) 1-36. Copyright permission was received from Copyright Clearance Center (Order number: 3670860211826) for use of the full article in the author's dissertation.

Chapter 2 of this dissertation was modified from the following published article: S. Gupta, M.K. Mahapatra and P. Singh. Phase transformation, thermal expansion and electrical conductivity of lanthanum chromite. Materials Research Bulletin 48 (2013) 3262-3267. Copyright permission was received from Copyright Clearance Center (Order number: 3667270496190) for use of the full article in the author's dissertation.

Chapter 3 of this dissertation was modified from the following published article: K. T. Jacob, S. Gupta and P. Singh. Electrochemical Determination of Gibbs Energy of Formation of $LaCrO_3$ Using a Composition-Graded Bielectrolyte. J. Am. Ceram. Soc. 96 (2013) 3272-3278. Copyright permission was received from Copyright Clearance Center (Order number: 3670931304250) for use of the full article in the author's dissertation.

Chapter 4 of this dissertation was modified from the following published article: K. T. Jacob, S. Gupta and P. Singh. Thermodynamic properties of $LaCrO_4$, La_2CrO_6 and $La_2Cr_3O_{12}$, and sub-solidus phase relations in the system lanthanum-chromium-oxygen. J. Am. Ceram. Soc. 96 (2013) 3933-3938. Copyright permission was received from Copyright Clearance Center (Order number: 3671521473258) for use of the full article in the author's dissertation.

Chapter 5 of this dissertation was modified from the following published article: S. Gupta and P. Singh. Manganese doped lanthanum-strontium chromite fuel electrode for solid oxide fuel cell and oxygen transport membrane systems. ECS Transactions 66 (2015) 117-123. Copyright permission was received from ECS for use of the full article in the author's dissertation.